

## INFORMATION TO USERS

This manuscript has been reproduced from the microfilm master. UMI films the text directly from the original or copy submitted. Thus, some thesis and dissertation copies are in typewriter face, while others may be from any type of computer printer.

**The quality of this reproduction is dependent upon the quality of the copy submitted.** Broken or indistinct print, colored or poor quality illustrations and photographs, print bleedthrough, substandard margins, and improper alignment can adversely affect reproduction.

In the unlikely event that the author did not send UMI a complete manuscript and there are missing pages, these will be noted. Also, if unauthorized copyright material had to be removed, a note will indicate the deletion.

Oversize materials (e.g., maps, drawings, charts) are reproduced by sectioning the original, beginning at the upper left-hand corner and continuing from left to right in equal sections with small overlaps.

Photographs included in the original manuscript have been reproduced xerographically in this copy. Higher quality 6" x 9" black and white photographic prints are available for any photographs or illustrations appearing in this copy for an additional charge. Contact UMI directly to order.

ProQuest Information and Learning  
300 North Zeeb Road, Ann Arbor, MI 48106-1346 USA  
800-521-0600

UMI<sup>®</sup>



**COMPUTER SIMULATION OF TEXTURAL AND  
MICROSTRUCTURAL CHANGES DURING  
ANNEALING PROCESSES**

By

Narayanan Rajmohan

A thesis submitted to the Faculty of Graduate Studies and Research  
in partial fulfillment of the requirements of the degree of  
Doctor of Philosophy



**Department of Mining and Metallurgical Engineering  
McGill University, Montreal, CANADA**

April, 2000.

©Narayanan Rajmohan, 2000.



National Library  
of Canada

Acquisitions and  
Bibliographic Services

395 Wellington Street  
Ottawa ON K1A 0N4  
Canada

Bibliothèque nationale  
du Canada

Acquisitions et  
services bibliographiques

395, rue Wellington  
Ottawa ON K1A 0N4  
Canada

*Your file Votre référence*

*Our file Notre référence*

The author has granted a non-exclusive licence allowing the National Library of Canada to reproduce, loan, distribute or sell copies of this thesis in microform, paper or electronic formats.

The author retains ownership of the copyright in this thesis. Neither the thesis nor substantial extracts from it may be printed or otherwise reproduced without the author's permission.

L'auteur a accordé une licence non exclusive permettant à la Bibliothèque nationale du Canada de reproduire, prêter, distribuer ou vendre des copies de cette thèse sous la forme de microfiche/film, de reproduction sur papier ou sur format électronique.

L'auteur conserve la propriété du droit d'auteur qui protège cette thèse. Ni la thèse ni des extraits substantiels de celle-ci ne doivent être imprimés ou autrement reproduits sans son autorisation.

0-612-64629-7

Canada

## ABSTRACT

Applicability of Monte-Carlo method for the textural and microstructural changes during annealing processes is studied. Models that are developed for explaining annealing processes are incorporated into Monte-Carlo procedures and the textural and microstructural changes are then followed. The simulated results are compared with the experimental observations to validate the proposed models. The three exemplary annealing processes selected for the present work are industrially important and diversified in their annealing characteristics. These are:

- I. Cube  $\{100\}\langle 001\rangle$  texture development during recrystallization of Al,
- II. Abnormal grain growth of Goss  $\{110\}\langle 001\rangle$  grains in Fe-Si steels.
- III. The competition between (111) and (100)-fiber textures during annealing of nanocrystalline Ni and Ni-Fe alloy electrodeposits.

The model for each annealing process is developed by analyzing the relevant metallurgical information obtained from the corresponding metals and alloys prior to annealing.

In Application-I, the texture and orientation-dependent stored energy measurements have been made on the cold rolled can-body aluminum alloy and the detailed discussion is presented. These results are analyzed for developing nucleation and growth models that would lead to the final cube texture formation during primary recrystallization of Aluminum. In order to overcome the complexity of the deformed microstructure, the orientation and location of the nuclei are selected by conditions based on texture and scatter in the measured orientation dependent stored energies in cold-rolled and stress-relieved states. The rate of release of stored energy plays a major role in deciding the rate of nucleation of new grains with different orientations. The developed growth model is based on the grain boundary misorientation distributions in deciding the possible high mobility boundaries for the development of the final texture and microstructure. The proposed recrystallization model for aluminum predicts the development of cube texture and equiaxed grain structure as observed in experiments.

For the abnormal grain growth in Fe-Si steel (Application-II), the role of high energy grain boundaries has been studied in detail using separate computer experiments to understand the importance of fraction of high mobility grain boundaries. From these experiments, it has been proved that the assumption of high mobility to CSL boundaries for the abnormal growth of Goss grains is not valid. The growth model that assumes high mobility to high-energy (or random) boundaries is examined by these computer experiments and is then incorporated into the Monte-Carlo procedure developed for the abnormal grain growth in conventional Fe-3%Si steel. The Monte-Carlo procedure takes into account the effect of Ostwald ripening of precipitate particles on the pinning of grain boundaries during secondary recrystallization. The proposed model predicts the abnormal growth of Goss grains.

Finally, the Monte-Carlo procedure is employed for testing the proposed model for the texture competition between (111) and (100)-fibers in nanocrystalline Ni, Ni-20% Fe and Ni-45% Fe electrodeposits (Application-III). Based on the texture analysis, the proposed model assumes high mobility to the grains boundaries, which are in high non-equilibrium states. The parameter, which specifies the deviation of energy of non-equilibrium nanocrystalline grain boundaries from their more stable microcrystalline counterparts, defines the mobility. As observed in experiments this assumption allows the (111)-fiber to grow faster than (100)-fiber during annealing. The results of the Monte-Carlo simulation using the proposed model are compared with experiments. The simulated results show that (111)-fiber grows faster than (100)-fiber as annealing progresses.

## RÉSUMÉ

La possibilité d'appliquer de la méthode de Monte-Carlo pour les changements de texture et microstructuraux pendant les procédés de recuit est étudiée. Des modèles qui sont développés pour expliquer des procédés de recuit sont incorporés aux procédures de Monte-Carlo et les changements de texture et microstructuraux sont alors suivis. Les résultats simulés sont comparés aux observations expérimentales pour valider les modèles proposés. Les trois exemples de procédés de recuit choisis pour le travail actuel sont industriellement importants et diversifiés dans leurs caractéristiques de recuit. Ceux-ci sont:

- I. Développement de texture cube  $\{100\}\langle 001\rangle$  pendant la recristallisation d'Al,
- II. Croissance anormale de grain de Goss  $\{110\}\langle 001\rangle$  grains en aciers de Fe-Si,
- III. La concurrence entre les textures (111) et (100)-fiber pendant le recuit des alliages nanocristallins électrodéposés de Ni et Ni-Fe.

Le modèle pour chaque procédé de recuit est développé en analysant l'information métallurgique appropriée obtenue à partir des métaux et des alliages correspondants avant le recuit.

Dans Application-I, la texture et les mesures d'énergie stockée dépendant de l'orientation ont été faites sur l'alliage d'aluminium laminé à froid des canettes pour boisson et la discussion détaillée est présentée. Ces résultats sont analysés pour les modèles de développement et de croissance des nucléations qui mèneraient à la formation finale d'une texture cubique pendant la recristallisation primaire de l'aluminium. Afin de surmonter la complexité de la microstructure déformée, l'orientation et l'emplacement des noyaux sont choisis par des conditions basées sur la texture et l'éparpillement dans l'aluminium laminé à froid dont l'énergie stockée dépendant de l'orientation et celui dont les contraintes sont éliminées. Le taux de dissipation de l'énergie stockée joue un rôle important concernant la cadence de nucléation de nouveaux grains avec différentes orientations. Le modèle développé de croissance est basé sur les distributions de désorientation de joints de grain

entraînant des joints avec une possible haute mobilité pour le développement de la texture et de la microstructure finales. Le modèle proposé de recristallisation pour l'aluminium prévoit le développement de la texture cubique et de la structure de grain equiaxiale comme observée dans les expériences.

Pour la croissance anormale de grain en acier-Fe-Si (Application-II), le rôle des joints de grain à haute énergie a été étudié en détail en utilisant de simples expériences par ordinateur pour comprendre l'importance de la part des joints de grain à haute mobilité. De ces expériences, on a montré que l'hypothèse de mobilité élevée aux joints de CSL pour la croissance anormale des grain de Goss est incorrecte. Le modèle de croissance qui suppose une mobilité élevée aux joints de haute énergie (ou aléatoires) est examiné par ces expériences par ordinateur puis est incorporé au procédé de Monte-Carlo développé pour la croissance anormale de grain en acier conventionnel de Fe-3%Si. Le procédé de Monte-Carlo tient compte de l'effet de maturation d'Ostwald des particules de précipité pour l'arrêt des joints de grain pendant la recristallisation secondaire. Le modèle proposé prévoit la croissance anormale des grains de Goss.

Enfin dans le travail actuel de thèse, le procédé de Monte-Carlo est utilisé pour tester le modèle proposé entre les texture (111) et (100)-fibres en compétition dans les électrodépositions de Ni, Ni-20% Fe et Ni-45% Fe nanocristallins (Application-III). Basé sur l'analyse de texture, le modèle proposé suppose une haute mobilité des joints de grains, qui sont dans les états élevés de non-équilibre. Le paramètre, qui indique l'importance de déviation des joints de grain nanocristallins hors-equilibres par rapport à leurs équivalent microcristallins stables, définit la mobilité. Comme observé dans les expériences, cette hypothèse permet (111)-fiber de mieux se développer par rapport au (100)-fiber et devenir un matériel microcristallin. Les résultats de la simulation de Monte-Carlo utilisant le modèle proposé sont comparés aux expériences.

## ACKNOWLEDGEMENTS

I would like to thank my thesis supervisor Prof. J.A. Szpunar for the help and support he has provided throughout my work. I would like to thank him for the academic and personal freedom that he encouraged and allowed during my thesis work. Jerzy understands the difficulty of living apart from one's family on a long-term basis for the purpose of work. I thank him for being very flexible and understanding.

I would like to thank my parents, wife, little son and others in my family for understanding my problems. I really appreciate them for enduring the days, when I was away from them in pursuit of this degree. Without their support, this personal dream could not have been possible.

I would like to thank the Fellowships Committee of McGill for awarding me the honorable J.W. McConnell McGill Major Fellowship and Neil Croll Memorial Award.

I would like to thank Dr. Y. Hayakawa for the useful and endless discussions I had with him regarding my research work on Fe-Si steels. I thank Mr. D. Hinz for the skeletal computer code that became the starting point of this thesis work. I would like to thank Prof. U. Erb and Dr. G. Polambo for the nanocrystalline specimens. I would also like to thank Dr. F. Czerwinski, Mr. B. Morris and Ms. F. Margret for their share in experimental work on Nanocrystalline Ni-Fe electrodeposits. I would like to thank Dr. J. Savoie of Alcan Research Ltd. for the cold rolled aluminum sample and also for the e-mail discussion I had with him. I would like to thank Dr. D. Juul Jensen for her valuable comments on my research work on aluminum recrystallization. Finally, I would like to thank Slavek Poplawski, Peter Blandford, Val Gertsman, Sasha Zhilyaev and Hualong Li, for their kindness and assistance. In addition, I would like to thank the people from the Texture lab who have made my stay more enjoyable. This includes: Mike Glavicic, Jae-Young Cho, Jianlong Lin, Andreas Brodtka, Ronny Keissling, Kitae Lee, Backyun kim, Todd J. Turner, Mattias Nilsson, Hyounsoo Park, Hyo-Tae Jeong, Jong-Tae Park, Yang Cao, Byeoung-Soo Ahn, Askar Ali, Jian Lu, Read Hazhaikch Neil D'souza and Delphine Gasparini.

# COMPUTER SIMULATION OF TEXTURAL AND MICROSTRUCTURAL CHANGES DURING ANNEALING PROCESSES

Contents	Page
<b>ABSTRACT</b>	<b>i</b>
<b>RÉSUMÉ</b>	<b>iii</b>
<b>ACKNOWLEDGEMENT</b>	<b>v</b>
<b>TABLE OF CONTENTS</b>	<b>vi</b>
<b>LIST OF FIGURES</b>	<b>x</b>
<b>LIST OF TABLES</b>	<b>xvi</b>
<b>1. INTRODUCTION</b>	<b>1</b>
<b>2. LITERATURE REVIEW</b>	<b>6</b>
<b>2.1. Annealing of metals</b>	<b>7</b>
<b>2.2. Deformed state</b>	<b>8</b>
2.2.1. Structure of deformed metals	9
2.2.2. Stored energy of cold work	12
<b>2.3. Grain boundary energy and mobility</b>	<b>14</b>
2.3.1. Classification of grain boundaries based on structure	14
2.3.2. Grain boundary energy and misorientation	17
2.3.3. Mobility of grain boundaries	19
<b>2.4. Primary recrystallization</b>	<b>21</b>
2.4.1. The JMAK model for recrystallization	22
2.4.2. The laws of recrystallization	23
2.4.3. Nucleation of recrystallization	24
<b>2.5. Abnormal grain growth</b>	<b>26</b>
<b>2.6. Thermal stability of nanocrystalline materials</b>	<b>28</b>

<b>2.7. Computer simulation of recrystallization and grain growth</b>	<b>30</b>
2.7.1. Classical Monte-Carlo grain growth model	30
2.7.2. Modified Monte-Carlo framework for grain growth	34
2.7.3. Computer presentation of microstructure and texture	36
2.7.4. A note on computer simulations	38
<b>2.8. Summary</b>	<b>39</b>
<hr/>	
<b>3. RECRYSTALLIZATION OF CAN-BODY ALUMINUM ALLOY – APPLICATION (I)</b>	<b>41</b>
3.1. Introduction to recrystallization of aluminum	42
3.2. Measurement of orientation dependent stored energy	44
3.2.1. Introduction to orientation dependent stored energy	44
3.2.2. Mathematical technique for the measurement of stored energy	46
3.2.3. Experimental technique for the measurement of stored energy	48
3.2.4. Results of stored energy measurement on aluminum	50
3.2.5. Comparison of stored energy and Taylor factor	57
3.3. Analysis of texture of cold rolled aluminum for nucleation model	59
3.3.1. Model of microstructure for cold rolled texture analysis	59
3.3.2. Probability of availability of a nucleus orientation	60
3.4. Stored energy analysis for nucleation model	65
3.4.1. Spread in the stored energy values	66
3.4.2. Nucleation condition based on stored energy	68
3.5. Growth model for recrystallization of aluminum	72
3.6. Monte-Carlo model for recrystallization of Al	78
3.7. Results of the simulation of recrystallization of Al	81
3.8. Summary	97
<hr/>	
<b>4. ABNORMAL GRAIN GROWTH IN FE-3%SI STEELS – APPLICATION (II)</b>	<b>98</b>
4.1. Introduction to abnormal grain growth in Fe-Si steels	99
4.1.1. Grain boundary energy vs. misorientation for Fe-Si steels	100

<b>4.2. Computer experiment on fractions of mobile boundaries in abnormal grain growth</b>	<b>102</b>
4.2.1. Models used to explain the abnormal growth of Goss grains	102
4.2.2. Methodology for computer experiment on grain boundary fractions	105
4.2.3. Fractions of grain boundaries and their importance	108
4.2.4. Preferential growth of Goss grains	113
4.2.5. Grain boundary character distributions (GBCD)	113
<b>4.3. Grain boundary mobility and misorientation</b>	<b>116</b>
<b>4.4. Monte-Carlo model with anisotropic mobility</b>	<b>119</b>
4.4.1. Simulation of grain growth with anisotropic mobility	120
<b>4.5. Precipitate particles and their importance in abnormal grain growth</b>	<b>122</b>
4.5.1. Ostwald ripening of precipitate particles	123
4.5.2. The Zener particle pinning	125
<b>4.6. Monte-Carlo simulation of abnormal grain growth with MnS particle pinning</b>	<b>128</b>
4.6.1. Simulated texture and microstructure using MnS particle pinning	129
4.6.2. Mobile boundary fractions around growing Goss grain	134
<b>4.7. Summary</b>	<b>135</b>
<b>5. ANNEALING OF NANOCRYSTALLINE Ni AND Ni-Fe ELECTRODEPOSITES – APPLICATION (III)</b>	<b>137</b>
<b>5.1. Review on annealing of nanocrystalline materials</b>	<b>138</b>
5.1.1. Grain boundaries in nanocrystalline materials	138
5.1.2. Grain growth in nanocrystalline electrodeposits	140
<b>5.2. Texture measurement</b>	<b>141</b>
<b>5.3. Analysis of texture in nanocrystalline Ni and Ni-Fe electrodeposits</b>	<b>143</b>
5.3.1. Cluster analysis	144
5.3.2. Grain misorientation distribution analysis	147
5.3.3. Grain boundary energy and mobility in nanocrystalline Ni and Ni-Fe	151
<b>5.4. Model for annealing of Ni and Ni-Fe electrodeposits</b>	<b>157</b>

5.4.1. Mechanism of abnormal grain growth in nanocrystalline Ni and Ni-Fe electrodeposits	157
<b>5.5. Monte-Carlo method for simulation of annealing of nanocrystalline Ni and Ni-Fe electrodeposits</b>	<b>160</b>
5.5.1. Parameters used for the simulation of annealing of nanocrystalline Ni and Ni-Fe electrodeposits	163
<b>5.6. Results of the Monte-Carlo simulations of annealing of nanocrystalline Ni and Ni-Fe electrodeposits</b>	<b>165</b>
5.6.1. Simulated microstructural transformation during annealing of nanocrystalline Ni and Ni-Fe electrodeposits	166
5.6.2. Simulated textural transformation during annealing of nanocrystalline Ni and Ni-Fe electrodeposits	168
<b>5.7. Summary</b>	<b>171</b>
<b>6. SUMMARY AND CONCLUSIONS</b>	<b>172</b>
6.1. Conclusions	173
6.1.1. Primary recrystallization of aluminum	173
6.1.2. Abnormal growth in Fe-Si steels	175
6.1.3. Annealing of Ni and Ni-Fe nanocrystalline electrodeposits	177
6.2. Statement of originality	179
6.3. Recommendations for further research	180
<b>REFERENCES</b>	<b>182</b>

## LIST OF FIGURES

<b>CHAPTER 2</b>	<b>Page</b>
Fig. 2.1. Schematic diagrams explaining the microstructural changes of important annealing process; (a) deformed, (b) stress relieved, (c) partially recrystallized, (d) fully recrystallized (e) normal grain growth and (f) abnormal grain growth.	8
Fig. 2.2. Schematic diagrams illustrating the deformation, transition and kink bands in a deformed microstructure.	10
Fig. 2.3. 90% cold rolled aluminum single crystal exhibiting slip bands.	11
Fig. 2.4. Schematic diagram of a symmetrical tilt boundary.	16
Fig. 2.5. A coincident site lattice ( $\Sigma 5$ ) formed from two simple cubic lattices rotated by $36.9^\circ$ about an $\langle 001 \rangle$ axis. The coincident sites are shown as filled circles.	17
Fig. 2.6. A typical recrystallization kinetics during isothermal annealing	23
Fig. 2.7. Schematic representation of change of grain size distribution during (a) normal grain growth and (b) abnormal grain growth.	28
Fig. 2.8. Discrete representation of 2-dimensional microstructure used in Monte-Carlo simulation by Anderson et al.	31
Fig. 2.9. A typical grain structure in Monte-Carlo simulation.	32
Fig. 2.10. Schematic representation of grain boundary movement in Monte-Carlo simulation.	33
<b>CHAPTER 3</b>	
Fig. 3.1. Orientation distribution function (ODF) of 88% cold rolled can-body aluminum AA3104.	42
Fig. 3.2. Locations on pole figure at which x-ray line broadening measurements were made.	49
Fig. 3.3. Stored energy distribution function for 88% cold rolled AA3104 can-body aluminum.	51

Fig. 3.4. Stored energy distribution function for stress relieved AA3104 can-body aluminum at 200°C for 15 minutes after 88% cold rolling.	52
Fig. 3.5. ODF intensity and stored energy after 88% rolling and subsequent stress relieving of AA3104 can-body aluminum along <001> direction in $\phi_2=0^\circ$ section.	53
Fig. 3.6. Schematic representation of the fcc rolling texture in the 3-dimensional Euler angle space.	55
Fig. 3.7. Calculated stored energy along $\beta$ -fiber for rolled and stress relieved can-body aluminum AA3104 (see text for more information).	56
Fig. 3.8. Calculated stored energy along $\alpha$ -fiber ( $\phi_2=90^\circ$ section) for rolled and stress relieved can-body aluminum AA3104.	57
Fig. 3.9. Computed misorientation angle distribution between nuclei of various orientations and cold rolled matrix. (a) Juul Jensen's [23] observation, (b) for random nucleation, (c) with the nucleation condition given by equation (3.7) & (3.8), and (d) with the nucleation condition given by equation (3.7) & (3.9) (see text).	62
Fig. 3.10. Diagrams showing the observed spread in the measured stored energy values as a function of angular deviation from the ideal orientation of Cube, C, B and S components. (a) After cold rolling $S_{cr}$ (b) after stress relieving $S_{sr}$ and (c) $S_{ratio}$	67
Fig. 3.11. Percentage fractions of grain boundaries with misorientation $> 35^\circ$ (assumed to have high mobility) around the nuclei of various orientation in the deformed aluminum matrix presented in the Euler angles space.	76
Fig. 3.12. Relative grain boundary energy for (a) <100> (b) <110> tilt boundaries and (c) average relative grain boundary energy for various misorientation angles.	80
Fig. 3.13. Fully recrystallized ODFs obtained from the simulations (a) for A1, (b) for A2, (c) for B1 and (d) for B2. The simulation conditons for these simulations are given in the Table 3.5. (see the text).	84 & 85
Fig. 3.14. Calculated ODF of 88% cold rolled and fully annealed aluminum AA3104 (at 400°C for 15 minutes) from the measured (111) (100) and (110) pole figures using X-rays.	86
Fig. 3.15. Recrystallization kinetics obtained from the simulation (B2).	87

Fig. 3.16. JMAK plot obtained from the simulation (B2).	88
Fig. 3.17. The nucleation rate of various texture components during simulation B2. (a) for cube and C, B and S texture components and (b) for random component and overall nucleation rate.	88
Fig. 3.18. The texture change during annealing at different % recrystallized fractions obtained from the simulation (B2). The $\phi_2 = 45^\circ, 65^\circ$ and $90^\circ$ ODF sections are presented.	90
Fig. 3.19. The average grain volume (in number of sites) for cube, rolling and random orientations as a function of MCS obtained from the simulation (B2).	91
Fig. 3.20. Microstructures of TD and RD sections during annealing at different % recrystallized computer specimen obtained from the simulation (B2). In this simulation, the migration of boundaries between the impinging recrystallized grain is not allowed.	93
Fig. 3.21. Microstructures of ND and RD sections during annealing at different % recrystallized computer specimen obtained from the simulation (B2). In this simulation, the migration of boundaries between the impinging recrystallized grain is not allowed.	94
Fig. 3.22. Microstructure of 96% recrystallized computer specimen obtained from the simulation (B2-NGG), with an assumption that the migration of boundaries between the impinging recrystallized grain is allowed.	96
 <b>CHAPTER 4</b>	
Fig. 4.1. Measured $\langle 100 \rangle, \langle 110 \rangle$ tilt grain boundary energy as a function of tilt angle for Fe-3%Si steel.	101
Fig. 4.2. Probability (%) of boundaries having misorientation angle $20^\circ$ - $45^\circ$ around grains having various orientations in Fe-Si steels a) conventional and b) high permeability steels. Both (a) and (b) are $\phi_2=45^\circ$ sections. Arrows indicate the Goss orientation, and the contour line of the average value is indicated by 'A'	103
Fig. 4.3. ODF of conventional electrical steel	109
Fig. 4.4. ODF of high-permeability electrical steel	109
Fig. 4.5. Simulated growth behavior of the grain with various percentage of mobile grain boundaries (MF) in the initial matrix	110

Fig. 4.6. Peripheral fraction of growing grains with various percentages of mobile grain boundaries in the initial matrix	112
Fig. 4.7. Volume as a function of growth step for grains having Goss {110}<001>, Main {111}<011>, and cube {001}<100> orientations obtained assuming that high energy boundaries have high mobility in the conventional Fe-3% Si steel	114
Fig. 4.8. Volume as a function of growth step for grains having Goss {110}<001>, Main {111}<112>, and cube {001}<100> orientations obtained assuming that high energy boundaries have high mobility in the high permeability Fe-3% Si steel.	114
Fig. 4.9. Average number fractions of mobile boundaries around the growing Goss grains as a function of number of growth steps in a) conventional and b) high-permeability electrical steel	115
Fig. 4.10. Comparison between the simulated and experimentally determined GBCD for grains bounding the growing Goss grains for the a) conventional and b) high-permeability Fe-3% Si steel.	116
Fig. 4.11. Grain boundary self diffusion coefficient as a function of misorientation	118
Fig. 4.12. Inherent grain boundary mobility as a function of tilt angle about <110> direction	119
Fig. 4.13. Recalculated ODF of conventional electrical steels from the computer specimen	120
Fig. 4.14. Calculated change of relative particle radius for various grain boundary energies	126
Fig. 4.15. Calculated change in pinning parameter $\Omega$ for grain boundaries with different grain boundary energy as a function of time	127
Fig. 4.16. Calculated ODF sections for $\phi_2 = 45^\circ$ obtained at 3000, 5000, 7000, 9000 and 11000 MCS of simulated annealing for Fe-3%Si conventional electrical steel	130
Fig. 4.17. Simulated change in maximum ODF intensity for Goss and Main texture components during annealing	132

Fig.4.18 Growth of the largest abnormally growing grain in the computer simulations of annealing 132

Fig.4.19 Microstructure showing the growth of two Goss grains (painted grey) in a 2-dimensional section of 3-dimensional computer specimen for a)MCS = 0, b)MCS = 1000, c)MCS = 3000, d)MCS = 5000, e)MCS = 7000 & f)MCS = 9000 133

Fig.4.20 Change in the area fraction of the mobile grain boundaries with misorientation between 20° and 45° around the growing Goss grains as a function of MCS during annealing 135

## CHAPTER 5

Fig.5.1 Fiber intensity observed in pole figures of (111) and (200) of Ni-45%Fe, Ni-20%Fe and Ni nanocrystalline electrodeposits measured after annealing at 673 K for various annealing periods 142

Fig.5.2 Orientation distribution function (ODF) of as electrodeposited nanocrystalline (a) Ni, (b) Ni-20% Fe and (c) Ni-45% Fe 145

Fig.5.3 Misorientation distribution calculated based on the as-electrodeposited nanocrystalline Ni, Ni-20%Fe and Ni-45%Fe textural information. (Here curves are drawn only as a visual aid to follow the data points unambiguously) 149

Fig.5.4 CSL distribution calculated based on the as-electrodeposited nanocrystalline Ni, Ni-20%Fe and Ni-45%Fe textural information. 152

Fig.5.5 (a),(b),(c) and (d) are the calculated grain boundary energies of symmetrical tilt boundaries for Cu [51]. (e) Calculated average relative grain boundary energy as a function of misorientation angle 155

Fig.5.6 Grain boundary energy deviation parameter as a function of misorientation from assumed nanocrystalline and theoretical microcrystalline grain boundary energies 156

Fig.5.7 Probability of boundaries of LH-type around grains of various orientations for (a) Ni, (b) Ni-20% Fe and (c) Ni-45% Fe nanocrystalline electrodeposits. The probability is presented for  $\phi_2 = 45^\circ$  section 158

Fig.5.8 Growth kinetics of the largest grain observed in computer simulation for various  $\alpha$  values in Ni-45% Fe nanocrystalline electrodeposit for constant  $\Delta E_{max} = 0.35$ . Along with  $\alpha$  values, angle of deviation (in degree) from the (111)-fiber texture component is given for each curve. 164

Fig.5.9 Growth kinetics of the largest grain observed in computer simulation for various  $\Delta E_{max}$  values in Ni-45% Fe nanocrystalline electrodeposit at constant  $\alpha=1$ . Along with  $\Delta E_{max}$  values, the angle of deviation (in degrees) from the (111)-fiber texture component is given for each curve. 165

Fig.5.10 Growth kinetics of the largest grains observed in various simulations having initial texture of as-electrodeposited (a) Ni, (b) Ni-20% Fe and (c) Ni-45% Fe. Each curve is specified with type of fiber texture and angle of deviation (in degrees) from that fiber orientation. 167

Fig.5.11 Comparison of simulated {(a), (b) & (c)} and experimental {(d), (e) & (f)} pole figure intensities during isothermal annealing of Ni, Ni-20% Fe and Ni-45% Fe nanocrystalline electrodeposites. 169

## LIST OF TABLES

<b>CHAPTER 3</b>	<b>Page</b>
Table 3.1. Stored energy values of selected orientation in 88% rolled and stress relieved (200°C, 15 minutes) can-body aluminum sheet AA3104.	54
Table 3.2. Computed average misorientation angles computed around the nuclei of various orientations and the neighboring deformed grains under different nucleation conditions (see text).	65
Table 3.3. Percentage number of nuclei observed with different nucleation conditons (see text)	71
Table 3.4. Fractions of grain boundaries with different misorientation ranges observed between the nuclei and the deformed matrix.	71
Table 3.5. Nucleation and growth conditons employed for the different simulations.	82
<b>CHAPTER 4</b>	
Table 4.1. The ratio between total relative grain boundary energy and grain volume and number of nearest neighbors at the beginning (MCS=0) of the simulation for all the Goss grains present in the computer specimen	122
<b>CHAPTER 5</b>	
Table 5.1. Computed number of clusters with angular deviation of 0°-5°, 0°-10° and 0°-15° and various cluster sizes for Ni-45% Fe. Average number of clusters computed from 10 different computer specimens is presented here. Each computer specimen has a total of 100674 grains.	146
Table 5.2. Comparison of fiber intensity and fraction of grain boundaries in Ni, Ni-20%Fe and Ni-45%Fe nanocrystalline electrodeposits	150

## **Chapter 1**

### **INTRODUCTION**

It is well-known for centuries that deformation and annealing are the fundamental processes by which the properties of a metal can be altered. Though a plethora of experimental observations and theoretical analysis are now available in this field, many aspects are still not well-clarified and the experimental evidence is often poor and conflicting. This is mainly due to the complexity in performing successful experimental or theoretical analyses. Therefore, quantification of all the aspects of these phenomena is still not possible and thus understanding them from the first principles is still a distant goal.

When a metal is deformed, though the crystal structure is preserved, the change in the grain structure poses numerous problems even to characterize the different features observed in the microstructure. These features depend on the crystal structure and chemistry of the metallic matrix, the deformation process employed and the temperature at which the deformation is carried out. Deformation of metals occurs either by slip or by twin mechanisms [1]. The assumption of homogeneous deformation by Taylor model [2] threw some light on the development of the deformation texture. However, this model and the other models, including the recent theoretical studies [3-6] in this subject, are too simple to explain the formation of deformation inhomogeneities such as

transition and shear bands and various complex dislocation cell structures. Though the recent Transmission Electron Microscopic (TEM) technique provided some insight into the arrangement of dislocations, still the understanding is not sufficient. Therefore, using the present knowledge, one cannot possibly construct the necessary features of deformed microstructure, which is a basic requirement for the theoretical analysis of annealing of deformed metals. However, it is clear that the complex microstructural features are due to the accumulation of crystal defects and the appearance of these features is the effect of variation in the dislocation population and differences in their arrangements. The step-scanning examination along a sample direction in heavily deformed specimens using Orientation Imaging Microscopy (OIM) shows the evidence of numerous additional grain boundaries in the microstructures [7,8] as well. These defects store energy in the structure, which leads to the instability of the metal.

Annealing at high temperatures reverts the defective structures to more stable forms by eliminating and rearranging crystal defects created during the deformation. This self-replenishing act is the result of thermally activated atomic fluctuations causing the recovery, recrystallization and grain growth in the deformed matrix. During recovery the annihilation and rearrangement of dislocations takes place and there is no migration of high-angle boundary noticed [1]. Recrystallization occurs at high temperatures, in sufficiently deformed metals by nucleation of new grains. These new grains grow by consuming the deformed grains through grain boundary migration [1]. Here the driving pressure for grain boundary migration is stored energy. Here the boundaries responsible are usually the high-angle boundaries [1]. Further annealing results in the reduction of interfacial regions dictated by grain boundary migration, which is referred to as grain growth. Here, the driving pressure is grain boundary energy. Grain growth processes can be categorized into either normal or abnormal grain growth. It was well proven that abnormal grain growth occurs only when the normal grain growth is hindered [1]. Annealing of recently developed nanocrystalline materials show both normal [9] and abnormal grain growth [10-11] on different occasions. A complete understanding of the annealing behavior of these materials can be understood only after a complete understanding of grain boundaries in their matrices.

In spite of the complexity posed by the changing structure and behavior of the metals during deformation and annealing, the insatiable appetite for understanding these processes is greater than ever before. Modern instruments are used for in-depth analysis all over the world. The research in this field is fueled by the growing need for improved and cheaper materials (and processes) desired by the aerospace, automotive and military applications.

There are a number of variables to be taken care of when the experimental or theoretical analysis is performed. The fundamental variables in a simple single-phase polycrystalline metallic matrix are the orientation of each grain present and topology of the grain structure. The next level of variables that have to be considered in order to explain the deformation and annealing phenomena are the variables concerning the properties associated with crystal defects such as grain boundaries and dislocations. These variables, for example, are grain boundary energy, grain boundary mobility, stored energy, deformation inhomogeneity, etc. The number of parameters to be considered gets uncontrollably larger when a multiphase metallic matrix is considered. At this juncture, the application of modern high-speed computers to understand the mechanisms of metallurgical process during deformation and annealing involving the variables mentioned above is on the rise. Within the past couple of decades, employing the computer techniques for this purpose grew at such an astonishing pace that one cannot possibly think of quantitative prediction of the effect of processing parameters on the final microstructure and texture without computers in the future.

Most of the early analyses in metallurgy and materials science do not consider the effect of orientation and are concerned only about the change in the 2-dimensional grain structure. This is mainly because it is possible to study the change in grain structure at a cross-section of the specimen using an optical microscope. Even the early Monte-Carlo computer models [12-14] disregard the effect of orientation on the change in the grain structure due to the complexity in developing a successful model. However, to study the influence of CSL boundaries on the Goss texture development, Hinz and Szpunar [15]

developed a computer program based on a modified Monte-Carlo framework that incorporates complete texture and microstructure description. By having this procedure as the precursor, in the present thesis, considerable efforts have gone into developing computer models that could lead to the understanding of the development of microstructure and texture during various annealing processes in different materials. These models incorporate the complete microstructure and texture and anisotropic properties such as grain boundary energy, mobility and orientation dependent stored energy in the 3-dimensional Monte-Carlo procedures. The integrity of the results of simulations has been evaluated by comparing them with the experiments. The application of Monte-Carlo procedures considered in the present thesis work are for the processes that are selected from three well-known and completely different annealing processes observed in three different metallic matrices. These are:

- Application I. Primary recrystallization of cold rolled metallic matrix, where nucleation and normal grain growth occur in order to transform the deformed structure into a more stable structure at high temperatures. As an example, industrially important  $\{001\}\langle 100\rangle$  (cube) texture development during annealing of heavily cold rolled can-body aluminum is chosen for the study.
- Application II. Secondary recrystallization or abnormal grain growth that takes place at high temperatures when certain metallic matrices are annealed after primary recrystallization. In this category, the celebrated  $\{110\}\langle 001\rangle$  (Goss) texture development during abnormal grain growth of Fe-Si steel has been selected for the computer analysis.
- Application III. The third category in the present thesis work comes from the unique annealing behavior of recently developed nanocrystalline Ni and Ni-Fe electrodeposits, which are the state-of-the-art materials in recording industries. The experimentally observed competition

between (111) and (100)-fiber during annealing in these cases is predicted using a computer model.

This thesis is organized into the following chapters. Chapter 2 presents a review on the necessary details of deformation and annealing processes. This chapter concentrates on variables such as deformation inhomogeneities, stored energy, grain boundary energy and mobility. The processes such as primary recrystallization, secondary recrystallization and thermal stability of nanocrystalline materials, which are required for the present analyses are also reviewed. The latter part of Chapter 2 reviews the computer models with a focus on the Monte-Carlo framework. As the role of stored energy is of paramount importance to the primary recrystallization of cold rolled materials, the determination of orientation-dependent stored energy using x-ray line broadening technique is explained in the first part of Chapter 3. It is then followed by the detailed presentation of the simulation of primary recrystallization using the Monte-Carlo computer model. In Chapter 4, quantification of the effect of different fractions of mobile boundaries is discussed in the early sections by taking the Fe-Si steel as examples. The Monte-Carlo computer procedure is then applied to the abnormal grain growth of Goss grains in Fe-3% Si conventional electrical steel in the presence of MnS particles. The Monte-Carlo procedure is also applied to the study of texture transformation in the recently developed nanocrystalline Ni and Ni-Fe electrodeposits and is presented in Chapter 5. Chapter 6 presents the conclusion and recommendations for the future research.

## **Chapter 2**

### **LITERATURE REVIEW**

This chapter provides a review of the literature and terminology relevant to the annealing processes and computer simulation of these processes. The initial part of the review is devoted to the discussion on the basic and necessary understanding of the deformed state (section § 2.2). This includes a subsection § 2.2.2 on the importance of the stored energy of the cold deformed state. Following this, there are discussions on the important variables of annealing processes namely, grain boundary energy and mobility in section § 2.3. Short reviews on primary recrystallization, abnormal grain growth and thermal stability of nanocrystalline materials are given in sections § 2.4, § 2.5 and § 2.6 respectively. These reviews are necessary, because the Monte-Carlo methods discussed in section § 2.7 are applied to simulate all these processes. Reviews of literature relevant to specific materials and annealing processes chosen for this research work are given in the corresponding chapters. In section § 2.7, a review of computer methods of simulating microstructure and texture changes during annealing is presented. Finally, a note on computer modeling with a focus on Monte-Carlo procedure is presented.

## 2.1. ANNEALING OF METALS

Annealing a metal is a process of heating it to a high temperature, generally above the  $\sim 0.5T_m$ , where  $T_m$  is the melting (sometimes the phase transition) temperature of the metal. During deformation, the free energy increases and is stored in dislocations and interfaces. A metal containing these defects is thermodynamically unstable. The atomistic mechanisms, those are responsible for the disappearances of thermodynamically unstable defects are often very slow at low homologous temperatures. This defect structure, when exposed to high temperatures is transformed through thermally activated processes such as solid state diffusion. These thermally activated processes cause the removal of defects or alternate arrangements of defect structure that creates a configuration of lower energy.

Upon heating a cold worked metal at an elevated temperature, the microstructure and also the properties may be partially restored to their original values by a process called *recovery* in which annihilation and rearrangement of the dislocations occurs. In this process the removal of dislocation structure is partial. At a suitable elevated temperature, a further restoration process may occur in which new dislocation-free grains are formed within the deformed or recovered structure. These new grains then grow and consume the existing deformed grains. This process is called (*primary*) *recrystallization*. This process removes the dislocations and lowers the free energy of the metal. Though the dislocation density in the metal at this state is not very high, the metal contains grain boundaries, which are thermodynamically unstable. Further annealing may result in *grain growth*, in which the grain size increases. If the grain growth process changes the grain size homogeneously throughout the metal then this is called *normal grain growth*. In certain circumstances this may give way to the selective growth of a few grains and this process is known as *abnormal grain growth* or *secondary recrystallization*. The self-explanatory schematic diagrams explaining these annealing processes are given in Fig. 2.1. Detailed and methodical explanations of the annealing processes and relevant information about the microstructure and texture of

deformed state of metals are discussed in books [1,16,17] and the issues related to this topic are discussed in [18].

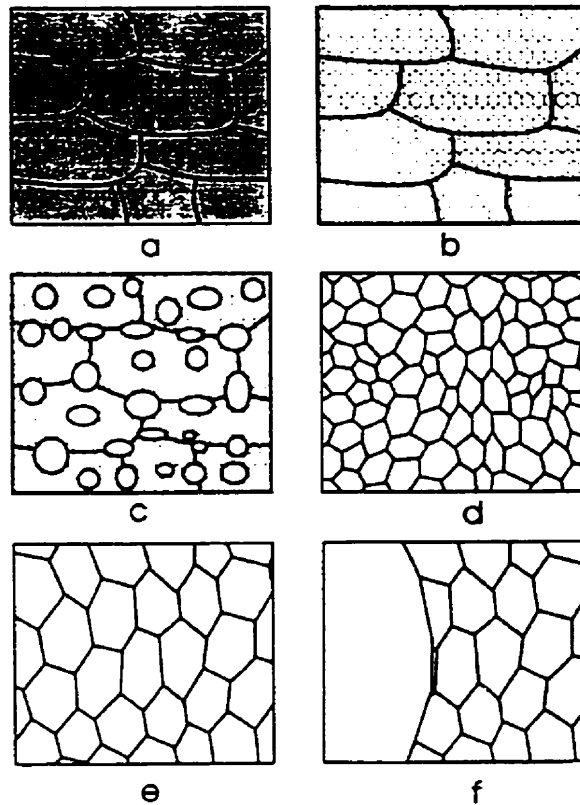


**Fig. 2.1.** Schematic diagrams explaining the microstructural changes of important annealing process; (a) deformed, (b) stress relieved, (c) partially recrystallized, (d) fully recrystallized (e) normal grain growth and (f) abnormal grain growth [1].

## 2.2. DEFORMED STATE

A knowledge of microstructural and textural changes during deformation would increase the understanding of the primary recrystallization process in a metal. A part of the energy spent during deformation gets stored in the metal as defects. Some of the most important changes in the microstructures are discussed in the following section.

### 2.2.1. Structure of deformed metals

First, and most obvious, the grains change their shape during deformation. There is a large increase in the total grain boundary area [1]. The new grain boundary area that has been created during deformation incorporates some of the dislocations that are created during the deformation process. A second feature is the appearance of an internal structure within the grains. This too results from the accumulation and rearrangement of dislocations. Summing up all the energy stored by dislocations and the new interfaces represents the stored energy of deformation. During deformation the orientation of each grain in a polycrystalline metal changes relative to the directions of the applied stresses. These changes are not random and involve rotations, which are directly related to the crystallography and geometry of deformation. As a consequence the grains acquire a *preferred orientation* or *texture*. This texture becomes stronger as the deformation proceeds.

In cubic metals the two basic modes of deformations are slip and twinning and the choice of mode is decided by the value of *stacking fault energy*. For example, Aluminum has a stacking fault energy of  $166 \text{ mJm}^{-2}$ , whereas the 70Cu: 30Zn brass has a stacking fault energy of only  $20 \text{ mJm}^{-2}$ . The deformation of high stacking fault energy metals like Al, takes place mainly by slip mechanism. On the contrary, the main mode of deformation for low stacking fault energy metals is twinning.

During homogeneous deformation, slip or twinning that is initiated in one grain is confined to that grain. These can be readily distinguished from those occurring in neighboring grains. However, inhomogeneity of deformation has been well recognized for a long time and the differently oriented regions within a deformed grain have been identified [19]. Following Barrett [19], region(s) of constant orientation that is (are) significantly different to the orientation(s) present elsewhere in that grain is termed as *deformation band*. A schematic illustration given in Fig. 2.2 shows various deformation features. The region B, which has a different orientation from the grain region A, is separated by a thin band of finite width. This thin band is called *transition band*. In

many cases deformation bands are parallel to each other and involve a double orientation change A to C and then C to A. This type of deformation band is called *kink band* [20]. Chin [21] identified that the origin of deformation band is either the ambiguity associated with the selection of the operative slip systems or the lack of strain homogeneity experienced by the same grain in different regions. The transition band develops when neighboring parts of a grain deform on different slip systems and rotate to different end orientations. In its most usual form the transition band consists of a cluster of long narrow cells or subgrains with a cumulative misorientation from one side of the cluster to the other [22]. Hjelen et al. [22] noted that in aluminum alloys even transition bands with very small widths show large orientation changes across the band.

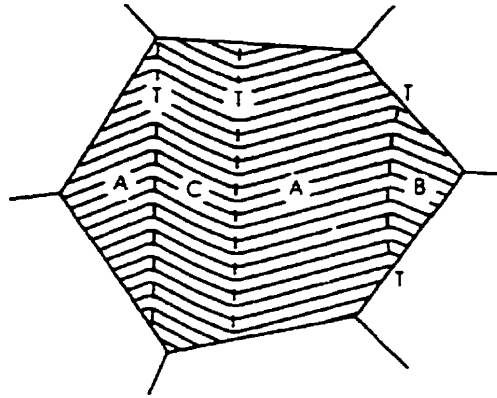


**Fig. 2.2.** Schematic diagrams illustrating the deformation, transition and kink bands in a deformed microstructure (refer text) [1].

Irrespective of whether slip or twinning is the major deformation mode, the microstructure is complicated by the presence of inhomogeneities that are smaller than deformation bands. In moderately deformed Al, Cu, Ni etc., the dislocations are arranged in a cellular structure that is approximately equiaxed [1]. The *microbands* are observed as long, thin, plate-like features that are superimposed on the cellular structure. At higher levels of strain ( $\epsilon > 1$ ) a macroscopic inhomogeneity known as a *shear band* also occurs. These have a morphology that is related explicitly to the deformation geometry and are easily seen in the optical microscope (Fig. 2.3)

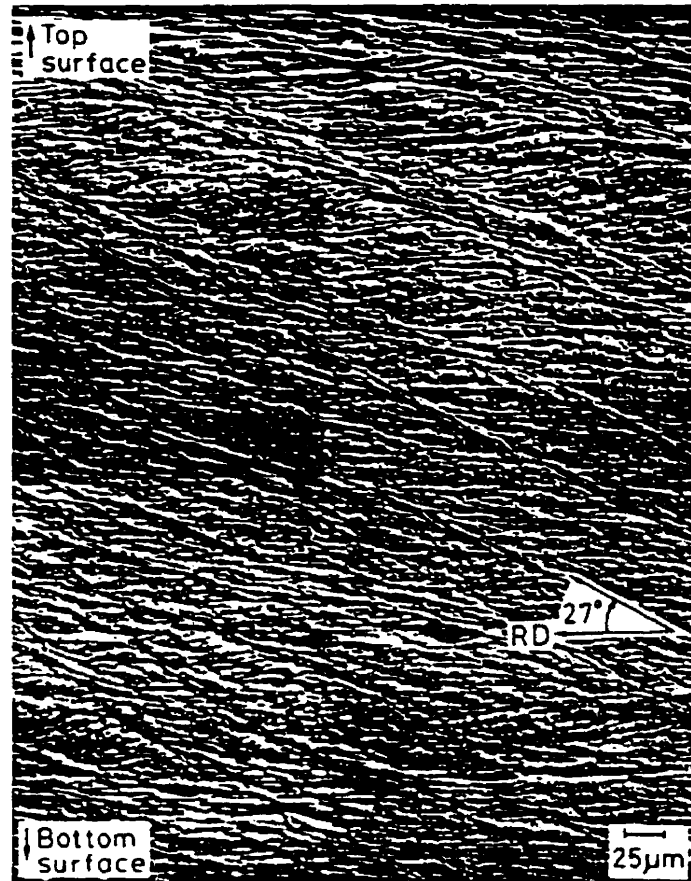


Fig. 2.3. 90% cold rolled aluminum single crystal exhibiting slip bands [31]

Typical microstructure of a metal that is deformed by slip mode comprises a three-dimensional structure of regions of low dislocation density, bounded by boundaries of high dislocation density. If the boundaries of this kind are diffused and consisting of tangled arrays of dislocations, then they form a *cell structure*. If the boundaries are sharp and consist of well ordered arrays, then they form a *subgrain structure*. It has been known for many years that the substructure of even moderately deformed, high-purity aluminum is better described in terms of subgrains rather than cells. This is a direct consequence of extensive dynamic recovery that takes place at room temperature. The most extensive work on this subject has been done by Hansen and his colleagues at Riso National Laboratory [7.23-25]. In their work, a number of structural inhomogeneities are distinguished and documented.

Shear bands can be seen under optical microscope. These bands correspond to narrow regions of intense shear that occur independently of the grain structure and independently also of normal crystallographic considerations. In rolled metals they occur at 25-40° to the rolling plane and are parallel to the transverse direction [26,27]. In metals that deform by slip, the shear bands form colonies. The colonies are usually several grains thick and the bands in alternate colonies are in opposite sense. The shear bands were first reported by Adcock (as given in [28]) who showed that, on annealing, nucleation occurred at the shear bands. Unlike deformation bands, those are inevitably restricted to a single grain [29], the shear bands cross grain boundaries. Stacking fault energy [30] largely influences the formation of shear bands in FCC metals during cold rolling. The shear bands are readily observed in moderately rolled low-stacking fault energy metals [16]. However, Kamijo et al. [31] experimentally observed that shear bands are formed also in the high-purity Al, which has high stacking fault energy. They also concluded that the formation of shear bands seems to depend strongly on rolling conditions.

So far the deformation inhomogeneities that are relevant to nucleation processes have been the focus of this section. These inhomogeneities are the locations in the deformed matrix (and also the prior grain boundary and vertices), where the new orientation nucleates during annealing. However, the discussion on nucleation and grain growth is incomplete without a discussion on stored energy and its dependence on orientation in the deformed matrix. The following section § 2.2.2 does that.

### ***2.2.2. Stored energy of cold work***

Most of the work expended in deforming a metal is given out as heat and only a small amount (1-10%) [28,32] remains as stored energy in the metal. This energy is stored in the form of crystal defects that have been described in the previous section § 2.2.1. Early works on stored energy [32-35] were based on calorimetric technique. The typical value of stored energy obtained by this method, as an example, in aluminum is ~30 J/g-atom

[35]. This method of measurement gives the overall value of the stored energy in the material. However, for a given macroscopically imposed stress, grains of different orientation are expected to develop microscopic defects at different rates. This is because each orientation behaves differently for the same imposed stress. This explains why stored energy may vary with crystallographic orientation. Thus, measuring stored energy by calorimetric method would not help much to understand the nucleation and growth behavior of each crystallographic orientation. Various attempts have been made by numerous researchers [29,36-41] to evaluate the stored energy by measuring the broadening of x-ray, neutron diffraction lines and by TEM (*transmission electron microscope*) analysis of substructure. These methods are capable of providing knowledge about the orientation dependence of stored energy in deformed materials. The x-ray and neutron diffraction techniques measure only the lattice strain energy. Further discussion on these techniques is offered in chapter 3 under the section § 3.2.1.

The TEM analysis of subgrain size and misorientation would provide a measure of stored energy [29,39] as function of crystal orientation. For example, Dillamore et al [29,39] found that the subgrains in deformed polycrystalline iron rolled 70% were 0.5-1  $\mu\text{m}$  in diameter and had average misorientation of from 2-6°. Differences in misorientation and size were observed for different orientation of the grains in which the substructure had formed. The combination of small subgrain size and high subgrain misorientation, and therefore high sub-boundary energy, means that the local values of stored energy is high. The stored energy varies with the orientation of grains in the rolling plane. For a  $\langle 110 \rangle$  rolling direction, the stored energy calculated in this way [39] are in the order  $E_{\langle 110 \rangle} < E_{\langle 111 \rangle} < E_{\langle 211 \rangle} < E_{\langle 100 \rangle}$ . This was then confirmed by independent x-ray line broadening studies [37]. This result has proved to be very useful in providing understanding of the recrystallization textures found in low carbon steels. However only rolling plane sections were examined in this early work and it was assumed that the subgrains were hexagonal prisms with height equal to the diameter, whereas, the actual shape of the subgrain in practice is much more complicated.

For an in-depth understanding of primary recrystallization, apart from the basic information such as deformed microstructure, texture and orientation-dependent stored energy, knowledge on grain boundary energy, mobility and fraction of mobile grain boundaries around the growing new grains is needed. Also, to understand the abnormal grain growth, where the only driving force is the reduction of grain boundary. knowledge of grain boundary structure, energy and mobility is of great importance. Therefore, the following section has been devoted to the review of this subject.

### 2.3. GRAIN BOUNDARY STRUCTURE, ENERGY AND MOBILITY

The annealing processes such as recovery, recrystallization and grain growth involve the migration of grain boundaries. Therefore, our ability to understand these phenomena may well be limited by our lack of knowledge of structures and properties of grain boundaries. The grain boundaries are the interfacial regions that separate two grains. There are five macroscopic degrees of freedom needed to define a boundary. In many cases it is sufficient or convenient to neglect the orientation of the boundary planes (which contribute two degrees of freedom) and consider only the remaining three parameters, which define the difference in orientation of two grains that form the boundary. The relative rotation of the two crystals can be described mathematically in various forms, among them *angle axis pair* notation is popular and will be used throughout this thesis. In cubic materials, because of the symmetry, the relative rotations of the two grains can be described in 24 different ways. In the absence of any special symmetry, it is conventional to describe the rotation by the smallest misorientation angle ( $\theta$ ) and the corresponding axis. The range of  $\theta$  which is allowed therefore is limited and Mackenzie [42] has shown that the maximum value of  $\theta$  is  $62.8^\circ$  for axis  $\langle 1, 1, \sqrt{2}-1 \rangle$ .

#### 2.3.1. Classification of grain boundaries based on structure

It is convenient to classify the grain boundaries based on misorientation angles. Generally the grain boundaries are grouped into two classes namely *low angle grain*

*boundaries* (LAGB) and *high angle grain boundaries* (HAGB). The angle at which transition from high angle to low angle boundaries occurs is typically between  $10^\circ$  and  $20^\circ$ . The boundaries with misorientation higher than the transition angle are called high angle grain boundaries. Low angle boundaries are those, which are composed of arrays of dislocations, and structure and properties of these boundaries vary as a function of misorientation. In general high angle boundaries have a random structure. However, there are '*special*' high angle boundaries, which may have characteristic structure and properties. There are also other classifications of boundaries generally based on the misorientation. As an example, in the case of primary recrystallization, nuclei of the main annealing texture component namely cube,  $\{100\}\langle 001\rangle$  seems to have high concentration of boundaries with misorientation higher than  $35^\circ$ . This will be discussed in chapter 3. Finally, based on grain boundary energy, for example in Fe-Si steels, the boundaries with misorientation of  $20\text{-}45^\circ$  have high energy and are classified as *high energy grain boundaries* (HEGB). A detailed discussion concerning these boundaries is presented in chapter 4.

As mentioned above a low angle grain boundary can be represented as an array of dislocations [43,44]. Simple boundaries of this kind are *tilt* and *twist boundaries*. The simplest boundary namely the *symmetrical tilt boundary*, which is shown in Fig. 2.4, consists of a wall of parallel edge dislocation aligned perpendicular to the slip plane. These are commonly observed by transmission electron microscopic techniques. If the spacing of the dislocations of Burger vector  $b$  in the boundary is  $h$  then the crystals on either side of the boundary are misoriented by a small angle  $\theta$  can be approximated as  $\theta = b/h$ . In the case of symmetrical twist boundary, the network of screw dislocation is responsible [1,45] for observed misorientation. Any arbitrary low angle boundary is built from dislocation that have both edge and screw components [45]. These low angle boundaries are of great importance in understanding the annealing processes.

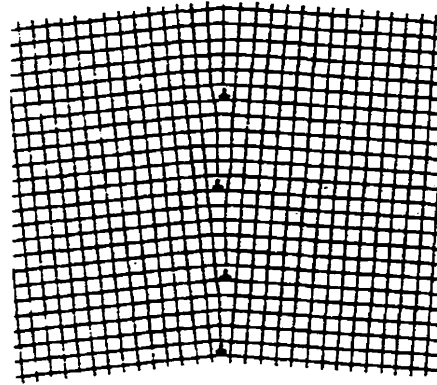


**Fig. 2.4. Schematic diagram of a symmetrical tilt boundary [1]**

The 'special' boundaries in the high misorientation angle range are specifically called *coincident site lattice* (CSL) boundaries [46]. The concept of CSL is geometrical. Consider two interpenetrating crystal lattices and translate them so as to bring a lattice point of each into coincidence as shown in Fig. 2.5. If other points in the two lattices coincide, then these points form the coincident site lattice. These types of special boundaries are denoted as  $\Sigma$ , which represents the reciprocal of the ratio of lattice sites to CSL sites. For cubic systems, these CSL boundaries have odd integers as  $\Sigma$  values. In the Fig. 2.5, the CSL boundary shown has a value of  $\Sigma=5$ . The *coherent twin* boundaries have  $\Sigma=3$  and low angle boundaries have  $\Sigma$  values closer to 1. Extensive details about the angles and axes at which these CSL relationships exist are given in [47,48]. Brandon [49] pointed out that the CSL boundaries maintain their 'special' coincidence status within the small deviation of misorientation that is calculated to be  $15/\Sigma^{1/2}$  degrees. This is called Brandon criterion. The grain boundaries that deviate from Brandon criterion are generally called *random boundaries*. As  $\Sigma$  values increase, the boundary structure becomes more random. The energy of the CSL boundaries is lower compared to the non-CSL random boundaries.

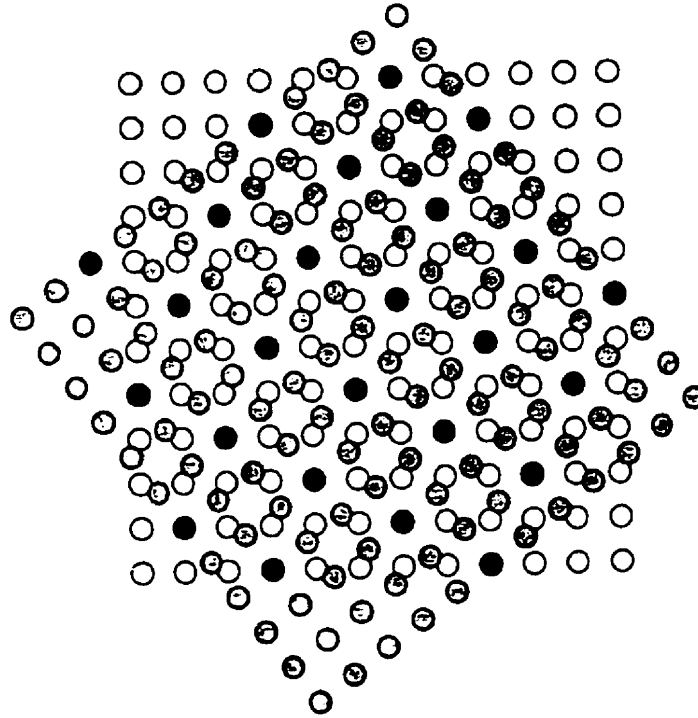


Fig. 2.5. A coincident site lattice ( $\Sigma 5$ ) formed from two simple cubic lattices rotated by  $36.9^\circ$  about an  $\langle 001 \rangle$  axis. The coincident sites are shown as black circles [1].

Even when the angular deviation from CSL is more than allowed, the boundary structure can be maintained by introducing grain boundary dislocations, which locally accommodates the mismatch in much the same way as dislocations preserve the grain boundary lattice in low angle grain boundaries. It is also predicted [50] that some grain boundary dislocations are associated with *steps* in the boundary. These boundary defects are of importance in understanding the mobility of boundaries.

### 2.3.2. Grain boundary energy and misorientation

It is generally accepted that the energy of the grain boundary is a function of misorientation. The famous relationship between them was first derived by Read and

Shockley [44] for a simple tilt boundary based on a dislocation model and is given in the following equation:

$$E = E_0\theta(A - \ln\theta) \quad (2.1)$$

Where  $E$  is the grain boundary energy,  $\theta$  is the misorientation angle,  $E_0$  and  $A$  are constants. It is assumed that the low angle grain boundary is an array of dislocations and strain energies; associated with them is the energy of the boundary. Energy  $E_0$  in equation (2.1) is defined by the following equation.

$$E_m = E_0\theta_m \quad (2.2)$$

Here,  $E_m$  is the maximum energy and  $\theta_m$  is the angle for which the maximum is observed. The equation (2.1) has been verified for relative energy of low angle grain boundaries on various systems and found to be in good agreement with experimental measurement [51]. Dunn et al. [52-54] experimentally verified the validity of the equation (2.1) for  $(110)^\circ$  and  $100^\circ$  tilt boundaries for Fe-3%Si system and found it to be in good agreement. Further discussion on this subject will be given in § 4.3, under the topic on computer simulation of abnormal grain growth in Fe-3%Si steel.

Experimental method of measuring the grain boundary energy is based on the fact that at high temperatures rapid atomic movements allow intersecting boundaries to approach an equilibrium configuration. The interfacial tensions, which act along the tangential vector to each boundary, and the torque due to the anisotropy of the interfacial tensions tends to rotate the interfaces into positions of lower energy [55-56]. This is a triangular force relationship by which the interfacial energies of two of the boundaries of a tri-crystalline configuration may be deduced relative to that of the third. To do this, one needs only to measure the equilibrium dihedral angles at the triple junction [56].

Due to the complexity involved in studying the structural features of the grain boundary on an atomic level, computer techniques such as *molecular dynamics* are increasingly being used for this purpose [45]. Few of the results of such calculations necessary for this thesis work with a focus on fcc transition metals such as Cu and Ni are discussed in section § 5.3.

### 2.3.3. *Mobility of grain boundaries*

The migration of low and high angle boundaries play an important role in the annealing of cold worked metals. Low angle boundary migration occurs during recovery and during the nucleation of recrystallization. and high angle boundary migration occurs both during and after primary recrystallization. The grain boundary mobility may be perceived as the ability of the boundary to migrate in the matrix. Suppose a grain boundary moves with a velocity ( $v$ ) in response to the net effective pressure  $P$  on the boundary. It is generally assumed that the velocity is directly proportional to the pressure as given below.

$$v = MP \tag{2.3}$$

Here, the constant of proportionality is the *Mobility* of the boundary. This kind of relationship is predicted by the reaction rate theory. Experimentally, various researchers [58-61] confirm this relationship on various materials. After a long discussion on various theories of grain boundary mobility, Humphreys and Hatherly [1] concluded the following. The random grain boundaries have high mobility and are often independent of the misorientation angle  $\theta$ . The mobility of LAGBs is a strong function of  $\theta$ . A detailed account on the dependency of mobility on orientation is discussed in detail by Gottstein and Schwarzer [62].

The mobility of high angle grain boundaries is temperature-dependent and is often found to obey an Arrhenius type relationship of the form

$$M = M_0 \exp\left(-\frac{Q}{RT}\right) \quad (2.4)$$

Here, the constant  $R$ ,  $M_0$  and the activation energy of grain boundary migration are independent of temperature  $T$ .

As far as the mobility is concerned, a lot of confusion still exists in deciding which type of boundary has high mobility and why. It is however, generally accepted that low angle boundaries ( $\Sigma 1$ ) and twin boundaries ( $\Sigma 3$ ) have low mobilities. The high mobility for the CSL [63-69] boundaries is highly questionable and in-depth research is required in this subject. For example, in the case of Fe-Si steels, one group of researchers [63-67] argues that certain coincidence site lattice (CSL) boundaries have high mobilities, which result in abnormal grain growth. Harase *et al.* [63,64] and Shimizu *et al.*, [65] argued that among various CSL boundaries,  $\Sigma 9$  played an important role in the development of  $\{110\}\langle 001\rangle$  texture. In their work a possible role of other CSL boundaries was not ruled out. Recently Lin *et al.* [67] stated that the low  $\Sigma$  boundaries including  $\Sigma 3$  are responsible for the AGG of Goss  $\{110\}\langle 001\rangle$  grains in Fe-Si steels. These authors argue that there is no energetic or structural basis for an enhanced stability of the  $\Sigma 3$  boundary in bcc materials such as Fe-Si. Different types of CSL boundaries are given importance from case to case ( $\Sigma 9$  [63],  $\Sigma 7$  [68], and  $\Sigma 5$  [69]); however, no clear explanation for the selection of Goss orientation in Fe-Si steels is offered. In the present research work, the computer simulation of Goss texture development is carried out under the assumption that high-energy boundaries have high mobility. Further discussion regarding this assumption will be given in chapter 4. However, discussion concerning the effects of temperature and impurities on the mobility of grain boundaries will be given here.

It is known that the activation energy depends on GB misorientation and is different at various concentrations of impurities. The results of Aust and Rutter [70,71] indicates that in high-purity metals, the differences in GB mobility arise primarily from an orientation dependence of solute segregation to the boundary, rather than an intrinsic

difference between GB mobilities. These authors demonstrated that the CSL boundaries are more mobile than random boundaries up to an impurity level of 0.006 wt % Sn in Pb. At higher impurity levels the difference between mobilities of CSL and random boundaries disappear [1,70,71]. Again, it has been reported that the specialty of the CSL boundaries vanishes at high temperature [1]. As a typical Fe-Si steel has around 3% Si with other alloying elements such as C, Mn, S, Al, N, etc., in considerable amount and the secondary recrystallization process is observed to happen above 1000° C, the special property of CSL boundaries may not apply to this case.

Similarly, there is still confusion in deciding whether the celebrated  $40^\circ\langle 111 \rangle$ , which is close to  $\Sigma 7$ , is responsible for the cube,  $\{100\}\langle 001 \rangle$  texture development in Aluminum. One of the best-known early investigations of the effect of misorientation on mobility is that by Liebmann et al. [72]. He measured the migration rate of  $\langle 111 \rangle$  tilt boundary in 99.8% aluminum crystals which had been lightly deformed, and found the mobility to be a maximum for a misorientation of  $\sim 40^\circ$  about a  $\langle 111 \rangle$  axis. This result also shows a very broad width of the mobility curve that spread from  $25^\circ$  to  $55^\circ$ . There are other works [8,73] supporting the high mobility of high angle boundaries with misorientation  $> 35^\circ$  in aluminum. A detailed discussion regarding this will be given in chapter 3.

Having discussed the important variables for the annealing processes such as structure of deformed metals, stored energy of cold work, grain boundary energy and mobility, one has to look into the details of mechanisms that are involved in the annealing processes. The following sections would deal with primary and secondary recrystallization processes.

#### 2.4. PRIMARY RECRYSTALLIZATION

The thermodynamically unstable defect structure created by the cold work is eliminated, by nucleation and grain growth at high homologous temperatures. This process is often called primary recrystallization in order to distinguish it from processes of exaggerated

grain growth, which may occur in fully recrystallized material. It is convenient to divide primary recrystallization into two regimes, *nucleation*, which corresponds to the first appearance of new grains in the microstructure and *growth* during which the new grains consume deformed matrix.

#### 2.4.1 The JMAK model for recrystallization

The progress of recrystallization with time during isothermal annealing is commonly represented by a plot of the volume fraction of material recrystallized ( $X_t$ ) as a function of time, usually  $\log(\text{time})$ . This plot has the characteristic sigmoidal form as shown in Fig. 2.6, and typically shows an apparent incubation time before recrystallization is detected. This is followed by an increasing rate of recrystallization, a linear region, and finally a decreasing rate of recrystallization mainly due to the impingement of growing grains. This phenomenon is analytically modeled by early researcher Kolmogorov [74], Johnson and Mehl [75] and Avrami [76] and is commonly known as the JMAK model. This model results in JMAK equation. A more general form of this equation is as follows

$$X_t = 1 - \exp(-Bt^n) \quad (2.5)$$

Where,  $B$  is a constant and  $t$  is time. The exponent  $n$  is called JMAK or Avrami exponent. Basic assumption of this equation is that the nucleation occurs uniformly and randomly throughout the deformed material and the growth rates of the nucleated grains are isotropic until the impingement. Typical values of  $n$  may be between 3-4 for 3-dimensional cases and 2-3 for 2-dimensional cases.

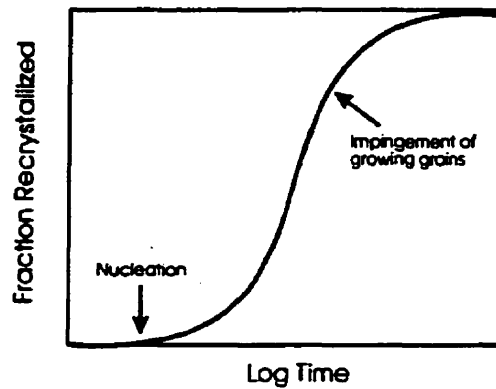


**Fig. 2.6.** A typical recrystallization kinetics during isothermal annealing [1]

Before attempting to discuss the nucleation and growth, it may be important to know at least the qualitative effect of various parameters on recrystallization itself. This is discussed under the following section on the laws of recrystallization [1.77.78].

#### 2.4.2. The laws of recrystallization

These rules are obeyed in most cases and are easily rationalized if recrystallization is considered to be a nucleation and growth phenomenon, controlled by thermally activated processes, whose driving force is provided by the stored energy of deformation. The rules are [1.77.78]:

- (i) A certain critical deformation is needed to initiate recrystallization.
- (ii) The temperature at which recrystallization occurs, decreases as the time of annealing increases.
- (iii) The temperature at which recrystallization occurs, decreases as strain increases.
- (iv) The recrystallized grain size depends primarily on the amount of deformation, being smaller for large amounts of deformation.
- (v) For a given amount of deformation, the recrystallization temperature will be increased by (a) a larger starting grain size and (b) a higher deformation temperature.

These rules tell us that the degree of deformation applied must be sufficient to produce a nucleus for the recrystallization and to provide the necessary driving force to sustain its growth. The microscopic mechanisms controlling recrystallization are thermally activated and the relationship between the recrystallization rate and the temperature is given by Arrhenius type equation. Increased strain increases the stored energy in the material. The nucleation and growth are therefore more rapid or occur at lower temperature in a more highly deformed material. The nucleation rate is more affected by strain than is the growth rate. Therefore, a higher strain will provide more nuclei per unit volume and hence a smaller final grain size. The grain boundaries are favored sites for nucleation, therefore a large initial grain size provides fewer nucleation sites, the nucleation rate is lowered, and recrystallization is slower or occurs at higher temperatures. At higher temperatures of deformation, more recovery occurs during the deformation. This is called *dynamic recovery*. The stored energy is thus lower than for a similar strain at a lower temperature.

Having discussed what effect the important parameters such as the initial grain size, deformation strain and annealing temperature have on time needed for recrystallization and the grain size after annealing, the micromechanisms that control the nucleation and grain growth during primary recrystallization are discussed below.

#### *2.4.3. Nucleation of recrystallization*

A recrystallization nucleus is a crystallite of low internal energy growing into deformed material from which it is often separated by a high angle grain boundary [1]. Nucleation can be classified according to the location of the nuclei [79]. Homogeneous nucleation is defined as nucleation, which takes place without regard to location in the microstructure. Heterogeneous nucleation, on the other hand, occurs at specific sites in the microstructure such as grain boundaries, particles, etc. These categories may be further subdivided according to nucleation rate. Site-saturated nucleation takes place when all nucleation events occur simultaneously. Continuous nucleation is the case when nucleation occurs throughout the annealing process. Continuous nucleation may be at

constant nucleation rate, which can be defined as the constant number of nuclei per unit volume of unrecrystallized material activated per unit time, or the non-constant nucleation rate [13].

Primary recrystallization texture is determined primarily by the orientation of nucleus grains and relative nucleation and growth rates of these grains. It has been known [1] that the recrystallization texture is produced either by "oriented nucleation" i.e., the preferred nucleation of grains with a particular orientation or by "oriented growth" i.e., the preferred growth of nuclei of specific orientations from available array of nuclei. Burke and Turnbull [78] proposed that the classical nucleation theory developed for phase transformations might be applicable to recrystallization. Here nucleation of new grain is assumed to occur through atom-by-atom construction. Calculations based on classical nucleation theory [80] indicate that the formation of new grains this way is not possible. However, these new grains grow from small regions. These regions are recovered subgrains or cells that are already present in the deformed microstructure. The exceptions are new grains generated by twinning [1].

The pre-existence of the nucleus in the deformed microstructure suggests the importance of the substructure and its response to the annealing temperatures. This preformed nucleus model was first postulated by Burgers [81]. Later, studies using high-resolution electron microscopic techniques [27,82-86] have shown that the mechanism of nucleation is either sub-boundary migration or subgrain coalescence. Dillamore et al. [29] pointed out that in order for a high angle boundary to be produced by rapid recovery, there must be an orientation gradient present. An area with a large orientation gradient will always have a high stored energy because the geometrically necessary dislocation or low angle grain boundaries are needed to accommodate the misorientation. Therefore, the nucleation of recrystallization can be considered to be a discontinuous subgrain growth at sites of high strain energy and orientation gradient [1].

Inhomogeneities in the deformed microstructure are the nucleation sites for the new grains. These inhomogeneities may either be present before deformation (grain

boundaries) or induced during deformation. The important classification of microstructural features observed in the deformed metals is given in § 2.2.1. At a microscopic level, the induced inhomogeneities that are important to the recrystallization process are transition bands and shear bands. As these inhomogeneities are associated with large misorientation gradient, they are all possible nucleation sites during recrystallization [87]. These inhomogeneities are important for the oriented nucleation mechanism. In the case of warm plain strain extruded commercial purity Al, authors [22,88,89] confirm the observation of orientated nucleation of cube orientation, which is the predominant recrystallization texture. In 7010 Al specimens, it was observed that the presence of inhomogeneity around precipitate particles after cold deformation increases the nucleation of random texture, thereby reducing the strength of cube texture after recrystallization [90].

As far as the growth of the nuclei is concerned, the mobility of different types of boundaries plays a main role in the preferential growth of a particular orientation. This has been already discussed in § 2.3.3 and the preferential growth of cube,  $\{100\}\langle 001\rangle$  texture during primary recrystallization of Al is discussed in the chapter 3. The high mobility of certain boundaries may influence the preferential growth of a particular orientation and the development of texture. This phenomenon can be illustrated in the case of abnormal grain growth. A short overview of parameters to be considered in the abnormal grain growth is given in the following section.

## 2.5. ABNORMAL GRAIN GROWTH

As mentioned before, abnormal grain growth or secondary recrystallization takes place in order to reduce the interfacial regions and thus the overall energy of the system. This phenomenon takes place when the already recrystallized metal is further annealed at high temperatures and is often associated with the presence of precipitates.

As far as grain growth is concerned, it can be divided in to two major types, *normal grain growth* (NGG) and *abnormal grain growth* (AGG). During normal grain growth,

the microstructure changes in a rather uniform way, therefore the shape of grain size distribution is usually independent of time. In this case, there is a relatively narrow range of grain sizes and shapes. The schematic drawing in Fig. 2.7(a) shows the nearly unaltered shape change but the average grain size shifts towards the higher values. In the case of abnormal grain growth (Fig. 2.7(b)), a few grains in the microstructure grow and consume the matrix of smaller grains and a bimodal grain size distribution develops. Eventually these large grains impinge and normal grain growth may then resume as shown in Fig. 2.7(b).

The main driving force for grain growth is the reduction of grain boundary energy. For an ideal array of grains, where there are no impurities and grain boundary energy is constant, the abnormal grain growth is not expected to happen. Under ideal conditions, as has been shown previously both by analytical [91] and computational analysis [12,92] a very large grain will always grow more slowly than the average grain and will eventually rejoin the normal grain size distribution. Abnormal grain growth can therefore occur only when normal grain growth is inhibited. The abnormally growing grain has some advantage over its neighbors and as a consequence a secondary recrystallization texture is developed. Among the factors such as surface energy, particle pinning, grain boundary groove, etc., which may affect the abnormal grain growth, an effect of second phase particles is considered to be of prime importance. At high temperatures, precipitate particles undergo Ostwald ripening. This causes the breakdown of grain boundary pinning by the particles and favors certain grain boundaries that become more mobile than the others and thus contributes to abnormal grain growth of certain grains. A specific study that has been undertaken in this research work is the abnormal growth of Goss grains in Fe-Si steels discussed in chapter 4. A similar interesting annealing phenomenon is seen in recently developed nanocrystalline materials. The following section is devoted to the discussion on annealing behaviors of nanocrystalline materials.

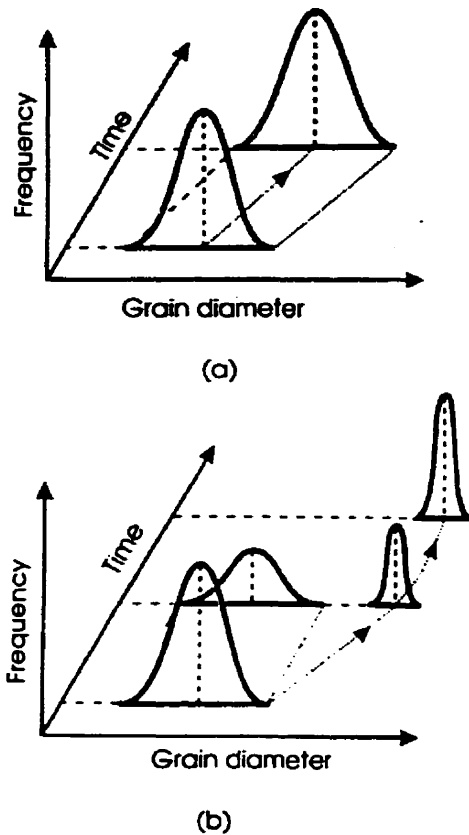


Fig. 2.7. Schematic representation of change of grain size distribution during (a) normal grain growth and (b) abnormal grain growth [1].

## 2.6. THERMAL STABILITY OF NANOCRYSTALLINE MATERIALS

Ever since the synthesis of ultrafine-grained polycrystals by consolidation of small clusters formed via gas condensation [93], a couple of decades ago, thermal stability of nanocrystalline materials has been given much attention. The nanocrystalline materials have a much higher volume percentage of intercrystalline regions [94,95] than conventional polycrystalline materials. The special properties associated with these materials are due to the presence of the high percentage of the intercrystalline regions. The grain boundary and triple junctions also considerably increase the internal energy of these materials. Thus, the nanocrystalline material is thermodynamically unstable, with a strong tendency to transform into a microcrystalline material with fewer grain

boundaries. Unlike in the conventional microcrystalline material, the heat release during grain growth is high enough to be detected by the differential scanning calorimetry (DSC) [96,97].

As mentioned several times before in this thesis, grain growth decreases the total energy of the system by reducing the interfacial area and thus the energy associated with it. Since the nanocrystalline materials have a highly disordered interfacial component, the driving force for grain growth is very high. As an extreme example, Gertsman and Birringer [98] observed an abnormal grain growth at room temperature in nanocrystalline copper produced via gas condensation technique.

Previous studies [10,11,99-104] on the thermal stability of nanocrystalline Ni and Ni-Fe alloy electrodeposits show that both normal or abnormal grain growth can occur depending on the composition of alloy, temperature, etc. In the case of vapor-deposited Ni thin film specimens [104], microstructure exhibits a more uniform grain growth after a heat treatment at 573 K. On the contrary, annealing of nanocrystalline Ni with P and S as impurities and the starting grain size of less than 10 nm showed at 573 K and also at 673 K [101] a transition from rapid grain growth at the initial stages to a very low growth rate. For the case of Ni-1.2% P alloy, the stable structure was observed up to 473 K. At intermediate temperatures up to 623K, the grain size initially increases by a factor of 2-3, then stabilizes at 15 to 25 nm. In Ni-1.2% P, the grain boundary immobilization was observed to coincide with the formation of Ni<sub>3</sub>P precipitates [102]. At 673 K, substantial grain growth was evident within few minutes of annealing [102]. In another research work, Mehta *et al.* [11] observed that grain growth in Ni-1.2% P nanocrystalline electrodeposits with a grain size of 25 nm was not significant up to 513 K. However, abnormal grain growth sets in at annealing temperatures above 513 K during in-situ annealing experiment.

For the present research work, the abnormal grain growth observed in the Ni and Ni-Fe alloy electrodeposits is modeled and using that model the competition between the (111) and (100)-fiber textures observed in these alloys is explained. A further overview of

research and detailed description of the model developed for explaining the microstructure and texture transformations in these alloys is presented in chapter 5.

## 2.7. COMPUTER SIMULATION OF RECRYSTALLIZATION AND GRAIN GROWTH

The past couple of decades have given us new insights into the problems of grain growth solely due to the advent of computer simulation. Computer simulation models can be classified as either direct or statistical. The statistical model deals with ensemble probabilities for a collection of grains and the computer solves a series of interrelated equations, so as to find the behavior of classes of grains (in terms of size classes or shape classes). These models do not take into account topological constraints. Direct simulations can be broken down into deterministic and probabilistic models. In the deterministic model each subsequent configuration of the boundary network is determined by the previous model. The probabilistic model, on the other hand, takes into account of probabilities on a microscopic scale rather than macroscopic ensemble probabilities. Probabilistic is synonymous with *random* or *stochastic*. The *Monte-Carlo* model is one of the probabilistic models.

### 2.7.1. Classical Monte-Carlo grain growth model

Anderson and colleagues [92,105] first proposed the model for computer simulation of grain growth. Later they went on to apply this model to various aspects of grain growth and recrystallization [13-15,105-112] such as abnormal grain growth [15], grain growth with particle pinning [106], primary recrystallization [13,14,110], dynamic recrystallization [109] and so on. The compiled edition on these simulations and results is given in [14].

In the Monte-Carlo model the microstructure is mapped on to a discrete lattice. This is equivalent to dividing it into elementary areas or volumes depending on whether the microstructure is assumed to be 2 or 3-dimensional. These lattices (areas or volumes) are

of identical shapes and sizes, each lattice site denoting one elementary unit. Such that the total number of lattice sites used for mapping the whole microstructure is, say,  $N_T$ . These lattice sites are assigned a number,  $a_i$ , where  $a_i = 1, 2, \dots, Q$ . Each number  $a_i$  corresponds to an orientation of the grain in which it is embedded. Any group of neighboring lattice sites with the same orientation number belongs to a single grain as represented in Fig. 2.8. A typical grain structure in Monte-Carlo simulation is shown in Fig. 2.9. The site having more than one neighbor with a different orientation will be a part of the grain boundary. In Fig. 2.9, each grain is given different grey shades to make them appear more like a real microstructure.

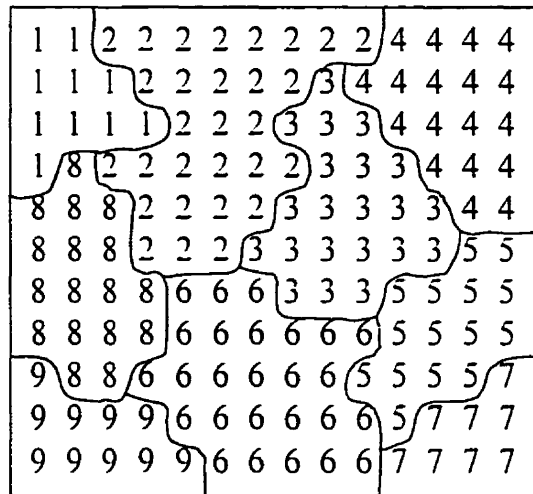


Fig. 2.8. Discrete representation of 2-dimensional microstructure used in Monte-Carlo simulation by Anderson et al. [12].

The energy of the system is described in terms of the *lattice site energy*,  $E_s$ , and is given as

$$E_s = \sum_{i=1}^N (1 - \delta_{s_i}) J_{s_i} \quad (2.6)$$

Where  $J_{s_i}$  is the magnitude of the grain boundary energy and  $\delta_{s_i}$  is the *Kronecker delta* and  $N$  is the total number of nearest neighbors. The kinetics of boundary motion

are simulated using Monte-Carlo technique developed initially by Metropolis et al. [113]. In the Monte-Carlo technique, a site is selected at random and its orientation is changed randomly to any of the other possible neighboring orientations ( $Q-1$ ). The transition probability,  $P$  is then given by

$$P = \begin{cases} 1 & , \Delta E \leq 0 \\ \exp[-\eta\Delta E/kT] & , \Delta E > 0 \end{cases} \quad (2.7)$$

Where  $\Delta E$  is the change in energy caused by the change in orientation. Here  $k$  is the Boltzmann constant and  $T$  is the temperature.

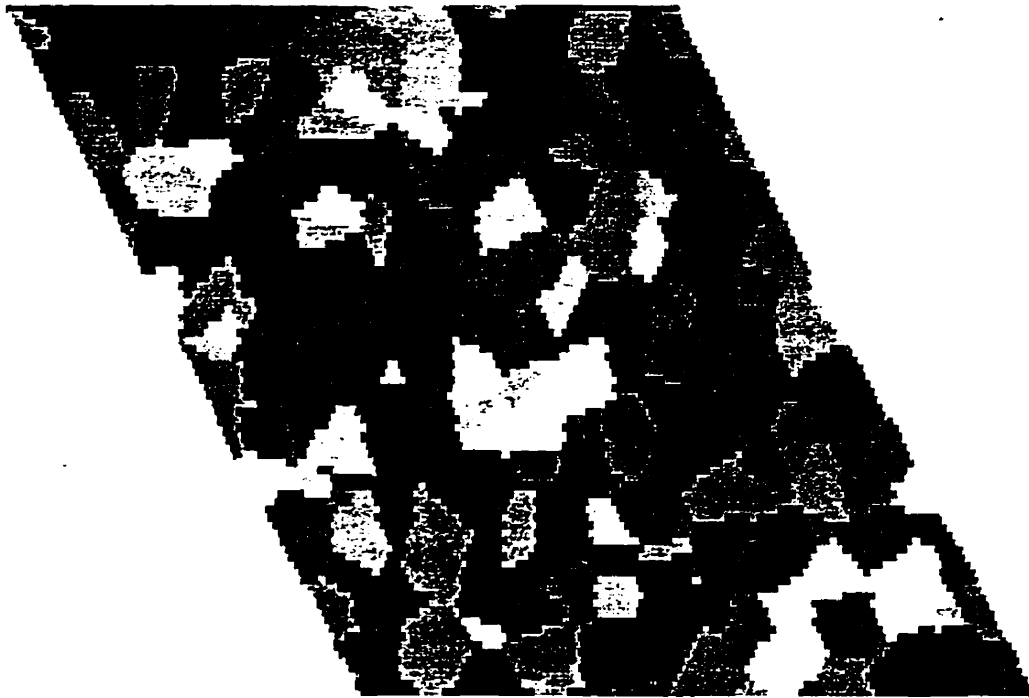


Fig. 2.9. A typical grain structure in Monte-Carlo simulation.

Successful transitions at the grain boundaries to orientations of nearest neighbor grains correspond to boundary migration. A schematic diagram explaining the boundary

motion in Monte-Carlo simulation is presented in Fig. 2.10. Among the two grains shown in Fig. 2.10, the grain numbered 2, grows into the grain numbered 1.

1	1	1	1	1	1	1	1	1
1	1	1	1	1	1	1	1	1
2	2	2	2	2	2	2	2	2
2	2	2	2	2	2	2	2	2

(a)

1	1	1	1	1	1	1	1	1
1	1	1	1	2	1	1	1	1
2	2	2	2	2	2	2	2	2
2	2	2	2	2	2	2	2	2

(b)

**Fig. 2.10. Schematic representation of grain boundary movement in Monte-Carlo simulation.**

The time scale for this simulation is based on the number of re-orientation attempts made. The unit time is defined as 1 Monte-Carlo Step (MCS), which is  $N_T$  re-orientation attempts, where  $N_T$  is the total number of lattice sites. The conversion from MCS to real time has an implicit activation energy factor, which is  $e^{-U/kT}$ , which corresponds to the atomic jump frequency [106]. Since the time, MCS, is normalized by the jump frequency, choosing the temperature  $T=0$  would restrict the accepted re-orientation attempts to those which lower the energy of the system. To reduce finite size effects, very large systems with periodic boundary conditions are employed.

Quantitative analysis of the structures evolved in both 2-D and 3-D simulations exhibit many of the features of grain growth. One of the important and striking similarities is that the scaling behavior for the grain size distribution is characterized by an approximately log-normal form. The normalized grain size distribution,  $f(R/\bar{R})$  is found to be time invariant, to peak at  $R/\bar{R}=1$  and to have an upper cut-off at  $R/\bar{R}=2.7$ . The variation in mean grain size ( $\bar{R}$ ) with time ( $t$ ) is found to obey the growth law

$$\bar{R}^n - \bar{R}_0^n = C_2 t \quad (2.8)$$

where,  $n$  is the *grain growth exponent*, and  $C_2$  is a constant. Most often the value of  $n$  from the simulation is found to be  $\sim 2$ . Another significant success of the simulation method is the observed stability of the grain size distribution under perturbations [108]. Sometimes very large grains introduced into the microstructure are found to grow at rates slower than the average growth and hence are included back into the equilibrium grain size distribution.

Another significant achievement in this area of research is the inclusion of texture by Tavernier and Szpunar [114,115]. These authors discuss texture development during nucleation and grain growth using Monte-Carlo methods, although the grain growth model has used only a semi-empirical concept of the energy of different grain boundaries. Following these works, Hinz and Szpunar [15] offered a more robust Monte-Carlo model with full description of texture and microstructure and facilities for incorporation of anisotropic mobility and grain boundary energy depending on the misorientation of the grain boundary. This modified framework of simulation is discussed in the next section.

### 2.7.2. *Modified Monte-Carlo Framework for grain growth*

The Monte-Carlo works presented on grain growth in the previous section § 2.7.1 has been approached from the traditional framework of a Q-stage statistical model quenched to sufficiently low temperatures to ensure the growth of domains. This is a formalism, which features nonzero probabilities for domains to nucleate within pre-existing domains at finite temperatures. Since this feature is undesirable in a macroscopic description of grain growth, Hinz and Szpunar [15] proposed a more robust framework for grain growth. These authors argue that the Monte-Carlo spin-flip kinetics are originally introduced with the intent of physically modeling the actions of statistical

fluctuations as they drive atomic systems toward thermal equilibrium. As such, the randomness inherent in the Monte-Carlo method and the form of the transition rules it employs, are all essential ingredients of the formalism in that they guarantee randomized Boltzmann distributions of the microscopic energy states. On the other hand, using Turnbull's Theory [116] as a basis for modeling boundary migration, Hinz and Szpunar [15] argue that the role of temperature and hence the fluctuation is limited to merely determining the rate of motion of a boundary and not its course. The boundary motions are assumed to be deterministic resulting from the collective motions of many atoms. As such, the randomness of the Monte-Carlo method can be exploited here as a tool to sample the otherwise untenable system of individual motions of the interacting boundaries. Fluctuations accordingly have no essential physical role to play and as such are an unnecessary ingredient of the formalism. These considerations should provide an adequate basis from which to distinguish between the microscopic theory of the traditional statistical formalism and the more pragmatic approach to the macroscopic grain growth problem at hand.

In this light, Hinz and Szpunar [15] formulated their model by partitioning the microstructure into a set of discrete points on a lattice whose sites are labeled  $i$  and each site is assigned one of the  $Q$  state labels,  $a_i$ , where  $a_i = 1, 2, \dots, Q$ . Then the rate of transition from state  $a_i$  to state  $b_j$  is appropriately given by

$$\Gamma_{a_i \rightarrow b_j} = \sum_{i=1}^N \delta_{a_i b_j} M_{a_i b_j} P(E_i, E_j) \quad (2.9)$$

Here,  $M_{a_i b_j}$  is mobility parameter. The Kronecker delta  $\delta_{a_i b_j}$  restricts the possible final state  $b_j$  to those of the  $N$  nearest-neighbor lattice sites. As in the traditional framework, grains are defined as domains of similarly labeled sites on the lattice and the site energies are given as sums over the interaction energies between dissimilar neighboring sites as previously given in equation (2.6). The form, the probabilities that determine the transitions between states, are necessarily modified from the Metropolis form [113].

which would guarantee an approach to equilibrium in the traditional statistical framework, to the more appropriate form as

$$P(E_a, E_b) = \begin{cases} 1 & , E_b < E_a \\ \exp[-\eta(E_a - E_b)/E_a] & , E_b > E_a \end{cases} \quad (2.10)$$

Here,  $\eta$  is fluctuation parameter. Now, the uphill energy fluctuations (refer equation (2.10)) are re-scaled in comparison to the traditional case (refer equation (2.7)) so that they affect boundaries of high and low energies equally; the low energy boundaries are no more disrupted than the high energy ones. The presence of fluctuations really just aids to overcome any geometrical restrictions that might be imposed by the discrete nature of the lattice and as such is not directly connected with any temperature-related process [15]. The temperature  $T$  is limited to determining the mobility constants  $M_{a, b}$ , which themselves reflect the rates of the atomic processes that stimulate the boundary displacement.

Apart from the modification on the spin-flip probability, this 3-dimensional computer model uses a 3-dimensional honeycomb lattice structure. The grain topology and structure of the computer specimen is discussed in the following section.

### 2.7.3. Computer presentation of microstructure and texture

The three-dimensional honeycomb lattice structure employed by Hinz and Szpunar [15] in their modified Monte-Carlo model has 12 nearest neighbors in order to minimize the anisotropic effect arising from the coarseness of the lattice. Throughout this thesis work, the computer models employed use the same lattice structure. This polygonal structure can be described by the following basis vectors [15]

$$\hat{a} = (1.0.0), \quad \hat{b} = (1/2, \sqrt{3}/2.0), \quad \hat{c} = (1/2, 1/2\sqrt{3}, \sqrt{2/3}) \quad \vec{T} = i\hat{a} + j\hat{b} + k\hat{c} \quad (2.11)$$

Thus the resulting transitional vectors are

$$L_x = l_0 N_a, \quad L_y = l_0 \frac{\sqrt{3}}{2} N_b, \quad L_z = l_0 \sqrt{2/3} N_c \quad (2.12)$$

The assumption of  $N_a=71$ ,  $N_b=82$  and  $N_c=87$  would give an approximate cubic geometry of the computer specimen with total number of  $N_a N_b N_c = 506514$  lattice sites. This number of lattice sites provides a practical yet possibly sufficient cubic geometry to prevent most of the adverse effects of finite lattice size. The periodic boundary conditions are assumed along each of the basis vector directions. An approximate cubic geometry of the computer specimen with a total of 506514 lattice sites is divided into 1500 Voronoi grains that are generated by randomly choosing a set of unique sites on the lattice to represent grain centers. Then by labeling lattice sites according to the nearest grain center, one generates a set of shapes that in the continuous limit approaches a Voronoi distribution. The Voronoi distribution of cell volumes is really just a special gamma distribution [15].

A quantitative description of grain orientation leads to the formalism of the *Orientation Distribution Function* (ODF) [117]. For parameterization of grain orientation in terms of three Euler angles  $\phi_1, \Phi$  and  $\phi_2$ , the ODF represents the volume fraction of grains in the specimen described by an orientation  $g$  and is defined by

$$f(g) dg = f(\phi_1, \Phi, \phi_2) \frac{1}{8\pi^2} \sin \Phi \, d\phi_1 d\Phi d\phi_2 \quad (2.13)$$

where  $f(g)=1$  for a random texture. Here the Euler angles  $\phi_1, \Phi$  and  $\phi_2$  are selected according to Bunge's notation [117] and it is followed throughout this thesis. Texture studies using Monte-Carlo models are specifically performed by ascribing orientation parameters to the labeled grains in keeping with the relevant crystal symmetry. In particular for cubic crystallites, the 24-fold rotation symmetry implies that the Euler angles describing the set of unique crystal orientations can be restricted to the domain

$$\left. \begin{aligned} \tan \Phi \sin \phi_2 &\geq 1, & 0 \leq \phi_2 &\leq \pi/4, \\ \tan \Phi \cos \phi_2 &\geq 1, & \pi/4 &\leq \phi_2 \leq \pi/2, \\ 0 &\leq \Phi &\leq \pi/2, \\ 0 &\leq \phi_1 &\leq 2\pi, \end{aligned} \right\} \quad (2.14)$$

Within this domain, each grain is assigned [118] an appropriate grain orientation in proportion to the experimental Orientation Distribution Function (ODF) by ignoring the clustering and spatial relations. Once the orientation is assigned to the grains then grain boundaries can be characterized by the misorientation angles. In cubic materials, because of the symmetry, the relative rotations of the two grains can be described in 24 different ways. It is conventional to describe the rotation by the smallest misorientation angle  $\theta$ . Then the interaction parameter  $J_{a,b}$  and mobility parameter  $M_{a,b}$ , given in equations (2.6, 2.7, 2.9 and 2.10) are calculated from the grain boundary energy and activation energy of grain boundary self-diffusion respectively as a function of the misorientation angle  $\theta$ .

#### 2.7.4. A note on computer simulations

In metallurgy and materials science, the use of computer methods to understand the underlying mechanisms has increased in recent times. This is mainly due to the complexity of the metallurgical problems at hand and of course the increased speed of computers. Once the real processes are successfully simulated, the reduction of experimental effort, time and cost by extending the computer simulations to the practical applications is well acknowledged. So far the computer simulation for the development of microstructure and texture is in its infancy. The major problems are the inadequate description of initial microstructure and texture of the computer specimen and incomplete description of the anisotropic variables such as grain boundary energy, stored energy and grain boundary mobility. Though the Monte-Carlo procedure promises a striking future for the simulation of the development of microstructure and

texture by facilitating the incorporation of complete topology of input microstructure, texture and required anisotropy of the necessary variables, this procedure still faces difficulties in representation of real time. The time in Monte-Carlo procedure namely the MCS (i.e., Monte-Carlo Step, refer section § 2.7.1) can be however correlated to the real time by an activation energy factor as discussed in section § 2.7.1. The description might get complicated for the system with full description of anisotropic variables related to the grain boundary migration.

The positive side of these computer simulation approaches is that it allows us to test various theories and derive possible conclusions from the simulated results in an inexpensive way, where the in-depth experimental work is neither possible nor reliable. One cannot expect, at the present condition in this research field, to obtain exact simulation of real situations. Further research is needed in this area during the decades to come. As suggested above, the computer simulation procedures for the development of microstructure and texture are at their infancy. However, these procedures can be successfully employed to test the theories by comparing the trends in the simulated results with experimental observations. Throughout this thesis, the Monte-Carlo procedures are used to test the ability and credibility of various proposed theories and mechanisms by comparing the trends of the simulated results with the experimental observations.

## 2.8. SUMMARY

In this chapter, the basic microstructural features of the deformed state are reviewed. The subgrain structure of the deformed grains is discussed, as it is important to understand the origin of nuclei during recrystallization. The basic rules of primary recrystallization are presented. The importance of anisotropic grain boundary energy and mobility and the stored energy for the nucleation and growth is discussed. The fact that the abnormal grain growth is initiated only when the normal grain growth is hindered in a primary recrystallized matrix has been explained. The review of annealing processes

provides a discussion on thermal stability of nanocrystalline materials with a special focus on the Ni alloy electrodeposits.

As the research work presented this thesis focuses on the application of Monte-Carlo simulation to annealing process, the detailed reviews on basic and modified Monte-Carlo frameworks are provided. This is then followed by the description of how the microstructure and texture are incorporated in the computer specimens. Finally a note on both positive and negative points of such Monte-Carlo models is included.

The developed Monte-Carlo framework is applied to three different metallurgical situations in this thesis. These are:

- Primary recrystallization of heavily deformed aluminum (Chapter 3)
- Secondary recrystallization in Fe-3% Si steels (Chapter 4) and
- The (111) and (100) fiber texture competition in nanocrystalline Ni and Ni-Fe electrodeposits (Chapter 5).

## **Chapter 3**

# **RECRYSTALLIZATION OF CAN-BODY ALUMINUM ALLOY – APPLICATION (I)**

The purpose of this chapter is to apply the Monte-Carlo computer model to the primary recrystallization of heavily cold rolled can-body aluminum alloy AA3104. This model predicts the microstructure and texture changes during primary recrystallization of the aluminum alloy by taking the cold rolled texture and stored energy values as input. The section § 3.1 provides the general introduction to the recrystallization of aluminum. This is followed by the section (§ 3.2) on the measurement orientation dependent stored energy. The results of these measurements are discussed in the subsections § 3.2.4 and § 3.2.5.

Analysis of the measured texture and orientation dependent stored energy for deducing conditions for the nucleation of recrystallization is provided in sections § 3.3 and § 3.4. Following nucleation conditions, the growth model for the recrystallization of aluminum is discussed in section § 3.5. Implementation of both nucleation and growth models in the Monte-Carlo procedure is given in the section § 3.6. The discussion on the results obtained from the Monte-Carlo simulation of recrystallization is provided in section § 3.7. Finally, the summary of Chapter 3 is given in the section § 3.8

### 3.1. INTRODUCTION TO RECRYSTALLIZATION OF ALUMINUM

In materials having high stacking fault energy such as Al, the formation of new orientations by recrystallization twinning does not play an important role. Thus, the sources of nuclei are the existing subgrains or cells in the deformed microstructure, as discussed previously in section § 2.4.3. Therefore, before discussing the recrystallization, one should understand the details of cold rolled texture, microstructure and stored energy distribution. During cold rolling, the initial microstructure is transformed into a band-like structure (section § 2.2). The orientation distribution function (ODF) of 88% cold rolled can-body Al alloy (AA3104) using Bunge's notation [117] is given in Fig. 3.1. The chemical composition of the can-body Al alloy AA3104 is 0.15-0.19% Cu, 0.36-0.44% Fe, 1.13-1.27% Mg, 0.80-0.94% Mn, 0.17-0.23% Si, <0.03% Cr, <0.03% V and remaining Al. The rolling texture essentially consists of the  $\beta$ -fiber running from the copper. 'C' orientation  $\{112\}\langle 111\rangle$  through the 'S' orientation  $\{123\}\langle 634\rangle$  to the brass. 'B' orientation  $\{011\}\langle 211\rangle$ .

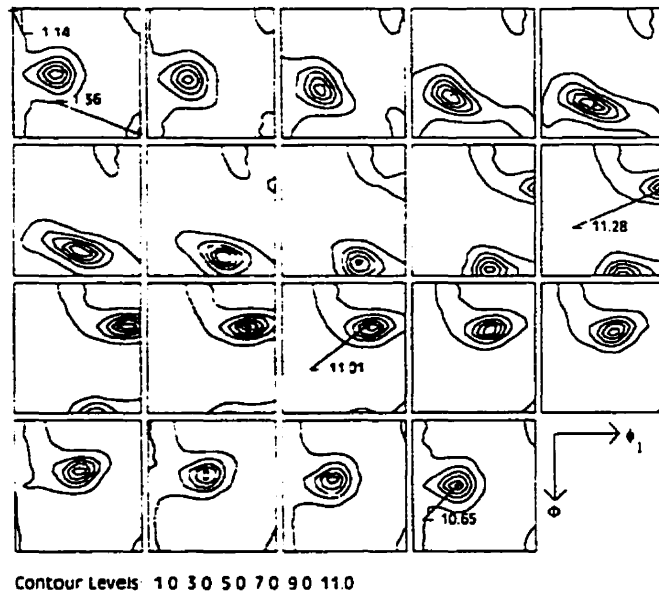


Fig. 3.1. Orientation distribution function (ODF) of 88% cold rolled can-body aluminum AA3104

During recovery the microband structure is transformed into a structure that consists of fairly globular subgrains [1,119,120]. Owing to the high stacking fault energy,  $166 \text{ mJm}^{-2}$  in Al [1], such recovery in most of the Al alloys occurs readily. Subsequently, the coarsening of the subgrains takes place. During the subgrain growth the misorientation between the neighbors increases [84]. Though there is a noticeable change in the microstructure at a submicroscopic level, not much change in the texture is usually observed except that the intensities of deformation texture components alter slightly.

Recovery of a deformed metal takes place at temperatures below the recrystallization temperature and during the initial stages of the annealing at high temperatures. As discussed in the section § 2.4.1, the recrystallization process usually shows an incubation period at the beginning. It is then followed by an increased rate of nucleation and growth. Finally, the rate of recrystallization is decreased due to the impingement of growing grains. As far as the change in texture during recrystallization is concerned, the rate of nucleation of particular orientation may be dependent on both the cold deformation texture and the texture of the material before the cold deformation [121]. In metallic materials, prior to cold rolling, usually hot rolling is carried out to have high percentage reduction of thickness. After the hot rolling, the material is subjected to annealing in order to homogenize properties such as grain size and yield strength through out the sheet. It is then followed by cold rolling and annealing to achieve desirable properties with final dimensional requirements. In aluminum alloys, Blade and Morris [122] have shown that differences in the texture formed after hot rolling and annealing lead to differences in recrystallization kinetics when the material is subsequently cold rolled and annealed. This observation suggests that the recrystallization behavior will be affected not only by the orientations present after cold rolling, but also by the orientations present before cold rolling. The "strain path history" [1] affects both the stored energy and heterogeneities of the microstructure and thus apparently identical texture components may recrystallize quite differently. The "strain path history" is the path taken by an orientation during deformation to reach a final orientation at the end of deformation. These phenomena result in different stored energy values for each orientation in the microstructure. This implies the importance of stored

energy as a function of crystal orientation for the understanding of recrystallization. The following section presents the detailed discussion of stored energy measurement in the can-body aluminum alloy and these stored energy values will eventually be used in the simulation of recrystallization.

### 3.2. MEASUREMENT OF ORIENTATION DEPENDENT STORED ENERGY

Recrystallization of deformed metallic materials starts with the nucleation of new grains and their subsequent growth into the deformed matrix. The major driving force for both the nucleation and growth during primary recrystallization is the energy stored after deformation. The stored energy is a small percentage of the energy expended in deforming a metal, which remains stored in the metal and causes an increase in the internal energy. This increment in internal energy is associated with the defects, mainly dislocations generated during deformation. The process of defects production and interaction between defects is expected to be different for different grain orientations. Thus, the stored energy is different for different crystallographic orientations. The following sections discuss in detail the necessary review of the subject, theoretical and experimental techniques of measurement of orientation-dependent stored energy.

#### 3.2.1. *Introduction to orientation dependent stored energy*

Various attempts have been made by numerous researchers [36-38] to evaluate the stored energy by measuring the broadening of X-ray and neutron diffraction lines. It was also pointed out that the subgrain size and misorientation [29,39] between grains would provide a measure of stored energy in a deformed matrix. Though these methods are very useful, they are restricted to a few specific orientations. Kallend and Huang [40] and Rajmohan et al [41] proposed a more general method which can be used to determine the stored energy for a much wider range of orientations using X-ray and neutron diffraction methods respectively. These works were carried out on copper [40] and interstitial free steel [41]. The present work is focused on the determination of stored energy in a can body aluminum alloy which is cold rolled to 88%. The stored

energy is also measured in the same specimen that is stress relieved at 200° C for 15 minutes. These measurements are undertaken, aiming to study the mechanism that governs the nucleation and growth of cube texture in this aluminum alloy.

One has to understand, however, that the method used in the present work to measure the stored energy reveals only a part of the energy stored during the deformation process. This method mainly measures the inhomogeneous lattice strain energy, which is short-range in nature and is not related to the long-range lattice strain energy. The inhomogeneous lattice strains that are caused by the lattice defects such as dislocations and point defects tend to broaden the diffraction peaks and this broadening depends on the anisotropic deformation characteristics of the grains in the polycrystalline matrix. This inhomogeneous lattice strain is the one that is very important for the prediction of recrystallization behavior during subsequent annealing. Unlike the short-range lattice strain energy, the long-range lattice strain energy shifts the diffraction peak depending on the nature of the existing strain.

Earlier stored energy data were obtained using the calorimetric technique [30.123]. By calorimetric method, Al (99.98%) deformed by compression to a strain of 0.6 was found to have 31 J/g atom of stored energy [35.124]. The release of stored energy during stress relieving is around 13 J/g atom. The remaining stored energy is released during the recrystallization stage. In this technique the demarcation between stress relieved and recrystallized stages is not always clear and it has to be supported by the microstructure analysis. It is also possible that the reactions like transformation of one phase to another (e.g., dissolution of precipitates) might take place during the measurement and thus affect the final result. This technique gives the total stored energy, which is always higher than the energy predicted by the X-ray and neutron diffraction measurement. This is mainly because during the calorimetric measurement, rearrangement of the dislocations and point defects occur and the density of these defects drastically decreases. The measured heat energy probably represents the energy associated with long-range lattice strain energy as well. On the contrary, the X-ray and neutron

diffraction techniques do not alter the defect structure in the matrix and also provide important information such as stored energy as a function of crystallographic orientation. This information is very useful for the prediction of texture development in a deformed matrix during primary recrystallization.

### 3.2.2. Mathematical technique for the measurement of stored energy

As mentioned previously [40,41], a scattered beam carries the average information from all the grains satisfying the diffraction condition. Let the stored energy in a grain with an orientation that is represented by the Euler angles  $\phi_1, \Phi$  and  $\phi_2$  as in Bunge's notation [117] is  $E(\phi_1, \Phi, \phi_2)$ . The measured value of energy for the  $j$ th scattering vector  $\bar{E}_j(\alpha, \beta)$  is then represented by

$$\bar{E}_j(\alpha, \beta) = \frac{\int_{p_j} E(\phi_1, \Phi, \phi_2) f(\phi_1, \Phi, \phi_2) dp}{\int_{p_j} f(\phi_1, \Phi, \phi_2) dp} \quad (3.1)$$

$p_j$  denotes the path through Euler Space corresponding to a rotation of  $2\pi$  about the scattering vector and  $f(\phi_1, \Phi, \phi_2)$  is the orientation distribution function (ODF).

The ODF and pole figure  $q_j(\alpha, \beta)$  are related through the following formula

$$q_j(\alpha, \beta) = \int_{p_j} f(\phi_1, \Phi, \phi_2) dp \quad (3.2)$$

Equation (3.1) can be rearranged using equation (3.2) as follows

$$\bar{E}_j(\alpha, \beta) q_j(\alpha, \beta) = \int_{p_j} E(\phi_1, \Phi, \phi_2) f(\phi_1, \Phi, \phi_2) dp \quad (3.3)$$

The  $E_j$  and  $q_j$  in equation (3.3), are measurable quantities. Using standard procedures [118,125], the product  $E(\phi_1, \Phi, \phi_2)f(\phi_1, \Phi, \phi_2)$  can be calculated. Finally with the ODF as a known parameter,  $E(\phi_1, \Phi, \phi_2)$  can be calculated.

The stored energy on a pole figure space,  $\bar{E}_j(\alpha, \beta)$  is calculated from the Stibitz procedure [126,127] as given below:

$$\bar{E}_j(\alpha, \beta) = \frac{3}{2} Y_{hkl} \frac{(\Delta d / d)^2}{(1 + 2\nu_{hkl}^2)} \quad (3.4)$$

Here  $Y_{hkl}$  and  $\nu_{hkl}$  are the directionally dependent Young's Modulus and Poisson's ratio respectively. The lattice strain  $(\Delta d / d)$  was calculated according to the formula

$$\frac{\Delta d}{d} = \frac{B}{2 \tan \theta} \quad (3.5)$$

Here  $B$  is the effective broadening. This is calculated from the measured full width at half-maximum values of the deformed and reference specimens as below:

$$B^2 = B_d^2 - B_r^2 \quad (3.6)$$

Where  $B_d$  and  $B_r$  are the measured values of full width at half-maximum of the deformed and reference specimens respectively. This is carried out to eliminate the instrumental broadening. These full width at half-maximum can be determined by fitting the diffraction peaks with Gaussian distribution.

Few problems are encountered using this diffraction technique in practice. For example, the strain energy distribution in real conditions may not necessarily be isotropic. The grains possessing symmetrical orientations (e.g. (200) and (002) planes) may have different strain energy distribution. Since the X-ray beam cannot differentiate between

these cases, the crystal symmetry is imposed on the results [40], which means that the stored energy is averaged out over the symmetrical orientations. In a strongly textured sample, there are usually regions of very low or zero intensity in the pole figure. Therefore it is difficult to obtain statistically reliable half-width values at these locations and the stored energy values are not reliable in the corresponding regions in Euler space.

### 3.2.3. *Experimental technique for the measurement of stored energy*

A can body aluminum sheet with a final thickness of ~ 0.3 mm after a cold rolling reduction of 88% is used for the investigation. The chemical composition for AA3104 is 0.15-0.19% Cu, 0.36-0.44% Fe, 1.13-1.27% Mg, 0.80-0.94% Mn, 0.17-0.23% Si, <0.03% Cr, <0.03% V and remaining Al. The grain size before the 88% cold rolling is ~20 micrometers. In order to compare the stored energy values before and after stress relieving, the cold rolled specimen is stress relieved at 200° C for 15 minutes. The reference diffraction peaks are obtained from the fully annealed and random powder specimens.

In general, the reference specimen could be a fully annealed specimen. If the fully annealed specimen is highly textured, a random specimen prepared from powder is preferable. This random specimen should possess a density very close to that of the conventional polycrystalline material and should be sintered for longer time to ensure no residual stress due to compaction. Finally the grain size should be in the micron scale in order to avoid the interference of grain size broadening with the lattice strain broadening. The fully annealed specimen is obtained by annealing the rolled specimen at 400° C for 30 minutes. The random specimen is prepared from the aluminum powder of average size of ~10 micrometer, compacted and sintered to 550° C in argon atmosphere for over 1 hour. All the specimens were polished to the mid-section and electropolished using standard perchloric acid solution.

For the rolled, stress relieved, fully annealed and sintered specimens {111}, {200} and {220} pole figures were measured using Siemen's texture diffractometer. The orientation distribution function (ODF) is then calculated using a discrete method proposed by Imhof [128-130]. The line broadening was measured at points on a polar grid having a spacing of  $10^\circ$  between points as shown in Fig. 3.2 for {111} and {200} diffraction. The obtained diffraction curves were then fitted with Gaussian distributions to determine the full width at half-maximum values. The error in the full width at half-maximum value was high for the diffraction peaks with low signal to noise ratio. The error in the peak values are also observed to be high for the polar angle,  $\alpha$  (in the pole figure space) above  $70^\circ$  and remains approximately constant for the azimuthal angle,  $\beta$  for any constant  $\alpha$ . For the case of low  $\alpha$  values, the full width half maximum (FWHM) are about  $0.41^\circ \pm 0.01$  for the 88% cold rolled specimen. The instrumental broadening is corrected using reference specimens. The relevant orientation dependent Young's module values and Poisson's ratios are taken from Ref. [131] and [132].

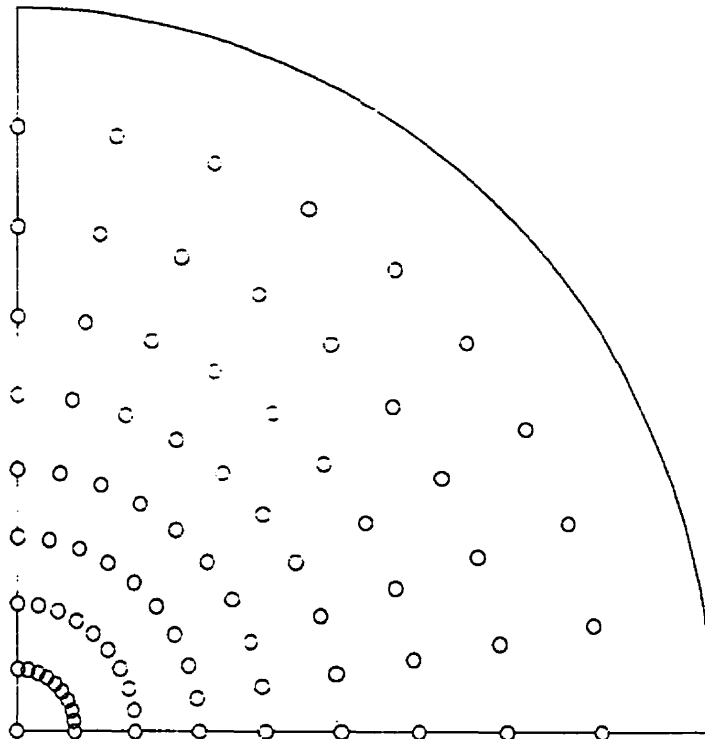


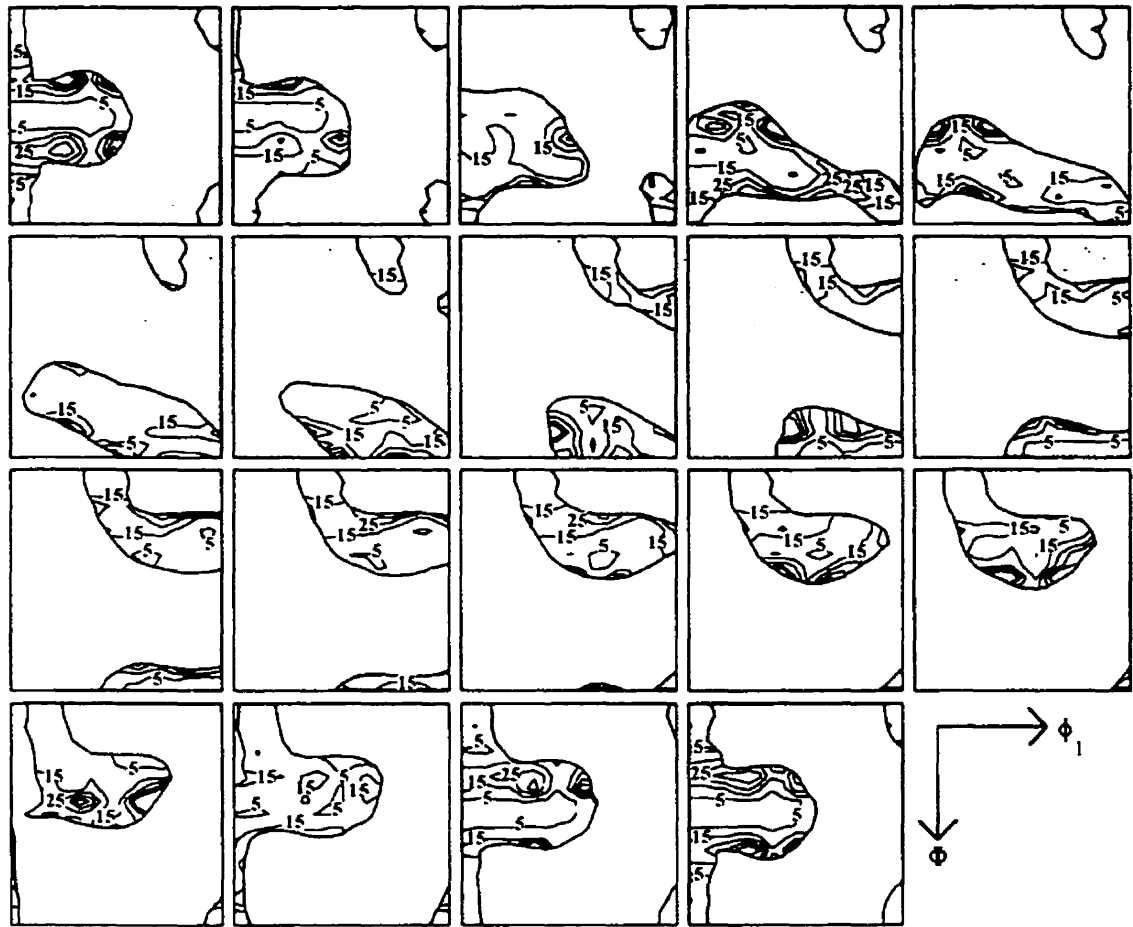
Fig. 3.2. Locations on pole figure at which x-ray line broadening measurements were made

### 3.2.4. Results of stored energy measurement on aluminum

The ODFs that are calculated for both rolled and stress relieved specimens are identical. The calculated ODF of 88% cold rolled can body aluminum specimen is already shown in Fig. 3.1. The Figs. 3.3 and 3.4 are the stored energy distribution functions (SEDFs) of cold rolled and stress relieved specimens. In these SEDFs, the stored energy values are not presented for the orientations that are poorly represented, specifically for the orientations that have values below the random intensity value. These orientations have regions of zero or nearly zero intensities in a highly textured matrix and therefore calculated SEDF will be statistically unreliable. The error in the stored energy values as a function of ODF intensity is similar to the one presented in our previous work [41]. As ODF intensity decreases, the error in the stored energy value increases.

From the stored energy values (refer Fig. 3.3), it is observed that the maximum stored energy of 76.9 J/g-atom is at the orientation with Euler angles of  $\phi_1, \Phi$  and  $\phi_2$  equal to  $60^\circ, 45^\circ$  and  $70^\circ$  respectively. The next highest value of stored energy of 72.7 J/g-atom is found for the orientation  $\phi_1 = 25^\circ, \Phi = 30^\circ$  and  $\phi_2 = 0^\circ$ . The lowest stored energy of 1.8 J/g-atom corresponds to the Goss i.e.,  $\{110\}\langle 001\rangle$  orientation. The recrystallization cubic texture component namely  $\{100\}\langle 001\rangle$  has an average stored energy of 13.6 J/g-atom.

After stress relieving for 15 minutes at  $200^\circ\text{C}$ , the lowest stored energy of 0.1 and 0.01 J/g-atom is found (refer Fig. 3.4) for the orientation  $\{110\}\langle 001\rangle$  (Goss) and  $\{310\}\langle 001\rangle$  respectively. The cubic orientation has the stored energy of 6.3 to 6.7 J/g-atom. The highest stored energy of  $> 60$  J/g-atom is observed again in the orientation with Euler angles  $\phi_1 = 60^\circ, \Phi = 45^\circ$  and  $\phi_2 = 70^\circ$  and  $\phi_1 = 25^\circ, \Phi = 30^\circ$  and  $\phi_2 = 0^\circ$ .



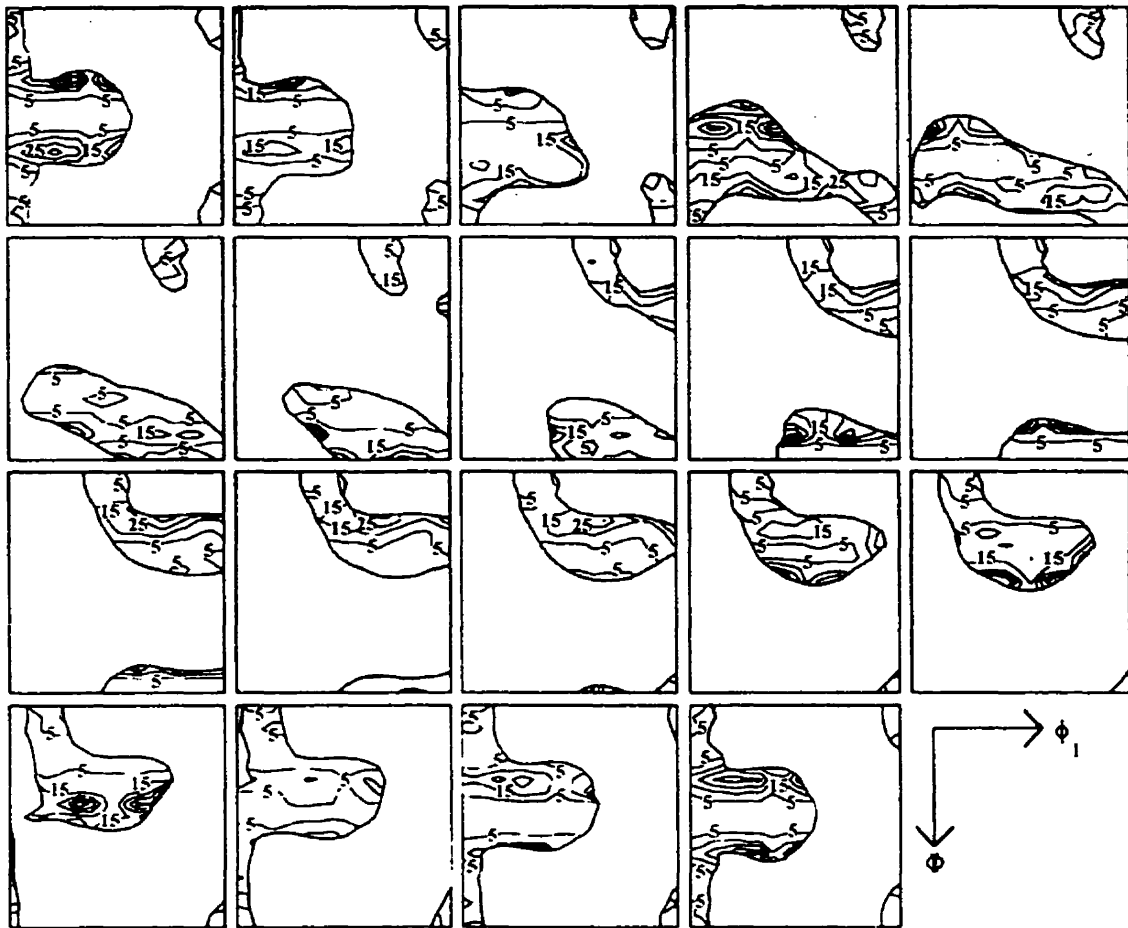
Contour Levels: 5.0 15.0 25.0 35.0 45.0 J/g-atom

□ < 1 x Random intensity

**Fig. 3.3. Stored energy distribution function for 88% cold rolled AA3104 can-body aluminum**

The Table 3.1 summarizes the important orientations that are commonly observed in both rolled and stress relieved aluminum specimens and their stored energy values. The rolling texture components of aluminum (such as S, Copper or C and Brass or B) lose part of the stored energy after stress relieving for 15 minutes at 200°C but the magnitude of stored energy reduction is more for cube texture component. The cube texture component has a stored energy of 13.5 J/g-atom after rolling and releases the energy of about 7.2 J/g-atom during stress relieving. The other recrystallization texture

components such as Goss (or G) and  $\text{Cube}_{\text{RD}}$  (rotated cube along the rolling direction) reach the lowest stored energy value of 0.01 to 0.1 J/g-atom after stress relieving.



Contour Levels: 5.0 15.0 25.0 35.0 45.0 J/g-atom

< 1 x Random intensity

**Fig. 3.4.** Stored energy distribution function for stress relieved AA3104 can-body aluminum at 200°C for 15 minutes after 88% cold rolling

The recrystallization textures such as cube,  $\text{cube}_{\text{RD}}$  (rotated cube along the rolling direction) and Goss lie on the  $\langle 100 \rangle$  direction, which runs along the  $\Phi$  axis at  $\phi_1 = 0^\circ$  on  $\phi_2 = 0^\circ$  section in Euler space. To have a better idea about how the stress relieving affects the stored energy of the recrystallization texture in aluminum alloys, it would be

useful to plot the stored energy along  $\langle 100 \rangle$  direction in the SEDF section of  $\phi_2 = 0^\circ$  for both deformed and stress relieved specimens as in Fig. 3.5. The intensity of the various texture components of the rolled specimen is also plotted along  $\langle 100 \rangle$  fiber in Fig. 3.5. Among the texture components shown in the plot, the Goss component has the highest intensity of 2.5. The  $\text{cube}_{\text{RD}}$  and ideal cube texture components have the intensity of 2 and 1.17. The stored energy of G-component goes from 1.9 to 0.1 J/g-atom as the rolled specimen is stress relieved whereas the  $\text{cube}_{\text{RD}}$  texture component decreases to 0.01 from 3.6 J/g-atom.

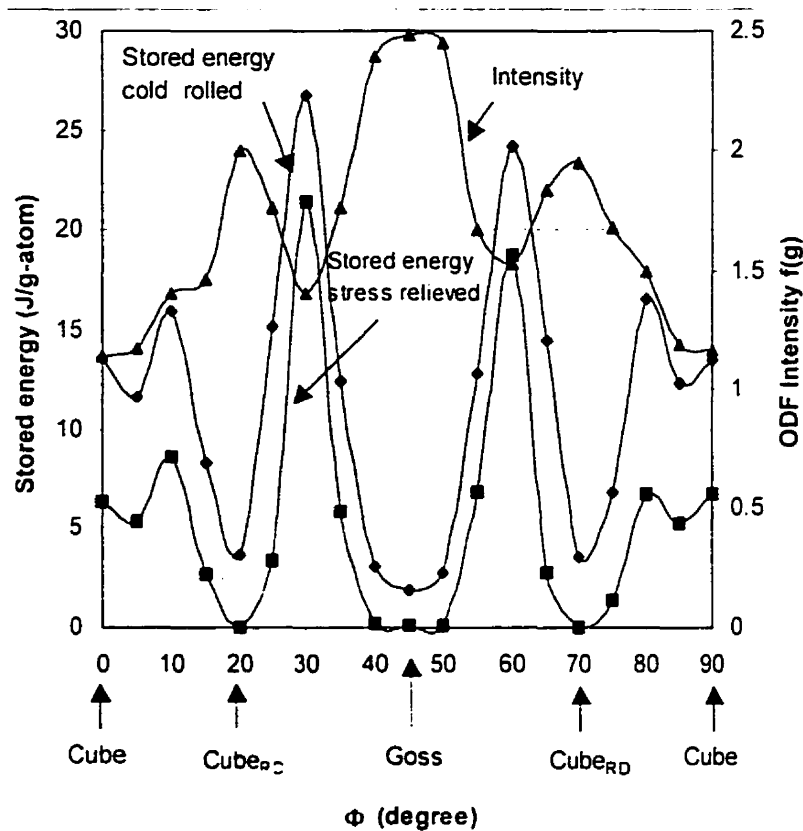


Fig. 3.5. ODF intensity and stored energy after 88% rolling and subsequent stress relieving of AA3104 can-body aluminum along  $\langle 001 \rangle$  direction in  $\phi_2 = 0^\circ$  section

**Table 3.1. Stored energy values of selected orientation in 88% rolled and stress relieved (200°C, 15 minutes) can-body aluminum sheet AA3104.**

Orientation	$\phi_1$	$\Phi$	$\phi_2$	Intensity	Stored energy (J/g-atom)	
					after deformation	after stress relieving
Cube	0	0	0	1.14	13.6	6.4
	90	0	0	1.16	13.4	6.3
	0	90	0	1.17	13.5	6.7
	90	90	0	1.17	13.5	6.7
Cube(RD)	0	20	0	2	3.6	0.01
	0	20	90	2	3.6	0.01
Cube(ND)	20	0	0	0.39	7.5	3.0
	20	0	90	0.45	6.8	3.1
Goss	0	45	0	2.48	1.9	0.1
	90	90	45	2.29	1.8	0.1
Copper	90	30	45	11.28	8.2	5.04
S R	60	35	65	9.42	4.7	2.52
	55	35	60	6.06	4.6	2.64
Brass	35	45	90	10.65	3.2	1.16

The well-known fcc rolling texture component namely  $\beta$ -fiber is presented in Fig. 3.6 as a 3-dimensional plot. The  $\beta$ -fiber runs from the copper orientation C  $\{112\}\langle 111\rangle$  through the S orientation  $\{123\}\langle 634\rangle$  to the brass orientation B  $\{011\}\langle 211\rangle$ . The positions of these orientations are marked in Fig. 3.6. The stored energy release during stress relieving along  $\beta$ -fiber can be analyzed more clearly from the plot shown in Fig. 3.7. In this plot, the stored energy is represented as a function of  $\phi_2$  angles with  $5^\circ$  intervals from  $45$ - $90^\circ$ , which corresponds to the lower part of the  $\beta$ -fiber shown in the

Fig. 3.6. The stored energy is presented for the orientations with the highest  $\beta$ -fiber intensity on each  $\phi_2$  section given in the abscissa. The intensity varies from 11.4 to 9.6 times the random intensity along the  $\beta$ -fiber. From Fig. 3.7, it can be seen that the highest stored energy along  $\beta$ -fiber after cold rolling is 8.2 J/g-atom that corresponds to the C component and it is 40% less than the stored energy of the cube texture component. The minimum stored energy after rolling along the  $\beta$ -fiber is 3.02 J/g-atom for  $\phi_1 = 55^\circ$ ,  $\Phi = 35^\circ$  and  $\phi_2 = 65^\circ$  and is close to S component. Whereas, the actual S component namely,  $\phi_1 = 60^\circ$ ,  $\Phi = 35^\circ$  and  $\phi_2 = 65^\circ$  has a stored energy value of 4.7 J/g-atom.

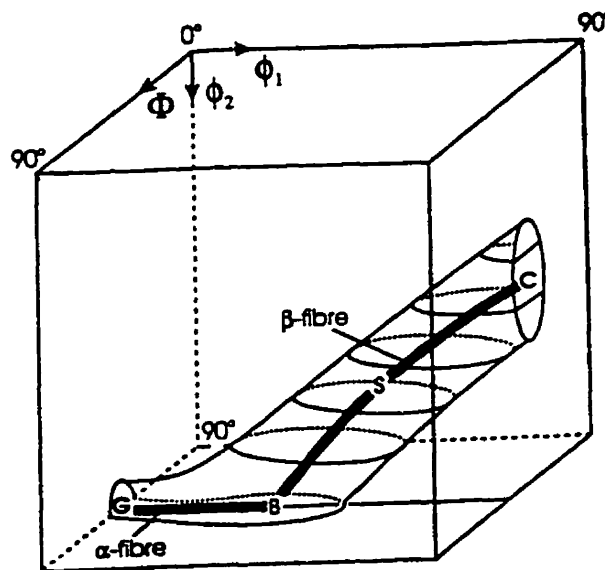


Fig. 3.6 Schematic representation of the fcc rolling texture in the 3-dimensional Euler angle space (after Hirsch and Lucke [21])

The cold rolled aluminum specimen also shows a partial  $\alpha$ -fiber, which extends from G-component to B-component. The Fig. 3.8 shows the stored energy along the  $\alpha$ -fiber for both rolled and stress relieved specimen. The reduction in stored energy after stress relieving along this partial  $\alpha$ -fiber mildly fluctuates between 1.8 to 2.6 with an average value of 2.2 J/g-atom. The stored energy slowly increases along the partial  $\alpha$ -fiber with

little fluctuations as  $\phi_1$  increases from  $0^\circ$  to  $35^\circ$  for both rolled and stress relieved aluminum specimens. On the contrary, the deformation texture intensity increases drastically as  $\phi_1$  increases from G-component to B-component. Generally, it is observed that the reduction in stored energy after stress relieving is higher for cube component than the deformation texture components.

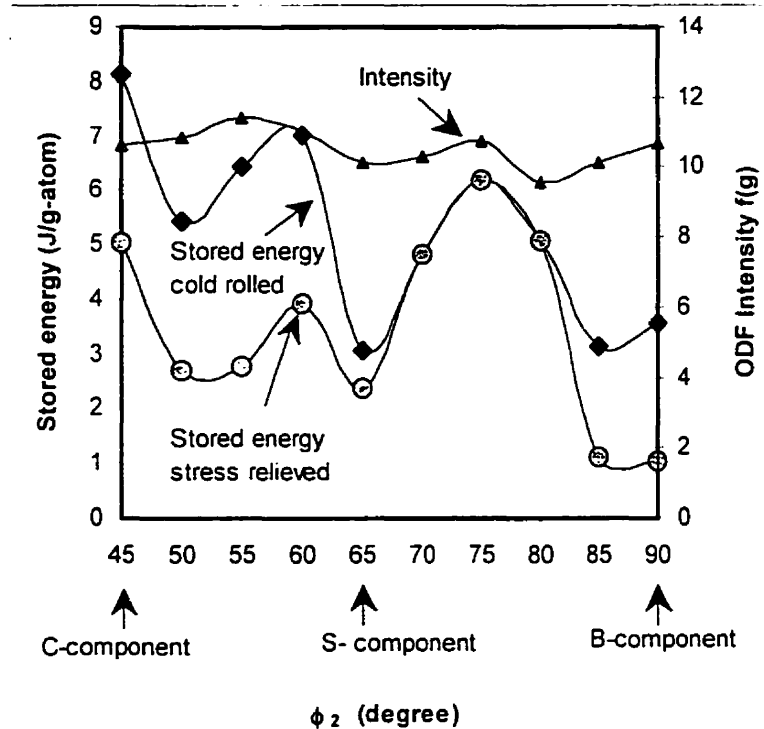


Fig. 3.7. Calculated stored energy along  $\beta$ -fiber for rolled and stress relieved can-body aluminum AA3104 (see text for more information)

In all the discussion presented above the calculated stored energy values at exact orientations in the orientation space are considered. For example, the stored energy value for the cube orientation is taken at Euler angles  $\phi_1 = 0^\circ$ ,  $\Phi = 0^\circ$  and  $\phi_2 = 0^\circ$ . The Euler angles for some other orientations are given in Table 3.1. In practice one would prefer however to identify an ideal texture by accepting a deviation of few degrees from the ideal orientation. Therefore, the study of scatter in the stored energy as a function of

angle deviation from the ideal orientation for the cube, C, B and S texture components is useful. As the scatter plays an important role in the nucleation and growth observed during recrystallization aluminum, the detailed discussion about this is given under recrystallization model (section § 3.4.1).

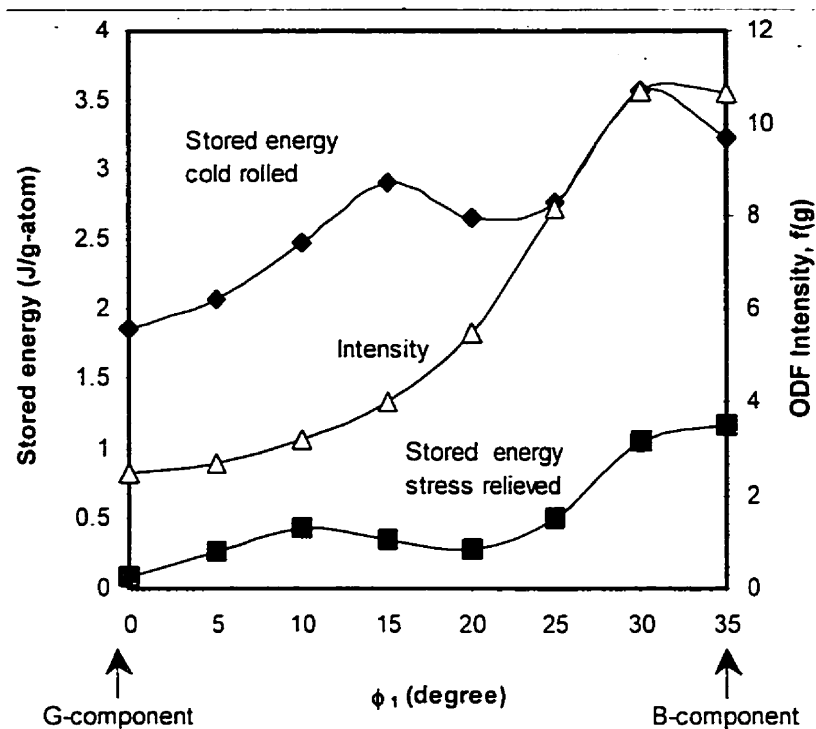


Fig. 3.8. Calculated stored energy along  $\alpha$ -fiber ( $\phi_2=90^\circ$  section) for rolled and stress relieved can-body aluminum AA3104

### 3.2.5. Comparison of the stored energy with Taylor factor

Discussing the results obtained, one has to address a relationship between the measured stored energy and the Taylor factor. It is well known that the strain fields associated with dislocations are predominantly responsible for the stored strain energy. Therefore, the measured stored energy is usually compared with the Taylor factor [133], which is a measure of resistance to plastic deformation. Usually the assumption is made that increase in the Taylor factor increases the stored energy. The measured stored energy

values shows that this increasing trend is not observed for the orientations with high Taylor factor values [40,41]. Kallend and Huang [40] reported that the measured stored energy values for 50% cold rolled Cu show an increasing trend only up to the Taylor factor value of  $\sim 4.4$  and then start to decrease. This behavior reflects the fact that the Taylor model oversimplifies the deformation of polycrystalline metals by assuming a homogeneous deformation of all the crystallites in the matrix. But in practice, during deformation materials undergo inhomogeneous deformation to an extent of producing well-defined microstructural features like shear bands. More recently, it was reported that for the 80% cold rolled interstitial free steel [41], the orientation  $\{110\}\langle 011\rangle$  with a very high Taylor factor value ( $\sim 4.3$ ) has a very low stored energy. This also supports the statement that the assumption of homogeneous deformation made in the Taylor model is not universally true. Such inhomogeneous deformation is reported by Vanderschueren [41a], who observed that the shape of some of the high Taylor factor grains with orientation such as  $\{110\}\langle 011\rangle$  have equiaxed shape even after 80% deformation. Also in the present paper, the high Taylor factor orientation  $\{110\}\langle 011\rangle$  has a stored energy value of 5.39 J/g atom, whereas the low Taylor factor cube orientation ( $\phi_1 = 0^\circ$ ,  $\Phi = 0^\circ$  and  $\phi_2 = 0^\circ$ ) has a stored energy value of 13.6 J/g atom. Because the resistance to deformation of the high Taylor factor grains is much larger than that of their neighbors of other orientations, most of the deformation work might be expended on deforming the relatively softer neighboring grains.

So far in this chapter, the focus is diverted to the measurement of orientation-dependent stored energy, which is, as mentioned earlier, one of the important parameters to be considered for the study of development of recrystallization model. The main goal of this chapter is to discuss the Monte-Carlo simulation of recrystallization of aluminum. To achieve the goal, the texture and stored energy analysis, which have been carried out to understand the nucleation and growth mechanisms, are discussed in the following sections.

### 3.3. ANALYSIS OF TEXTURE OF COLD ROLLED ALUMINUM FOR NUCLATION MODEL

Before discussing the texture analysis, it is important to recapitulate the texture information of the deformed matrix. The orientation distribution function (ODF) calculated from the measured (110), (100) and (111) pole figures of 88% cold rolled can-body aluminum alloy (AA3104) using x-ray in Siemens diffractometer has been already given in Fig. 3.1. It was also discussed in the section § 3.1 that the ODF shows the typical aluminum cold rolled texture [1,18,120] with characteristic B, S and C texture components of  $\beta$ -fiber and partial  $\alpha$ -fiber, the latter runs from Goss 'G' component to B texture component.

#### 3.3.1. Model of microstructure used for cold rolled texture analysis

Textural analysis is carried out using a computer specimen that was discretized with sites having 3-dimensional honeycomb lattice structure as given in section § 2.7.3 (Hinz and Szpunar [15]). The described 3-dimensional honeycomb lattice sites have 12 nearest neighbors. In the present work, in order to have an approximate 88% cold rolled specimen geometry: the number of sites specified along the specimen co-ordinate axes RD, TD and ND are 568, 82 and 11 respectively. Here, RD, TD and ND denote rolling, transverse and normal directions respectively. In this lattice, 500 Voronoi grains have been generated and elongated in proportion to the cold rolling reduction of the specimen. The aspect ratio of the grains in the directions RD:TD is 8:1, and in the direction RD:ND is 64:1 in terms of lattice sites. The dimensions of the elongated grains are between 2-5  $\mu\text{m}$  along the ND, 5-18  $\mu\text{m}$  along TD and 50-150  $\mu\text{m}$  along RD. These dimensions determine the length of computer specimen lattice site as  $\sim 1.5 \mu\text{m}$ . The site size of 1.5  $\mu\text{m}$  can be considered as an observed size of a nucleus [134]. The grain orientations are assigned in agreement with the ODF of cold-rolled specimen as described by Morawiec et al. [118]. Though here the orientation is distributed assuming a random correlation between grains, because of the nature of the grain structure imposed on the computer

specimen, band-like features are observed. The orientation distribution of the initial grains agrees with the experimental ODF.

In this computer specimen, the deformation heterogeneity and subgrain structures are not directly incorporated. However, each lattice site is assumed to have subgrain structure. Nucleation is carried out by randomly choosing a lattice site and assuming that the chosen site is associated with certain degree of deformation inhomogeneities in order to give birth to a successful nucleus. Because each nucleus orientation is experimentally observed to have a unique misorientation distribution [8], the location of each nucleus orientation in the deformed matrix is of great importance. The growth kinetics of each nucleus depends on the grain boundaries it has with the surrounding cold rolled matrix. Therefore, by preserving this unique misorientation distribution for each nucleus orientation in the computer specimen, a growth model can be built. The following section focuses on the probability of nucleation of a particular orientation ( $g$ ) and its location in the computer specimen during annealing.

### 3.3.2. Probability of availability of a nucleus orientation

After defining the cold rolled grain structure and texture as explained before, the nucleation experiment is conducted. As mentioned earlier, the orientation of the nucleus comes from the pre-existing subgrains in the deformed matrix. Thus, as a first rule, one can assume that the number of new grains with certain orientation  $g$  is proportional to the ODF intensity,  $f(g)$  of that orientation found in the cold rolled matrix. This assumption can be mathematically expressed as below:

$$n(g) \propto f(g) \quad (3.7)$$

Here,  $n(g)$  is the number of nuclei. This assumption will yield an approximately identical recrystallization texture to that of the deformed texture. To begin with, 4000 nuclei with orientations generated according to equation (3.7) are randomly placed in the computer

specimen. Then the average misorientation distribution function (MODF) is computed by grouping similar nucleus orientations together. Here, nucleus orientations are categorized into three groups: 'cube', 'rolling' (C + S + B) and 'random'. The random orientation is simply every orientation deviated by more than  $15^\circ$  from the cube and rolling components. The resulted misorientation distribution functions (MODF) for these categories are given in Fig. 3.9(b). For comparison, the misorientation distribution function (MODF) experimentally measured by Juul Jensen [8] is given in Fig. 3.9(a). According to the histograms presented in Fig. 3.9(a) and (b), the calculated misorientation distribution of cube texture is similar to that obtained from the experimental observation [8]. On the contrary, the rolling and random does not compare well with the experimental data. This implies that the nucleation of new grains occurs not randomly but in the restricted places in the cold rolled microstructure.

In order to restrict the locations of nuclei, a second rule of nucleation has been introduced base on the argument that in the metals with high stacking fault energy like aluminum, the nuclei originate from the pre-existing subgrains. Therefore in a deformed grain, probability of finding a subgrain of similar orientation (to that deformed grain) is high. Thus, it can be assumed that the probability of finding a nucleus orientation  $g$  (hereafter this probability will be called probability of availability,  $P_d(g)$ ) is high in the similarly oriented regions of deformed matrix. However in these regions, one cannot rule out the possibility of finding a completely different orientation of nuclei in a vicinity of deformation inhomogeneities like transition and shear bands, where nucleation often takes place. Thus, the probability of availability of a nucleus  $P_d(g)$  with an orientation  $g$  is presented by assuming a linear empirical function as in equation (3.8).

$$P_d(g) = 1 - 0.015\theta_{n-d} \quad (3.8)$$

Here,  $\theta_{n-d}$  is the misorientation between the orientation of the nucleus ( $g_n$ ) that is assigned to the nucleation site and the original orientation ( $g_d$ ) that occupied the same

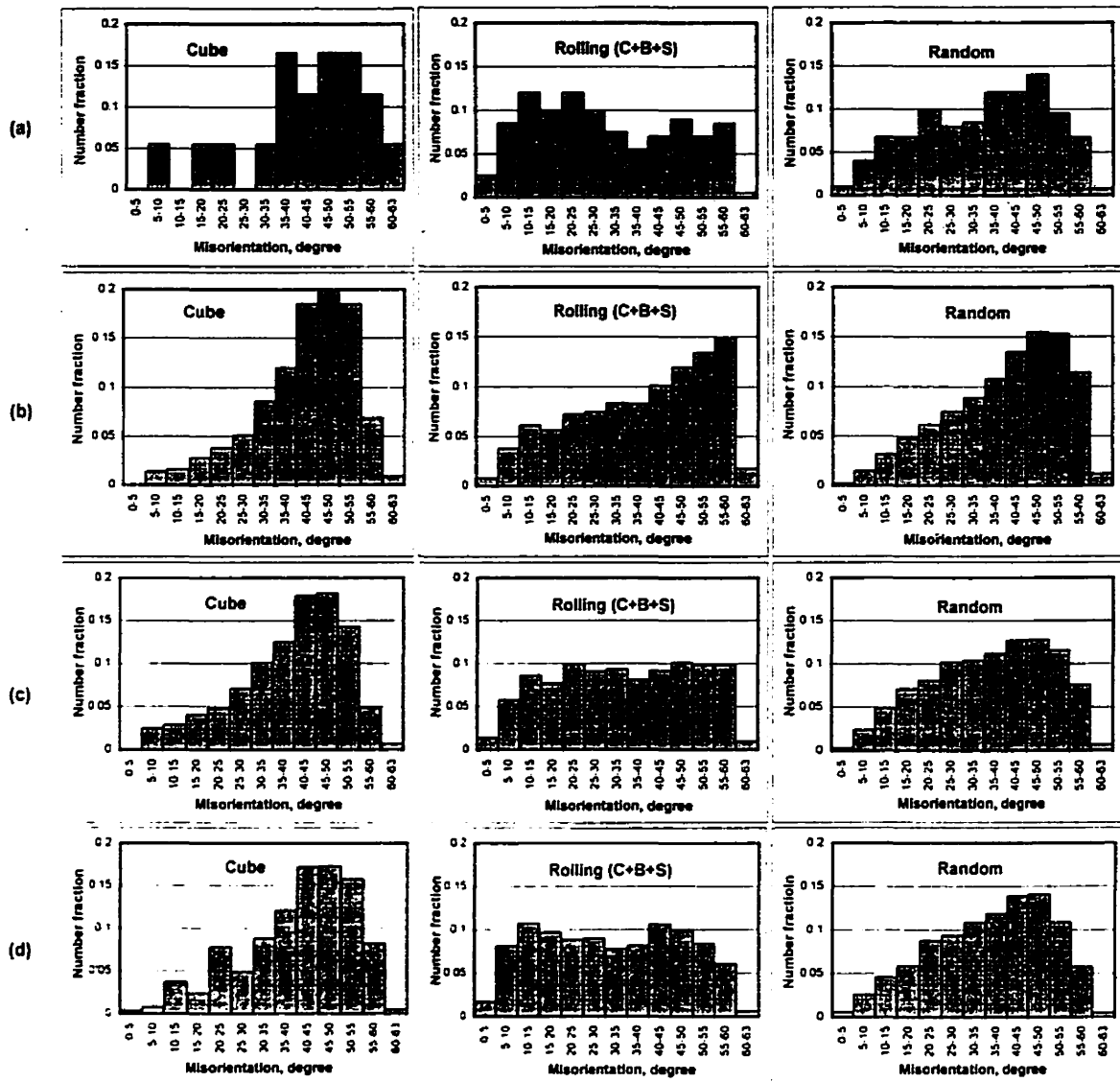


Fig. 3.9. Computed misorientation angle distribution between nuclei of various orientations and cold rolled matrix. (a) Juul Jensen's [23] observation, (b) for random nucleation, (c) with the nucleation condition given by equation (3.7) & (3.8), and (d) with the nucleation condition given by equation (3.7) & (3.9) (see text).

site prior to the nucleation. The values of the constants are computed such that the misorientation distribution around the nuclei of different orientation are close to the experimental data of Juul Jensen [8] (Fig. 3.9(a)).

To understand this assumption, one can imagine that each lattice site before nucleation is composed of numerous subgrains. During annealing, one of the subgrains might grow and becomes a successful nucleus. The orientation of the nucleus,  $g_n$  that is generated by the growth of subgrains may be close to the orientation  $g_d$  or it can be different due to the presence of deformation heterogeneity assumed in that site. From the equation (3.8), the computed misorientation distributions of the generated nucleus orientations are given in Fig. 3.9(c). These distributions are comparable with the experimental distributions [8] given in Fig. 3.9(a). The distributions observed for cube and random after the incorporation of  $P_d(g)$  seem to agree well with the experimental observation. Though, the distribution for the rolling component is slightly different, the trend in the calculated distribution is closely related to the experimental findings. A close observation of these distributions reveals that nuclei with 'rolling' orientations seem to have a higher number of boundaries with misorientation  $< 30^\circ$ . This is clearly evident in the Table 3.2, where the average misorientation of the three main texture categories: namely cube, rolling and random, are given for comparison. Though the computed misorientation distributions for these texture categories are comparable to the experimentally observed distributions (Fig. 3.9(a) and (c)), the calculated average misorientation angles deviates from the experimental values (Table 3.2). A close observation implies that if the intensity of an orientation  $g$  in the cold rolled matrix is strong, then the probability  $P_d(g)$  is higher for lower values of  $\theta_{n-d}$  than predicted by equation (3.8). Furthermore, the  $P_d(g)$  decreases more drastically than given by equation (3.8) for the high values  $\theta_{n-d}$ . In addition corrections are required to account for the fact that cube nuclei are not only generated within cube bands but also at transition bands of Copper (C) and ND-rotated copper texture components [22]. Therefore, the probability of nucleation of cube component is in fact higher than estimated by equation (3.8). These corrections are implemented in equation (3.9) and is given below

$$\left. \begin{aligned}
 P_a(g) &= 1 - 0.015a\theta_{n-d} \\
 a &= f(g)/f_{\max}(\text{cube}) \quad \text{if } f(g) > f_{\max}(\text{cube}) \\
 a &= 1 \quad \text{if } f(g) \leq f_{\max}(\text{cube})
 \end{aligned} \right\} \quad (3.9)$$

Here,  $f(g)$  is the ODF intensity for the orientation  $g$  and  $f_{\max}(\text{cube})$  corresponds to the maximum ODF intensity for the cube orientation. This assumption implies that the probability of finding a nucleus with orientation corresponding to the rolling texture components namely C, B and S is much higher in the neighborhood of the corresponding rolling texture components than predicted by the equation (3.8). The misorientation distribution obtained by applying equation (3.9) is given in Fig. 3.9(d) and the average misorientation angle for this condition is also presented in the Table 3.2. Now both the distributions and average misorientation angles are close to the experimental observation.

By incorporating the rules mentioned above, selection of location of a nucleation site for any orientation can be made in the cold rolled matrix. The other important nucleation parameter namely the nucleation rate for a given orientation,  $\dot{n}(g)$ , which decides the number of new grains with the given orientation  $g$ , is expected to depend on the magnitude of the stored energy at the cold rolled state and also how fast the stored energy is released during annealing. For this purpose the measured stored energy distribution (SEDF) of both cold rolled and stress relieved states are analyzed in the following section.

**Table 3.2. Computed average misorientation angles between the nuclei of various orientations and the neighboring deformed grains under different nucleation conditions (see text).**

Texture components	Equation (3.7)	Equation (3.7) and (3.8)	Equation (3.7) and (3.9)	Equation (3.7), (3.9) and with $S_{ratio} < 2.8$	Equation (3.7), (3.9) and with $1.5 < S_{ratio} < 2.5$	Experimental observation [8]
Cube	44.18	40.74	40.30	38.77	38.57	41.7
C	40.21	35.51	34.40	34.95	32.35	-
B	36.96	34.00	29.92	27.95	28.22	-
S	37.58	33.75	29.89	30.55	30.09	-
Rolling	38.09	34.39	31.14	30.94	30.36	29.8
Random	40.54	37.00	36.41	35.25	35.09	35.1

### 3.4. STORED ENERGY ANALYSIS FOR NUCLEATION MODEL

The orientation dependent stored energy distributions are calculated from the x-ray diffraction analysis for both 88% cold rolled and stress relieved states and are presented in the section § 3.2.4. As mentioned previously, the stored energy values are available only for the orientations that are abundantly present in the deformed specimen [40,41]. A detailed comparison of the stored energy values of important texture components namely cube,  $\beta$ -fiber and partial  $\alpha$ -fiber was discussed in section § 3.2.4. Generally, the cube component has a higher stored energy than the rolling texture components. The C-component has a higher stored energy than B and S components. Further discussion on stored energy values is given in the following section § 3.4.1.

As mentioned earlier in this chapter, the "strain path history" [1] affects both the stored energy and heterogeneities of the microstructure and thus often make the identical texture components recrystallize in quite different fashion. The spread in the stored energy data that were measured [40,41] seems to support this hypothesis.

### 3.4.1. Spread in the stored energy values

To illustrate the spread in the stored energy, the plots of stored energy (for the 88% cold rolled,  $S_{cr}(g)$  and stress relieved,  $S_{sr}(g)$  conditions) as a function of angular deviation from the ideal orientations of cube and rolling texture components (C, B and S) are presented in Fig. 3.10. In these plots the stored energy values are presented for the orientations that have the intensity values higher than 0.6 (refer Fig. 3.1). The  $S_{cr-sr}(g)$  is defined as the difference between the stored energies of both cold rolled and stress relieved states. The spread in the ratio,  $S_{ratio}(g)$  defined in equation (3.10) is also given in Fig. 3.10 for cube and rolling texture components.

$$S_{ratio}(g) = S_{cr}(g) / S_{cr-sr}(g) \quad (3.10)$$

This ratio,  $S_{ratio}(g)$  can be a measure of how fast the orientation  $g$  can reach a low stored energy state during annealing to become a possible nucleus. This ratio is always greater than 1, as the  $S_{cr-sr}(g)$  can reach a maximum value of only  $S_{cr}(g)$ . Further discussion concerning  $S_{ratio}(g)$  is given in the section § 3.4.2.

The method by which the points in these plots are generated can be explained by taking cube orientation as an example. The spread of stored energy for cube orientation is plotted by calculating the misorientation between the cube and any orientation in the Euler angle space ( $5^\circ \times 5^\circ \times 5^\circ$  discretized). If the calculated misorientation is less than  $15^\circ$ , then this orientation is accepted as the cube orientation and the corresponding values of stored energy and the angular deviation (in degree) from the ideal cube orientation are displayed. This method is repeated until all the orientations in the Euler angle space are exhausted. A similar procedure is carried out for C, B and S orientation components for cold rolled ( $S_{cr}$ ) and stress relieved ( $S_{sr}$ ) conditions and also for  $S_{ratio}$  (Fig. 3.10). In the case of rolling texture components, a considerable number of orientations do not release noticeable stored energy during stress relieving.

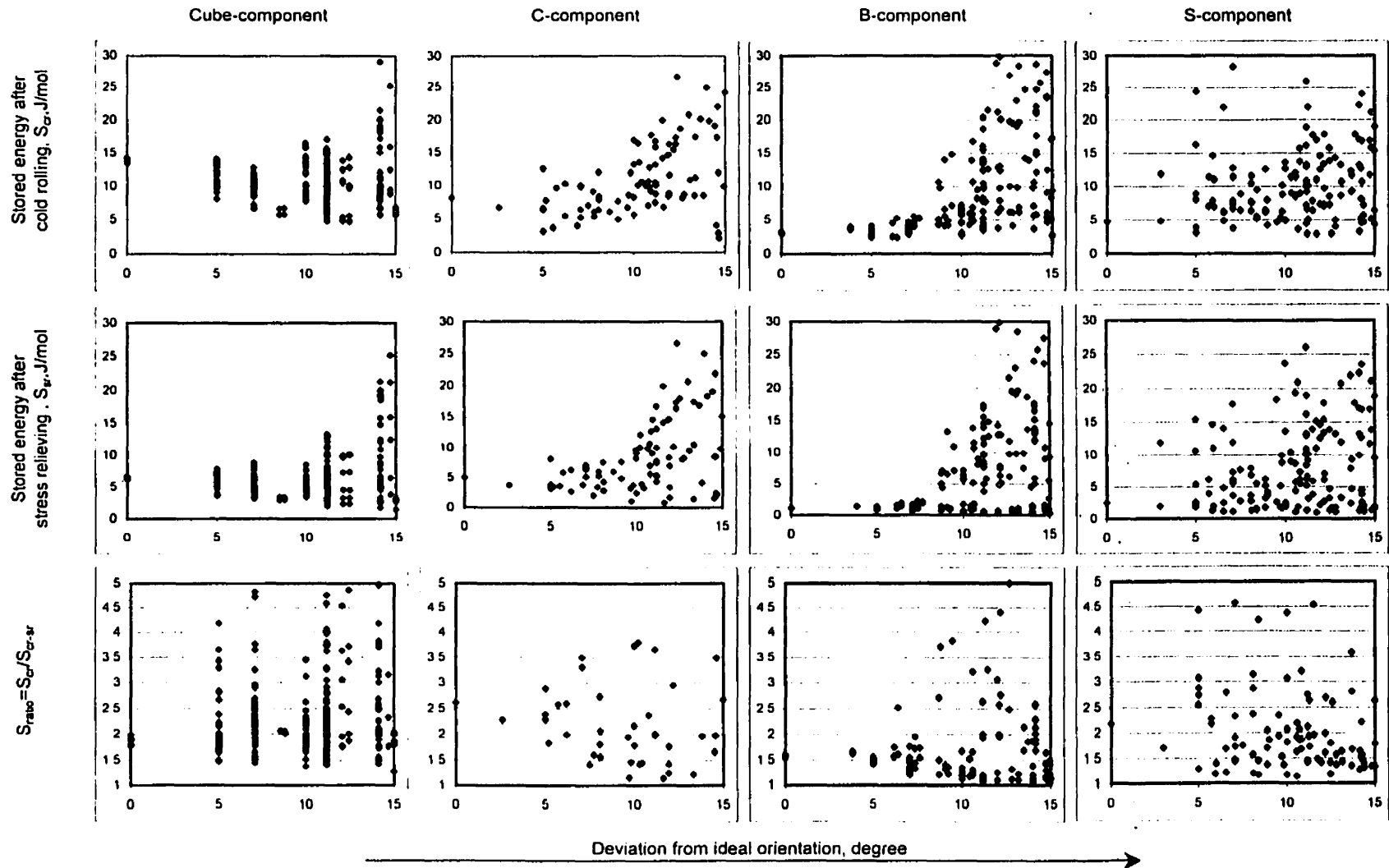


Fig. 3.10. Diagrams showing the observed spread in the measured stored energy values as a function of angular deviation from ideal orientations of Cube, C, B and S components. (a) after cold rolling  $S_{cr}$  (b) after stress relieving  $S_{sr}$  and (c)  $S_{ratio}$

In Fig. 3.10, the stored energy  $S_{cr}$  values are higher than 5 J/mol observed for the cube texture. The rolling texture components seem to have stored energy ( $S_{cr}$ ) values  $> \sim 2$  J/mol. Among the rolling components, the number of orientations having stored energy,  $S_{cr}$  values less than 5 J/mol is the smallest for the C and highest for B-component. The stored energy values in all these components increase with angular deviation. After stress relieving at 150° C for 15 minutes, the average stored energy value decreases for all texture components. For the case of B and S texture components, most of the points are very close to zero after stress relieving. In the case of plots for  $S_{ratio}$  given in Fig. 3.10 (see the series of plots presented in the bottom row), the highest concentration of points observed to be between 1.5 and 2.5 for cube component than the rolling texture components. Therefore, this region must play a favorable role in the nucleation of cube component. For B the scatter diagram of  $S_{ratio}$  shows a concentration of points between 1 and 1.5 and for S. the concentration of points is between 1 and 2.

#### 3.4.2. Nucleation condition based on stored energy

As mentioned earlier,  $S_{ratio}(g)$  gives the measure of how soon an orientation releases its stored energy and gets ready to nucleate as a new grain in the deformed matrix. This can be visualized by assuming that the deformed state is the initial stage, when time (in arbitrary units)  $t=0$ . Let  $t_{sr}$  be the time taken for the material to stress relieve to a state where the stored energy  $S=S_{sr}$ . It can be approximated that at this stage, the material is ready to initiate nucleation upon further heating at a high temperature. By assuming linear reduction of stored energy during recrystallization, the stored energy at any time  $t$  can be calculated as

$$S = S_{cr}(g) - \{S_{cr-sr}(g) / t_{sr}\}t \quad (3.11)$$

By using a normalized time unit  $\tau = t / t_{sr}$ , the equation (3.11) can be simplified as

$$S = S_{cr}(g) - S_{cr-sr}(g) \cdot \tau \quad (3.12)$$

In this time scale, formation of the nucleus occurs only when  $\tau > 1$ . Thus, the stored energy of an orientation  $g$  at  $\tau=0$  is  $S_{cr}(g)$  and at  $\tau=1$  is  $S_{sr}(g)$ . Therefore, the time taken by an orientation  $g$  to reduce its stored energy to zero during recrystallization,  $\tau_{nuc}$  can be arrived at by reducing the equation (3.12) for the condition when  $S=0$  and can be given as below:

$$\tau_{nuc} = S_{cr}(g) / S_{cr-sr}(g) = S_{ratio}(g) \quad (3.13)$$

In the above approximation, it is assumed that an orientation is ready for nucleation when the stored energy approaches zero and in the following discussion it will be called as the zero stored energy concept. Here, one should note that the stored energies  $S_{cr}$  and  $S_{sr}$  are the average values of stored energies for a particular orientation and its symmetrical components (e.g. orientation (002) and (200)) [40,41]. Furthermore, here grains with same orientations are assumed to have same stored energy values. However, in real situation the deformation is not isotropic [40,41]. Therefore, the stored energy values may have different values for the same grain. But since x-rays can not differentiate these details, this gives an average of stored energy values for an orientation  $g$ . Therefore, the  $\tau_{nuc}$  explained in the equation (3.13) is an average value for the orientation  $g$ . However, the rate of stress relieving depends on the location. That is why, in the present model, the location of the nuclei is selected first according to the probability  $P_d(g)$  (refer equation (3.9)) and then the possibility of nucleation is computed based on the zero stored energy concept. The assumption here is that the selected location (using  $P_d(g)$ ) is ready to nucleate a grain with orientation  $g$ , if the stored energy at time  $\tau$  is sufficiently low. At this stage, when an orientation  $g$  successfully nucleates, certain other orientations may not nucleate and it depends on the rate of stored energy release of those orientations.

Before attempting to modify the nucleation condition using the zero stored energy concept given by equation (3.13), the percentage fraction of number of nuclei that is generated for any orientation  $g$  assuming conditions specified by the equations (3.7) and (3.9) is calculated. The values obtained are given in Table 3.3. Using equation (3.7) alone gives the percentage fraction proportional to the texture intensity after rolling. By assuming probability of finding a nucleus  $P_a(g)$  for any orientation  $g$  as in equation (3.7) combined with equation (3.8) (as explained in section § 3.3.2), the misorientation distributions computed for each texture component (see Fig. 3.9) is closer to the experimentally observed values. As discussed in section § 3.3.2, using the modified equation (3.9) and (3.7), one can obtain approximately the same misorientation angles as observed experimentally [8] (see Fig. 3.8 and Table 3.2). Introducing the zero stored energy concept stated in the equation (3.11) along with equation (3.9) and (3.7), one should therefore, expect to observe an improvement in the percentage of cube nuclei without changing the misorientation distribution and average misorientation angle. That is because, the equation (3.13) influences only the number and not location of the nuclei in the deformed matrix. By implementing the condition that the nucleation of a new orientation  $g$  occurs only when the  $S_{ratio}(g) < 2.8$ . This means that during annealing, the orientation that reaches zero stored energy stage earlier (within the value 2.8 of arbitrary time unit) are most likely to nucleate in the cold rolled matrix. In other words the recrystallization may be completed before the other orientations having higher  $S_{ratio}$  can form nuclei. The percentage fraction of nuclei of different orientations computed based on this condition  $S_{ratio}(g) < 2.8$  is also given in the Table 3.4. The percentage of cube orientation after the implementation of this condition can rise from 5.0% to 9.1%. From Table 3.4, we can also see that the random component decreases from 82.2% to 76.4% while, the rolling components increase by only 2%.

**Table 3.3. Percentage number of nuclei observed with different nucleation conditons (see text)**

Texture components	Equation (3.7)	Equation (3.7) and (3.8)	Equation (3.7) and (3.9)	Equation (3.7), (3.9) and with $S_{ratio} < 2.8$	Equation (3.7), (3.9) and with $1.5 < S_{ratio} < 2.5$
Cube	2.30	2.65	4.95	9.10	16.04
C	6.75	7.55	3.55	4.35	5.55
B	9.05	10.19	5.65	5.20	4.40
S	7.90	7.05	3.70	4.95	6.10
Rolling	23.70	24.79	12.90	14.50	16.05
Random	74.01	72.56	82.16	76.41	67.92

**Table 3.4. Fractions of grain boundaries with different misorientation ranges observed between the nuclei and the deformed matrix.**

Texture components	GB misorientation around nuclei		
	<20°	>35°	35°-55°
Cube	0.095	0.67	0.6
C	0.24	0.54	0.44
B	0.41	0.34	0.28
S	0.38	0.41	0.33
Random	0.18	0.533	0.47

Consider the orientations that have the  $S_{cr-sr}(g) < 1.5$ . these orientations have attained the low stored energy state either due to the lower  $S_{cr}(g)$  values, or higher  $S_{cr-sr}(g)$  values or both. Lower stored energy after cold rolling ( $S_{cr}(g)$  values) means that the misorientation gradient between the subgrains is low. Imagine a case, where both  $S_{cr}(g)$  and  $S_{cr-sr}(g)$  values are high. In this case, perhaps due to homogeneous recovery the subgrains may release most of their stored energy. The homogeneous growth of subgrains may not result in suitable choices of nuclei. The  $S_{cr-sr}(g)$ , in this case, is high due to the release of

stored energy all over the deformed grain that is considered. On the similar lines, the orientations that have the  $S_{ratio}(g) > 2.8$  have neither released sufficient energy nor possess suitable subgrain structure after stress relieving to produce successful nuclei for recrystallization. For the medium range, where  $1.5 < S_{ratio}(g) < 2.5$  most of the orientations, probably, experience an abnormal and discontinuous growth of subgrains. This occurs when the  $S_{cr}(g)$  is moderately high and  $S_{cr-sr}(g)$ , i.e., reduction in the stored energy values after stress relieving are such that only few subgrains grow out of millions in the deformed grains and produce a successful nuclei for recrystallization. In this case, the remaining part of the deformed grain is not recovered properly and therefore the release of energy is not very high. In conclusion, the abnormal grain growth of subgrains thus results from highly misoriented regions (high value of  $S_{cr}(g)$ ) and medium release of stored energy during stress relieving. The remaining part of the deformed grain in this case will be consumed after the birth of a successful nucleus simply by the stored energy driven growth of the high-misoriented boundaries around that nucleus. The growth model used in this research work based on the grain misorientation distribution arrived from the texture analysis discussed previously in section § 3.3 and is presented below.

### 3.5. GROWTH MODEL FOR RECRYSTALLIZATION OF ALUMINUM

Once the nucleus is formed, it will grow in the deformed matrix due to the stored energy differences between the nucleus and the nearby matrix grains. This trend will continue till all the deformed matrix grains are consumed. By analyzing the newly formed grains and the neighboring matrix grains using the orientation imaging microscopy (OIM), Juul Jensen [8] observed that the misorientation distribution function of the 'cube', 'rolled' and 'random' texture components in cold rolled aluminum and copper do not change much as a function of annealing time. The results of that research work [8], suggest that the misorientation axes between the nuclei of particular orientation and the neighboring matrix have random distribution, whereas the distribution of misorientation angles is not

random. The author argues that this unique distribution might be responsible for the enhanced growth rate of the cube-oriented grain in the rolled matrix during annealing.

According to Juul Jensen [8], the cube grains grow faster than the rolling and random texture components. Among rolling and random components, the random component grows little faster than the rolling texture components. It has been observed that in aluminum [8], cube grains grow ~1.5 times faster than random grains and ~1.7 times faster than grains with rolling texture components. Though the differences in the growth rates of cube, random and rolling texture components are not large, this preferential growth seems to be responsible for the further sharpening of cubic texture. After detailed analysis of misorientation angle and axes distribution between the nuclei and the deformed matrix in 90% cold rolled Al of commercial purity, Juul Jensen [8] came to a conclusion that the misorientation axes and angles are very broad and that very few boundaries (< 0.5%) have the  $40^\circ\langle 111 \rangle$  misorientation. In her work, she observed practically all possible rotation angles and axes. This is true for cube and also other grains oriented differently: yet cube grains are observed to grow faster than the other grains. This observation is in contradiction to the earlier observations by Beck [135-138] that the preferential growth of the fast growing grains is due to the  $40^\circ\langle 111 \rangle$  misoriented boundaries. The differences in the misorientation distributions observed by both research works, namely the sharp  $40^\circ\langle 111 \rangle$  [135-138] distribution and the broad ones observed by Juul Jensen [8] are related to the difference in the distribution of orientations present in the deformed specimens employed for the respective study. In the Beck experiments the deformed specimens are single crystals. It was stated [8] that even in the heavily deformed single crystals the texture of the deformed crystal is sharp [138]. Therefore, a growing grain will meet a fairly homogeneous orientation distribution. In heavily deformed polycrystals, however, the deformed matrix is very turbulent, containing many different orientations even in a limited area. Due to the large local orientation variations in the deformed matrix, the misorientation distribution between the nuclei/grains and the surrounding matrix must therefore, in heavily cold deformed polycrystals, be broad and not sharp. This is the situation for all nuclei, also the faster

growing cube ones. It was concluded by Juul Jensen [8] that the assumption of  $40^\circ\langle 111 \rangle$  misorientation that could explain preferential growth does therefore not apply to heavily deformed polycrystals. The other reason for the observed difference is the difference in the fractions of low angle boundaries. The cube grains had  $\leq 10\%$  and rolling textured grains that had  $\geq 30\%$  of these types of boundaries. In deformed Al single crystals it was reported that the migration rate of twist boundaries with misorientation below  $15^\circ\text{-}20^\circ$  and general boundaries with misorientation  $< 10^\circ$  were close to zero, whereas other boundaries had a migration rate of 1-5 cm/s [139]

In the present work, the results of misorientation angle distribution between the nuclei and deformed matrix are presented in Fig. 3.9. This suggests that the fraction of low angle boundaries of cube component is the lowest and the fraction of high angle boundaries with  $\theta > 35^\circ$  is the highest when compared to the other texture components. For comparing the fractions of grain boundaries between nuclei and deformed matrix of various orientation components, these values are presented in Table 3.4 for the orientation cube, rolling and random texture components. In this table along with fractions of low angle ( $< 20^\circ$ ) and high angle ( $> 35^\circ$ ) boundaries, the fractions for the  $35^\circ\text{-}55^\circ$  misoriented grain boundaries are also presented. The  $35^\circ\text{-}55^\circ$  is the misorientation interval, where the cube orientation found to have a higher concentration of such boundaries than the rolling and random texture components. Further discussion of results presented in Table 3.4 will be given later in this section.

In the case of primary recrystallization of heavily cold rolled aluminum, the assumption of high mobility to grain boundaries having misorientation higher than  $35^\circ$  seems to be valid based on the experimental observation [8]. In the lightly deformed aluminum crystals, Liebmann et al. [72], who measured the migration rate of  $\langle 111 \rangle$  tilt boundaries, found that the mobility is the highest for a misorientation of  $\sim 40^\circ$ . Even in this case, though the maximum was near  $40^\circ$  misorientation, the spread was found to be between  $30^\circ$  and  $55^\circ$ . In the present computer simulation work, the assumption of high mobility of grain boundaries with misorientation higher than  $35^\circ$  is supported by Juul Jensen's [8]

observation and is used for the recrystallization of 88% cold rolled Al. The assumption of high mobility of grain boundaries having misorientation  $35^\circ$ - $55^\circ$  is also tested (see section § 3.7). The percentage fractions of boundaries with different misorientation ( $\theta$ ) (between the nuclei and deformed matrix) is calculated for any nuclei orientation. These percentage fraction values are presented in the form of contours in Euler angle space identical to the ODF space. The nuclei are generated according to the conditions specified in the equations (3.7) and (3.9) (see section § 3.3.2). The percentage fractions of boundaries around the nuclei that are assumed to be mobile are calculated. The assumed boundary ranges are: case (i) boundaries with  $\theta > 35^\circ$  and case (ii) boundaries with  $35 \leq \theta \leq 55^\circ$ . Here case (ii) is a subset of case (i). The results of the calculation for the case (i), where the fractions of boundaries with misorientation  $\theta > 35^\circ$  are considered to be mobile, is presented in Fig. 3.11. One should note that the values presented in Fig. 3.9 and Table 3.4 have been computed for the selected orientations by accepting a deviation of  $\sim 15^\circ$  from the ideal texture components. Whereas, the values given in Fig. 3.11 are computed for all the orientations in the ODF space (without considering any deviation of orientation).

The calculation presented in Fig. 3.11 demonstrates that the cube orientation is surrounded by about 69% of boundaries with misorientation  $> 35^\circ$  (case (i)). The common deformation components B, C and S have mobile boundary fractions of  $\sim 26\%$ ,  $\sim 32\%$  and  $\sim 30\%$  respectively. The G (Goss) component has a value of  $\sim 45\%$ . Therefore, the difference between percentage fractions of mobile boundaries of the cube and B-component is  $\sim 43\%$  and between the cube and C or cube and S is around 38%. This striking difference in mobile boundary fractions between the rolling and the cube orientation must provide the necessary growth rate difference observed [8] between them during primary recrystallization.

Another important result of the Fig. 3.11 is that the orientation  $\{011\}\langle 110 \rangle$  has a maximum percentage fraction of mobile boundaries (grain boundaries with misorientation  $> 35^\circ$ )  $\sim 90\%$ , which is  $\sim 21\%$  more than the cube orientation. Though the

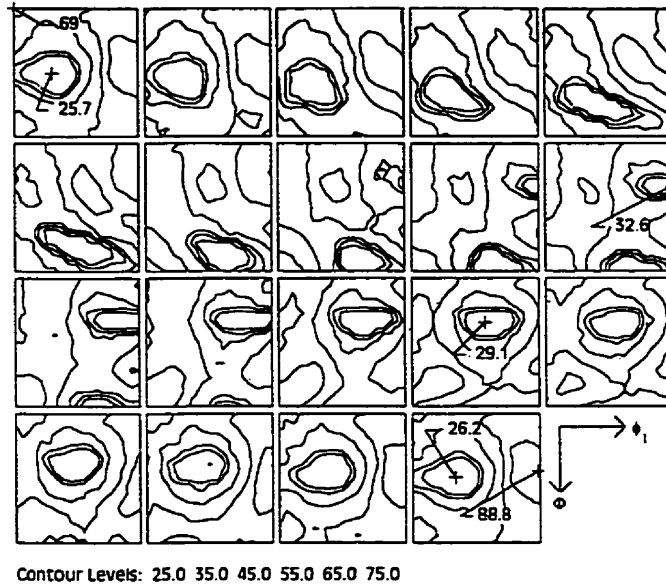


**Fig. 3.11.** Percentage fractions of  $> 35^\circ$  misoriented grain boundaries (assumed to have high mobility) around the nuclei of various orientations in the deformed aluminum matrix presented in Euler space.

$\{011\}\langle 110 \rangle$  orientation has a higher value of the fraction of boundaries with misorientation  $> 35^\circ$ . the number of nuclei with this orientation during nucleation stage is very low. Therefore, no significant contribution of this orientation component is observed after the recrystallization. The simulated ODF by Monte-Carlo method is discussed in section § 3.7 of the present work.

For the other condition (ii), where the fraction of boundaries with misorientation in the range of  $35\text{-}55^\circ$  is considered mobile, the shape of the contours (Fig. 3.11) is very similar, except the actual contour values. The differences between the percentage fractions of mobile boundaries for case (i) and (ii) are discussed here. As the case (ii) is a subset of case (i), the percentage of grain boundaries for case (i) is always greater than case (ii). The difference between the percentage fraction values for the cube orientation in both cases is  $\sim 5\%$ . The lowest percentage fraction value, which is observed for the rolling components, for the case (i) is further lowered by as much as  $\sim 10\%$  in the case (ii). Thus, the difference between the mobile boundary fraction of cube and rolling

component is the maximum for the second case (ii). The reduction of nearly  $1/3^{\text{rd}}$  of the value of the fraction of mobile boundary is observed for the case of rolling components when the boundaries with misorientation of  $35^{\circ}$ - $55^{\circ}$  are considered mobile as compared to boundaries with  $\theta > 35^{\circ}$ . Whereas, the percentage fraction for the ideal cube component reduces by only  $\sim 5\%$ , which is only  $\sim 1/13^{\text{th}}$  of its original value i.e., 69%.

A summary of the analysis of various grain boundary fractions is presented in Table 3.11. Here the average mobile boundary fraction of cube orientation is computed for the nuclei orientations, which deviate less than  $15^{\circ}$  from the exact cube orientation. Similar averages of the mobile boundaries are computed for other orientations namely C, B and S by allowing  $15^{\circ}$  deviation from the exact orientation. The average values of the fractions of the mobile boundaries of orientations that do not fall within the C, B and S categories are given under the random texture category. From the value presented in Table 3.4, the fraction of low angle boundaries with  $\theta < 20^{\circ}$  (having low mobility) is the lowest for the cube orientation. The rolling texture components namely C, B and S have the values of the fraction of low angle boundaries 0.24, 0.41 and 0.38 respectively. This fraction value for the random texture component, which is 0.18, falls between the cube and rolling texture components. From grain boundaries with misorientation  $\theta > 35^{\circ}$  (case (i)) and  $35^{\circ} \leq \theta \leq 55^{\circ}$  (case (ii)) the difference between the cube and rolling texture components is the highest for the latter case namely  $35^{\circ} \leq \theta \leq 55^{\circ}$ . The fraction of mobile boundaries for cube orientation is reduced from 0.67 (case (i)) to 0.6 (case (ii)). Whereas, the fraction of mobile boundaries of orientation components C, B and S is lower in case (ii) than in case (i) by 18-20%. The fraction of mobile boundaries of random component diminishes by 11%. This suggests that the assumption of high mobility to grain boundaries with misorientation  $35^{\circ} \leq \theta \leq 55^{\circ}$  will increase the growth rate of Cube grains as observed in the experiment [8]. This is verified using Monte-Carlo computer model and is discussed below.

### 3.6. MONTE-CARLO MODEL FOR RECRYSTALLIZATION OF Al

Essentially, the framework of the Monte-Carlo model used for the present work has been described in the section § 2.7.2. The computer specimen used for the present work has the deformed specimen geometry as explained earlier in section § 3.3.1. The number of sites specified along the three specimen co-ordinate axes namely RD, TD and ND are 568, 82 and 11 respectively. The adjacent lattice sites equivalent to the deformed grains are grouped into 500 Voronoi grains with orientations assigned using the algorithm described by Morawiec et al [118], according to the orientation distribution function (ODF) of the cold rolled specimen (refer Fig. 3.1). The length of the computer specimen lattice site is  $\sim 1.5 \mu\text{m}$ , which is equivalent to the observed size of a nucleus [134].

The nucleation model as explained in sections § 3.3.2 and 3.4.2 has been incorporated into the simulation program. In these simulations, the nucleation site is randomly selected in the deformed matrix. A new orientation generated in accordance with the deformed ODF (according to equation (3.7)), is assigned to the selected site only if it satisfies the probability of availability given in equation (3.9) and one of the stored energy conditions (A) or (B) explained above. Otherwise the nucleation to the selected site is not assigned and the site is left as it is. This testing of the nucleation site and possible nucleation is called a *nucleation loop*. The new grains are allowed to grow and the deformed matrix grains are not. The growth would stop once the newly growing grains impinge each other.

The growth model in the present work uses the algorithm proposed in Hinz and Szpunar [15] (given in section § 2.7.2) with a modification for the stored energy term as explained previously by Srolovitz et al. [13,111]. In short this model can be recapitulated as follows. If discrete points on a lattice of the partitioned microstructure whose sites are assigned labels  $i$  and each site is assigned one of  $Q$  states labeled as  $a_i$ , where  $a_i = 1, 2, 3, \dots, Q$ . Then according to the Hinz and Szpunar [15], the rate of transition from state  $a_i$  to  $b_j$  is appropriately given by equation (2.9). The grain boundary

energy,  $J_{a,a}$ , in these models is specified by associating positive energy with grain boundary sites and zero energy with sites in the grain interior. In order to incorporate the energy stored ( $H$ ) within the grain due to deformation, a positive energy is associated with unrecrystallized regions [13,111]. The resulting site energy is given by

$$E_{a_i} = Hf(a_i) + \sum_{j=1}^N (1 - \delta_{a_i, a_j}) J_{a_i, a_j} \quad (3.14)$$

Here,  $f(a_i)$  is a function, which has positive value in the unrecrystallized grains and zero in the recrystallized grains. The probabilities that determine the transitions between the states is as per the equation (2.10) and is discussed in the section § 2.7.2. The presence of the fluctuation parameter  $\eta$  only aids to overcome any geometrical restrictions that might be imposed by the discrete nature of the lattice. The parameter  $\eta$  assumes a value of unity in the present work. Time in these simulations is related to the number of re-orientation attempts.  $N_T$  re-orientation attempts are traditionally used as the unit of time and are referred to as one Monte Carlo step (MCS), where  $N_T$  is the total number of lattice sites present in the computer specimen (refer section § 2.7.2).

The positive energy values associated with grain boundary sites for the present simulation work are taken from the work of Hasson and Goux [57] and Sutton and Balluffi [140] and are shown in Fig. 3.12(a) and (b) for  $\langle 001 \rangle$  and  $\langle 011 \rangle$  directions respectively. An approximate composite curve of relative grain boundary energy as a function of grain misorientation is derived from these data and is given in Fig. 3.12(c).

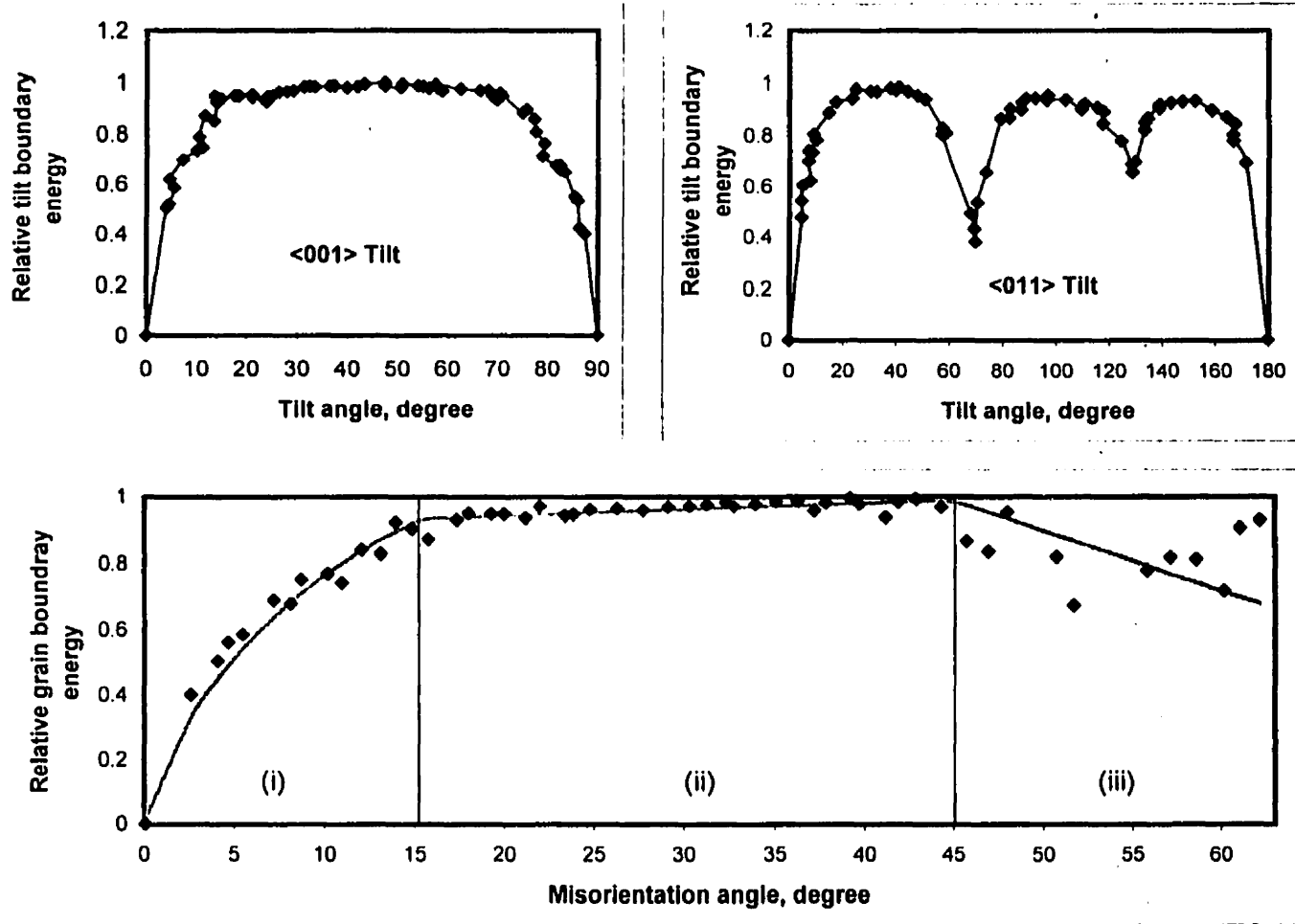


Fig. 3.12. Relative grain boundary energy for (a)  $\langle 100 \rangle$  (b)  $\langle 110 \rangle$  tilt boundaries [1,57,140] and (c) average relative grain boundary energy for various misorientation angles

The Fig. 3.12(c) has been partitioned into three regions based on grain boundary misorientation and these regions are for the angles  $<15^\circ$ ,  $15^\circ-45^\circ$  and  $>45^\circ$  respectively. In the first region, for misorientation angle  $\theta < 15^\circ$ , the obtained conventional grain boundary energy data is fitted with Read-Schockley [44] and for the other two regions the energy data in each region is fitted with the linear equation.

The stored energy values are taken from the measured orientation-dependent stored energy data presented in section § 3.2.4 of the present work. Here the problem of units and relative values of the relative grain boundary energy and stored energy values have to be addressed. As mentioned in Srolovitz et al. [13,111] the ratio of stored energy to grain boundary energy formally has a dimension of inverse length. Whereas, the  $H/J$  is a dimensionless quantity since the energy expression in equation (3.13) is written in terms of a dimensionless lattice constant. In order to obtain a numerical value of this ratio, the length scale of this simulation, i.e., lattice constant is assumed to be  $1.5 \mu\text{m}$ . As this simulation takes into account the measured grain boundary energy as a function of grain misorientation and measured stored energy as a function of grain orientation, anisotropic properties expected in the specimen due to the observed texture in the material are well-represented. Therefore, the near-complete description of important anisotropic variables such as stored energy, grain boundary energy and grain boundary mobility for primary recrystallization is a step closer towards the real situations.

### 3.7. RESULTS OF THE SIMULATION OF RECRYSTALLIZATION OF Al

The simulation of primary recrystallization using the model explained above is carried out for the following 4 conditions as given in the Table 3.5. Here the simulations (A1) and (A2) have different nucleation condition (refer section § 3.4) namely  $S_{r_{\text{nuo}}(g)} < 2.8$ , whereas the simulations (B1) and (B2) use the nucleation condition of  $1.5 < S_{r_{\text{nuo}}(g)} < 2.5$ . One of the two mobility conditions (refer section § 3.5) employed in this study, namely grain boundaries with misorientation  $>35^\circ$  have high mobility is assigned to

simulations (A1) and (B1). The other mobility condition, namely  $35^{\circ}$ - $55^{\circ}$  misoriented boundaries have high mobility is assigned to (A2) and (B2).

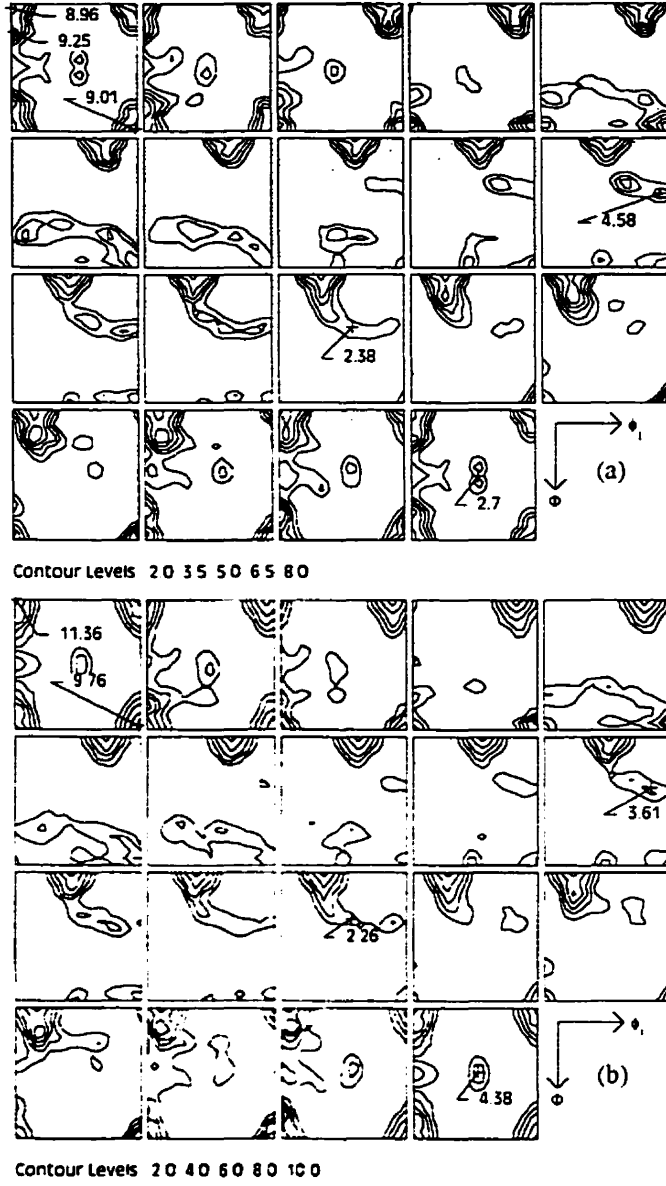
**Table 3.5. Nucleation and growth conditons employed for the different simulations.**

Stored energy conditions	Mobility boundary condition	
	$> 35^{\circ}$	$35^{\circ}$ - $55^{\circ}$
$S_{\text{ratio}} < 2.8$	(A1)	(A2)
$1.5 < S_{\text{ratio}} < 2.8$	(B1)	(B2)

All these simulations are executed with the assumption that there is no grain boundary movement between deformed matrix grains. The movement of grain boundaries between annealed grains is also not allowed. In all these simulations the high mobile boundaries are assigned a constant mobility of 0.5 and the remaining boundaries have zero mobility. The mobility value of 0.5 has been arrived at by trials in order to optimize the grain growth rate for the assumed nucleation rate. The nucleation rates are decided by number of nucleation loops (explained in the section § 3.6) allowed to be executed per MCS. In the simulations (A1) and (A2), the number of nucleation loops is 500 per MCS, whereas, for the (B1) and (B2) simulations it is 700. These values are selected by trial such that the overall number of successful nuclei before the end of the simulation is above 1000. Depending on the selected nucleation sites and nucleation conditions, only few nuclei become successful. Often nucleation loops are executed without producing a successful nucleus. This entire process of nucleation can be visualized as each lattice site in the computer specimen of heavily cold rolled matrix associated with certain amount of deformation inhomogeneities depending on its orientation, stored energy and location. These inhomogeneities may give raise to subgrains of various orientations that are dictated by the nucleation conditions.

The obtained results show that the complete recrystallization takes place in all the simulations at around 250 MCS. The resulted ODF for all 4 simulations are given in Fig. 3.13. In all the 4 simulations, characteristic annealing texture component, namely the cube orientation, is found to grow. In the case of (A1) and (A2) simulations (Figs. 3.13(a) and (b)), the texture components cube,  $\text{cube}_{(RD)}$  and G (or Goss) develop to high intensities after complete annealing. Here  $\text{cube}_{(RD)}$  denotes the cube orientation rotated about the rolling direction with the Euler angle of  $\phi_1=0^\circ$ ,  $\Phi=20^\circ$ , and  $\phi_2=0^\circ$ . The intensities of rolling texture components get weaker as the annealing proceeds and at the end of annealing they reach a value of between 2.4 to 4.6, whereas cube intensity goes as high as 9. Apart from the cube component, there is another recrystallization texture component, namely the  $\text{cube}_{(RD)}$ , found to have high intensities in these cases. In the case of (A1), the intensity of the  $\text{cube}_{(RD)}$  is higher than the cube orientation itself.

In the simulations (B1) and (B2) (refer Fig. 3.13 (c) and (d)), cube orientation is found to be the strongest. In the case of (B1), though the cube intensity is  $\sim 20$ , it is rotated  $\sim 5^\circ$  around the transverse direction. For the case of (B2), where the nucleation condition is  $1.5 < S_{ratio}(g) < 2.5$  and the  $35^\circ$ - $55^\circ$  misoriented boundaries are assigned high mobility, the intensity of exact cube component is  $\sim 20$  times stronger than the random intensity. The rolling texture components have low intensities. For comparison the 88% cold rolled AA3104 specimen has been annealed isothermally at  $400^\circ\text{C}$  for 15 minutes. The ODF calculated from the pole figures of the fully annealed AA3104 is presented in Fig. 3.14. On comparing the shape of the intensity contours observed in Fig. 3.14 with that of the ODFs obtained from all the 4 simulations (Fig. 3.13(a), (b), (c) and (d)), the simulation (B2) is closer to the experimental ODF. The absolute intensity values are higher for the simulated case. This concludes that if the nucleation of orientations that have  $S_{ratio}(g)$  between 1.5 and 2.5 is allowed and a high mobility is assumed for the grain boundaries around the nuclei with misorientation between  $35^\circ$  and  $55^\circ$ , the cube texture components develop as observed in the experiment. Though the final texture seems to be satisfactory for the simulation (B2), the integrity of this simulation has to be



Caption of Fig. 3.13 is on next page

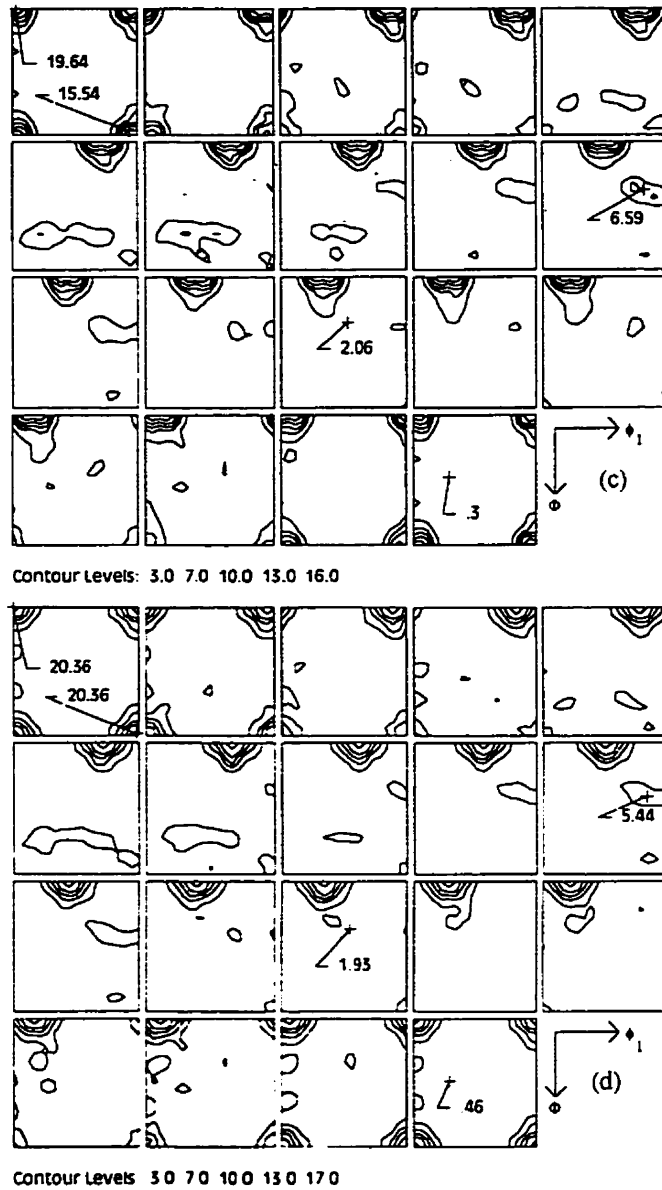


**Fig. 3.13.** Fully recrystallized ODFs obtained from the simulations (a) for A1, (b) for A2, (c) for B1 and (d) for B2. The simulation conditions for these simulations are given in the Table 4. The ODFs (a) and (b) are given in the previous page.

studied by analyzing the changes in the texture and microstructure during each stage of annealing.

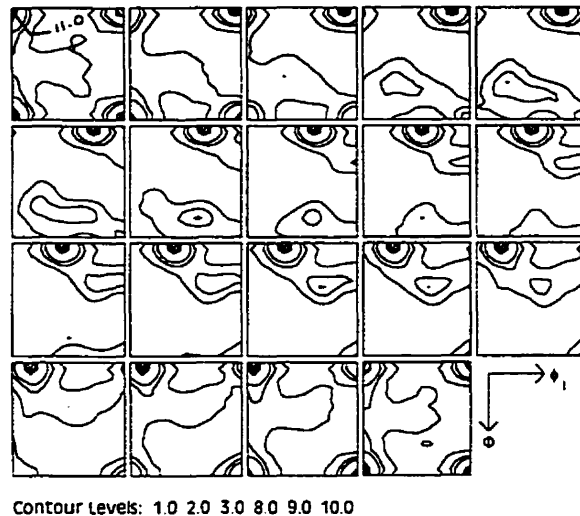


**Fig. 3.14.** Calculated ODF of 88% cold rolled and fully annealed aluminum AA3104 (at 400°C for 15 minutes) from the measured (111) (100) and (110) pole figures using X-rays.

A plot of the volume fraction of material recrystallized ( $X_v$ ) with time is commonly used for representing the progress of recrystallization during isothermal annealing. The recrystallized fraction as a function of annealing time (MCS) for the simulation (B2) exhibits the characteristic sigmoidal recrystallization behavior and is shown in Fig. 3.15. At about 100 MCS, ~100% recrystallization is reached. Theoretically, this can be expressed by the equation described by Johnson and Mehl [75] and Avrami [76] and is given by equation (2.5), which is presented in section § 2.4.1. It is customary to express the recrystallization kinetics by JMAK exponent, which can be derived from the logarithmic plot of  $\ln(1/(1-X_v))$  with logarithmic time. This plot is given in Fig. 3.16. The plot shows a non-linear behavior. As the annealing time increases, the slope of the curve decreases. The linear portion of the curve shows a slope of 3.4. For the 3-dimensional situation with complete random nucleation of site saturation, the exponent is expected to have a value of 3, whereas for the constant nucleation rate the slope is 4 [1.13]. In the present case the nucleation rate is neither constant, nor the site saturation

type. The nucleation rate of various texture components and overall nucleation rates are given in Fig. 3.17(a) and (b). In Fig. 3.17(b), the collective or overall nucleation rate shows a peak at the early stages of annealing and later the nucleation rate decreases. As far as the nucleation rates of individual components are concerned (Fig. 3.17(a)), the cube texture component has the highest rate and the C and S components show approximately the same characteristics. The nucleation rate of B component is found to be little lower than C and S components. The incubation time is not clearly exhibited in these simulations. The reason for this is that the nucleation rate is computed as the number of nuclei created for every 10 MCS, but the nucleation starts within the first 10 MCS.

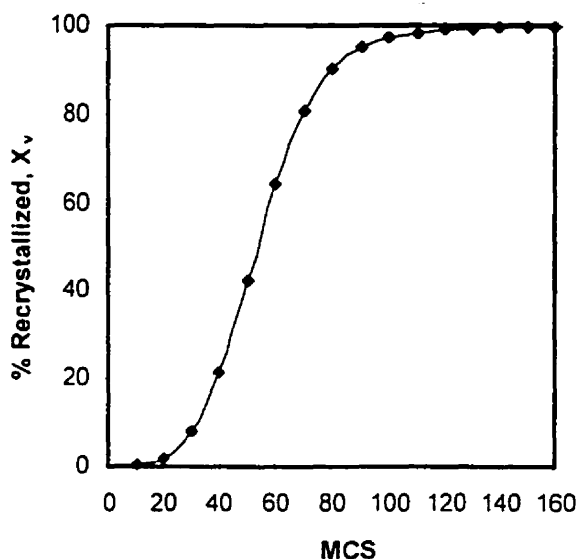


Fig. 3.15. Recrystallization kinetics obtained from the simulation (B2)

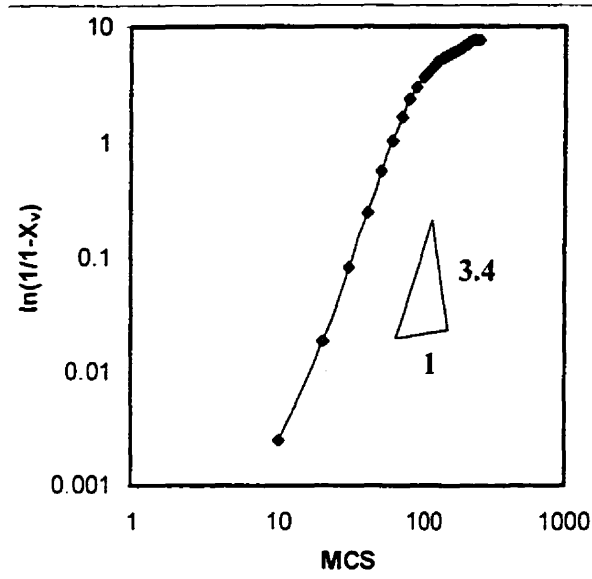


Fig. 3.17. JMAK plot obtained from the simulation (B2).

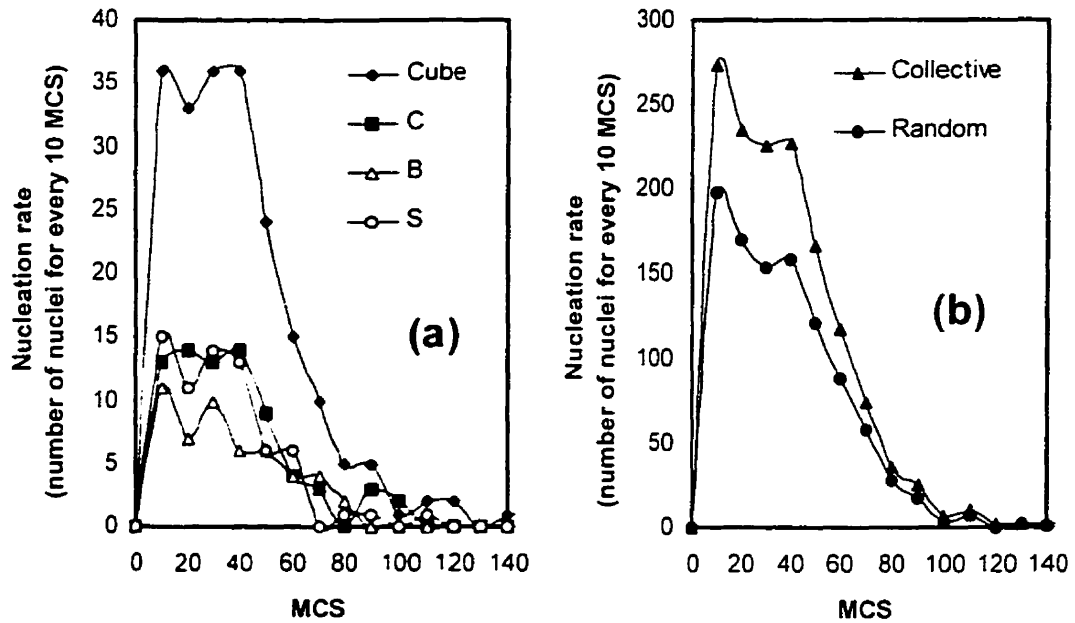


Fig. 3.16. The nucleation rate of various texture components during simulation (a) for cube and C, B and S texture components and (b) for random component and overall nucleation rate.

The development of crystallographic texture can be investigated by analyzing the ODFs, which are calculated from grain orientations and grain volume at various stages of the recrystallization simulation. The  $\phi_2 = 45^\circ$ ,  $65^\circ$  and  $90^\circ$  sections of the ODFs are presented in Fig. 3.18 for the ~21.6%, 42.6%, 64.4%, 80.7% and 100% recrystallized volume fraction in the specimen. The most obvious observation is the increase in the intensity of cube component and decrease in the intensity of rolling texture components. As the annealing progresses, the intensity of cube goes from 1.1 to 20.4 times that of the random component. Employing the nucleation and growth conditions used for the (B2) simulation, intensity of B, S and C-components decrease from of ~9 to <1, 2 and 5 respectively after complete annealing. The selection of exact cube orientation in this case is excellent. The texture changes during annealing in the unrecrystallized and recrystallized parts of the specimen can also be computed as a function of time. This is computed at each stage of annealing by separating recrystallized grains from unrecrystallized and computing the ODFs from the orientation and grain volume of those grains separately. The analysis of this result reveals that as the annealing progresses there is not much change in the texture in both the cases as a function of annealing time. The cube intensity in recrystallized portion stays with approximately the same intensity throughout the annealing with the value between 19 and 21. In the recrystallized part the intensity of B and S components are as low as <1 and <2 respectively throughout the recrystallization process. The copper component seems to be little stronger with an intensity value of ~5. Approximately the same proportion is found in the completely recrystallized texture at the end of annealing (see the ODF sections corresponds to 100% recrystallized in Fig. 3.18). As far as the unrecrystallized portion of the specimen is concerned, the texture changes do not show any preferential consumption of particular texture components. The C-component stays close to the value of  $7 \pm 1$ , whereas B and S fluctuate with the values of  $8 \pm 0.8$  and  $9 \pm 0.5$  respectively. The intensity of cube component in the unrecrystallized portion seems to increase a little from 1.4 to 2.2, but eventually, this component is consumed by the recrystallized grains.

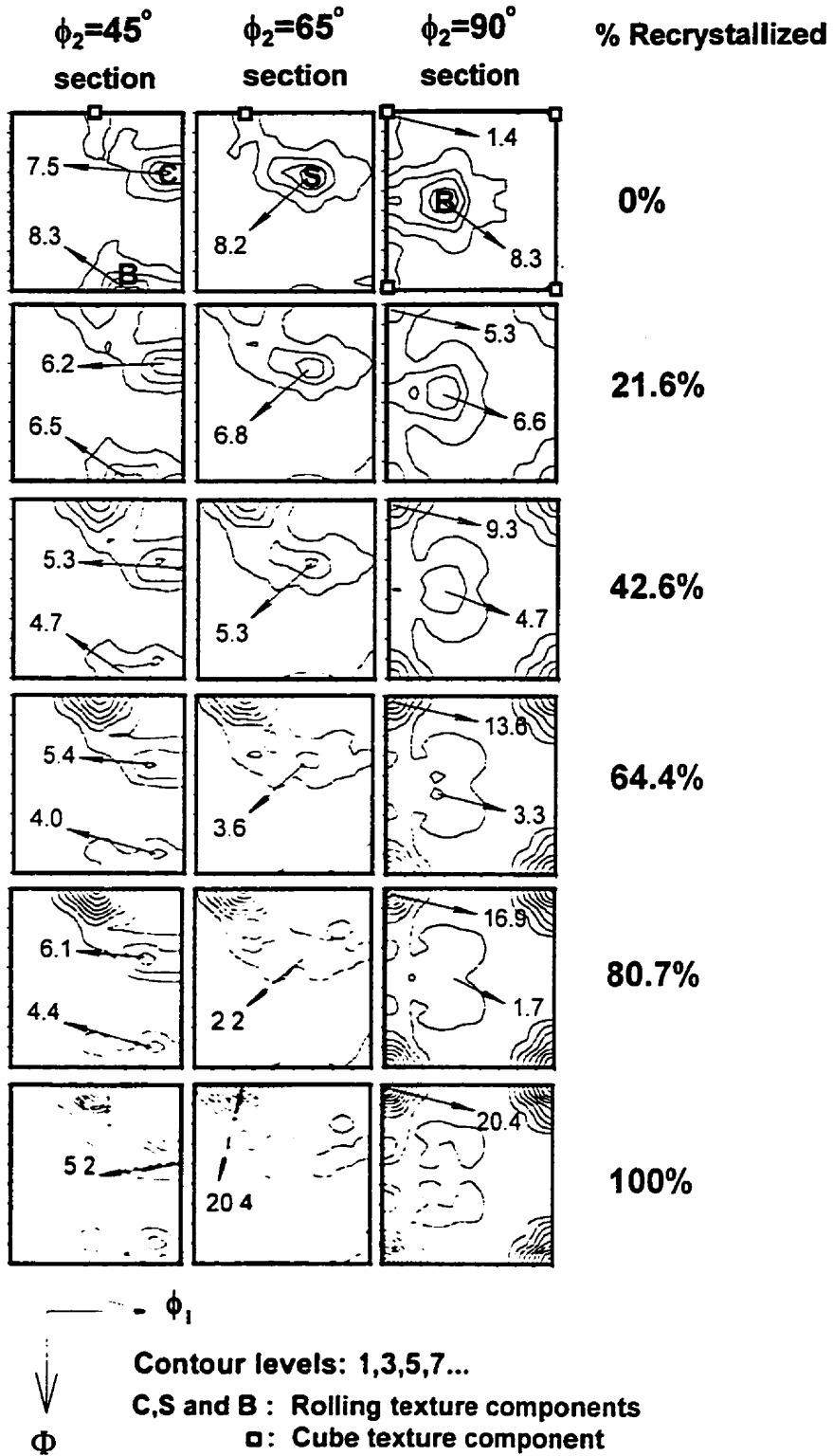
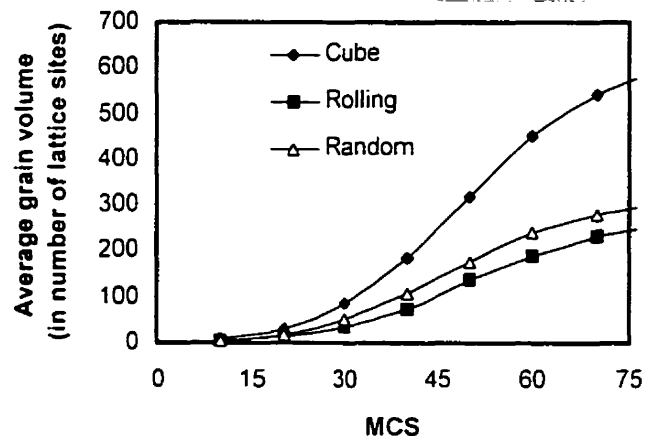


Fig. 3.18. The texture change during annealing at different % recrystallized fractions obtained from the simulation (B2). The  $\phi_2 = 45^\circ, 65^\circ$  and  $90^\circ$  ODF sections are presented.

Juul Jensen [8] compared the grain sizes of the recrystallized texture components as a function of time and observed that the cube grains grow faster than the grains of rolling and random texture components. The grain size of random component is little higher than the rolling texture components throughout the annealing. The author [8] reports that the growth advantage (which can be measured by the ratio between the average grain sizes) of cube component relative to that of random texture component is  $\sim 1.5$ . In the present research, using the growth condition that assumes high mobility to the boundaries misoriented  $35^\circ$ - $55^\circ$  gives raise to the development of cube texture component with an average grain volume higher than that of rolling and random texture components. The growth kinetics of cube, rolling and random components are presented in the Fig. 3.19, which is a plot of grain volume as a function of annealing time. Comparing rolling and random texture components, the random texture component has larger grain size. The approximate relative grain diameters between cube, rolling and random components are close to that reported by Juul Jensen [8] for commercial purity aluminum.



**Fig. 3.19.** The average grain volume (in number of sites) for cube, rolling and random orientations as a function of MCS obtained from the simulation (B2).

The progress of the microstructural changes during recrystallization is given in Fig. 3.20 at four different stages viz.: (a) 0%, (b) 7.8%, (c) 64.4% and (d) 100% recrystallized fractions for the TD RD cross-section. The Fig. 3.21 shows the corresponding ND/RD

cross-sections of the microstructure. In Figs. 3.20(a) and 3.21(a), the deformed grain structures are presented. The Fig. 3.20(b) and 3.21(b) depict the new growing grains at their early stages. These microstructures exhibit the characteristic grain structure of the primary recrystallization. In the case of fully recrystallized microstructures that are given in Figs. 3.20(d) and 3.21(d), some of the recrystallized grains have elongated grain shape and few of those grains are marked by arrows in the microstructure. This is mainly due to the initial assumption of no grain boundary migration between the impinged annealed grains as mentioned previously (at the beginning of this section). According to Srolovitz et al. [111], when the ratio  $H/J = 1$  (refer section § 3.6), the growth of the nucleus is along the grain boundary. This is a consequence of the fact that growth along the grain boundary makes use of the energy stored in the grain boundary itself. In their work, it was observed that in order for the nucleus to grow into the interior of the neighboring grains, the energy ratio must be at least  $H/J = 2$ . But in reality, one cannot rule out the possibility for normal grain growth between the new grains during recrystallization.

In order to study the effect of normal grain growth between the impinging recrystallized grains on the recrystallization texture and microstructure, a separate simulation of recrystallization has been carried out. This simulation is named as (B2-NGG) to denote that it is identical to the simulation (B2) in all other conditions except that the grain boundaries between the impinging recrystallized grains can move. As explained in section § 3.6, a high mobility to grain boundaries with misorientation  $35^\circ$ - $55^\circ$  between the nuclei and the deformed matrix is assumed. Once the recrystallized grains impinge, the boundary between these grains is allowed to migrate in the simulation (B2-NGG). Among these boundaries, the mobility of all high-energy (random) boundaries with misorientation between  $15^\circ$  and  $55^\circ$  is assumed to be higher than other boundaries. The range  $15^\circ$ - $55^\circ$  is selected according to the high-energy values presented for these grain boundaries in Fig. 3.12. The assumption of high-energy boundary having high mobility at the annealed stage is similar to the assumption employed in the next chapter

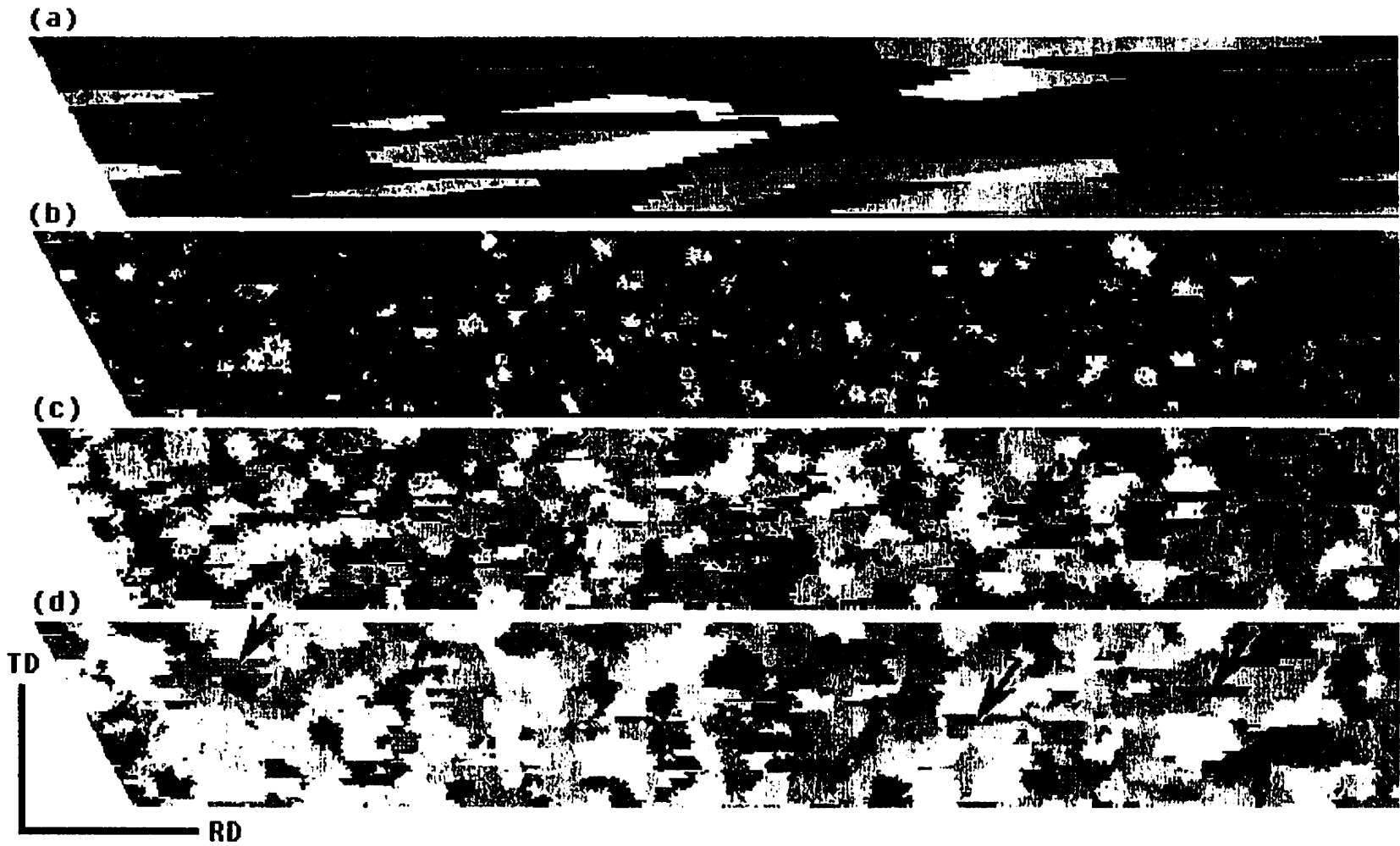


Fig. 3.20. Microstructures of TD and RD sections during annealing at different % recrystallized computer specimen obtained from the simulation (B2). In this simulation, the migration of boundaries between the impinging recrystallized grain is not allowed.

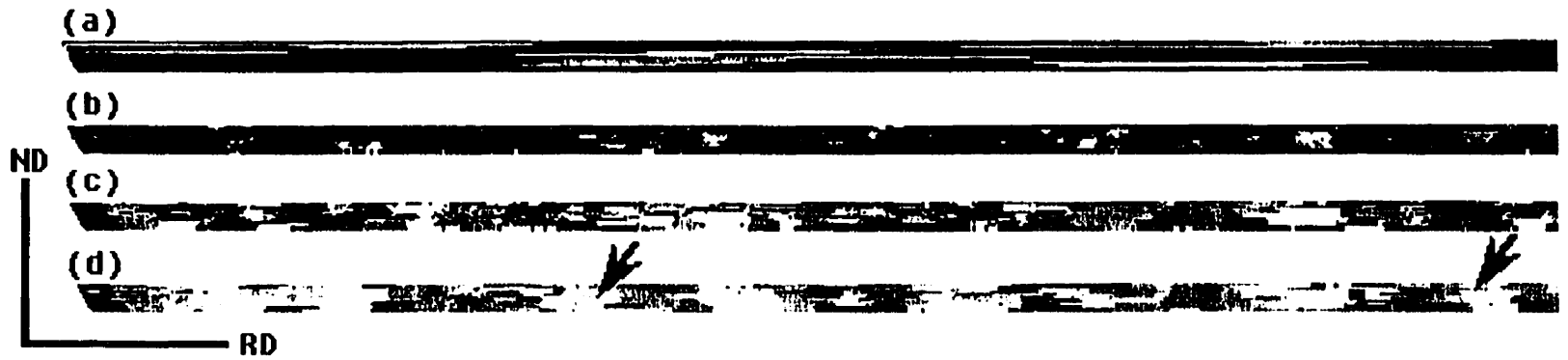


Fig. 3.21. Microstructures of ND and RD sections during annealing at different % recrystallized computer specimen obtained from the simulation (B2). In this simulation, the migration of boundaries between the impinging recrystallized grain is not allowed.

on abnormal grain growth in Fe-Si steel, where further annealing of primary recrystallized material at high temperature is considered. The mobility value is arbitrarily chosen as 0.2 (which is less than the mobility value of the mobile grain boundaries between nuclei and the deformed matrix) to test the effect of normal grain growth between the recrystallized grains that have impinged. In the case (B2-NGG), the simulated texture results show a further sharpening of the cube intensity during recrystallization. The 99.6% recrystallized computer specimen shows an ODF intensity of 27 for the cube-component. The ODF intensities of C, B and S components are ~5, 1.2 and 1 respectively. The shape of the curve in percentage recrystallized vs. MCS plot is similar to the one shown in the Fig. 3.15 and the JMAK plot shows a non-linearity similar to the Fig. 3.16 with a JMAK exponent of 3.26. For the case of simulation (B2) explained in Table 3.5, without considering the normal grain growth between annealed grains, the JMAK exponent is slightly higher with a value of 3.4. The differences between the grain volumes of cube and the other orientation components are identical to that shown in Fig. 3.19. From the simulation (B2-NGG), the 99.6% recrystallized microstructures for both TD/RD and ND/RD are presented in Fig. 3.22. These microstructures show a typical equiaxed grain structure as usually observed in recrystallized microstructure. The shapes of all the annealed grains in the simulation (B2-NGG) do not show any similarity to the cold rolled grain shape, which is different from the simulation (B2) (refer Figs. 3.20 and 3.21). One should also note that it is not unusual to see the elongated recrystallized grain shape in the recrystallized microstructure [22]. Therefore, the presence of normal grain growth between the recrystallized grains may play a role in converting the elongated annealed grains to the equiaxed one. If this normal grain growth is not significant, then the elongated annealed grain structure remains in the microstructure.

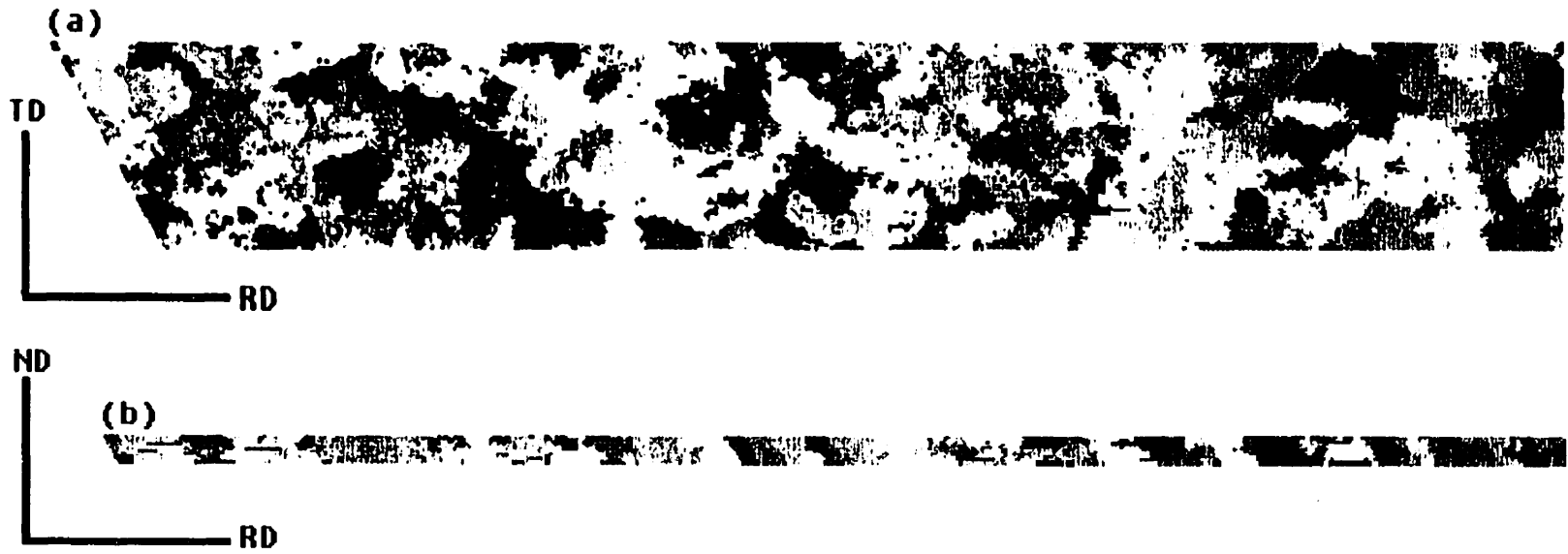


Fig. 3.22. Microstructure of 96% recrystallized computer specimen obtained from the simulation (B2-NGG), with an assumption that the migration of boundaries between the impinging recrystallized grain is allowed.

### 3.8. SUMMARY

As a first part of this chapter, the technique for the measurement of orientation dependent stored energy has been described. The measured stored energy distributions of 88% cold rolled and stress relieved aluminum specimen (at 200°C for 15 minutes) are discussed in detail. The stored energy values for the poorly represented orientations in the matrices are not presented due to high error values. The stored energy along the  $\beta$ -fiber is observed to be 40-77% less than the stored energy of cube texture component after cold rolling. The stored energy of Cube orientation is decreased by  $\sim 7.2$  J/g-atom upon stress relieving at 200°C for 15 minutes, whereas, the  $\beta$ -fiber orientations release  $< 3.1$  J/g-atom. The spread in the stored energy for an orientation increases as the angular deviation from the corresponding ideal orientation increases (Fig. 3.10). This spread in the stored energy has a major role in the development of recrystallization texture.

In order to overcome the complexity of the deformed microstructure, the nucleation conditions are deduced from the texture analysis and followed such that the obtained misorientation distributions are similar to the experimentally observed distributions. These conditions imposed on the simulation restrict the locations of a nucleus and its orientation in the deformed matrix. These conditions for (the location of) nuclei with a particular orientation and the rate of release of stored energy of that orientation affect the number of nuclei formed during recrystallization. By incorporating these nucleation conditions and assigning high mobility to boundaries with misorientations of 35°-55°, the Monte-Carlo simulation predicts the development of texture and microstructure of recrystallized specimen.

**Chapter 4****ABNORMAL GRAIN GROWTH IN Fe-3%Si STEEL  
- APPLICATION (II)**

In this chapter, the Monte-Carlo computer model is applied to the simulation of abnormal grain growth of Fe-3%Si steels. The first section § 4.1 of this chapter focuses on the literature review concerning this topic. Following this section, a discussion on the novel computer experiment on mobile boundary fractions, which is necessary for the abnormal grain growth, is presented in section § 4.2. As the anisotropic grain boundary mobility is important for realizing the abnormal grain growth, section § 4.3 gives the derivation of grain boundary mobility as function of grain misorientation. The remaining portion of this chapter is devoted to the explanation of the Monte-Carlo computer model employed for the simulation of abnormal grain growth in Fe-3%Si conventional electrical steel. In subsection § 4.4.1, the model explained in section § 4.4 is modified for the simulation of grain growth using calculated anisotropic mobilities of different grain boundaries. The Monte-Carlo simulation in the presence of MnS particles is discussed in the section § 4.6 after a short review of particle coarsening and particle pinning is presented in section § 4.5. Finally, the summary of this chapter is presented in section § 4.7.

#### 4.1. INTRODUCTION TO ABNORMAL GRAIN GROWTH IN Fe-3% Si STEELS

Although the grain-oriented silicon steels have been known since the work of Goss [142], the mechanism of the development of  $\{110\}\langle 100\rangle$  (or Goss) texture during secondary recrystallization (SR) is still debatable among researchers. Various mechanisms of the development of Goss texture have already been proposed. One theory assumes that Goss grains in the case of conventional grain-oriented electrical steel form colonies. Coalescence of these colonies during annealing gives them the size advantage for further growth [143,144]. However, as mentioned earlier in section § 2.5, when grain boundary energy and mobility are uniform, even a very large grain will always grow more slowly than the average-sized grains and will eventually rejoin the normal size distribution. This phenomenon has been shown previously both by theoretical [91] and computational analyses [12,15,92]. Therefore, the abnormal grain growth (AGG) can only occur when normal grain growth is inhibited. In conclusion, unless the abnormally growing grain enjoys some growth advantage other than size of its neighbors, secondary recrystallization will not take place. In the case of high-permeability steel, the Goss grains do not form colonies [145,146] and abnormal grain growth is observed in practice.

It is known that the grain growth in polycrystalline materials is entirely controlled by grain boundaries. The driving force for grain growth is the reduction of grain boundary area, and thus the total energy of the system. The kinetics of grain growth is determined by grain boundary mobility. Among many factors such as surface energy, particle pinning, grain boundary grooving, etc., which may influence abnormal grain growth, effect of second phase particles is considered to be of prime importance in the case of Goss texture development in Fe-Si steels. At higher temperatures, precipitate particles undergo Ostwald Ripening (OR). This causes the breakdown of grain boundary pinning and favors certain grain boundaries that move faster than others and are responsible for abnormal grain growth. Having known the importance of grain boundary energy as a parameter characterizing the boundary structure, it is necessary to discuss the

dependence of grain boundary energy on misorientation angle between grains and the following section is devoted to that discussion.

#### 4.1.1. Grain boundary energy vs. misorientation for Fe-Si steel

The relationship between grain boundary energy and grain misorientation was first derived by Read and Shockley [44] for a simple tilt boundary based on a dislocation model. This relationship is given in the equation (2.1). In this case, Among the 5 degrees of freedom which define both the misorientation between grains and grain boundary plane, only the misorientation angle,  $\theta$  is taken into account and the orientation of the boundary plane is averaged out. This assumption may be justified by the fact that the grain shape in Fe-3%Si steel after primary recrystallization is virtually isotropic [147] and no apparent anisotropy of faceting of grain boundary is observed. Experimental measurement of grain boundary energy for Fe-3% Si steels has been carried out by Dunn et.al [52-54] and is shown in Fig. 4.1. Their results are shown as a plot of the relative grain boundary energy  $E_{rel}$  vs.  $\theta$ . Here relative grain boundary energy is given by the following equation (4.1)

$$E_{rel} = E/E_m \quad (4.1)$$

As explained in equation (2.2),  $E_m$  is the maximum energy when  $\theta = \theta_m$ . The experimental data can be fitted using the equation (2.1). The Fig. 4.1 does not show any energy minima for CSL boundaries except  $\Sigma 3$ . The curve that corresponds to the equation (2.1) may be used to describe energy changes up to  $45^\circ$ . In the case of  $\langle 111 \rangle$  tilt boundary, the available energy data [51] shows a large energy cusp for  $\Sigma 3$  and both the misorientation angle and maximum energy ( $E_m$ ) are similar to that observed for  $\langle 110 \rangle$  tilt boundary. It is very difficult to find any experimental data on twist boundaries. From the calculations based on the dislocation theory of grain boundary [51] and molecular dynamics [148] one can conclude that the relation between the

misorientation angle and energy of twist boundary is similar to that of tilt boundary. The experimental curve (Fig. 4.1) shows that the grain boundaries with middle misorientation namely  $20^\circ$ - $45^\circ$  are high-energy grain boundaries. The grain boundaries with misorientation in other ranges namely  $< 20^\circ$  and  $> 45^\circ$  have lower energies than boundaries in  $20^\circ$ - $45^\circ$  range. The direction of grain boundary migration is dictated by grain boundary energy and grain boundary curvature. However, the thermal activation energy of grain boundary migration controls the kinetics of grain growth. For understanding the texture and microstructure development in abnormal grain growth, one has to study not only the magnitude of the mobility of various grain boundaries and their interactions with the precipitates but also the fractions of highly mobile boundaries. In the case of Fe-3% Si steel, the selective growth of Goss texture component is dictated by all these characteristics of grain boundaries.

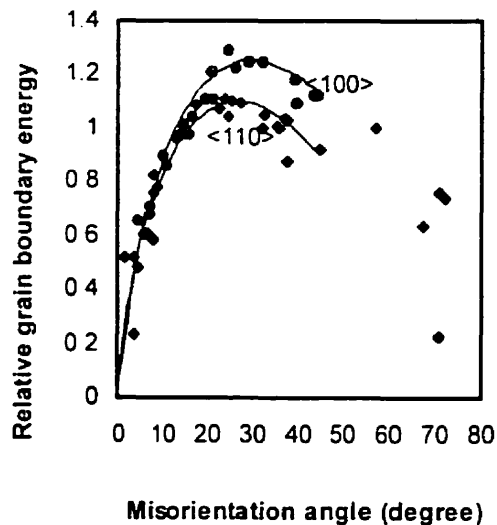


Fig. 4.1. Measured  $\langle 100 \rangle$ ,  $\langle 110 \rangle$  tilt grain boundary energy as a function of tilt angle for Fe-3%Si steel [51].

## 4.2. COMPUTER EXPERIMENT ON FRACTIONS OF MOBILE BOUNDARIES IN ABNORMAL GRAIN GROWTH

Which types of boundaries are responsible for the abnormal growth of Goss texture is debatable. Various models to explain such growth are discussed below. This is followed by the discussion on a series of computer experiments carried out to ascertain the importance of random or high-energy boundaries.

### 4.2.1. Models used to explain abnormal growth of Goss grains

There are two different models that were proposed to explain the mechanism of abnormal grain growth in Fe-Si steels. One model [64-67,149] suggests that certain coincidence site lattice (CSL) boundaries have high mobility and are responsible for AGG. Harase et al [64,65] argued that among the various CSL boundaries,  $\Sigma 9$  played an important role in the development of  $\{110\}\langle 001\rangle$  texture. In their work a possible role of other CSL boundaries was not ruled out. Recently Lin *et al.* [67] stated that the low  $\Sigma$  boundaries including  $\Sigma 3$  are responsible for the AGG of Goss grains in Fe-Si steels. These authors argue that there is no energetic or structural basis for an enhanced stability of the  $\Sigma 3$  boundary in b.c.c. materials such as Fe-Si. Different type of CSL boundaries are given importance from case to case ( $\Sigma 9$  [64],  $\Sigma 7$  [68] and  $\Sigma 5$  [69]); however, no explanation for the selection mechanism has been offered. Although a lot of work has been published on the possible role of CSL boundaries on AGG, this has not been confirmed satisfactorily or accurately. The fact is that the fraction of CSL boundaries other than the low angle grain boundary ( $\Sigma 1$ ) is very small, usually less than 10% [145,150], and it cannot be responsible for a major change in texture.

The other model is based on the assumption that the high-energy boundaries in Fe-3%Si steels have high mobility. Based on Orientation Imaging Microscopy measurements and computer simulations, Hayakawa and Szpunar [151-155] argue that the high-energy grain boundaries in the misorientation range of  $20^\circ$  to  $45^\circ$  play an important role in

AGG. Titorov [156,157] also argued that the boundaries between  $20^\circ$  and  $45^\circ$  are responsible for growth of the Goss orientation by analyzing the orientations of the large grains in a 5-10% rolled single crystal of commercial purity Fe-3%Si steel. In his experiment, the mildly rolled single crystal is deformed locally (to initiate nucleation during annealing) and annealed subsequently. Hayakawa and Szpunar [151,152] demonstrated that the Goss grains in both the high-permeability and conventional electrical steels are surrounded by a high number of grain boundaries with misorientation between  $20^\circ$  and  $45^\circ$ . The probability of finding a grain boundary with misorientation between  $20^\circ$  and  $45^\circ$  around any orientation in the primary recrystallized Fe-3% Si steels is given in Fig. 4.2 (a) and (b) for conventional and high-permeability steels. Here the probability is presented in the ODF space described by

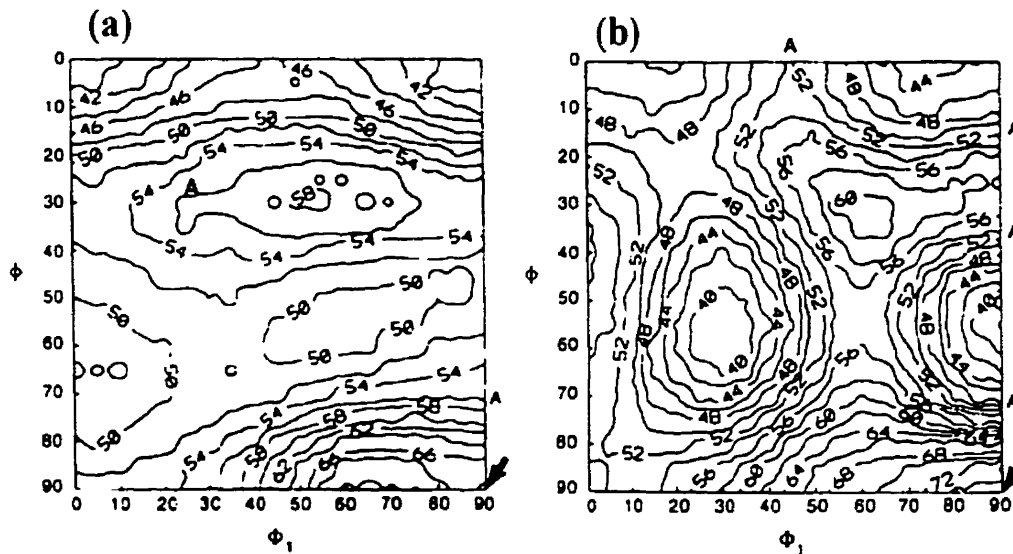


Fig. 4.2. Probability (%) of boundaries having misorientation angles of  $20^\circ$ - $45^\circ$  around grains having various orientations in Fe-Si steels a) conventional and b) high permeability steels. Both (a) and (b) are  $\phi_2 = 45^\circ$  sections. Arrows indicate the Goss orientation, and the contour line of the average value is indicated by 'A'

the Euler angles using Bunge's notation [117]. They observed that in high-permeability steels, the probability of this type of boundaries shows a sharp maximum of 76% at the Goss orientation and a minimum that is 37% at the main texture component. It must be noted that such difference in the probability is very large at approximately  $40^\circ$ . In the

case of conventional steels, the Goss grain has a higher probability of being surrounded by the middle misoriented high-energy boundaries, however the maximum position is rotated by  $20^\circ$  from the Goss orientation around the  $ND \parallel \langle 110 \rangle$  axis. Here, ND denotes the direction normal to the sheet.

A dispersion of second-phase particles retards the movement of grain boundary. It is known that growing and shrinking precipitates influence the AGG of Fe-Si electrical steels. It is conceivable that random grain boundaries would move more easily than special boundaries because the lower energy of the special boundaries provides a greater barrier to the transitory structure modification required when a boundary moves. Apart from this, the average growth of precipitates located at the low angle grain boundaries (LAGB) and special grain boundaries is slower than that of the precipitates located at the high-energy boundaries. This is a direct consequence of the higher grain boundary diffusivity associated with the random boundary than the LAGB or CSL boundaries. Higher diffusivity is responsible for a higher rate of precipitate coarsening and a reduction of pinning of grain boundary movement by precipitates. Thus, the coarsening of the precipitates is expected to occur much faster on the random boundary regions. This would cause an earlier release of those boundaries during grain growth. Based on this argument, Hayakawa and Szpunar [153,154] assumed in their Monte-Carlo simulation that at the beginning of annealing, all the grain boundaries are pinned by precipitates. As the rate of coarsening of precipitates is higher for high-energy boundaries, at the early stages of annealing, only the high-energy boundaries move when the precipitates on these boundaries coarsen to some critical size for the pinning. In other words, the grain boundaries having higher energy than a critical value ( $E_c$ ) can move and the others cannot. This critical value decreases as the annealing proceeds allowing even lower energy boundaries to move at the latter stages of annealing. By assuming a linear decrease of critical grain boundary energy as a function of Monte-Carlo steps (MCS), the authors observed that the Goss grains grow abnormally for a specific rate of precipitate coarsening. The same research group also used x-ray texture measurement and Orientation Imaging Microscopy (OIM) to analyze the role of high-energy grain

boundaries. The OIM observation produced evidence that at the initial stages of annealing, the growing Goss grains are surrounded by a higher number of high energy grain boundaries [151,154,155] than the other matrix grains.

Also, the experimental findings by Watanabe [158] demonstrate that the large growing grains have a high number of high-energy grain boundaries. At high concentrations of alloying elements and at high temperatures, the high-energy grain boundaries have the highest mobility and the highest precipitate coarsening rate and consequently are unpinned from precipitates earlier than other boundaries. The high mobility of the high-energy grain boundary and low mobility of the low energy grain boundaries (LEGB) in industrial purity metals is observed even if the precipitates are not present and can be explained using vacancy mechanisms. It is well known that grain boundary migration takes place because of the exchange of atoms between grains through vacancies [62,159,160]. The high-energy grain boundary is more capable of absorbing and emitting vacancies [161] because the number of vacancies is related to the disorder in the grain boundary structure. The high-energy grain boundary has a more disordered structure: therefore a high number of vacancies and dislocations should contribute to a high mobility of these boundaries.

In the present research, a computer procedure has been developed and employed for studying the importance of mobile boundary fractions and the role of different classes of boundaries that are responsible for the growth of Goss grains in a matrix which conforms to the primary recrystallized texture.

#### *4.2.2. Methodology for computer experiment on grain boundary fractions*

In a polycrystalline material, various microstructural features play an important role in deciding the frequency of occurrence of a particular type of grain boundary. These microstructural features are the orientation distribution function (ODF), the correlation between neighboring grains, all types of microstructural inhomogeneities like bands of

different kinds observed in deformed metals, clusters of grains of similar orientation, and the grain size distribution. Under the assumption that a primary recrystallized specimen with equiaxed grains has very little inhomogeneity, Morawiec et al. [118] developed a computer procedure for calculating the frequencies of various types of grain boundaries in Fe-3%Si steel in accordance with the measured ODF. In their calculation, these authors ignored the clustering and spatial relations between the grains in the matrix. The electron microscopic analysis of grain orientation and size in Fe-Si, by Böttcher et al. [147] demonstrated that the Goss grains are randomly dispersed in a primary recrystallized matrix. The computer simulation and experiments described by Hayakawa et al. [152,153] for primary recrystallized Fe-3% Si steel also indicate that the spatial distribution of grains is random.

An equiaxed grain structure of a primary recrystallized matrix can be modeled using a uniform 3-dimensional polygonal structure. This polygonal structure should be such that it has a high number of nearest neighbors in order to minimize the anisotropic effects arising from the structure. The computer model developed for this work is composed of three-dimensional honeycomb grains with 12 nearest neighbors as discussed in section § 2.7.3. Each honeycomb polygonal structure is a lattice unit in this computer specimen and corresponds to a primary recrystallized grain. This is different from the Monte-Carlo modeling, where the number of neighboring honeycomb polygonal lattice structures are grouped to form a grain. The present model is employed to check the type of boundaries responsible for abnormal grain growth and understand the importance of mobile boundaries. The polygonal structure used as a grain structure in this model can be described [15] by the basis and transitional vectors as in equations (2.11) and (2.12). In this work,  $N_a=71$ ,  $N_b=82$  and  $N_c=87$  have been assumed to get an approximate cubic computer specimen with total number of  $N_a N_b N_c = 506514$  primary recrystallized grains.

The algorithm developed by Morawiec et al [118] is used to assign crystal orientation to the generated grains in accordance with the experimentally measured ODF. Grain misorientation angle, which is defined as the lowest among the 24 equivalent angles and

the corresponding rotation axes. are calculated by using the unit quaternion [162]. The CSL boundary is defined by comparing the quaternion of the grain misorientation with that of CSL using the Brandon criterion [49], which allows  $15/\Sigma^{1/2}$  degree of deviation from the ideal position. To study the growth behavior of an orientation, at the beginning of the computer run, that orientation is assigned to a grain at the center of the computer specimen. Then the grain can be allowed to grow by assuming that certain type of grain boundaries with specific misorientation are 'allowed' and others are 'forbidden'. If the encountered grain boundary is an allowed boundary, then the grain, which has that type of grain boundary, is assigned the same orientation as the growing grain. When the growing grain meets a forbidden boundary, then the grain, which is surrounded by that boundary, is left unaffected. The same procedure is carried out for all the nearest neighbors of the growing grain at each instant, which is called a growth step. Thus, the growth step in this computer experiment corresponds to the time. At any particular time, the grain boundary character distribution (GBCD) around the growing grain can be computed based on the orientations of its neighbors. It should be added that if an active grain is allowed to grow equally in all directions, then the total number of nearest neighbors,  $N$  at each growth step,  $n$  is dictated by the following equation:

$$N = 10n^2 + 20n + 12 \quad \text{where } n = 0,1,2,3,\dots \quad (4.2)$$

Equation (4.2) assumes that at each step, only the nearest neighbors are consumed. The kinetics of the growing grain in the computer experiment can be expressed by recording the volume of the grain as a function of growth step. The volume of a grain is defined as the number of lattice units it has. In each growth step, all the peripheral lattice units that bound the growing grain are allowed to grow further depending on the type of the boundaries they make with the growing grain.

It is important to note that the main purpose of this computer experiment is to assess the capability of a particular orientation to grow abnormally in the matrix of known ODF. As only the central grain (with an assigned arbitrary orientation) in the computer

specimen is analyzed, this computer model can be applied to the initial stages of abnormal grain growth. During the initial stages of abnormal grain growth either very slow growth or normal grain growth of the matrix grains is expected. Because of the normal or slow growth of the matrix grain, the statistical average of misorientation between the abnormally growing grain and matrix grains is not altered significantly as assumed in this computer model.

The two different types of primary recrystallized textures are investigated using the assumption that the middle misorientation boundaries ( $20^\circ$ -  $45^\circ$ ) are highly mobile for the case of both the conventional and high-permeability electrical steels. The orientation distribution function, ODF (using Bunge's notation [117]) of both steels are presented in Fig. 4.3 and 4.4. These ODFs are calculated from the experimentally measured pole figures (110), (200) and (211) of the conventional and high-permeability steels. The conventional Fe-3%Si steel has a main texture component of  $\{111\}\langle 110 \rangle$  with the maximum intensity of 7.4 whereas the high-permeability steel has a main texture component of  $\{111\}\langle 112 \rangle$  with a maximum intensity of 11.8.

#### 4.2.3. Fractions of grain boundaries and their importance

Several investigations [67,151,152] were made to evaluate the fractions of different types of grain boundaries around the Goss grain in specimens obtained after primary recrystallization in Fe-3%Si steels. It was shown that there is 13% of  $\Sigma 3$ - $\Sigma 9$  CSL boundaries [67] around the Goss grain. The next highest frequency of  $\Sigma 3$ - $\Sigma 9$  CSL boundaries is ~10% for  $\{111\}\langle 112 \rangle$  orientation component [67]. These two orientations have a difference in the probabilities of  $\Sigma 3$ - $\Sigma 9$  CSL boundaries of only 3%. If  $\Sigma 3$ - $\Sigma 29$  CSL boundaries are considered, then the Goss and  $\{111\}\langle 112 \rangle$  orientations have the probabilities of being surrounded by 20% and 19%, respectively. On the other hand the fraction of high-energy grain boundaries around the Goss grains is

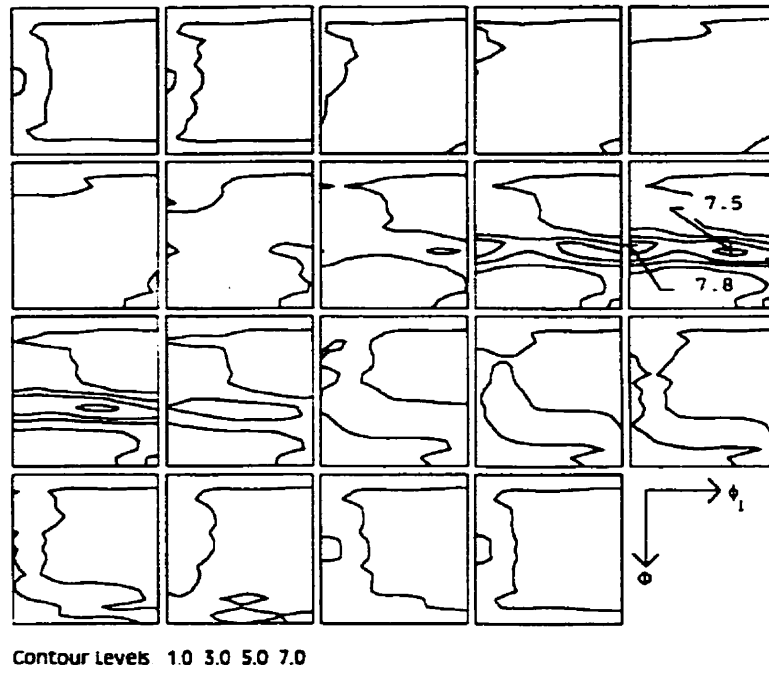


Fig. 4.3. ODF of conventional electrical steel

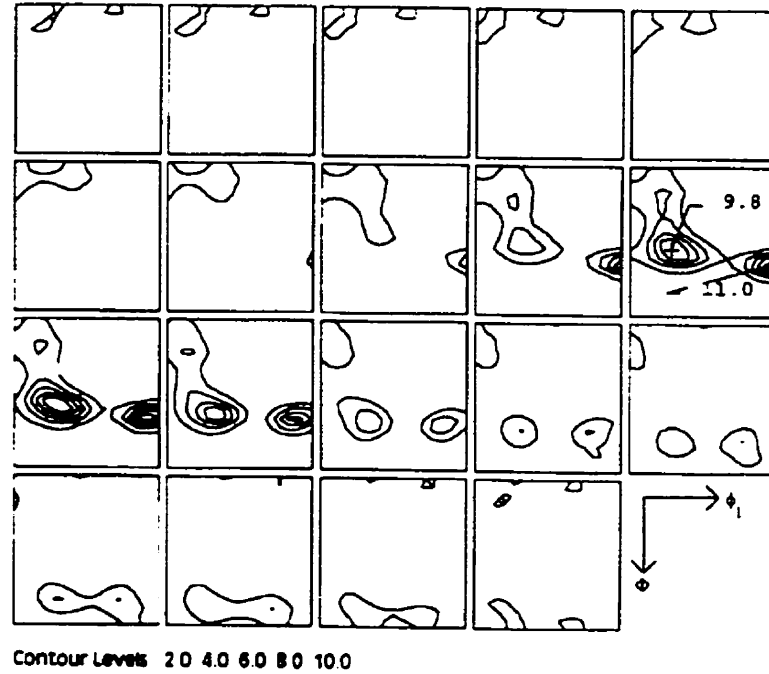
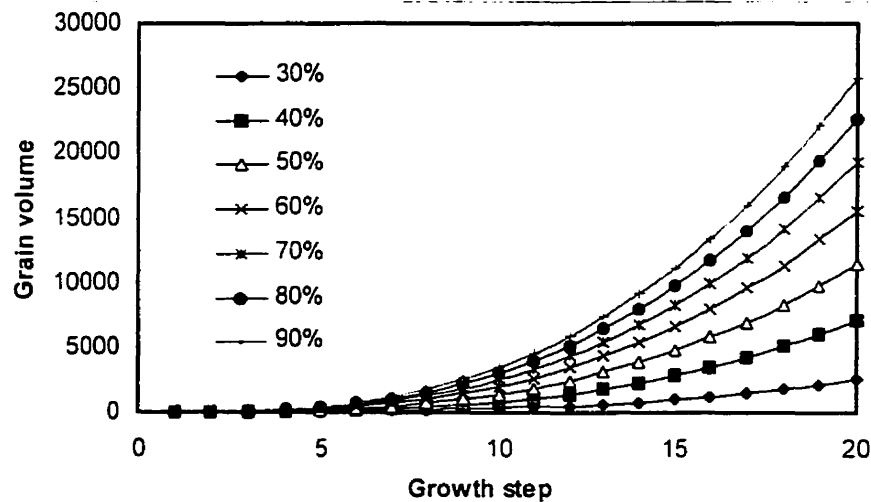


Fig. 4.4. ODF of high-permeability electrical steel

approximately 69% [151,152] (refer Fig. 4.2) and the difference between the Goss and that of the main texture components  $\{111\}\langle 112 \rangle$  in the high-permeability steels is approximately 40%. Apart from the difference in mobility and energy between the grain boundaries that surround the grains of these orientations during grain growth, the fraction of the mobile boundaries around these grains is the most important factor to be considered. On various occasions [151,152], it has been demonstrated that the fractions of CSL boundaries are too small to be responsible for major textural changes that take place in electrical steels.

At this stage it is important to introduce the concept of two kinds of fractions of mobile boundaries. The first one will be called the matrix fraction (MF) of mobile boundaries of a given orientation and is defined as the average initial fraction of mobile boundaries the given grain would make with other grains having orientations defined by the orientation



**Fig. 4.5. Simulated growth behavior of the grain with various percentage of mobile grain boundaries (MF) in the initial matrix**

distribution function. Therefore, the matrix fraction is a constant for a given orientation of grain. As an example, the matrix fraction of Goss orientation in the matrix of primary recrystallized high-permeability steel, under the assumption that middle misorientation angle boundaries are 'mobile', is about 76%. One can introduce now the peripheral

fraction (PF), which can be defined as the average fraction of mobile boundaries bounding a growing grain at any instant of the growth process. Contrary to the matrix fraction (MF) that is a constant, the peripheral fraction (PF) varies as the grain grows and reaches a steady state after a certain number of growth steps.

Abnormal growth of certain grains requires a high MF. The higher the MF, the higher the growth rate is. The computer experiments carried out for various MFs shows (Fig. 4.5) that the grain size is larger if the MF is higher. The growth of almost all the grains stops when the MF is 10% and 20%. On the other hand, 100% of mobile boundaries around the growing grain in a real metallurgical specimen would lead to normal grain growth. In Fig. 4.5, calculated grain volumes of the grains that have the MFs of 30% to 90% are given. As these grains grow, the fraction of mobile boundaries around a growing grain (PF) decreases. This phenomenon is illustrated in Fig.4.6. It can be observed that the PF reaches a steady state after a certain number of growth steps and then remains constant. Also, we observe that for high MF values the steady state is easily achieved within a few growth steps, but for the low MF it takes several growth steps. It is also evident that PF is always smaller than MF. During the grain growth, a reduction in the peripheral fraction around the growing grain for the grains with low MF values is considerable. As an example, for the MF of 30% the steady state PF is approximately 10%; however, for the case of MF equals to 80% the steady state PF is above 70%. In a real situation, abnormally growing Goss grains reach a steady state growth rate after a certain period of time [163]. Because the growth rate at any instant is also a function of the fraction of mobile boundaries around the growing grain, the steady state growth rate corresponds to the steady state PFs as is observed in the computer experiments.

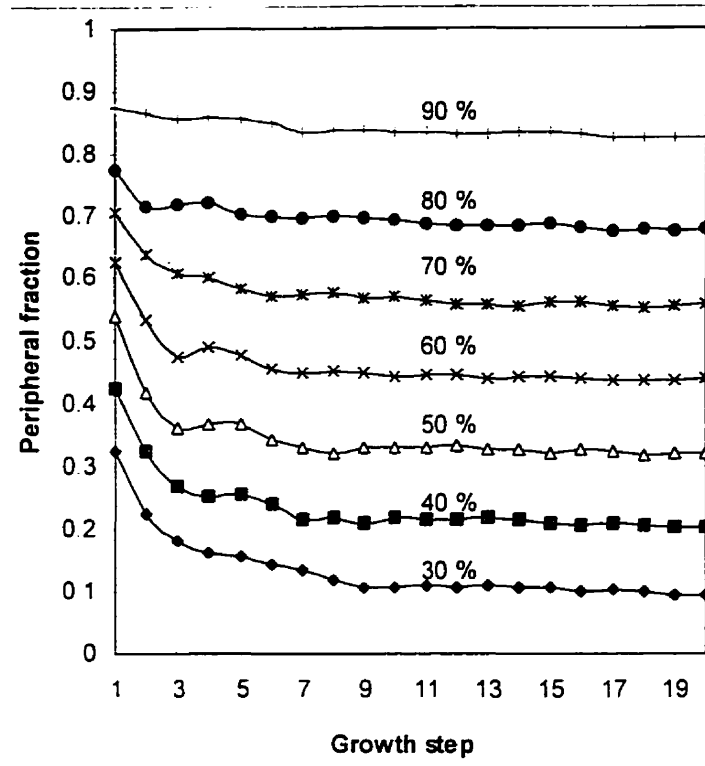


Fig. 4.6. Peripheral fraction of growing grains with various percentages of mobile grain boundaries in the initial matrix

From the results obtained by Lin et al [67], if the mobile boundaries are  $\Sigma 3$ - $\Sigma 9$  CSL boundaries then the Goss grain would not grow as it has the MF value of only 13%. Harase and his co-workers [64,65,149] stressed the role of  $\Sigma 9$  CSL boundaries on the development of Goss texture in electrical steels. If the  $\Sigma 9$  CSL boundaries are the only boundaries considered as the allowed boundaries then the MF for the Goss grain would be 3%. This extremely small percentage cannot influence the growth of the Goss grain.

#### 4.2.4. Preferential growth of Goss grains

Applying the growth algorithm explained in section § 4.2.2 to investigated specimens and assuming that the middle misorientation boundaries are highly mobile, one obtains grain size changes as given in Figs. 4.7 and 4.8 for the conventional and high-permeability steels respectively. Each curve presented in the graph is an average of 10 simulations. The Figs. 4.7 and 4.8 show that the Goss orientation grows considerably faster than other orientations in both the steels. In conventional Fe-3%Si steels, the main component  $\{111\}\langle 110 \rangle$  grows faster than the cubic  $\{100\}\langle 001 \rangle$  orientation. On the other hand, the main component  $\{111\}\langle 112 \rangle$  in the high-permeability steel grows slower than the cubic component. Comparing the conventional and the high-permeability steels, it is evident that grains with the Goss orientation grow much faster in the high permeability steel than in the conventional steel. As the Goss grains grow, the change in the average PF as a function of growth step is recorded and presented in Figs. 4.9 (a) and (b) for both conventional and high-permeability steels respectively. The steady state is reached approximately after seven growth steps.

#### 4.2.5. Grain boundary character distributions (GBCD)

An important use of this computer experimentation is that the grain boundary character distribution (GBCD) can be computed and followed as the grain grows in the matrix. In this work, the GBCDs was simulated under the assumption that the high-energy grain boundaries are highly mobile, using an average of the 10 different experiments. In each experiment, the GBCD around Goss grain is computed only after the growing grain has more than 500 neighbors. This is to ensure a good statistical average. The computed GBCD around the growing Goss grain in the matrices of conventional and high-permeability steels are compared with the experimental results in Figs. 4.10 (a) and (b) respectively. For the conventional electrical steel (refer to Fig. 4.10 (a)), a comparison is

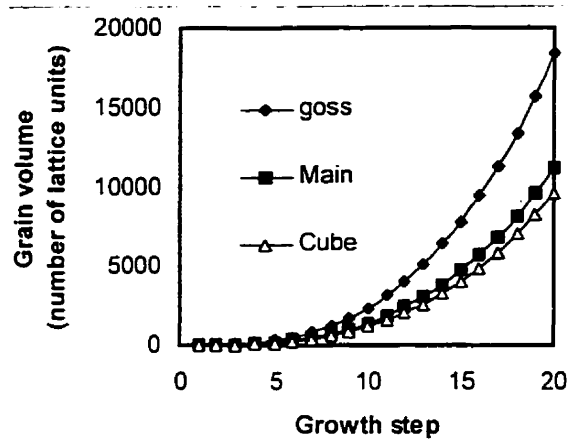


Fig. 4.7. Volume as a function of growth step for grains having Goss  $\{110\}\langle 001\rangle$ , Main  $\{111\}\langle 011\rangle$ , and cube  $\{001\}\langle 100\rangle$  orientations obtained assuming that high energy boundaries have high mobility in the conventional Fe-3% Si steel

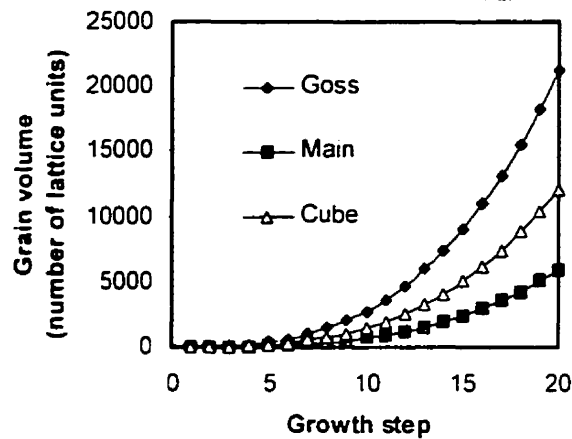


Fig. 4.8. Volume as a function of growth step for grains having Goss  $\{110\}\langle 001\rangle$ , Main  $\{111\}\langle 112\rangle$ , and cube  $\{001\}\langle 100\rangle$  orientations obtained assuming that high energy boundaries have high mobility in the high permeability Fe-3% Si steel.

made between the calculated and experimental percentage of CSL boundary in the specimens annealed at 950°C and 1000°C [67]. The simulated average frequencies (except  $\Sigma 1$ ) are similar and lie between the frequencies experimentally observed in the specimens annealed at 950°C and 1000°C. EBSD data by Hayakawa et al. [155] is compared in Fig. 4.10(b) with the simulated data obtained for the high permeability steel.

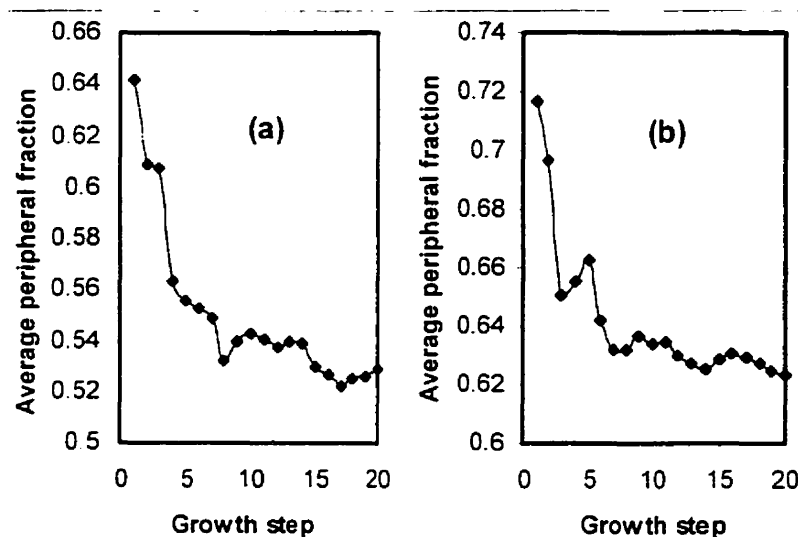


Fig. 4.9. Average number fractions of mobile boundaries around the growing Goss grains as a function of number of growth steps in a) conventional and b) high-permeability electrical steel

Overall, these computer experiments demonstrate that the role of high energy grain boundaries with the misorientation between 20°-45° on the growth of Goss orientation in Fe-Si steel is of decisive importance. As far as the CSL boundaries are concerned they do not play an important role in the AGG, because the value of MF for  $\Sigma 3$ - $\Sigma 9$  is about 13% for both the conventional and the high-permeability Fe-3%Si steels. The simulations also demonstrated that if the MF is less than 20 %, the grain never grows abnormally.

The properties of grain boundaries govern the development of microstructure and texture during an annealing process. It is logical to expect that the energy, mobility and the diffusion along various grain boundaries should be taken into account to explain the grain growth phenomena. As a next step toward understanding the abnormal grain growth in Fe-3% Si steels, an analysis on grain boundary mobility and its dependence on misorientation is presented in the following section.

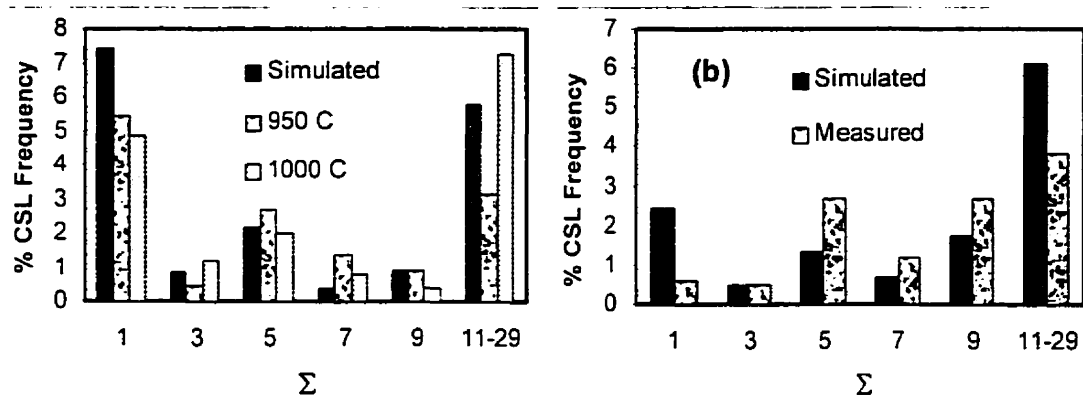


Fig. 4.10. Comparison between the simulated and experimentally determined GBCD [Σ] for grains bounding the growing Goss grains for the a) conventional and b) high-permeability Fe-3% Si steel.

#### 4.3. GRAIN BOUNDARY MOBILITY AND MISORIENTATION

The mobility of atoms and ions is considerably higher at grain boundaries than inside the grain. A detailed account of grain boundary diffusion in metals is dealt by Peterson [164]. It is expected that a relation between boundary diffusion and grain boundary energy might exist, since both the activation energy of diffusion and the grain boundary energy are dependent upon the atomic binding forces within the boundary region. Borisov et al. [165] studied this problem and derived an equation which relates the grain

boundary diffusion and the grain boundary energy. This equation has the following form.

$$E = \left( \frac{kT}{\alpha a^2} \right) m \left[ \left( \ln \frac{\delta \Theta}{a \lambda^2} \right) - \ln m \right] \quad (4.3)$$

where  $E$  is the grain boundary energy,  $m$  is the number of atomic layer forming the boundary and assumed to be unity [165],  $a$  is the mean distance between the equilibrium positions of the atoms,  $T$  is the temperature and  $\delta = ma$  is the width of the grain boundary. Borisov et al [165] estimated parameter  $\lambda$  as being approximately unity and because the diffusion of Fe and S in  $\alpha$ -Fe occurs by a vacancy mechanism, the parameter  $\alpha$  assumes a value of 2. The relative diffusion coefficient  $\Theta = D_{gb}/D_l$  is given by the ratio of grain boundary ( $D_{gb}$ ) and lattice diffusion ( $D_l$ ) coefficients. As pointed out by Pelleg [166], in spite of the many simplifying assumptions of Borisov et al. [165], the values obtained using equation (4.3) compare well with the results observed for cubic metals.

By substituting the above values in equation (4.3), and by simple rearrangement, the following relationship is obtained.

$$\ln \Theta = \left[ \ln \frac{D_{gb}}{D_l} \right] = 2\alpha^2 E_{rel} \frac{E_m}{kT} \quad (4.4)$$

Since the relative grain boundary energy  $E_{rel} = E/E_m$  is a function of misorientation angle, then equation (4.4) can be used to express the relative diffusion coefficient as a function of misorientation angle. The Fig. 4.11 shows the computed relative values of grain boundary self-diffusion coefficient as a function of misorientation angle. The grain boundary diffusion data compiled by Kaur and Gust [164] is comparable with the calculated values. In the present work, the same method is used to compute the values of sulfur diffusion coefficient as a function of misorientation angle. The average

[164,165] experimental grain boundary diffusion coefficient is in agreement with the calculated average value. These diffusion coefficients are used in this simulation work to compute inherent mobility and particle radius.

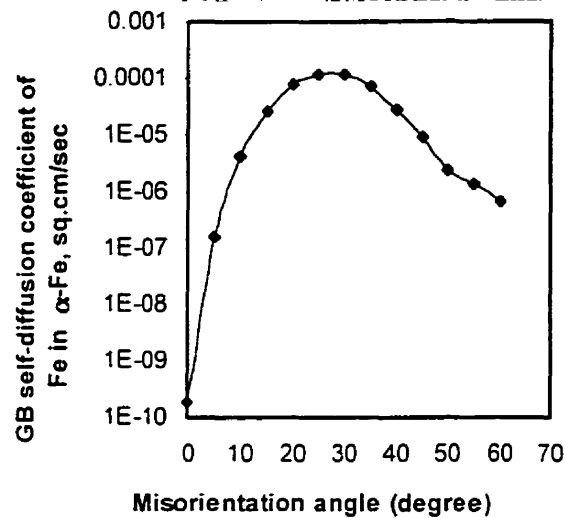


Fig. 4.11. Grain boundary self diffusion coefficient as a function of misorientation

The mobility is calculated from the activation energy  $Q_{gb}$  of grain boundary self-diffusion (which is a function of misorientation angle) as

$$M = M_{rel} \exp\left(-\frac{Q_{gb}}{RT}\right) \quad (4.5)$$

Here the relative inherent mobility parameter  $M_{rel}$  is computed by normalizing the mobility with that of the maximum inherent mobility. The calculated relative inherent mobility as a function of misorientation is given in Fig. 4.12. According to this curve, the relative mobility is the highest for the middle misorientation grain boundaries.

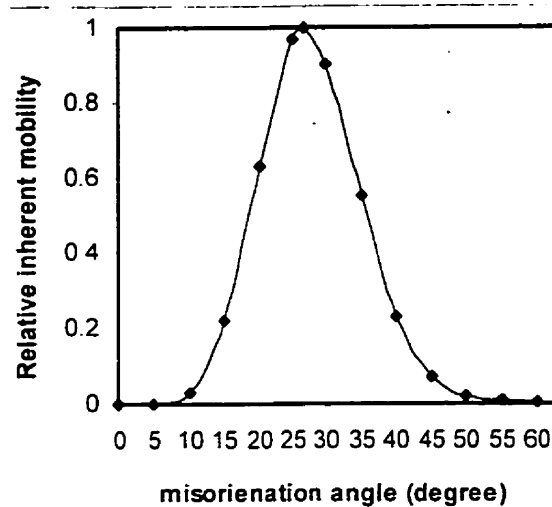


Fig. 4.12. Inherent mobility as a function of misorientation for Fe-Si steels

#### 4.4. MONTE-CARLO MODEL WITH ANISOTROPIC MOBILITY

The same Monte-Carlo model described in the section § 2.7.2 is used to analyze the growth of Goss texture in the conventional electrical steel. In the first test the effect of precipitate particles pinning was not implemented. The computer specimen employed for this simulation work is described in section § 2.7.3. The computer specimen represents the ODF of conventional electrical steel given in Fig.4.3. This ODF has the main texture component of  $\{111\} 011$  with the maximum intensity of 7.4 and the Goss component has an intensity of 3.8. The grain orientations were assigned to the computer specimen and the recalculated ODF of 5 such specimens that is given in Fig 4.13 exactly matches the original ODF. Among the 1500 Voronoi grains generated, a maximum of 73 grains have the orientations with a deviation of less than 15 degrees from the ideal Goss orientation. The number of such grains is dependent on the intensity of Goss orientation

in the ODF determined from experiment. The grains with a deviation of less than  $15^\circ$  from the ideal Goss orientation are considered to be Goss grains in this simulation work. This is mainly because, there are only 1500 grains used in each simulation work and grains having a small deviation from the Goss orientation are very few.

#### 4.4.1. Simulation of grain growth with anisotropic grain boundary mobility

The Monte-Carlo simulation was carried out using the calculated inherent mobility of grain boundaries, without considering the presence of pinning by particles. The result of this simulation suggests that the inherent mobility itself has a major influence on the selection of Goss orientation. However, the selected Goss grains grow normally (particle pinning is necessary for abnormal grain growth). At this juncture, it is meaningful to understand the parameters, which dictate the growth behavior of the grains in the matrix. To do so, each Goss grain is followed in the simulation and the results obtained at MCS=0 and 1000 are analyzed in detail.

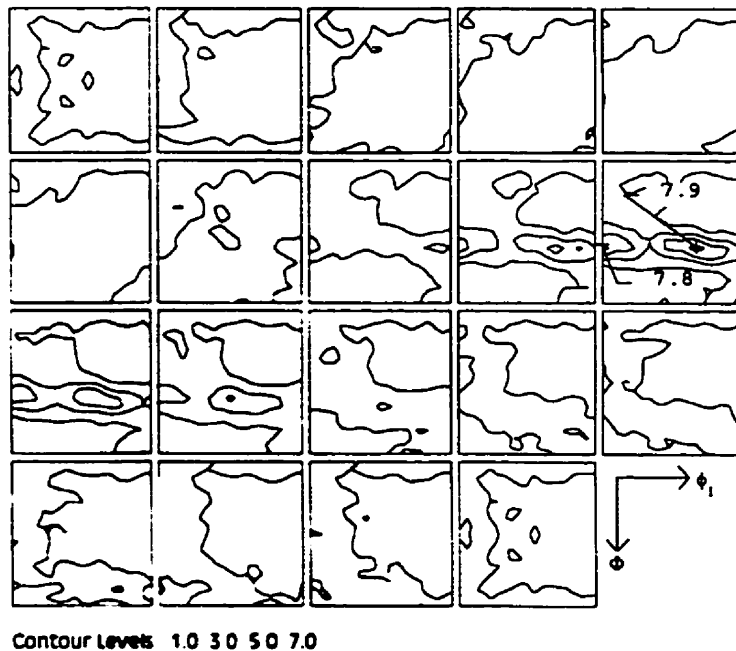


Fig. 4.13. Recalculated ODF of conventional electrical steels from the computer specimen

At the initial stage there are 1500 grains in the computer specimen. Out of them 73 are Goss grains. After 1000 MCS only 19 Goss grains remain out of the total 694 grains. At this stage, among the first 11 larger grains, all the grains are Goss grains except 2. Within the first 1000 MCS, 54 Goss grains are consumed by other growing grains. This means that the shrinking rate is higher for the Goss grains. Among the 19 Goss grains present at the end of 1000 MCS, 4 grains have less than its original grain volume (i.e., they are in a shrinking mode) and the remaining 15 grains are in growing mode. At the end of 12000 MCS where only 34 grains dominate the whole computer specimen, out of them, the first 7 largest grains are all Goss grains. From the beginning of the simulation, the grains with deviation of  $12.07^\circ$  and  $7.66^\circ$  from the ideal Goss orientation grow faster than the other grains.

The analysis of the results from this simulation work shows that whether the Goss grains grow or not is strongly influenced not only by the grain volume but also the grain boundary energy to volume ratio and the number of neighbors. These parameters decide which grain would grow and which grain would shrink at each stage during annealing. The value of relative grain volume, grain boundary energy to grain volume ratio and the number of nearest neighbors for the growing and shrinking Goss grains are given in Table 4.1. The growing and shrinking Goss grains are identified by comparing the grain volumes at MCS=0 and MCS=1000.

It is important to note that the GB energy to grain volume ratio for the growing Goss grains is 2.4, which is much less than the overall average that equals 2.9. The latter ratio is less than the ratio for the shrinking Goss grains which is 3.0. The energy used here is the relative energy given in Fig 4.1. The average number of neighbors for all grains is 16.6, which is greater than the average number of neighbors of shrinking Goss grains, which is 15.5. The growing Goss grains have 20.9 neighbors, which is much greater than the overall average.

**Table 4.1. The ratio between total relative grain boundary energy and grain volume and number of nearest neighbors at the beginning (MCS=0) of the simulation for all the Goss grains present in the computer specimen.**

Status of Goss grains	Number of Goss grains	Relative grain volume	Ratio between total Relative GB energy & grain volume	Average number of neighbors
Growing Goss grains	15	1.6	2.4	20.9
Shrinking Goss grains	58	0.9	3.0	15.5
All the Goss grains	73	1.1	2.9	16.6

According to Hillert's [60] the size advantage is considered to be the prime controlling factor for the grain growth. From the relative grain volume data given in Table 4.1, it is clear that the grain volume has a positive influence on the selection of growing grains. However, two out of 15 growing Goss grains that are present after 1000 MCS in this simulation had volumes, which were lower than the average grain volume at the beginning of simulation. Apart from that, about four Goss grains, which had volume more than 1.5 times the average volume at the beginning shrank and disappeared after 1000 MCS. Among the grains having volume more than the average, some grains grow and some grains shrink. Thus, based on grain volume alone, the probability of growth of a grain cannot be predicted. One must take into account the shape of the grain and where it is located in the microstructure. Also a growing grain should preferably have high volume, low energy to volume ratio and a high number of neighbors compared to other grains. Analysis of growth behavior of the existing grains after 1000, 2000 and higher number of MCS values confirm this observation.

#### 4.5. PRECIPITATE PARTICLES AND THEIR IMPORTANCE IN ABNORMAL GRAIN GROWTH

Since the analysis on pinning of grain boundaries by particles by Zener (published by Smith) [56], much research was focused on the effect of particles on recrystallization

and grain growth. This phenomenon has been modeled by various authors [106,167-170] using a constant particle size (inert particles) throughout the simulation. To understand the real behavior of metals, during annealing it is very important to model both interdependent processes, namely the particle growth and grain growth. This problem has been analytically modeled [91,171] by combining particle coarsening kinetics with grain growth kinetics. Like previous analytical works [86,167,168], this procedure suffers from the inability to deal with texture and does not account for topological information about grains. This topological information is handled well in Monte-Carlo models. Although some work on computer simulation of secondary recrystallization [15,106,172] has been carried out, very little is known on the effect of the presence of second phase particles on the dynamics of the recrystallization during the process of particle coarsening. The main reason is the complexity involved in managing various important microstructural parameters in the computer programs. In this work, an attempt is made to study the effect of growth of the second phase particle on the kinetics of growth of grains of different orientation in grain-oriented silicon steel.

#### *4.5.1. Ostwald ripening of precipitate particles*

It is well-established that the Zener pinning of grain boundaries by precipitates like MnS, AlN, etc. stabilizes the grain size during normal grain growth and the Ostwald ripening at high temperature favors the abnormal grain growth in silicon steels. Any system of dispersed soluble particles randomly distributed in a medium will be thermodynamically unstable due to a large interface area. The different diffusion rates of particle forming elements in the matrix and grain boundaries allow the particles to grow or to shrink with different rates depending on their location. The fundamental theory of particle coarsening in the supersaturated solid solution by diffusion processes has been developed by Lifshitz and Slezhov [173] and further by Wagner [174] and will be referred in this paper as LSW theory. This theory assumes that the particles are distributed at random over the matrix volume. However, at the end of primary recrystallization, the presence of grain boundary pinning can enforce transition from the statistically random distribution of precipitates over the entire volume of the matrix to

the preferentially ordered distribution along grain boundaries. The mathematical treatment of coarsening of precipitates along grain boundaries is dealt in detail by various researchers [175,176]. The overview on the Ostwald ripening theory by Vengrenovitch [177] summarizes the formulae for coarsening of particles at various conditions. The diffusional growth of particles in the matrix is governed by the equation given below

$$r_t^3 - r_{0t}^3 = \frac{3 \sigma C_\infty v_m^2 D_t}{2 RT} t \quad (4.6)$$

Here  $r_{0t}$  and  $r_t$  are the radii of the particle corresponding to the initial state and to the state when time equals to  $t$ . The energy of the particle-matrix interface is  $\sigma$  and  $v_m$  is the molar volume. The parameter  $C_\infty$  represents the equilibrium concentration of solute atoms in the boundary away from the precipitates.

On the other hand the growth of particles by the diffusion of solute atoms only along the grain boundary is governed by [177]

$$r_{gt}^4 - r_{0gt}^4 = \frac{8 \sigma C_\infty v_m^2 D_{gb}}{9 ABRT} t \quad (4.7)$$

Here  $r_{0gt}$  and  $r_{gt}$  are the radii of particles at  $t$  equals zero and  $t$  respectively. The parameter  $A$  and  $B$  are defined by the following equations

$$A = \frac{2}{3} - \frac{E_{gb}}{\sigma} + \left( \frac{E_{gb}}{\sigma} \right)^2 \quad (4.8)$$

and

$$B = \frac{1}{2} \ln \left( \frac{n}{f_a} \right) \quad (4.9)$$

Here  $f_a$  is the area fraction occupied by  $n$  precipitates on the boundary.

The equation (4.7) is derived based on the assumption that the significant transfer of matter occurs through the grain boundaries. Recently, Hoyt [178] has come up with a mathematical formulation for coarsening of precipitates located on grain boundary, with a more realistic assumption that the diffusion of solute occurs both through the bulk and along the grain boundary. This formulation makes use of a parameter, which is similar to the one known in the heat transfer literature as the convection coefficient. Unfortunately, very little is known about this parameter except that when bulk diffusion coefficient  $D_i$  is zero, this parameter must also be equal to zero.

In this study, coarsening of precipitates on the grain boundaries is approximated by combining the effect of equations (4.6) and (4.7). All the necessary data have been taken from the work published by Swift [179,180]. The particle growth is assumed to be controlled by the diffusion of sulfur [180]. The relative radius,  $r^{(rel)}$  namely the ratio of particle radius at any time ( $t$ ) to the initial radius (at time  $t=0$ ) is plotted as a function of real time for various grain boundary energies and is shown in Fig. 4.14. The initial average radius is assumed to be 220 nm [179].

#### 4.5.2. Zener particle pinning

Dispersed particles of different radii have different pinning pressures on the migrating boundary. This phenomenon was first identified by Zener [56]. By assuming the shape of the particles to be spherical with radius  $r$  and incoherent with the matrix grains, the pinning pressure that is exerted on the boundary is given by

$$\Omega_z = \frac{3}{4} \frac{f_v E_{gb}}{r} \quad (4.10)$$

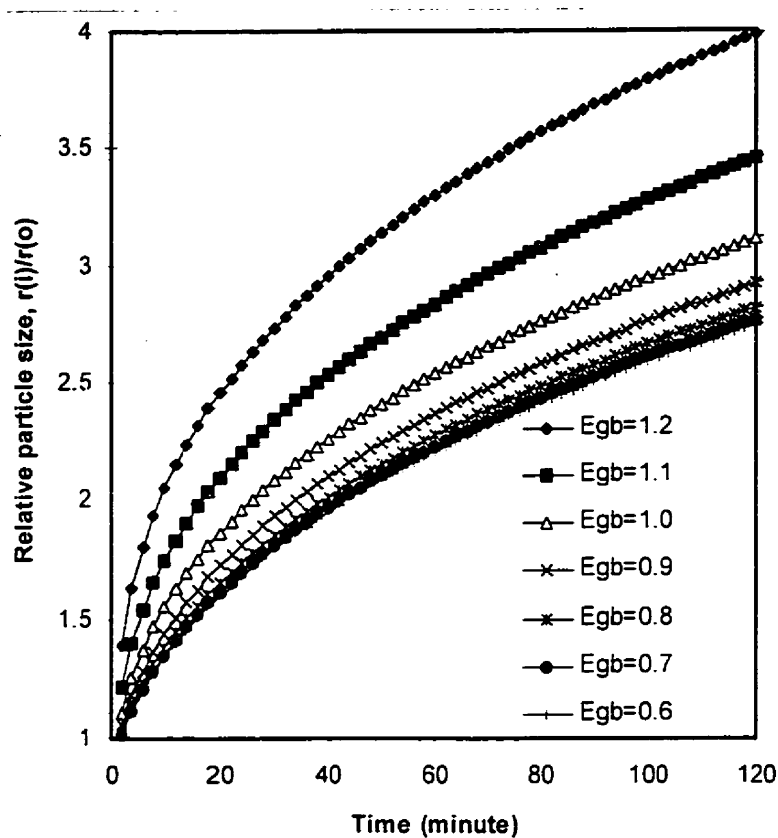


Fig. 4.14. Calculated change of relative particle radius for various grain boundary energies

Here  $f_v$  is the volume fraction of the precipitates. Various researchers questioned the Zener's assumption, but finally ended up with essentially similar results. Hellman and Hillert's [181] approach to this problem suggested that a correction factor  $\beta$  is to be introduced in the equation as below

$$\Omega_s = \beta \left[ \frac{3}{4} \frac{1}{r} \frac{E_{gb}}{r} \right] \quad (4.11)$$

The  $\beta$  parameter ranges between 0.4 and 2 for values of  $\rho/r$  between 1 and  $10^5$  where  $\rho$  is the net radius of curvature of the moving boundary. Thus general agreement is that

for a constant volume fraction of the particles in the matrix, the pinning pressure is directly proportional to the grain boundary energy and also inversely proportional to the average radius of the particles. In order to incorporate the pinning effect in the Monte-Carlo simulation employed in this study, a dimensionless parameter  $\Omega$  is introduced and is defined as:

$$\Omega = z \left( \frac{E_{gb}^{(rel)}}{r^{(rel)}} \right) \quad (4.12)$$

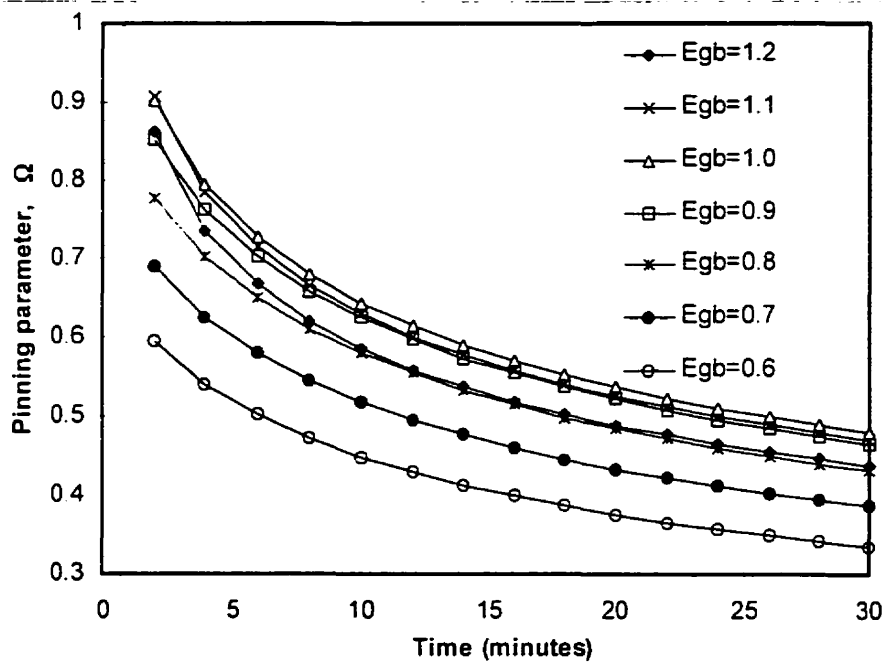


Fig. 4.15. Calculated change in pinning parameter  $\Omega$  for grain boundaries with different grain boundary energy as a function of time

The values of  $\Omega$  as a function of time were calculated based on equation (4.12) and the results obtained are given in the Fig. 4.15 for various grain boundary energies  $z = 1$ . It is interesting to note that the pinning effect for higher relative grain boundary energies such as 1.2 and 1.1 is lower when compared to the grain boundary energy of 1.0. In fact

the pinning parameter for  $E_{gb}^{(rel)}=1.2$  is comparable to that of  $E_{gb}^{(rel)}=0.8$ . This means that the grain boundary with high energy (e.g.  $E_{gb}^{(rel)}=1.2$ ) has a lower pinning pressure when compared to the grain boundary with lower energy (e.g.  $E_{gb}^{(rel)}=1.0$ ). Though this result is a direct consequence of the concept of Zener pinning, consideration of different particle coarsening rates at different grain boundaries yields a new result. This differs from the usual assumption that the higher the grain boundary energy, the higher is the pinning pressure.

Having parameterized the particle radius and pinning as a function of time, it is possible now to incorporate them into the Monte-Carlo model and study the development of Goss texture by abnormal grain growth.

#### 4.6. MONTE-CARLO SIMULATION OF ABNORMAL GRAIN GROWTH WITH MnS PARTICLE PINNING

The Monte-Carlo procedure with precipitate particles is run to simulate the grain growth and texture development in conventional grain-oriented electrical steel. Specifically, the enhancement of size of Goss grains by the presence of precipitate particles is studied. The MnS particle growth function shown in Fig. 4.14 is used. The Zener pinning parameter,  $\Omega$  (discussed in section § 4.5.2) is incorporated in the program [106] such that presence of particle always opposes the grain boundary migration. Initially all the boundaries are pinned with the same-sized particles, which is 220 nm [179]. In order to initiate the difference in pinning effect on different grain boundaries, the particle radius is allowed to grow for 4 minutes, before the actual grain growth simulation starts. This is carried out to initiate the anisotropy of particle size on different grain boundaries. The approximation that each grain boundary is associated with a particular type of particle growth rate is derived from the anisotropic grain boundary energy. This approximation is justifiable [165] as the bulk diffusion is much lower than the grain boundary diffusion.

The main problem is to correlate the MCS to real time. In a simple Monte-Carlo simulation, where grain boundary mobility and energy are constant, the MCS and real time ( $t$ ) are related by an exponential factor [13] as below.

$$MCS = t \exp(-W/RT) \quad (4.13)$$

Here,  $\exp(-W/RT)$  corresponds to atomic jump frequency. In a complex simulation such as the one used in this work, it is very difficult to deal with this problem. Here, the Monte-Carlo simulation incorporates anisotropic energy of grain boundary, anisotropic mobility and anisotropic pinning of the moving boundaries. The main aim of this work is to incorporate the kinetics of particle growth and the changes of grain boundary pinning that take place with time, into this Monte-Carlo computer procedure. To find a relation between the computer and true time scales, this Monte-Carlo simulation is run with different particle growth rates and the growth of the largest grain is followed. Among the various time scales used namely 20 MCS, 100 MCS, 200 MCS and 500 MCS equals to one second: the 100 MCS assumed to be equal to one second scale gave an abnormal growth of Goss grain. This Goss grain is deviated by  $7.66^\circ$  from the ideal orientation and has a grain size of the order of 35 times the average grain size after 7000 MCS. All the diffusion coefficients used in this work correspond to the temperature of  $975^\circ\text{C}$ .

#### 4.6.1. Simulated texture and microstructure using MnS particle pinning

In order to obtain a reliable statistical result five similar simulations with different computer specimens mapped to represent the same primary recrystallized experimental ODF (refer Fig. 4.3) were followed. The ODFs were calculated during the grain growth at every 1000 MCS. The Figs. 4.16 represents the ODF sections  $\phi_2=45^\circ$ , calculated at 3000, 5000, 7000, 9000 and 11000 MCS respectively. The calculation of ODF beyond 7000 MCS is not very accurate, because each of the 5 simulations was of less than 300 grains each, which is statistically insufficient to calculate the ODF.

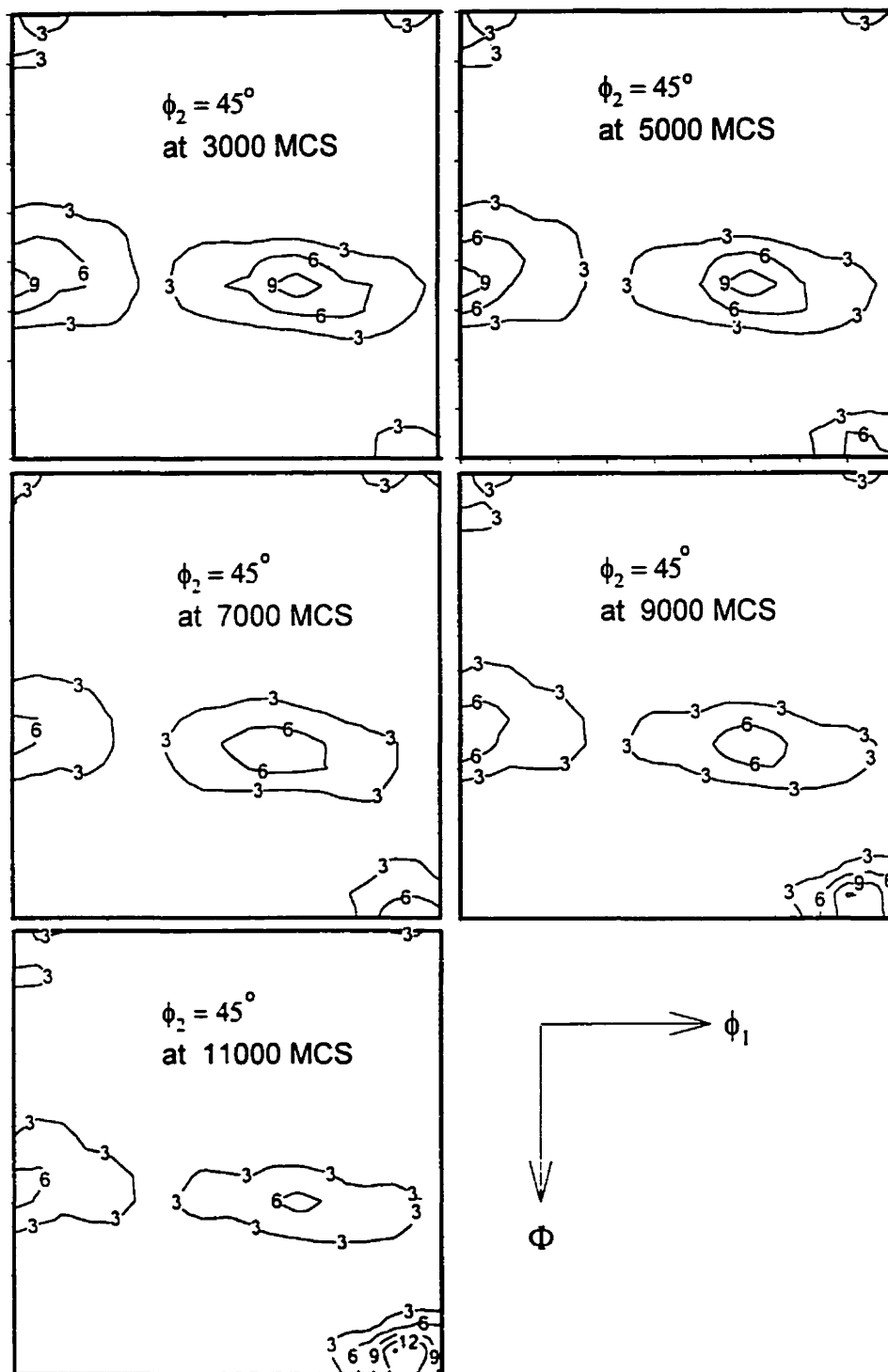


Fig. 4.16. Calculated ODF sections for  $\phi_2 = 45^\circ$  obtained at 3000, 5000, 7000, 9000 and 11000 MCS of simulated annealing for Fe-3%Si conventional electrical steel

The section of ODFs presented clearly indicates that the intensity of both the Goss and main texture components grows at the beginning. Later in the consecutive grain growth process, the intensity of the Goss component starts to increase at the cost of the main texture component. The Fig. 4.17 shows the change in the ODF intensity function  $f(g)$  during grain growth for various MCS. As mentioned previously by Hayakawa et al [155], the grain with the main texture orientation, which grows normally, is then consumed by the abnormally growing Goss grains. The largest Goss grains that are grown in each one of the 5 computer simulations with different starting microstructures have the deviation of 7.7, 9.6, 9.5, 11.5 and 11.7 from the ideal Goss orientation. The growth behavior of the largest grain is given in Fig. 4.18. The growth of the grain reaches a steady-state growth rate after 2000 MCS. Beyond 7000 MCS, the growth rate remains approximately constant. This trend is close to the experimentally observed steady state growth rate during abnormal grain growth in electrical steel [163]. Usually, the end of the abnormal grain growth is associated with the existence of low angle grain boundaries that surround the growing Goss grains, as the Goss grains meet each other. In this simulation work, the final microstructure has two other Goss grains, which are in the shrinking mode. All these Goss grains occupy almost 80% of the computer specimen.

Two-dimensional sections of the simulated microstructures for various MCS values viz., 0, 1000, 3000, 5000, 7000 and 9000 MCS are shown in Fig. 4.19. The two growing Goss grains are painted gray.

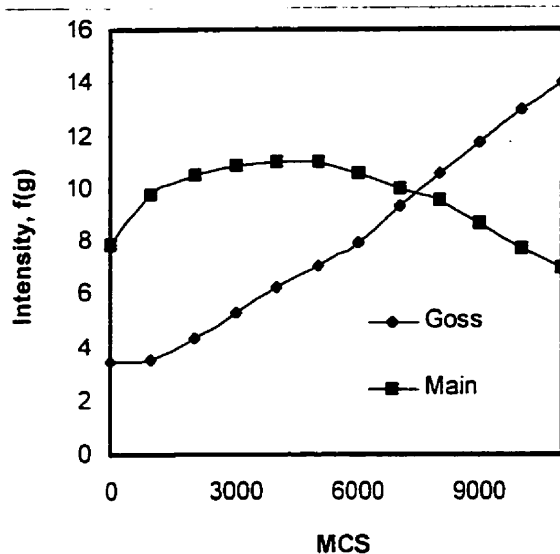


Fig. 4.17. Simulated change in maximum ODF intensity for Goss and Main texture components during annealing

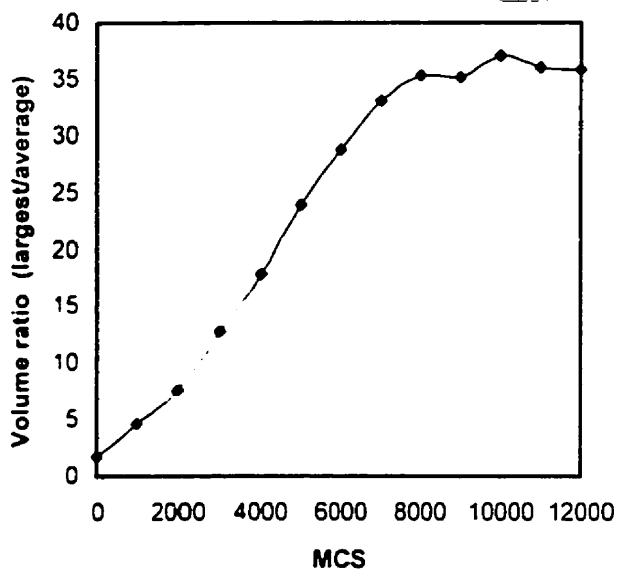
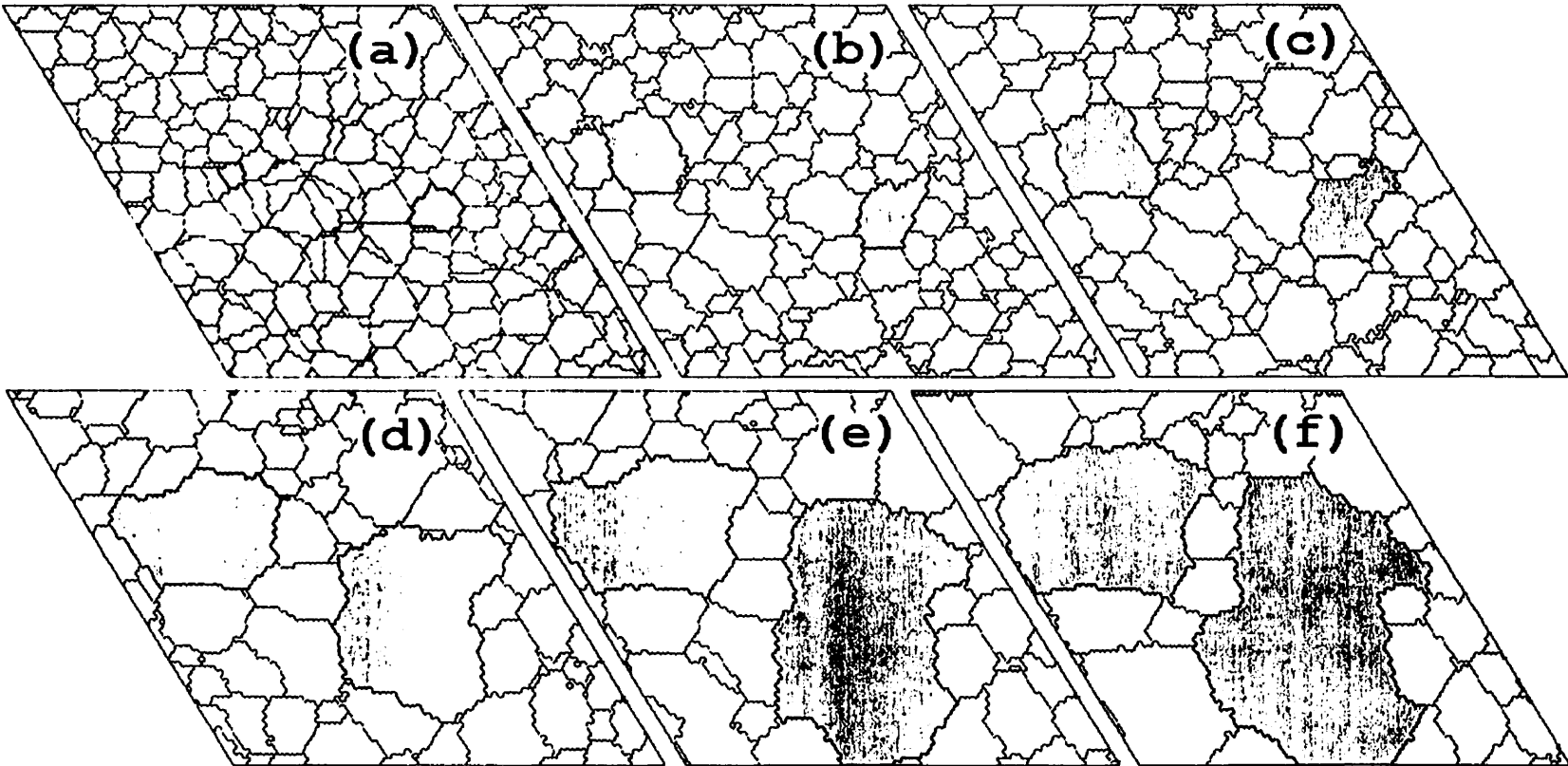


Fig. 4.18. Growth of the largest abnormally growing grain in the computer simulations of annealing



**Fig. 4.19.** Microstructure showing the growth of two Goss grains (painted grey) in a 2-dimensional section of 3-dimensional computer specimen for a)MCS = 0, b)MCS = 1000, c)MCS = 3000, d)MCS = 5000, e)MCS = 7000 & f)MCS = 9000

The matrix grains clearly show a normal grain growth, whereas, the Goss grains show an abnormal grain growth similar to the experimental observation [67,155]. In the initial stage of the simulation of grain growth, both the Goss grains have dimensions that are close to the average grain size. As the time proceeds, these Goss grains grow bigger in size than other matrix grains and finally occupy nearly the whole specimen.

#### **4.6.2. Mobile boundary fraction around growing Goss grains**

In the previous section § 4.2.3. the importance of mobile boundary fractions has been elucidated using a simple computer procedure. From those computer experiments [182,183], it was pointed out that the fraction of mobile boundaries around the growing grain called the peripheral fraction (PF) decreases with time. There are experimental evidences for this phenomenon obtained using the orientation imaging microscopic (OIM) technique by Hayakawa et al [155]. In the present work, the area fraction of the mobile boundaries (with grain misorientation of 20 - 45°) is followed for the three large Goss grains discussed in the previous section and is shown in Fig. 4.20. All the growing Goss grains have initially the mobile boundary area fraction of about 0.9. As the simulation proceeds, the area fraction decreases and reaches a sort of steady state. Here, the area fraction decreases to a value between 0.3 and 0.2. In experiments this value is not as low as the value predicted by this simulation. The reason is that, in the computer experiment the growing large Goss grains impinge each other, therefore reducing the area fraction of mobile boundaries around Goss grains as presented in Fig. 4.20. One should also bear in mind that this simulation has only 1500 grains. This is also another reason for the early impingement of growing large Goss grains.

Apart from the grain volume, grain boundary energy to volume ratio and the number of nearest neighbors, the mobile boundary fraction is also a deciding factor in predicting the Goss texture development.

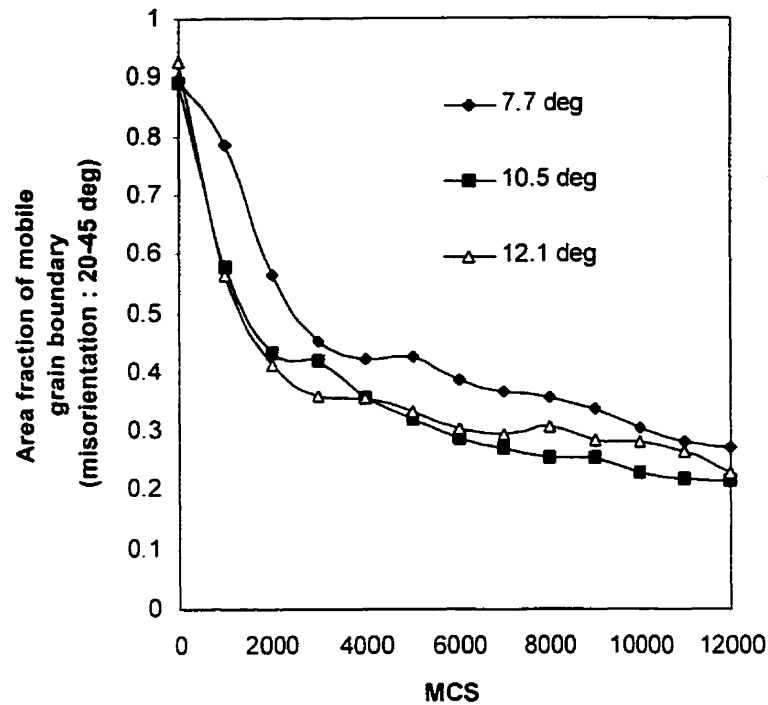


Fig. 4.20. Change in the area fraction of the mobile grain boundaries with misorientation between 20 and 45° around the growing Goss grains as a function of MCS during annealing

#### 4.7. SUMMARY

A simple computer technique has been developed to study the conditions for abnormal grain growth in a matrix of primary recrystallized Fe-Si steel. The importance of the fractions of mobile boundaries is discussed. The orientation that grows abnormally requires a high matrix fraction (MF) of high mobility boundaries. From the computer experiments it can be concluded that, a steady state of peripheral fraction (PF) is reached during grain growth. The preferential growth of the Goss grains is simulated in both conventional and high-permeability steels by assigning a high mobility to grain boundaries with misorientation angles between 20° and 45°. This assumption

satisfactorily reproduces the experimentally observed GBCD around the Goss orientation during grain growth.

The assumption of the high mobility of CSL boundaries  $\Sigma 3$ - $\Sigma 9$  does not support the abnormal growth of Goss grains because these boundaries may contribute only 13% to the total number of boundaries that surrounds the Goss grains. According to the results presented, such a low number of mobile boundaries is not sufficient for abnormal grain growth of these grains.

Computer simulation of abnormal grain growth is carried out using a modified Monte-Carlo procedure that incorporates a full description of microstructure and texture. This computer procedure takes into account the anisotropic grain boundary energy, mobility and the kinetics of growing particles. It is observed that in the simulation, the anisotropic energy and calculated anisotropic mobility of the grain boundaries ensures the excellent selection of Goss grains. The presence of growing MnS particles enhances the grain size of the Goss component and produces abnormal grain growth.

It is also noted that at the initial stage of the simulation the intensities of both the main texture component (i.e.,  $\{111\} 011$ ) and the Goss texture components increase. However, at the latter stages, the intensity of Goss component increases at the expense of the main texture component. The simulated microstructure shows that the matrix grains grow normally whereas the Goss grains grow abnormally.

Among the physical parameters that decide the abnormal grain growth, namely the grain volume, grain boundary energy to volume ratio, the number of nearest neighbors and the fraction of mobile boundaries around a growing grain are the most important.

**Chapter 5****ANNEALING OF NANOCRYSTALLINE Ni AND Ni-Fe ELECTRODEPOSITES - APPLICATION (III)**

The main goal of this chapter is to apply the Monte-Carlo model to the study of texture and microstructure development in nanocrystalline Ni and Ni-20% Fe and Ni-45% Fe electrodeposits. The first section § 5.1 of this chapter reviews the annealing behavior of the nanocrystalline materials with a major focus on Ni and Ni-Fe alloy electrodeposits. The discussions on texture analysis of these electrodeposits are given in section § 5.2. The predicted grain growth model is presented in section § 5.3. This model is implemented into the Monte-Carlo procedure and is described in section § 5.4. Finally in the section § 5.5, the discussion on the Monte-Carlo simulation and the results obtained are described in detail. The summary of results obtained is given in section § 5.6.

## 5.1. REVIEW ON ANNEALING OF NANOCRYSTALLINE MATERIALS

As discussed previously in section § 2.6, the nanocrystalline materials may exhibit special properties during annealing due to the high percentage of intercrystalline regions, which makes them thermodynamically unstable. Most methods currently used for the synthesis of nanostructured materials produce materials with considerable residual porosity. The porosity, residual trapped species from processing, etc. are the parameters introduced by the processing methods used for synthesis, which would eventually affect the thermal behavior of the nanocrystalline materials. Electrodeposition is one of the most promising techniques available for producing fully dense nanocrystalline material [184] that is economically viable for bulk production. The impurities introduced in this processing technique are mainly in their elemental forms. On the contrary, in the gas condensation technique, the impurities that are mainly in the form of oxides, nitrides, etc., are concentrated at the surface of the nanocrystalline particle and could be carried over to the interface during further processing. Therefore, a study on grain growth of fully dense electrodeposited nanocrystalline material does not need to consider the effect of the residual porosity and trapped species.

### 5.1.1. Grain boundaries in nanocrystalline materials

Before attempting to solve the grain growth problem, it is important to know the structure of the grain boundaries that exist in the nanocrystalline materials. There are two different opinions in the literature about the nature of the grain boundaries. The non-equilibrium high-energy structure of atoms along the grain boundaries [185-190] in extremely small grained materials appears plausible, given that in a 5 nm grain electrodeposit there is up to 50% of the atoms situated in the highly distorted and defected environments provided by the high density of grain junctions. The grain boundaries in nano and conventional polycrystalline materials are often different. Wunderlich *et al.* [189] noted that the grain boundaries in nanocrystalline Pd appeared to be different from that observed in conventional coarse-grained Pd and have a smaller grain boundary thickness of 0.4-0.6 nm than the generally accepted value of 1 nm for conventional polycrystalline materials. A

quantitative difference in the contrast in a vicinity of 0.6 nm at general grain boundaries when compared with the similar one in conventional microcrystalline boundaries was observed. This was attributed to the high-energy states of the grain boundaries in nanocrystalline materials. Wunderlich *et al.* [189] also noted that in the nanometer-sized crystals ordering of the grain boundary structure necessary to minimize the interfacial energy does not take place since the curvature of the grain boundary has a much different effect on the energy than in materials with larger grain size.

Various other investigations on nanocrystalline materials [191-194] indicate that the grain boundary structures are no different from those observed in conventional coarse-grained polycrystalline materials. In his review about nanocrystalline materials, Suryanarayana [94] raises however concerns regarding the interpretation of results on grain boundary structure by high resolution TEM. First, electron microscopic observation is done under ultrahigh vacuum. Second, the influence of high-energy electron beam on the shape and stability of the nanostructures is yet to be defined. Third, since very thin specimens are required for ultrahigh resolution TEM, the 3D crystal arrangement of a bulk nanocrystalline specimen gets transformed into a 2D arrangement. This process might change the boundary structure. In fact, thin foil specimen preparation may modify the internal stresses and hence the free energy of the entire system. As the grain boundaries in the nanocrystalline materials are highly mobile at temperatures far below the melting, the specimen preparation methods, ultrahigh vacuum, high-energy electron beam and 2D structure of the specimen may induce structural change.

Though the controversy over the structure of the grain boundaries in nanocrystalline material is still not resolved as experimental observations are concerned, molecular-dynamics computer simulation works recently carried out by Wolf and his co-researchers [195,196] support the argument that the grain boundaries are indeed in an amorphous state. These authors observed that the grain boundaries in fully dense nanocrystalline materials, by contrast with bicrystalline boundaries, lack strict long-range structural periodicity parallel to the interface because many short-grain boundary segments with locally different atomic structures can coexist in these highly constrained microstructures. As a

consequence, the grain boundary energy is considerably more isotropic than in polycrystalline materials and the grain boundary width is rather uniform. Such greater isotropic energy of grain boundaries may result from a high density of junctions which makes rigid body translations in the grain boundary plane more difficult and therefore, energy of boundaries in nanocrystalline materials is high. The distribution of energy in nanocrystalline materials is also more isotropic because a considerable portion of energy is stored in the grain junctions and the density of junctions is high. One has to stress however, that the type of grain boundary in nanocrystalline materials depends on the method by which this structure is formed. For example, Gertsman *et al.* [197] have demonstrated that the nanocrystalline monoclinic zirconium oxide may have a large fraction of CSL boundaries.

### 5.1.2. Grain growth in nanocrystalline electrodeposits

Grain growth occurs in order to decrease the total energy of the system by reducing the interfacial area. Since the nanocrystalline materials have a highly disordered large interfacial component, the driving force for grain growth is very high. As an extreme example, Gertsman and Birringer [98] observed an abnormal grain growth at room temperature in nanocrystalline copper produced via gas condensation technique.

As discussed in section § 2.6, the nanocrystalline Ni and Ni-Fe alloy electrodeposits show both normal and abnormal grain growth depending on temperatures and alloy compositions. A detailed grain growth study [10] on Ni electrodeposits with the starting grain sizes of 10 and 20 nm shows that the temperature at which the materials tend to become unstable is as low as 353 K. With increasing temperatures an anomalous grain growth takes place forming a dual microstructure consisting of large grains that grow in a nanocrystalline matrix until a uniform microcrystalline grain structure is developed at a temperature of 562 K. Isothermal annealing [10] of Ni nanocrystalline electrodeposits with a grain size of 20 nm at 523 K results in an abnormal grain growth, leading to a dual microstructure after an annealing treatment of 60 minutes. From the recently published work on isokinetic analysis on nanocrystalline Ni, Wang *et al.* [103] observed a similar

result. These researchers suspect that the abnormal grain growth of pure nanocrystalline Ni electrodeposit may be due to subgrain coalescence. However they also pointed out that this mechanism might not apply to nanocrystalline materials produced by other techniques. They also suspect that the grain boundary properties such as grain boundary structures and selective solute segregation to different boundaries might be the reason for the abnormal grain growth. The microstructure evolution during the abnormal grain growth of nanocrystalline Ni is described in the form of TEM micrographs [11,103] and these micrographs show the clear coexistence of abnormally growing grain and nanometer-sized grains. All these experiments show that when annealing the Ni electrodeposits at 673 K, an abnormal grain growth take place. Similar to this observation, Ni-20% Fe alloy and Ni-45% Fe alloy [100] also show abnormal grain growth at annealing temperature of 673 K.

## 5.2. TEXTURE MEASUREMENT

The texture measurements made on the as-electrodeposited nanocrystalline Ni [104], Ni-20% Fe [9] and Ni-45% Fe [198] using Siemens x-ray diffraction equipment. The results show that the matrix is composed of (100) and (111)-fibers. During annealing at 673 K, all three materials show the growth of (111)-fiber texture and decrease of strength of (100)-fiber texture. The Fig. 5.1 shows the change of fiber intensities obtained from their respective pole figures as a function of annealing time for all these electrodeposits at two different temperatures, namely 573 K and 673 K. The electrodeposited Ni shows the x-ray pole figure intensities of 5.3 and 1.8 for (100) and (111)-fiber texture components respectively. In the case of Ni-20% Fe the intensities of (100) and (111)-fiber texture components are 7.1 and 1.4 respectively. For Ni-45% Fe case, the pole figure intensities are 5.3 for (100)-fiber and 3.4 for (111)-fiber texture components. As these grains grow abnormally at 673 K, the (111)-fiber texture grows more rapidly than (100)-fiber. In Ni-45% Fe, (111)-fiber attains a maximum intensity of 13 after 7 hrs of annealing. In Ni-20% Fe electrodeposits, the (111)-fiber grows but not so rapidly as Ni-45% Fe, however continues to grow to the intensity of 6.4 even after 20 hrs of annealing. The (111)-fiber intensity in Ni electrodeposits, as in other cases is higher than that of (100) but the difference is much lesser than in other cases and does not exceed 2.6. In all these cases the

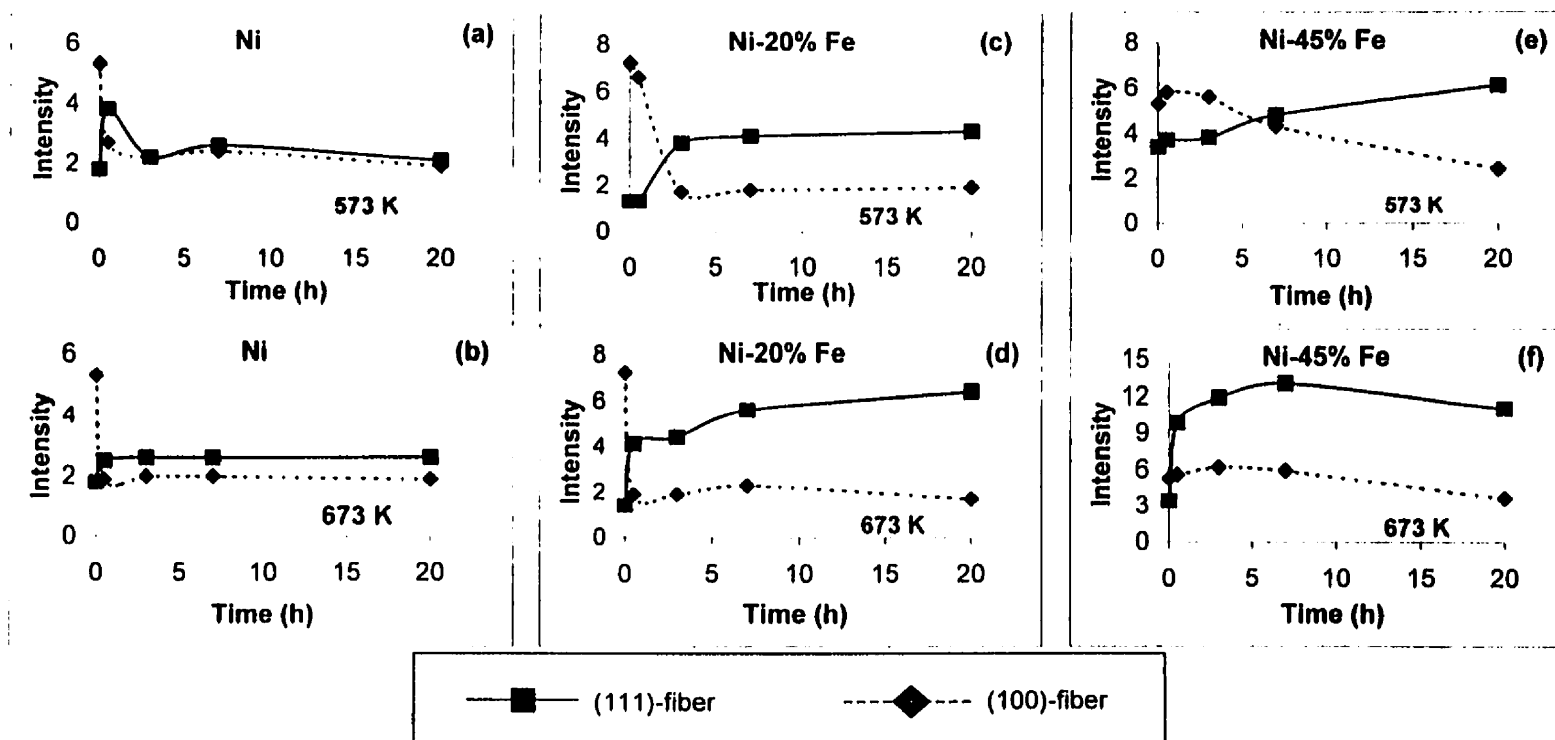


Fig.5.1 Fiber intensity observed in pole figures of (111) and (200) of Ni-45%Fe, Ni-20%Fe and Ni nanocrystalline electrodeposits measured after annealing at 573K and 673 K for various annealing periods

intensity of (100)-fiber component decreases during annealing. The (100) fiber intensity after 20 hrs of annealing has been found to be 3.6, 1.7 and 1.9 for Ni-45% Fe, Ni-20% Fe and Ni electrodeposits respectively at 673 K. On comparing the pole figure intensities of these alloys annealed at 573 K and 673 K, it can be observed that the growth of (111)-fiber at 673 K is stronger than the growth at 573 K. Similarly, an increase in Fe content increases the tendency for the (111)-fiber to grow stronger than (100)-fiber. The grain size of all the nanocrystalline electrodeposits used in this study is between 5-10 nm.

In the present work, an attempt is made to understand the basic mechanisms of grain growth that dictate the competition in growth between (111) and (100)-fibers. Systematic analysis of texture transformation obtained from experiments will be presented.

### 5.3. ANALYSIS OF TEXTURE IN NANOCRYSTALLINE Ni AND Ni-Fe ELECTRODEPOSITS

As far as production technology and sample preparation techniques of Ni and Ni-Fe alloy electrodeposits are concerned, the readers may refer to the research works [9,100,102,198]. Titanium has been employed as the substrate for all the nanocrystalline Ni and Ni-Fe electrodeposits used in the present study. These electrodeposits are free of micro-twins [199]. In the case of as-produced Ni-20% Fe and Ni-45% Fe nanocrystalline electrodeposits, the x-ray diffraction revealed the presence of the  $\gamma$ -phase only. Even in Ni-45% Fe electrodeposits, as it has been reported [100]: the alloy existed as  $\gamma$ -phase even after annealing at 1173 K for 0.5 hr followed by slow cooling. The  $\gamma$ -phase is a solid solution of Fe in Ni and has fcc structure. Though the traces of  $\alpha$ -phase has been noticed in other occasions of annealing [100], the essential component of the studied alloy deposit is  $\gamma$ -phase.

Grain growth behavior in nanocrystalline electrodeposits is similar, though not the mobility conditions, to that of conventional polycrystalline bulk material. This is substantiated by

the observation [103] of nuclei of abnormally growing grains even in the mid-section of nanocrystalline Ni foil.

As far as the texture information is concerned, a complete description of texture can be given in the form of orientation distribution function (ODF). The orientation distribution functions (ODFs) of as-electrodeposited Ni, Ni-20% Fe and Ni-45% Fe are given in Fig. 5.2. These ODFs clearly show that the deposits have typical fiber textures. All these nanocrystalline electrodeposits show a strong (100)-fiber and a weak (111)-fiber.

### 5.3.1. Cluster analysis

As shown previously by various researchers [12,92] both analytically [12] and using computer simulation [92] in conventional polycrystalline materials, an initial grain size advantage alone would not be sufficient to give a grain with a particular orientation the ability to grow abnormally. For successful abnormal grain growth, there should be a mobility condition, which allows only a particular type of grain boundaries, to move faster than the other grain boundaries. The fraction of grain boundaries [182,183] with high mobility at the periphery of the growing grain is as important as the mobility parameter. The higher the difference between the fractions of high mobility boundaries between the growing grain and other grains in the matrix, the higher is the probability that this grain grows abnormally. Similarly, the higher the mobility of the grain boundary surrounding the growing grain, the higher is the probability for abnormal grain growth.

As given earlier, various authors [98,103] proposed that in the annealing of nanocrystalline materials the sub-grain coalescence initiates the abnormal grain growth. In order to understand the influence of grain coalescence in the present study, cluster analysis is made using the information about texture. In accordance with the measured ODFs, by assuming an equiaxed grain structure and a random correlation between each grain in the matrix, orientation of each grain in a computer specimen can be assigned using an algorithm developed by Morawiec *et al.* [118]. For this cluster analysis, a computer specimen having 3D-honeycomb grain structure [15] with 12 nearest neighbors is created. In this case, each

lattice site of the computer specimen described in section § 2.7.3 is assumed to be a grain.

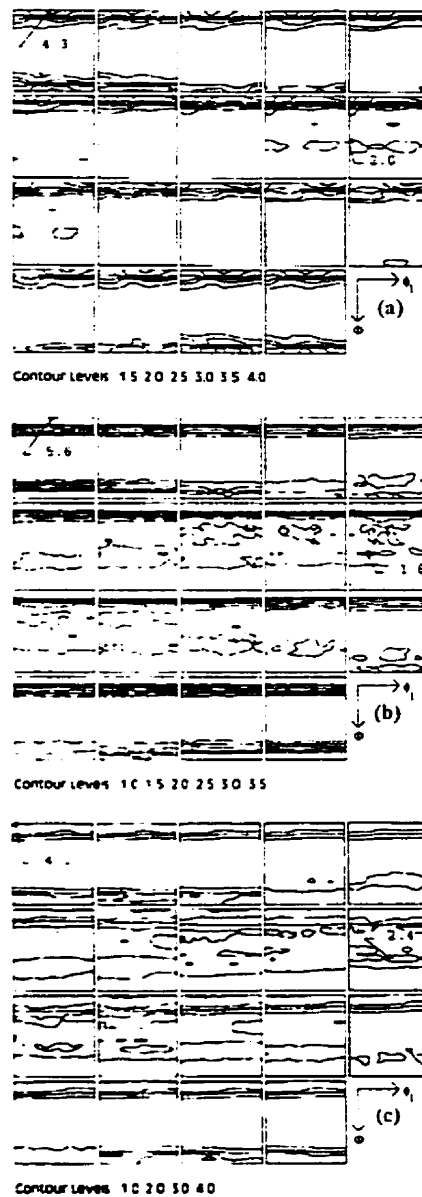


Fig.5.2 Orientation distribution function (ODF) of as electrodeposited nanocrystalline (a) Ni, (b) Ni-20% Fe and (c) Ni-45% Fe

These grains are then assigned grain orientation in accordance with the experimentally observed ODF by assuming random correlation between neighboring grains [118]. Using the computer specimen with 100674 grains, the number of clusters with the deviations in grain orientation of 5°, 10°, and 15° have been calculated and presented for Ni-45% Fe nanocrystalline electrodeposit in the Table 5.1. These values represent the average values of 10 such computations. In the calculation (100) fiber orientation is identified as the orientation that corresponds to  $\phi_1=0^\circ-90^\circ$ ,  $\Phi=0^\circ$  and  $\phi_2=0^\circ$  and their symmetrical orientations. Similarly, for the case of (111)-fibers, the Euler angles are  $\phi_1=0^\circ-90^\circ$ ,  $\Phi=54.7^\circ$  and  $\phi_2=45^\circ$ . This analysis is expected to yield the difference between the number of clusters of (100) and (111)-fibers under the assumption of random correlation of grain orientation among the neighboring grains.

**Table 5.1. Computed number of clusters with angular deviation of 0°-5°, 0°-10° and 0°-15° and various cluster sizes for Ni-45% Fe. Average number of clusters computed from 10 different computer specimens is presented here. Each computer specimen has a total of 100674 grains.**

Cluster size (in number of grains)	Number of clusters					
	Fiber-(100) angular deviation from fiber orientation			Fiber-(111) angular deviation from fiber orientation		
	<5 deg	<10 deg	<15 deg	<5 deg	<10 deg	<15 deg
2	27.9	266.3	561.8	10.0	134.9	369.1
3	0.2	3.6	3.4	0.1	2.1	3.6
4	0.0	0.0	0.1	0.0	0.0	0.0
Number of Single grains	4073.2	14456.7	28151.7	2391.2	8832.9	18388.8
Total number of fiber grains	4129.6	15000.1	29285.9	2411.5	9109.0	19138.4

As these values are calculated based on the ODF of as-electrodeposited specimen, the clusters of (100) fiber are comparatively larger than the clusters of (111)-fiber. Similar results are obtained for Ni-25% Fe and for Ni nanocrystalline electrodeposits; however these results are not discussed here. In principle, the results obtained by this cluster analysis would favor the growth of (100)-fiber over the (111)-fiber and is in contradiction with the experimental observation that demonstrates that (111)-fiber grows more rapidly during annealing. Even if the coalescence does promote the formation of nucleus of (111)-fiber grains in the matrix, the abnormal growth can be achieved only by applying special mobility criteria and assuming favorable mobile boundary fractions depending on the grain misorientation distribution function. The calculation of misorientation distribution function is presented in the following section § 5.2.2.

### 5.3.2. Grain misorientation distribution analysis

Measuring grain boundary misorientation distribution in nanocrystalline material is practically not possible at present. However, by using the algorithm developed by Morawiec *et al.* [118], one can compute the grain misorientation distribution function (GMDF) between the selected grain orientation and other grain orientations in the matrix. This calculation is carried out by finding out the misorientation between the selected grain orientation and a randomly created orientation of grain that is selected in accordance with the measured ODF. This procedure is repeated  $10^5$  times in order to minimize the statistical error. The grain misorientation distribution function (GMDF) of a fiber orientation is computed by repeating the same procedure for each orientation in the fiber component and by averaging the obtained results. The GMDF of the average texture component is computed by calculating the misorientation between a pair of grain orientations generated in accordance with the ODF. The Fig. 5.3 shows the grain misorientation distribution function (GMDF) for Ni-45% Fe, Ni-20% Fe and pure Ni nanocrystalline electrodeposits. The grain boundary fraction values in these graphs are shown as curves instead of histograms, merely to follow the peak values clearly and to avoid confusion while comparing the fractions. In all these plots, it is clearly indicated that the grains representing (111)-fibers have a characteristic distribution in which the

percentage of grain boundaries with misorientation of  $45^{\circ}$ - $63^{\circ}$  is higher than for the (100)-fiber texture and the average texture component. As it is now known, the grain growth and texture development is the result of the anisotropic grain boundary mobility and causes the abnormal grain growth and texture change in the matrix. It becomes important to analyze in detail the differences in the GMDF of (111) and (100)-fiber components. For that purpose, the results of the grain misorientation analysis for all the three nanocrystalline electrodeposits are given in Table 5.2. In conventional polycrystalline materials,  $15^{\circ}$ - $45^{\circ}$  misorientation represents the highest energy and the most random grain boundary region. In order to distinguish the random boundaries from other boundaries, hereafter the middle-misoriented boundaries will be called MM-type boundaries and others i.e., low ( $< 15^{\circ}$ ) and high misoriented ( $> 45^{\circ}$ ) boundaries will be called LH-type boundaries. Such classification may be considered rather unusual at first, but it reflects differences in grain boundary energy and it is necessary to explain the differences in mobility of grain boundaries in nanocrystalline materials. In each electrodeposit, as shown in the Table 5.2, it is evident that the (111)-fiber component has nearly 15-20% more of the LH-type boundaries than the (100)-fiber components. The fractions of LH-type boundaries in the average texture component have intermediate values between (111)-fiber and (100)-fiber components. Among the three alloys Ni-45% Fe and Ni-20% Fe have values 0.57 and 0.586 respectively which are higher than in the pure Ni which has LH-type fraction of 0.535. As the nucleus for the abnormally growing grain comes from the similarly oriented grains in the matrix prior to the annealing, it is important to study the difference in the intensities of the fiber orientation in the electrodeposited matrices. The Table 5.2 gives the ODF intensity for both (100) and (111) fibers as observed in electrodeposited Ni and Ni-Fe alloys prior to the annealing treatment. In here, Ni-45% Fe and pure Ni have intensities of 2.5 and 2.8 respectively for (111)-fiber component, whereas, Ni-20% Fe has an intensity of 1.6. The intensity of (100)-fiber component in Ni-45% Fe is the lowest among the nanocrystalline electrodeposits analyzed in this study. The Ni-20% Fe and pure Ni electrodeposits have the intensity of 5.71 and 4.9 respectively. From this analysis it is clear that the fraction of LH-type boundaries is much higher than the MM-type boundaries in all these alloys around (111)-fiber components.

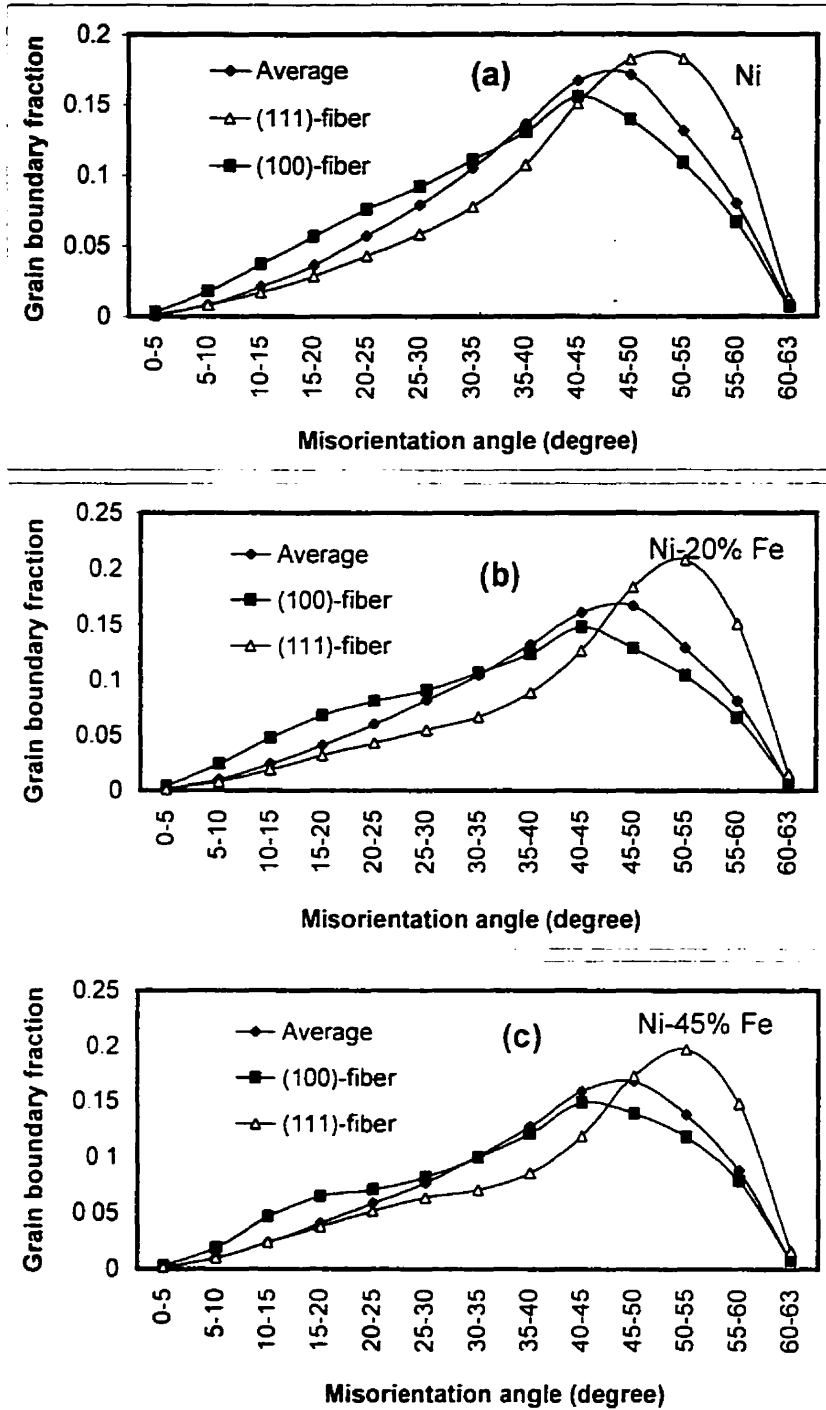


**Fig.5.3** Misorientation distribution calculated based on the as-electrodeposited nanocrystalline Ni, Ni-20%Fe and Ni-45%Fe textural information. (Here curves are drawn only as a visual aid to follow the data points unambiguously)

**Table 5.2. Comparison of fiber intensity and fraction of grain boundaries in Ni, Ni-20%Fe and Ni-45%Fe nanocrystalline electrodeposits**

	Ni-45%Fe	Ni-20%Fe	Ni
<b>ODF Intensity of the fiber components</b>			
(100)-fiber	3.590	5.710	4.880
(111)-fiber	2.510	1.630	2.880
Ratio (111)/(100)	0.699	0.285	0.590
<b>Fraction of LH-type grain boundaries</b>			
(100)-fiber	0.413	0.382	0.379
(111)-fiber	0.57	0.586	0.535
<b>Fraction of MM-type grain boundaries</b>			
(100)-fiber	0.588	0.619	0.62
(111)-fiber	0.43	0.413	0.466

\* MM-type is 15°-45° misoriented boundaries and LH-type is remaining low and high misoriented boundaries

There is no evidence that the CSL boundaries in nanocrystalline materials exist. However in conventional polycrystalline materials, there has been a belief among the researchers [64,66,68,145] that certain "special" boundaries namely coincidence site lattice (CSL) boundaries might play a significant role in grain growth in metallic materials. Thus, the grain misorientation analysis is incomplete without a discussion on CSL boundary distribution and its possible effect on grain growth in the Ni and Ni-Fe nanocrystalline electrodeposits. By using the same algorithm developed by Morawiec *et al.* [118], the CSL boundary distribution is computed and presented in Fig. 5.4, in the form of histograms. The CSL boundary is defined by comparing the quaternion of the grain misorientation with that of CSL using the Brandon criterion [47], which allows  $15/\Sigma^{1/2}$  degree of deviation from the ideal position. The percentage fractions of CSL boundaries are given for (111), (100)-fibers and the average texture component for individual categories from  $\Sigma 1$  to  $\Sigma 19b$  and then for categories of  $\Sigma 21-29$ ,  $\Sigma 31-39$  and  $\Sigma 41-49$ . Here also,  $10^5$  boundaries were analyzed in order to minimize the statistical error. As far as the CSL distributions are concerned, only about 18 to 23% of the boundaries are special boundaries in all the three electrodeposits. In all histograms (Fig. 5.4), it can be seen that  $\Sigma 1$  and  $\Sigma 3$  have the highest frequency for (100)-fiber and (111)-fiber respectively. Except  $\Sigma 1$  and  $\Sigma 3$ , all other  $\Sigma$

boundaries have a percentage fraction which is less than 2%. In the majority of the cases % fraction is often <1%. The boundaries above  $\Sigma 11$  in all the nanocrystalline electrodeposits have frequency <1% and these are approximately the same for (100) and (111)-fiber and the average texture component in Ni, Ni-20% Fe and Ni- 45% Fe nanocrystalline electrodeposits. According to our previous research [182,183], the fraction of high mobility boundaries should be higher than 30% for an orientation that can grow abnormally. Even the assumption that all the CSL boundaries have high mobility cannot be responsible for the abnormal growth of (111)-fiber for two reasons. The first reason is that the overall difference in percentage fraction of CSL boundaries around the (100) and (111)-fiber grains is too small (only 3%). The second reason is that the overall percentages of CSL boundaries for (111)-fiber in all these cases are too small (not more than 20%). It is important to note that under the non-equilibrium conditions CSL boundaries may not possess the same characteristics as in the case of conventional polycrystalline materials. By considering all these points, it can be concluded that the role that would be expected by the CSL boundaries to play in the abnormal growth of (111)-fiber texture component is insignificant.

Contrary to the CSL boundary distributions, the distribution of general boundaries around both texture fibers is different. The percentage of LH-type boundaries around the (111)-fiber is approximately 15-20% higher around the (100)-fiber in all the electrodeposits considered in the present study. The total fraction of LH-type boundary around (111)-fiber is about 53-59%. Having analyzed the GMDFs of (111) and (100)-fiber, energy and mobility associated with relevant groups of grain boundaries have to be analyzed to understand the mechanism of grain growth and texture development.

### *5.3.3. Grain boundary energy and mobility in nanocrystalline Ni and Ni-Fe*

According to Wolf and his co-researchers [195,196], grain boundary in nanocrystalline materials is amorphous (non-equilibrium state) and the energy of grain boundaries changes very little. Such a statement may be controversial and some researchers may not

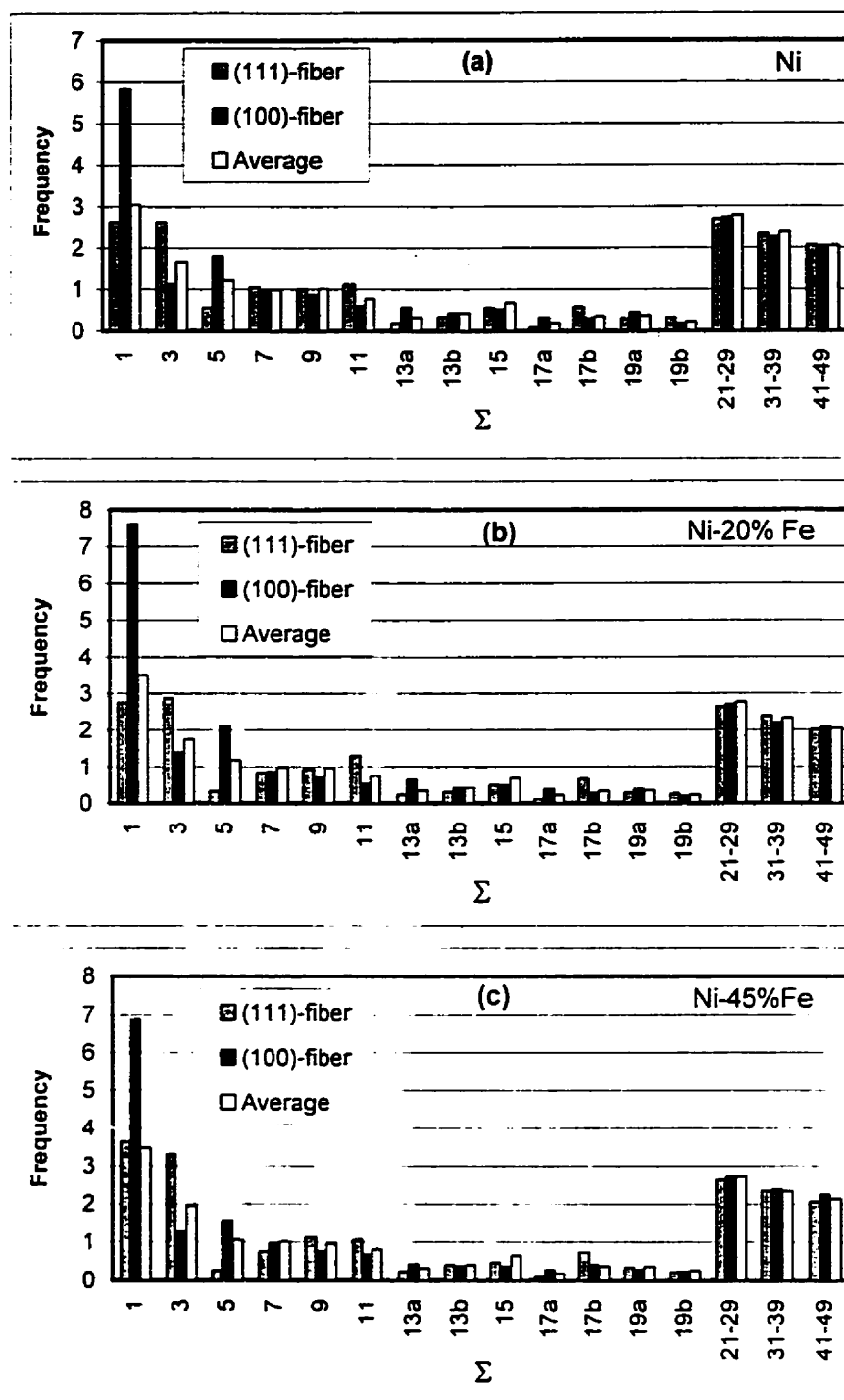


Fig.5.4 CSL distribution calculated based on the as-electrodeposited nanocrystalline Ni, Ni-20%Fe and Ni-45%Fe textural information.

agree with it. However, the model presented in this is based on the assumption that in nanocrystalline materials the relative boundary energy ( $E_{\text{nano}}$ ) does not change much with grain misorientation. We argue that energy is stored in short segments of grain boundaries and in a dense network of the grain boundary junctions that cannot relax irrespective of grain misorientation. Therefore,  $E_{\text{nano}}$  can be assumed constant for all misorientation angles. On the contrary, the conventional polycrystalline material has definite different grain boundary energy,  $E_{\text{micro}}$  for various grain misorientation angles. During annealing, the nanocrystalline material transforms to a more stable microcrystalline structure. The difference between the nanocrystalline and microcrystalline grain boundary energies can be assumed to be a measure of the deviation of a non-equilibrium grain boundary state from its equilibrium state as below:

$$\Delta E_{\text{dev}} = E_{\text{nano}} - E_{\text{micro}} \quad (5.1)$$

Hereafter,  $\Delta E_{\text{dev}}$  will be referred to as "grain boundary energy deviation parameter". From the early research by Valiev *et al.* [200,201] non-equilibrium grain boundary structure, as observed in deformed metals, results in high mobility. By assuming a model based on this finding we concluded that the LH-type boundaries in nanocrystalline materials would have experienced higher mobility than the MM-type boundaries. The grain surrounded by this type of boundaries will start growing first because they are more deviated from the equilibrium state. During this process the length of the grain boundary segments will increase and therefore, energy of the grain boundaries will lower and will approach that of the equilibrium state. This condition is expected to favor the growth of (111)-fiber in the Ni-45% Fe, Ni-20% Fe and pure Ni electrodeposits because the probability of encountering the grains that form LH-type misorientation is higher for (111)-fiber orientation than for the other orientations.

To have a quantitative description of mobility parameter, one has to know the deviation of nanocrystalline grain boundary energy from the corresponding conventional polycrystalline grain boundary energy. The equilibrium grain boundary energy i.e., conventional

microcrystalline grain boundary energy can be obtained from experimental or computed data. Though there are some experimental works on conventional microcrystalline or bicrystalline grain boundary energy, and data is available for some common engineering metals such as Fe-Si [52] and Al [140], there is, to our knowledge, no satisfactory experimental work on grain boundary energy on Ni or Ni-Fe alloys. There are few computational works on grain boundary energy of fcc metals by Wolf *et al.* [202-204]. The Lennard-Jones potential [205] used for molecular dynamics calculations for Fe, Cu and Ni are similar. Thus, the shape of the tilt grain boundary energy plot as a function of tilt angle for various tilt boundaries would be more or less the same for Cu and Ni and Ni-Fe alloys because they all have fcc crystal structure. Under this assumption, the "relative" boundary energy calculated from the molecular dynamics computations by Wolf *et al.* [202] for tilt boundaries of copper is assumed for Ni and fcc Ni-Fe alloys. The Figs. 5 (a), (b), (c) and (d) give the relative energies of  $\langle 001 \rangle$ ,  $\langle 011 \rangle$ ,  $\langle 111 \rangle$  and  $\langle 112 \rangle$  tilt boundaries respectively. The Fig. 5.5 (e) gives the curve of average relative boundary energy drawn for various misorientation angles through the points collected from all the tilt boundary energy curves. The Fig. 5.5 (e) has been partitioned into three regions based on grain boundary misorientation and these regions are for the angles  $<15^\circ$ ,  $15^\circ-45^\circ$  and  $>45^\circ$  respectively. In the first region, for misorientation angle  $\theta < 15^\circ$ , the obtained conventional grain boundary energy data is fitted with a Read-Schockley [44] equation and for the other two regions is fitted with straight lines for simplicity. This kind of simplified grain boundary energy as a function of grain misorientation is justified because the energy values that correspond to the CSL boundaries are not very different from the others, except  $\Sigma 1$  and  $\Sigma 3$ . This is taken care of in the simplified grain boundary energy function presented in Fig. 5.5 (e). One should also note that this grain boundary energy function would simplify the already complex computer program and reduce the time of calculation.

Having assumed the equilibrium relative grain boundary energy  $E_{\text{micro}}(\theta)$ , we may assume that a non-equilibrium relative energy  $E_{\text{nano}}(\theta)$  is 1. The parameter, which measures the deviation of nanocrystalline grain boundary from the equilibrium state,  $\Delta E_{\text{dev}}$  is shown in Fig. 5.6. The grain boundaries having misorientation less than  $5^\circ$  are not considered in this

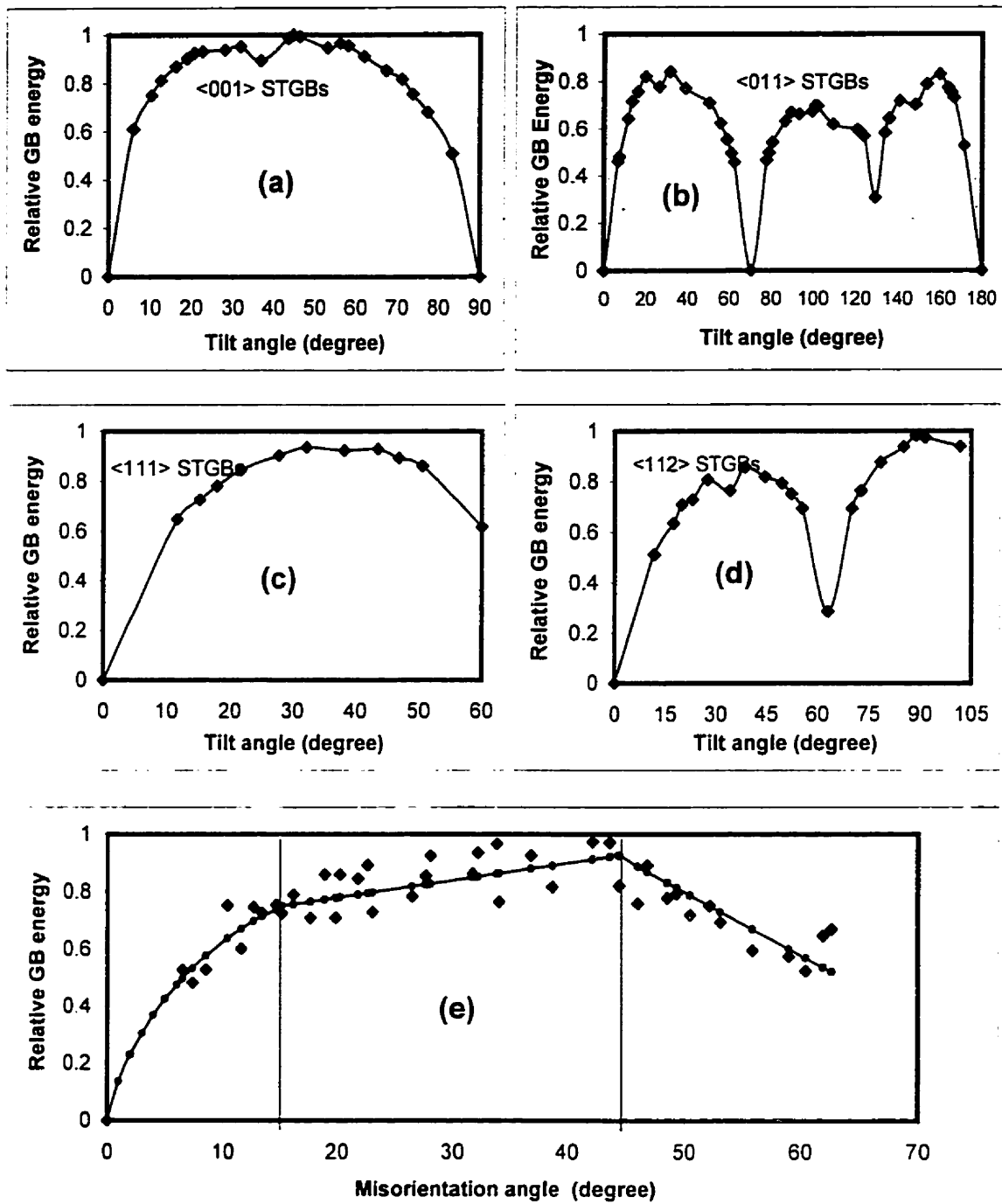
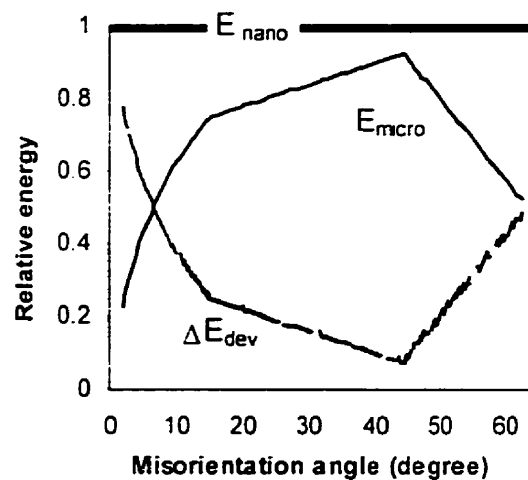


Fig.5.5 (a),(b),(c) and (d) are the calculated grain boundary energies of symmetrical tilt boundaries for Cu [202]. (e) Calculated average relative grain boundary energy as a function of misorientation angle

calculation. They have less than 1% probability of being present in all cases investigated and in addition the value of energy these boundaries would have in nanocrystalline materials is hard to estimate. From the Fig. 5.6, it is evident that the deviation of MM-type boundaries in nanocrystalline materials from equilibrium structure observed in conventional polycrystalline materials is much lower than the LH-type boundaries. Thus, the LH-type boundaries have higher mobility than MM-type boundaries because the deviations from equilibrium structure is higher for LH-type boundaries than MM-type boundaries.



**Fig.5.6** Grain boundary energy deviation parameter as a function of misorientation from assumed nanocrystalline and theoretical microcrystalline grain boundary energies

Having analyzed the importance of LH-type boundaries in controlling grain growth in nanocrystalline materials, the grain misorientation in electroplated nanocrystalline materials will be analyzed and probability of finding a LH-type boundary around various crystal orientations will be calculated. The Figs. 7 (a), (b) and (c) show the plot of probability of finding LH-type boundaries for pure Ni, Ni-20% Fe and Ni-45% Fe nanocrystalline electrodeposits. These figures show the contours of the iso-probability in the Euler angle space. Only the  $\phi_2 = 45^\circ$  section are presented. It is evident that, the (111)-fiber has the

highest probability of 54 to 58 % of LH-type boundaries, higher than any other orientation. Another interesting observation is that the (100)-fiber component has the lowest probability, which ranges from 37 to 43 %. That means that the (111)-fiber texture is well-positioned to grow during the annealing process.

#### 5.4. MODEL FOR ANNEALING OF Ni AND Ni-Fe ELECTRODEPOSITS

For a polycrystalline material to experience abnormal grain growth, normal grain growth has to be hindered by pinning forces such as precipitates, solute, etc. In the classical case of Fe-Si steels, abnormal grain growth is favored only when the normally growing grains are pinned by precipitates during primary recrystallization at around 800°C [1,179]. When the pinned grains in the matrix of Fe-Si are further annealed at high temperature around 1000°C [179], the selective unpinning of certain grain boundaries take place, thereby activating a particular orientation to grow faster than the others [152,206]. As a result, completely new texture and grain structure is formed.

In the case of fully dense Ni, Ni-Fe alloy electrodeposits at the ambient temperature, even though the matrix has sufficient driving force for grain growth, due to the pinning forces grain growth is not observed. The pinning force could be offered by triple junction, vertices, excess vacancies, impurity atoms [103], and metastability of microstructural features such as grain boundaries. At 673 K, some grains start growing abnormally and the growth of (111)-fiber texture is strongly favored because the grain boundaries that surround this fiber component are highly deviated from their equilibrium state.

##### 5.4.1. Mechanism for abnormal grain growth in nanocrystalline Ni and Ni-Fe electrodeposits

Based on the analysis made in the previous sections, a simple model for the abnormal grain growth and (111)-fiber texture development in studied nanocrystalline materials can be formulated. Here, it can be assumed that all the grain boundaries at the beginning of the

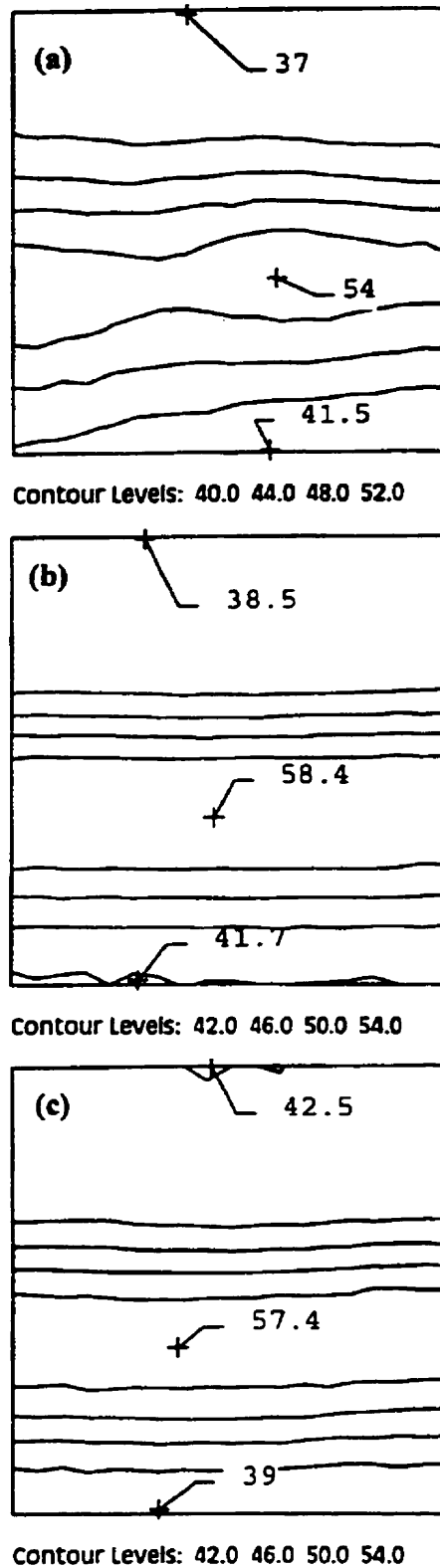


Fig.5.7 Probability of boundaries of LH-type around grains of various orientations for (a) Ni, (b) Ni-20% Fe and (c) Ni-45% Fe nanocrystalline electrodeposits. The probability is presented for  $\phi_2 = 45^\circ$  section

annealing process are pinned by point defects such as impurity atoms and inherent resistance offered by structural factors such as triple junctions and vertices. It is assumed that the rate of unpinning of the grain boundaries is decided by the amount of deviation of the nanocrystalline grain boundaries from their equilibrium microcrystalline counterparts. This assumption can be supported by the argument that high deviation of grain boundary energy in nanocrystalline materials from the corresponding microcrystalline structure would result in high driving force sufficient to overcome the pinning forces at the early stage of annealing. As these boundaries are expected also to have high mobility because of their deviation from equilibrium structure, they are expected to move faster at the early stages of annealing. Taking these assumptions into account, it is possible to conclude that the boundary having a higher grain boundary deviation parameter i.e.,  $\Delta E_{dev}$  than a certain critical value  $\Delta E_c$ , can move. Let the probability of finding a grain boundary around a grain of arbitrary orientation  $S$ , that has a value of  $\Delta E_{dev}$  higher than  $\Delta E_c$ , be denoted as  $P(S, \Delta E_{dev} > \Delta E_c)$ . This probability value represents the existence of mobile boundaries around the orientation  $S$ . By comparing such probability of orientation  $S$  and the average orientation, a measure of growth advantage,  $\Delta P(S)$  of orientation  $S$  can be defined as below:

$$\Delta P(S) = P(S, \Delta E_{dev} > \Delta E_c) - P(average, \Delta E_{dev} > \Delta E_c) \quad (5.2)$$

At the early stages of annealing, when the value of  $\Delta E_c$  is high, only a very small number of boundaries have high mobility. As the annealing progresses further,  $\Delta E_c$  is decreased. The decrease in the value  $\Delta E_c$  marks the release of more and more boundaries that have been pinned earlier. Physically this can be attributed to the step-by-step restructuring of grain boundaries towards their microcrystalline equilibrium state as the grains grow. Theoretically, this trend should continue till the grain boundaries reach their equilibrium states. The grain boundary equilibrium structure is attained when the grain structure becomes microcrystalline.

In conclusion, the proposed model is based on the deviation of energy of nanocrystalline grain boundaries from their microcrystalline counterparts and it takes into account the controlled unpinning of these boundaries during annealing. The proposed assumption cannot be fully justified by experiments, because such experiments cannot be done at present. However, the model based on these assumption explains abnormal grain growth and the competition between (111)-fiber and (100)-fiber texture observed in Ni, Ni-20 Fe and Ni-45% Fe nanocrystalline electrodeposits. This model is tested using the Monte-Carlo simulation procedure. The following sections are devoted to the description of the Monte-Carlo procedures employed and to report the results obtained from the simulation.

### 5.5. MONTE-CARLO METHOD FOR ANNEALING OF NANOCRYSTALLINE Ni AND Ni-Fe ELECTRODEPOSITS

The framework of the Monte-Carlo simulation model used in this work has been described in the research work of Hinz and Szpunar [15]. The 3-dimensional computer specimen consists of nearly half a million sites with a 3-D honeycomb lattice structure [15]. The adjacent lattice sites are grouped into 1500 Voronoi grains with an orientation, which is assigned, according to the orientation distribution function (ODF) using the algorithm developed by Morawiec et al [118]. This algorithm assumes a random spatial correlation between the grains in the matrix. This simulation work has only one important parameter, namely the mobility of grain boundaries that is related to grain misorientation. As the nanocrystalline material is assumed to have isotropic grain boundary energy because of its disordered nature [195-196], the relative grain boundary energy in this simulation is assumed to be 1 for all the boundaries. Based on the previous analysis of CSL boundaries in these materials, no special importance is attached to CSL boundaries. The mobility of the boundary is assumed to depend on the energy deviation parameter ( $\Delta E_{dev}$ ) in the following way:

$$\text{Mobility} = 1, \text{ when } \Delta E_{dev} > \Delta E_c$$

$$\text{Mobility} = 0, \text{ when } \Delta E_{dev} < \Delta E_c \quad (5.3)$$

The conditions above imply that only those boundaries having energy deviation parameter higher than the critical value  $\Delta E_C$  can move and all other boundaries are assumed to have zero mobility. The critical energy deviation parameter ( $\Delta E_C$ ) decreases as the simulation progresses according to the following equation.

$$\Delta E_C = \Delta E_{max} \cdot MCS \cdot 10^{-5} / a \quad (5.4)$$

Here,  $\Delta E_{max}$  is the highest energy deviation parameter at the start of the simulation.  $MCS$  is the number of Monte-Carlo steps [15] and  $a$  is a coefficient that describes the rate of decrease of energy deviation parameter during the annealing process of the computer specimen. The equation (5.3) is similar to the one used for the Monte-Carlo simulation of abnormal growth of Goss grains in microcrystalline high-permeability steel by Hayakawa and Szpunar [153]. In their research, the equation relates the grain boundary energy to the time of annealing expressed as the number of  $MCS$ . However, in the present work, the  $\Delta E_{dev}$  parameter describes the deviation of a particular grain boundary in nanocrystalline material from the equilibrium state and is employed to estimate the mobility of the boundary.

Physically, this assumption can be interpreted as follows: the energy deviation parameter given in equation (5.1) qualitatively accounts for the amount of deviation of a particular grain boundary in nanocrystalline metastable state from the microcrystalline more stable state. The higher the deviation, the higher is the tendency for the boundary to be more mobile. Thermodynamically, the boundaries with high-energy deviation parameter would have a high driving force to reach their equilibrium state. This can be achieved only by grain growth. Thus, as the grains grow, the atoms in the grain boundary region arrange themselves towards a more stable state, thereby reducing their mobility. This explains the higher mobility of grain boundaries in nanocrystalline materials (even at relatively low temperatures) than in microcrystalline materials. Internal stability of the boundaries might come also from the presence of triple lines and vertices. Often, the presence of impurity atoms might restrict [101.102] the grain boundary migration in the nanocrystalline

materials. The equation (5.3) and (5.4) state that at any point in time (i.e., MCS) the boundaries, with the energy deviation parameter value above the critical value,  $\Delta E_C$ , are assumed to be mobile. This means that these boundaries have enough driving force (high energy deviation parameter) to overcome the resistance offered by the impurities, other intercrystalline defects or the combination of both. These boundaries would move while other boundaries remain pinned in the matrix. As the annealing progresses, the moving boundaries would restructure themselves step by step towards the corresponding boundaries in microcrystalline state. This can be attributed to the increase of the length of the grain boundary segment being considered. As the moving boundary approaches the equilibrium state, the energy deviation parameter and relative mobility would be reduced. Now, the other boundaries with lower values of energy deviation parameter would also have the relative mobility as high as those boundaries that moved first. Thus, as the annealing simulation proceeds, the boundaries with progressively lower  $\Delta E_{dev}$  would start to move. It can also be argued that in general the microcrystalline boundaries are less affected by impurities and intercrystalline defects, such as triple lines and vertices, than the nanocrystalline boundaries. The effect of intercrystalline defects on the movement of boundaries in the microcrystalline materials is probably small mainly due to the considerably small concentration of such defects. On the contrary, the small segments of grain boundaries observed in nanocrystalline materials may be sensitive to the presence of impurities and high concentration of other intercrystalline defects. As the grains grow, the concentration of triple junctions and vertices decreases, thereby allowing the boundaries with low energy deviation parameter to move as well. This trend continues until the grain boundaries reach their equilibrium state. The grain boundary equilibrium structure is reached when the nanocrystalline material is transferred into microcrystalline. Due to a number of constraining factors such as computation time and memory, the computer specimen employed in this work has only 1500 grains. The grain growth simulated using this procedure is restricted to the nanocrystalline region itself. Due to the coarseness and the usage of statistically small number of grains to calculate necessary texture information, the simulation results are taken only up to the stage where the total number of grains in the computer specimen is approximately 250.

The method of grain growth simulation is already discussed in the research work of Hinz and Szpunar [15]. During the simulation, sites are randomly selected from the total number of 506514 sites and flipped to one of the few possible neighboring orientations based on physical assumptions concerning the energy and mobility. The results are then compared with the experimental data and the similarities of the trends obtained are discussed.

#### 5.4.1 Parameters used for the simulation of annealing of nanocrystalline Ni and Ni-Fe electrodeposits

The simulation of annealing is carried out for three different cases, namely for Ni, Ni-20% Fe and Ni-45% Fe nanocrystalline electrodeposits. The experimentally measured orientation distribution functions (ODFs) of as-electrodeposited materials given in Fig. 5.2(a), (b) and (c) are used for assigning the orientations of the grains in the computer specimens.

A role of parameters  $a$  and  $\Delta E_{max}$  given in the equation (5.4) are first investigated. Various values are given for  $a$  at a constant  $\Delta E_{max}$  value and for the selected  $a$ , simulations are carried out for various  $\Delta E_{max}$  values. Because of high sharpness of the texture experimentally observed in Ni-45% Fe electrodeposits during annealing (refer Fig. 5.1), these tests are carried out for the Ni-45% Fe. The Fig. 5.8 shows the ratio of volumes of the largest to the average grain size as a function of Monte-Carlo steps ( $MCS$ ), for various  $a$  values for a constant value of  $\Delta E_{max} = 0.35$ . Among the curves presented here,  $a = 1$  has the maximum value of volume ratio of 58 for  $MCS$  of 24000 and the grain that has the largest volume has (111)-fiber orientation with a deviation of  $6.25^\circ$ . In Fig. 5.8 and 5.9, along with the values of  $a$  or  $\Delta E_{max}$  for each curve presented, the type of the fiber orientation and the degree of deviation from the fiber orientation are presented. The method of calculation of the degree of deviation from a fiber orientation is given in the following section. By keeping  $a = 1$ , the  $\Delta E_{max}$  values are changed and the grain growth curves are presented in Fig. 5.9. Among the values presented, the maximum value of the volume ratio of 120 is

obtained in the case where  $\Delta E_{max} = 0.37$  and the grain with the largest volume has a deviation of 5.45 from (111)-fiber, which is the smallest deviation among the curves presented. The parameters are  $a=1$  and  $\Delta E_{max} = 0.37$  have been selected for the simulation work. The same simulation parameter values are employed for the other two materials. Ni-20% Fe and pure Ni nanocrystalline electrodeposits. It has to be noted here that according to the classical theory of grain growth by Hillert [207], if this volume ratio is greater than 8, it can then be assumed that abnormal grain growth has occurred.

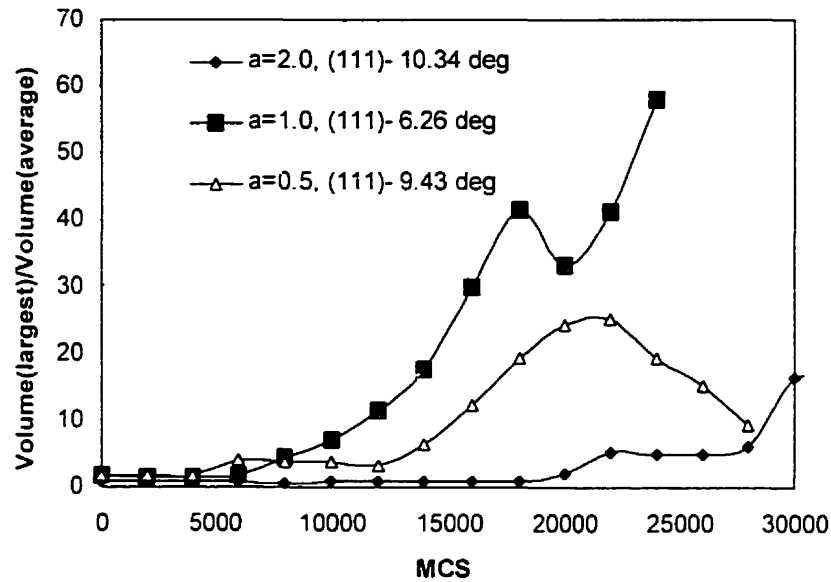
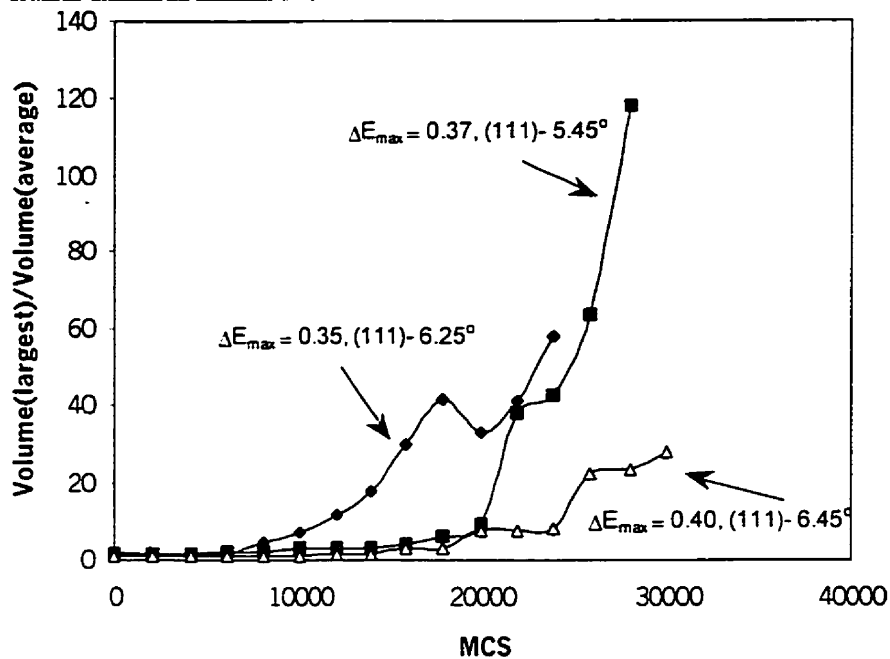


Fig.5.8 Growth kinetics of the largest grain observed in computer simulation for various  $a$  values in Ni-45% Fe nanocrystalline electrodeposit for constant  $\Delta E_{max} = 0.35$ . Along with  $a$  values, angle of deviation (in degree) from the (111)-fiber texture component is given for each curve.



**Fig.5.9** Growth kinetics of the largest grain observed in computer simulation for various  $\Delta E_{max}$  values in Ni-45% Fe nanocrystalline electrodeposit at constant  $\alpha=1$ . Along with  $\Delta E_{max}$  values, the angle of deviation (in degrees) from the (111)-fiber texture component is given for each curve.

## 5.6. RESULTS OF THE MONTE-CARLO SIMULATIONS OF ANNEALING OF NANOCRYSTALLINE Ni AND Ni-Fe ELECTRODEPOSITES

A series of simulations were carried out using the computer specimen describing the as-electrodeposited texture of Ni, Ni-20%Fe and Ni-45% Fe, which is depicted in Fig. 5.2. The results obtained are presented in two sections. The first section focuses on the microstructural features and the second part is devoted to the discussion of the texture transformation.

### 5.6.1. Simulation of microstructural transformation during annealing of nanocrystalline Ni and Ni-Fe electrodeposits

The compiled results of the simulation are shown in Fig. 5.10, where the grain volume ratio is represented as a function of  $MCS$ . The Fig. 5.10(a) shows that among the 5 simulations carried out using ODF of Ni nanocrystalline electrodeposits, 2 simulations resulted in an abnormal growth of grains with the volume ratios exceeding 125. The initial microstructure and microtexture of the computer specimen employed for these simulations seem to accommodate the nuclei with the potential for such an abnormal growth. Other simulations show growth of grains with maximum grain volume ratio equal to 25. Then the grains that grew start to decrease in size. This is mainly due to the competition in growth between various other grains in the matrix. Among the abnormally growing grains, one grain has the orientation of (111)-fiber and the other has the orientation of (100)-fiber. In Fig. 5.10 the degree of deviation of an abnormally growing grain from ideal fiber orientation is presented. To calculate the degree of deviation of a grain from the (111)-fiber, the misorientation angles are computed between the orientations of the grain and the orientations that represent the (111)-fiber, namely,  $\phi_1 = 0^\circ-90^\circ$ ,  $\Phi = 54.7^\circ$  and  $\phi_2 = 45^\circ$ . Among the misorientation angles calculated, the minimum angle is taken as the degree of deviation from the (111)-fiber. Grain misorientation angle, which is defined as the lowest among the 24 equivalent angles and rotation axes, is calculated by using the unit quaternion [162]. Similarly, the degree of deviation of a grain from the (100)-fiber orientation is computed. The orientations that represent the (100)-fiber are  $\phi_1 = 0^\circ-90^\circ$ ,  $\Phi = 0^\circ$  and  $\phi_2 = 45^\circ$ .

In the case of Ni nanocrystalline electrodeposits shown in Fig. 5.10(a), the angle of deviation of abnormally growing grains having a volume ratio exceeding 125 are  $3.5^\circ$  from the (111)-fiber and  $5.7^\circ$  from (100)-fiber orientation. Among the 5 simulations, 3 of them show the largest grain is close to the (100)-fiber while in the 2 other simulations, the (111)-

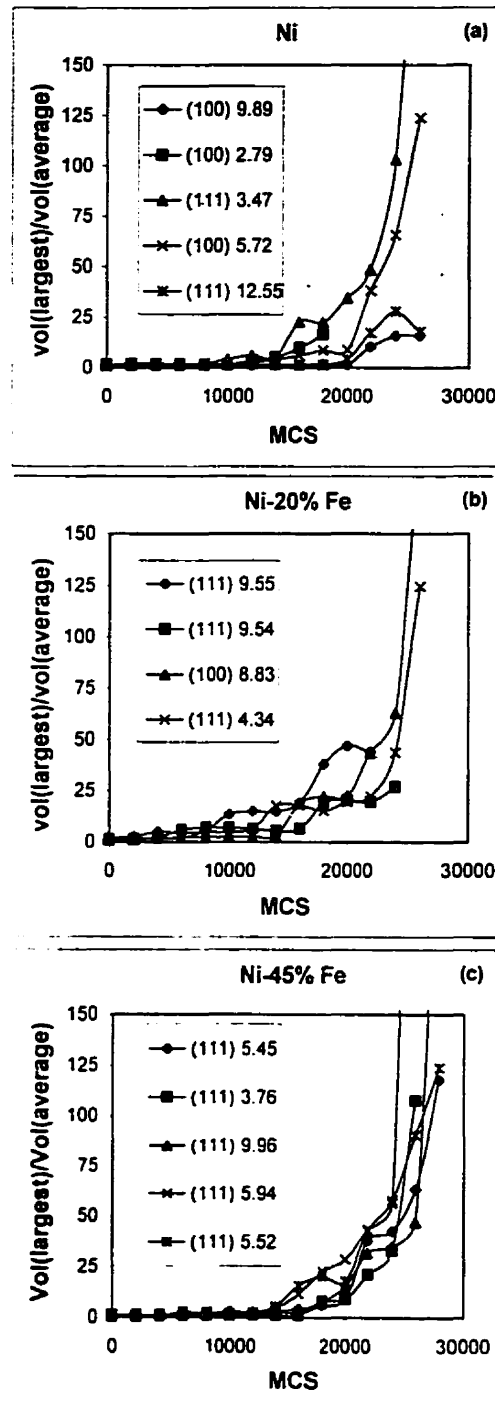


Fig. 5.10 Growth kinetics of the largest grains observed in various simulations having initial texture of as-electrodeposited (a) Ni, (b) Ni-20% Fe and (c) Ni-45% Fe. Each curve corresponds to a type of fiber texture and angle of deviation (in degrees) from that fiber orientation.

fiber grains are the largest. In Ni-20% Fe, among the simulation results presented in Fig. 5.10 (b), two cases of abnormal growth are observed. In this case, 3 out of the 4 simulations performed show the (111)-fiber grains as the largest grains in the microstructure. The remaining simulation has the (100)-fiber grain as its largest grain. In all of the cases, the grain volume ratio is more than 25. In Ni-45% Fe case, all the computer simulations result in an abnormal growth of the (111)-fiber grain with a grain volume ratio equal to or greater than 125. From these results, it is clear that in all three cases, simulation of abnormal grain growth gives results that agree with the experiments [100,103]. Theoretically, in all the cases, both (111) and (100)-fiber grains should grow abnormally to eliminate the metastable nanocrystalline microstructure with a strong preferential growth of (111)-fiber. As the Fe content increases, the tendency for the (111)-fiber grain to grow abnormally is higher as it can be observed from Fig. 5.10. In the pure Ni nanocrystalline electrodeposits, the 2 out of 5 simulations show (111)-fiber grains as the largest grains. In the remaining 3 simulations the growth of (100)-fiber grains is observed, whereas, in Ni-20% Fe nanocrystalline electrodeposits, (111)-fiber grains grow in 3 out of 4 simulations. In the Ni-45% Fe case, all the 5 simulations produce similar grain structure, where (111)-fiber grains are the largest.

#### *5.6.2. Simulated textural transformation during annealing of nanocrystalline Ni and Ni-Fe electrodeposits*

To obtain a clear picture of the texture transformation observed in these simulations, the textures in the resulting computer specimen can be analyzed. The results are presented as the plots of fiber intensities as a function of MCS and are given in Fig. 5.11 (a), (b) and (c). These fiber intensities of pole figures are calculated from the ODFs obtained from the simulation. To facilitate a comparison between the materials investigated, the experimental results are also presented in Fig. 5.11. The experimental observation recorded for annealing of these specimens at 673 K are given in Fig. 5.11 (d), (e) and (f). Each of the computer specimens has only 1500 grains at the beginning of the simulation. For the texture analysis, the simulation results are taken only up to the stage, where the remaining number of grains

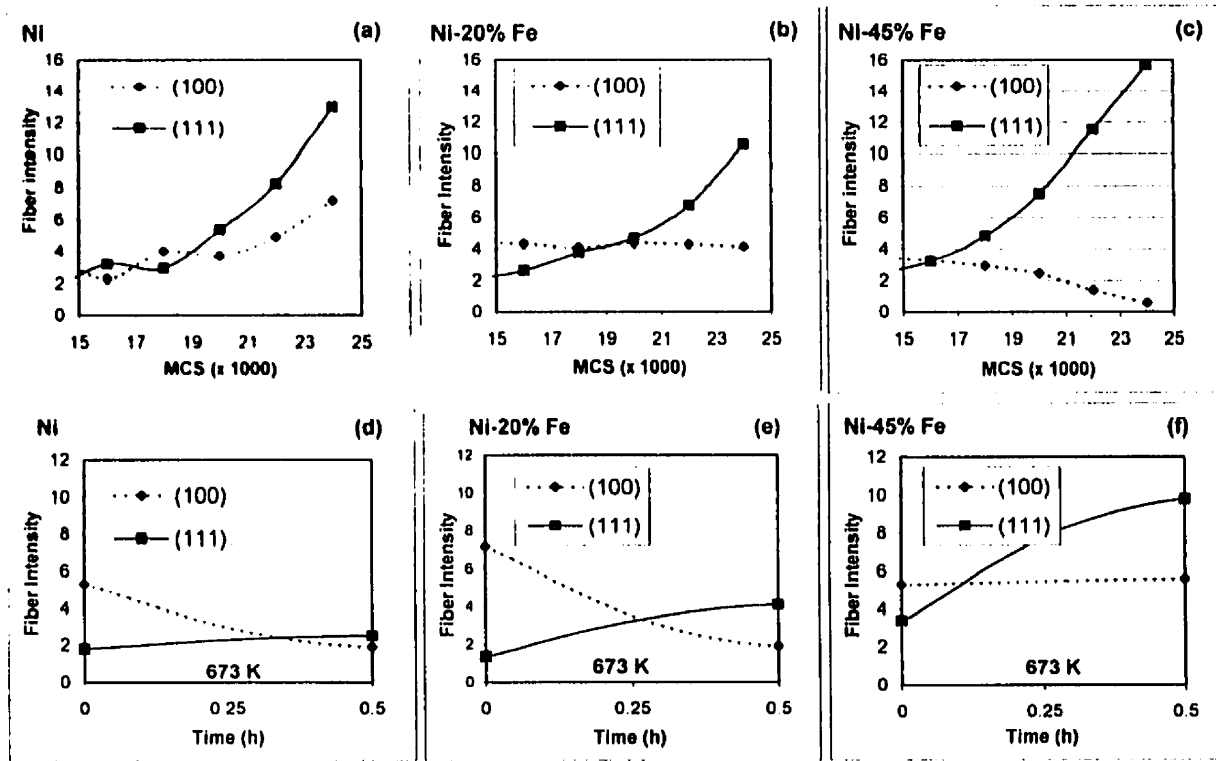


Fig.5.11 Comparison of changes in simulated {(a), (b) & (c)} and experimental {(d), (e) & (f)} pole figure fiber intensities during annealing (673 K) of Ni, Ni-20% Fe and Ni-45% Fe respectively.

in the computer specimen is around 250. Thus, the grains in the model simulation are well within the nanometer size range and the results obtained can only be used to explain the initial state of the annealing process. At the end of each simulation, the remaining number of grains is too small to provide accurate information about texture. On the other hand, these simulations can be used to compare general trends observed during the annealing experiments of nanocrystalline electrodeposits. In all these plots, the maximum pole figure intensities of the (111) and (100) fibers are shown as a function of annealing time. Observation of the simulation results shows that below 15000 MCS, no considerable textural change happens. However, beyond 15000 MCS, there is considerable texture transformation, which also coincides with the abnormal growth of the fiber grains. Therefore, to verify the model proposed in this work, the texture transformation trend in all these cases is studied by comparing the intensities beyond 15000 MCS. In all these electrodeposits, intensity of (111)-fiber increases as a function of annealing time. In nanocrystalline Ni electrodeposit case, intensity of (111)-fiber increases rapidly, however the intensity of (100)-fiber also increases. In the case of Ni-20% Fe, (111)-fiber intensity increases, whereas, the intensity of (100)-fiber does not show any change as a function of time. Contrary to this, in Ni-45% Fe electrodeposit, as MCS increases, (111)-fiber intensity also increases rapidly, however the (100)-fiber intensity decreases. Therefore the trend is similar to the one observed in experiments {refer to Fig. 5.11 (d), (e) and (f)}. In Fig. 1, it is clear that for Ni-45% Fe case, the intensity of (111)-fiber increases much more rapidly than (100)-fiber, when compared to other Ni-20% Fe and Ni electrodeposits. Among Ni-20% Fe and Ni electrodeposits, Ni-20% Fe shows faster growth of (111)-fiber than Ni electrodeposits. As computer specimen has only few grains (1500 in the beginning of Monte-Carlo simulation and around 250 at the end), when compared to real specimen, one may not compare the exact intensities obtained from experiments and simulation. However, the trend that is observed in intensities and relative growth of (111) and (100) fiber are very important.

From the simulation results, it is evident that general trends observed using the proposed model agree with the experimental observation. In all these electrodeposits, the (111)-fiber

intensity grows faster than the (100)-fiber. An increase in the Fe concentration increases the (111)-fiber intensity during annealing.

### 5.7. SUMMARY

Grain misorientation analysis of the electrodeposited Ni, Ni-20% Fe and Ni-45% Fe nanocrystalline matrix indicates that (111)-fiber grains are surrounded by the highest number of grain boundaries that are highly deviated from the corresponding microcrystalline equilibrium structure. Assuming that all the grain boundaries in nanocrystalline materials have non-equilibrium structure and the grain boundary energy is isotropic, the deviation of energy of LH-type boundaries (with misorientation  $<15^\circ$  and  $>45^\circ$ ) from their corresponding microcrystalline equilibrium structure is established. This deviation is considered responsible for the migration of nanocrystalline boundaries in the initial stage of annealing.

Based on the analysis of texture transformation, a model is proposed to explain the competition between (111)-fiber and (100)-fiber texture observed in Ni, Ni-20% Fe and Ni-45% Fe nanocrystalline electrodeposits. This model stresses the importance of the deviation of the energy of nanocrystalline grain boundaries from their microcrystalline counterparts and it takes into account the controlled unpinning of these boundaries during annealing.

The proposed model has been verified using the Monte-Carlo simulation and the results obtained are in general agreement with the experimental observation. The model predicts that the (111)-fiber orientation should grow. It also predicts that at higher Fe content the (111)-texture is stronger than (100)-fiber texture. The model also predicts the abnormal grain growth of nanocrystalline grains during annealing.

## Chapter 6

### SUMMARY AND CONCLUSIONS

The main goal of this thesis is to develop computer procedures to simulate various annealing processes and propose suitable models of texture and microstructure transformation during annealing. To achieve this goal, three different computer models were proposed for three diversified annealing processes, namely 1) primary recrystallization, 2) abnormal grain growth and 3) thermal stability of nanocrystalline electrodeposits. A well-known metallurgical system in each category is analyzed. The cube texture development upon annealing of heavily deformed aluminum is studied using the computer simulation of primary recrystallization. For the abnormal grain growth, the Goss texture development in Fe-3%Si conventional electrical steel is studied including the effect of Ostwald ripening of MnS precipitates on the grain boundary migration. Finally, the proposed model for the annealing behavior of the state-of-the-art nanocrystalline Ni and Ni-Fe electrodeposits is tested using the Monte-Carlo methods and the texture competition between (111) and (100)-fibers is explained.

## 6.1. CONCLUSIONS

The following conclusions are drawn from the work presented in this thesis.

### 6.1.1. *Primary recrystallization of heavily deformed aluminum*

From the work on the measurement of orientation-dependent stored energy of aluminum the following conclusions are drawn.

- The stored energy distribution function for the 88% cold rolled and stress relieved (at 200°C for 15 minutes) can body aluminum specimen can be calculated from the measured X-ray line broadening data.
- The stored energy in orientations with less than the random intensity is not presented due to high error in the stored energy. Reliable stored energy values can however be obtained for all other abundantly represented orientations.
- The stored energy along the  $\beta$ -fiber is about 40 – 77% less than the stored energy of cube texture component after cold rolling. Upon stress relieving at 200°C for 15 minutes the cube texture releases about ~ 7.2 J/g-atom of stored energy, whereas the reduction in stored energy on C, S & B orientations is between 2 and 3.1 J/g-atom. Goss texture component  $\{011\}; \langle 100 \rangle$  has the lowest stored energy before and after the stress relieving process.
- The spread in the stored energy values for the rolling texture components seems to be much higher than for the cube component. In the cold rolled state the scatter in the stored energy for the cube orientation (up to a deviation of 13 degrees from the ideal cube orientation) is found to be between 5 and 15 J/g-atom. For the stress relieved state, the spread is between 2.5 and 7.5 J/g-atom.

From the work on the Monte-Carlo simulation of recrystallization of aluminum the following conclusions are drawn

- According to the texture analysis, in heavily cold rolled aluminum, the nucleation of a cube orientation takes place randomly throughout the specimen, whereas, the nucleation of rolling texture components is not random. The nuclei with orientation C, B and S-components nucleate mainly in the deformed grains of respective cold rolled texture components.
- Nucleation of cube orientation is favored by the condition that  $1.5 < S_{cr}/S_{cr-sr} < 2.5$ . Here,  $S_{cr}$  is the stored energy after cold rolling and  $S_{cr-sr}$  is the stored energy difference between cold rolled and stress relieved states. In this region, the abnormal growth of subgrain of cube orientation might take place and a successful nucleus is formed.
- Assigning a high mobility to grain boundaries with misorientation between  $35^\circ$  and  $55^\circ$  yields a growth advantage for the cube texture. With this growth condition, cube grains grow to a size of  $\sim 1.5$  times that of the grain size of rolling texture components and  $\sim 1.3$  times the size of random texture components.
- The Monte-Carlo model that incorporates proposed nucleation and growth conditions, simulates an excellent selection of cube orientation and also reduction in the strength of rolling texture components.
- The simulated recrystallized microstructures show elongated grains when the migration of grain boundaries between the impinged recrystallized grains is not allowed. However, when this grain boundary migration is allowed to move, the simulated recrystallized microstructures show equiaxed grains.

### 6.1.2. Abnormal grain growth in Fe-3% Si steel

From the analysis on fraction of high mobility grain boundaries, the following conclusions are drawn:

- There is ~40% difference in the fraction of mobile boundaries that surrounds the Goss and main texture components in Fe-Si steels. This is an important factor, which promotes the abnormal grain growth of Goss grains. The boundaries with 20°-45° misorientation have high mobility. This assumption simulates the grain boundary character distribution (GBCD) around the abnormally growing Goss grains as observed in experiments.
- Computer experiments demonstrate that the fractions of  $\Sigma 3$ - $\Sigma 29$  CSL boundaries that surround the Goss and the main texture component correspondingly is 20 and 19%. Such difference between those orientations is too small to explain the abnormal growth of Goss grains by assuming high mobility to CSL boundaries.
- The mobile boundary fractions, namely matrix fraction (MF) and peripheral fraction (PF), are introduced. Abnormal grain growth of a particular orientation can be expected only when the MF value for that orientation in the primary recrystallized matrix is high. In addition it should be higher than that of the other orientations.
- During abnormal grain growth, the value of peripheral fraction (PF) decreases up to a certain point and then it reaches a steady state value.

From the Monte-Carlo simulation of abnormal grain growth of Fe-3% Si conventional electrical steel, the following conclusions can be derived.

- Assumption of high mobility to grain boundaries with misorientation  $20^{\circ}$ - $45^{\circ}$  in Monte-Carlo simulation offers excellent selection of Goss orientation during annealing. However abnormal growth of Goss orientation is realized only when the effect of particle pinning on grain boundary mobility is considered.
- It is shown that the grain size advantage alone cannot be responsible for the growth of Goss grains in the primary recrystallized microstructure. However, abnormally growing grains have low ratio between the total energy of grain boundaries that surround a grain to its grain volume and high number of nearest neighbors.
- The abnormal growth of Goss grains is realized by incorporating the selective particle pinning in the Monte-Carlo simulation. It is pointed out that the precipitate particles grow faster at grain boundaries with high energy (e.g., 1.2 in relative scale) and thus these boundaries are less strongly pinned than low energy boundaries (e.g., 1.1 and 1 in relative scale). This phenomenon facilitates the abnormal growth of Goss grains, as these grains are surrounded by a high number of high-energy boundaries.
- Finally, the decrease in the value of peripheral fraction of mobile boundaries around the growing Goss grain is also simulated by the Monte-Carlo procedure. The steady state PF value corresponds to the steady state growth rate of the abnormally growing Goss grains observed in experiments.

### 6.1.3 Annealing of nanocrystalline Ni and Ni-Fe electrodeposits

The following conclusions are derived from the model proposed to explain the texture transformation in Ni, Ni-20% Fe and Ni-45% Fe nanocrystalline electrodeposits during annealing.

- The analysis of texture of nanocrystalline Ni, Ni-20% Fe and Ni-45% Fe electrodeposits reveals that the (111)-fiber grains are surrounded by a high number of grain boundaries having structures that are highly deviated from the corresponding equilibrium (annealed microcrystalline) grain boundary structures. The proposed model assumes that the grain boundaries with such structure have high mobility. Under the assumption that all the grain boundaries in nanocrystalline materials have non-equilibrium structures, the difference in energy between the nanocrystalline grain boundaries and the corresponding microcrystalline equilibrium structure was calculated. This difference is high for the grain boundaries with a misorientation less than  $15^\circ$  and greater than  $45^\circ$ , therefore these nanocrystalline boundaries should have high mobility. This is the fundamental assumption in the proposed model of texture transformation.
- The cluster analysis does not favor the growth of (111)-fiber texture by grain coalescence mechanism. However, experimental observation demonstrated that as annealing proceeds, intensity of (111)-fiber increases, whereas intensity of (100)-fiber decreases.
- Analysis of possible role of CSL boundaries in the annealing process was also ruled out because fractions of CSL boundaries around the (111) and (100) fibers are around 20%, which is too small a percentage to support the abnormal grain growth observed in these materials. Also the difference between CSL fractions for (111) and (100)-fibers is too small to explain the domination of (111)-fibers observed in the annealing process.

- The Monte-Carlo simulations using the proposed model predict a higher rate of growth of (111)-fiber orientation than any other orientation in the nanocrystalline matrix. This result agrees with x-ray diffraction measurements of texture transformation.
- The proposed model also predicts that as the Fe content increases, the growth of the (111)-fiber is faster than (100)-fiber.
- The model predicts an abnormal grain growth during annealing as observed experimentally.

## 6.2. STATEMENT OF ORIGINALITY

The following aspects of the present work constitute original contributions in the field of annealing textures.

- The measurement and analysis of orientation-dependent stored energy for heavily cold rolled can-body aluminum alloy.
- Development of Monte-Carlo model of recrystallization that incorporates stored energy in deformed grains, restricted nucleation and selective growth. This model predicts the cube texture development during recrystallization of heavily cold rolled aluminum.
- The effect of various fractions of mobile boundaries in abnormal grain growth was evaluated by computer experiments.
- Development of Monte-Carlo procedure that incorporates the effect of grain boundary pinning of growing MnS particles to explain the abnormal grain growth of Goss grain.
- Development of the Monte-Carlo model for texture transformation during annealing of Ni, Ni-20% Fe and Ni-45% Fe nanocrystalline electrodeposits.

### 6.3. RECOMMENDATION FOR FUTURE WORK

For the recrystallization of aluminum

- To understand the importance of selection of nucleation sites, a better description of deformed microstructure in the computer is required. Towards achieving this, as a first step, a fully quantitative characterization of deformed microstructure is necessary. Therefore, careful electron microscopic study is needed for a more detailed description of deformed microstructure.
- Similar to the study described by Juul Jensen [8], orientation relations between the nuclei and the deformed matrices have to be analyzed in different materials for different deformation conditions in order to consolidate the findings and to achieve a more unified model that could explain the recrystallization in different materials.

For the abnormal grain growth of Fe-Si steels

- Electron microscopic technique should be used for characterization of the type of grain boundaries, size distribution and the coarsening rate of precipitates at various types of grain boundaries. This research has to be carried out to improve the understanding of grain boundary pinning by precipitates.
- The description of the microstructure in the computer specimen can be improved in order to accommodate the individual precipitates in the microstructure. Incorporating the kinetics of particle coarsening in the grain growth model, the interrelated mechanisms of grain boundary migration and precipitate coarsening can be studied more directly.

For the annealing of nanocrystalline electrodeposits

- Further examination of grain boundary structure, energy, mobility and solute interaction in nanocrystalline materials would provide a great deal of understanding of their annealing behavior. A role of triple junction in controlling the grain growth

should be established. Careful examination using high-resolution electron microscopic technique should throw some light on this subject.

## REFERENCE

1. F.J.Humphreys and M.Hatherly. *Recrystallization and Related Annealing Phenomena*. Pergamon, Oxford. U.K. (1995)
2. G.I. Taylor. *J. Indl. Met.*, **62**, 307 (1938)
3. J.F.W. Bishop and R.Hill. *Phil. Mag.*, **42**, 414 (1951), *ibid.* p. 1298
4. P. Van Houtte. Proc. *ICOTOM 6*, Tokyo. 428 (1981)
5. U.F. Kocks and H. Chandra. *Acta Metall.* **30**, 695 (1982)
6. H.T. Jeong. *Ph.D. Thesis*, Seoul National Univ. (1997)
7. J.H.Driver, D.Juul Jensen and N.Hansen. *Acta Metall. Mater.* **42**, No.9, 3105 (1994)
8. D.Juul Jensen. *Acta Metall. Mater.* **43**, No.11, 4117 (1995)
9. C.Cheung, G.Palumbo and U.Erb. *Scripta Metall. Mater.*, **31**, No.6, 735 (1994)
10. U.Klement, U.Erb, A.M.El-Sherik and K.T.Aust. *Mater. Sci. Eng.*, **A203**, 177 (1995)
11. S.C.Mehta, D.A.Smith and U.Erb. *Mater. Sci. Eng.* **A204**, 227 (1995)
12. M.P Anderson, D.J.Srolovitz, G.S. Grest, and P.S. Sahni, *Acta Metall.*, **32**, No.5, 783 (1984)
13. D.J.Srolovitz, G.S.Grest and M.P.Anderson, *Acta Metall.* **34**, No.9, 1833 (1986)

14. M.P.Anderson and A.D.Rollett, (editors), *Simulation and Theory of Evolving Microstructure*, The Minerals, Metals and Materials Society, New York (1990)
15. D. Hinz, and J.A. Szpunar. *Phys Rev.*, **B52**, 9900, (1995)
16. H.Margolin, *Recrystallization, Grain Growth and Textures*. ASM, Ohio, USA (1966)
17. F.Haessner, *Recrystallization of Metallic Materials*, Dr. Riederer-Verlag. GMBH Stuttgart (1978)
18. R.D.Doherty, D.A.Hughes, F.J.Humphreys, J.J.Jonas, D.Juul Jensen, M.E.Kassner, W.E.King, T.R.McNelly, H.J.McQueen and A.D.Rollett, *Mat. Sci.and Eng.* A238, 219 (1997)
19. C.S.Barrett, *Trans. Metall. Soc. AIME*. 135. 296 (1939)
20. E. Orowan, *Nature*. 149, 643 (1942)
21. G.Y.Chin. in *Textures in Research and Practice*. Eds. Grewen and Wassermann. Berlin. 236 (1969)
22. J.Hjelen, R. Ørsund and E.Nes. *Acta Metall. Mater.* **39**, No. 7, 1377 (1991)
23. N.Hansen. *Mat. Sci. and Tech.* 6. 1039 (1990)
24. N.Hansen and D.Juul Jensen. in *Hot Deformation of Aluminum alloys*, ed. Langdon et al. TMS, Warrendale. 3. (1991)
25. B.Bay, N.Hansen, D.A.Hughes and D.Kuhlmann-Wilsdorf, *Acta Metall.Mater.* 40, No. 2., 205 (1992)
26. F.Adcock. *J. Inst. Metals.* **27**, 73 (1922)
27. R.K.Ray, W.B.Hutchinson and B.J.Duggan. *Acta Met.*, **23**, 831 (1975)
28. R.D.Doherty, p23 in Ref [17]
29. I.L.Dillamore, P.L.Morris, C.J.E.Smith and W.B.Hutchinson. *Proc. Roy. Soc. (London)* **329A**, 405 (1972)
30. M.Hatherly and A.S.Malin. *Scripta Metall.*, **18**, 449 (1984)
31. T.Kamijo, A.Fujiwara and H.Inagaki. *Scripta Metall. Mater.*, **25**, 949 (1991)

32. M.B.Bever, D.L.Holt and A.L.Titchener, in *Progress in Materials Science*, eds. B.Chalmers, J.W.Christian and T.B.Mssalski, Pergamon Press, Oxford, **17**, 1 (1973)
33. L.Himmel, (ed), *Recovery and Recrystallization of metals*, Interscience Publishers, New York, 63 (1963)
34. P.Gordon, *Trans. Metall. Soc. AIME*, **203**, 403 (1955)
35. H.U.Astrom, *Acta Metall.* **3**, 508 (1955)
36. M. Matsuo, S. Hayami and S. Nagashima, *adv. X-ray anal.*, **14**, 214, (1971)
37. H. Takechi, H. Katoh and S. Nagashima, *Trans. AIME*, **242**, 56. (1968)
38. R. L. Every and M. Hatherly, *Texture*, **1**, 183. (1974)
39. I. L. Dillamore, C. J. E. Smith, and T.W. Watson, *Mat. Sci. J.*, **1**, 49, (1967)
40. J. S. Kallend and Y. C. Huang. *Met. Sci.*, **18**, 381. (1984)
41. N.Rajmohan, Y.Hayakawa, J.A.Szpunar and J.H.Root, *Acta Mater.* **45**, No.6, 2485 (1997)
- 41a. D. Vanderschueren, *Proc. Conf. On 'Physical metallurgy of IF steels'*, Tokyo, Japan, Iron and Steel Institute of Japan, 145. (1994)
42. J.K.Mackenzie, *Biometrika*, **45**, 229 (1958)
43. J.M.Burgers, *Proc. Phys Soc (London)*, **52**, 23 (1940)
44. W.T.Read and W.Shockley, *Phys. Rev.* **78**, 275 (1950)
45. G.A.Chadwick, D.A.Smith, (ed), *Grain Boundary Structure and Properties*, Academic Press, New York (1976)
46. M.L.Kronberg, F.H.Wilson, *Trans. Metall. Soc. AIME*, **185**, 501 (1949)
47. D.G.Brandon, B.Ralph, S.Ranganathan and M.S.Wald, *Acta Metall.* **12**, 813 (1964)
48. H.Grimmer, W Bollmann and D.H.Warrington, *Acta Cryst.* **A30**, 197 (1974)
49. D.G.Brandon, *Acta Metall* **14**, 1479 (1966)
50. A.H.King and D.A.Smith, *Acta Cryst.* **A36**, 335 (1980)
51. H.Brooks in *Metal Interface*, American Society for Metals (1952)

52. C.G. Dunn, and F. Lionetti. *AIME Trans.* **185**, 125 (1949)
53. C.G. Dunn, F.W. Daniels, and M.J. Bolton. *AIME Trans.* **188**, 368 (1950)
54. C.G. Dunn, F.W. Daniels, and M.J. Bolton. *AIME Trans.* **188**, 1245 (1950)
55. C. Herring, *Physics of Powder Metallurgy*, New York, Mac Graw Hill, 143 (1961)
56. C.S. Smith, *Trans. AIME.* **175**, 15 (1948)
57. G.C. Hasson and C. Goux. *Scripta Metall.* **5**, 889 (1971)
58. R. Viswanathan and C.L. Bauer. *Acta Metall.* **21**, 1099 (1973)
59. D.W. Demianczuc and K.T. Aust. *Acta Metall.* **23**, 1149 (1975)
60. G. Gottstein and L.S. Shvindlerman. *Scripta Metall.* **27**, 1521 (1992)
61. R.A. Vandermeer and H. Hu. *Scripta Metall.*, **42**, 3071 (1994)
62. G. Gottstein and F. Schwarzer. *Materials Science Forum*, **94-96**, 187 (1992)
63. J. Harase, R. Shimizu, K. Kuroki, T. Nakayama, T. Wada, and T. Watanabe. (1986)  
*Proc. 4th Japan Inst. Metals Symp. on Grain Boundary Structure and Related Phenomena. Supplement to Trans. Japan Inst. Metals*, **27**, 563.
64. J. Harase, R. Shimizu, and D.J. Dingley. *Acta Metall. Mater.*, **39**, No.5, 763 (1991).
65. R. Shimizu, J. Harase, and D.J. Dingley. *Acta Metall. Mater.*, **38**, No.6, 973 (1990)
66. G. Abbruzzese, S. Fortunati, and A. Campopiano. *Mat. Sci. Forum.* **94-96**, 405 (1992).
67. P. Lin, G. Palumbo, J. Harase, and K.T. Aust. *Acta Mater.* **44**, No.12, 4677 (1996)
68. J. Harase. *Materials Sci. Forum.* **94-96**, 419 (1992)
69. Y. Yoshitomi, Y. Ushigami, J. Harase, T. Nakayama, H. Matsui, and N. Takahashi.  
*Mater. Sci Forum.* **113-115**, 715 (1992)
70. K.T. Aust, and J.W. Rutter. *Trans. Metall. Soc. AIME*, **215**, 119 (1959)
71. K.T. Aust, and J.W. Rutter. *Trans. Metall. Soc. AIME*, **215**, 820 (1959)
72. B. Liebmann, K. Lücke, and G. Masing. *Z. Metallk.* **47**, 57 (1956)

73. R.A.Vandermeer and D.Juul Jensen, *Interface Science*, **6**, 95 (1998)
74. A.N.Kolmogorov, *Izv. Akad. Nauk. USSR-Ser-Matemat.*, **1**, No. 3. 355 (1937)
75. W.A.Johnson and R.F.Mehl, *Trans. Metall. Soc. AIME*, **135**, 416 (1939)
76. M.Avrani, *J. Chem. Phys.*, **7**, 1103 (1939)
77. R.F.Mehl, in *ASM Metals Handbook*, ASM, Metal Park, Ohio, 259 (1948)
78. J.E.Burke and D.Turnbull, *Prog. Metal Phys.* **3**, 220 (1952)
79. J.W.Christian. *The Theory of Transformation in Metals and Alloys. Part I.* Pergamon Press, Oxford. 424 (1975)
80. J.W.Christian. *The Theory of Transformation in Metals and Alloys*, Pergamon, Oxford (1965)
81. W.G.Burgers. *Rekristallisation. Verformter Zustand und Erholung.* Leipzig. (1941)
82. F.J.Humphreys. *Acta Metall.* **25**. 1323 (1977)
83. B.Bay and N.Hansen. *Metall. Trans.* **A10**. 279 (1979)
84. T.Furu. R.Ørsund and E.Nes. *Acta Metall. Mater.* **43**, No. 6, 2209 (1995)
85. R.D.Doherty and J.A.Szpunar. *Acta Metall.* **32**, No.10, 1789 (1984)
86. C.V.Thompson. H.J.Frost and F.Spaepen. *Acta Metall.*, **35**, 887 (1987)
87. P. Yang. O. Engler and G Gottstein. *Mat. Sci. Forum*, **157-162**. 1109 (1994)
88. R.D.Doherty. K.Kashyap and S.Panchanadeeswaran. *Acta Metall. Mater.* **41**, No. 10. 3029 (1993)
89. I. Samajdar. R D Doherty. S Panchanadeeswaran and K.Kunze. *Mat. Sci. Forum.* **157-162**. 2025 (1994)
90. O.Engler. E.Sachot. J.C.Ehrstrom. A.Reeves and R.Shahani. *Mat. Sci. Tech.*, **12**. 717 (1996)
91. I.Andersen. O.Grong. and N.Ryum. *Acta metall.mater.*, **43**, No.7. 2689 (1995).
92. D.J.Srolovitz. G.S.Grest. and M.P.Anderson, *Acta Metall.*, **33**, No.12, 2233 (1985)

93. H.Gleiter in *Proc. Second Risø Int. Symp. On Materials Science*, edited by N.Hansen, A.Horsewell, T.Leffers and H.Lilholt, Risø National Laboratory, Roskilde, Denmark. pp15-21 (1981)
94. C.Suryanarayana, *Int. Mater. Rev.*, **40**, No.2, pp 41-64 (1995)
95. M.A.Fortes, *Mater. Sci. Forum*, **126-128**, pp 343-346 (1993)
96. L.C.Chen and F.Spaepen. *Nature*. **336**. pp 366-368 (1988)
97. K.Lu. *Scripta Metall. Mater.*. **25**. No.9, pp 2047-2052 (1991)
98. V.Y.Gertsman and R.Birringer. *Scripta Metall. Mater.*. **30**. pp 577-581 (1994)
99. A.Cziraki, Zs.Tonkovics, I.Gerocs, B.Fogarassy, I.Groma, E.Toth-Kadar, T.Tarnoczi and I.Bakonyi. *Mater. Sci. Eng. A179/A180*, pp 531-535 (1994)
100. F.Czerwinski, H.Li, M.Megret and J.A.Szpunar. *Scripta Mater.*, **37**, No.12, pp 1967-1972. (1997)
101. A.M.El-Sherik, K.Boylan, U.Erb, G.Palumbo and K.T.Aust, *MRS Symp. Proc.*, **238**, 727 (1992)
102. K.Boylan, D.Ostrander, U.Erb, G.Palumbo and K.T.Aust. *Scripta Metall. Mater.*, **25**. pp 2711-2716 (1991)
103. N.Wang, Z. Wang, K.T.Aust and U.Erb. *Acta Mater.*, **45**, No. 4, pp 1655-1669 (1995)
104. P.Knauth, A.Charai and P.Gas. *Scripta Metall. Mater.*, **28**, 325 (1993)
105. M.P.Anderson. in *Proc. 2<sup>nd</sup> Risø Symposium*. Risø, Denmark. ed. Hansen. 15 (1986)
106. D.J.Srolovitz, M.P.Anderson, P.S.Sahni and G.S.Grest, *Acta Metall.* **32**, No.5, 793 (1984)
107. D.J.Srolovitz, M.P.Anderson, G.S.Grest and P.S.Sahni, *Acta Metall.* **32**. No.9, 1429 (1984)
108. D.J.Srolovitz, M.P.Anderson, P.S.Sahni and G.S.Grest, *Acta Metall.* **33**, No.3, 509 (1985)
109. A.D.Rollett, D.J.Srolovitz, and M.P.Anderson, *Acta Metall.* **37**, No.4, 1227 (1989)
110. A.D.Rollett, M.J.Luton, and D.J.Srolovitz, *Acta Metall. Mater.* **37**. No.1. 43 (1992)

111. D.J.Srolovitz, G.S.Grest, M.P.Anderson and A.D.Rollett, *Acta Metall.* **36**, No.8, 2115 (1988)
112. A.D.Rollett, D.J.Srolovitz, R.D.Doherty and M.P.Anderson. *Acta Metall.* **37**, No.2, 627 (1989)
113. N. Metropolis, A.W. Rosenbluth, M.N. Rosenbluth, A.H.Teller, and E.Teller. *J.Chem. Phys.*,**21**.1087 (1953)
114. Ph.Tavernier and J.A.Szpunar. *Acta Metall. Mater.*, **39**, No.4, 549 (1991)
115. Ph.Tavernier and J.A.Szpunar, *Acta Metall. Mater.*, **39**, No.4, 557 (1991)
116. D.Turnbull, *Trans. AIME.* **191**. 661 (1951)
117. H.J.Bunge, *Texture Analysis in Materials Science – Mathematical Methods*. Butterworths. London (1982)
118. A. Morawiec. J.A.Szpunar and D.C.Hinz. *Acta metall. mater.*. **41**, No.10. 825 (1993)
119. E.Nes. *Acta Metall. Mater.* **43**. No.6. 2189 (1995)
120. O.Engler. *Mater.Sci.Technol.* **12**. 859 (1996)
121. W.B.Hutchinson. *Metal Sci.*. **8**. 185 (1974)
122. J.C.Blade and P.L.Morris. *Proc. 4<sup>th</sup> Int. conf. On Textures*. Cambridge. 171 (1975)
123. B. L. Averbach. M. B. Bever. M. F. Comerford and J. S. Leach: *Acta Metall.*. **4**. 477 (1956)
124. L.M.Clarebrough. M.E.Hargreaves and M.H.Loretto in *Recovery and Recrystallization of Metals. Proceedings of symposium held in New York*. Edited by L.Himmel. Interscience Publishers. New York, 1963. 63
125. H. J. Bunge: *Z. Metallkd.*. 1965. **56**. 872
126. G. R. Stibitz: *Phys Rev.*. 1937. **49**. 862
127. G. R. Stibitz: *Phys Rev.*. 1947. **8**. 147
128. J. Imhof: *Textures and Microstructures*, 1982, **4**, 189
129. J. Imhof: *Textures and Microstructures*, 1982, **5**, 73

130. J. Imhof: *Phys. Stat. Sol. (B)*, 1983, **120**, 321
131. W.J.M. Tegart: 'Elements of Mechanical Metallurgy', 91; 1966, The Macmillan Company, New York
132. C.S. Barrett: 'Structure of metals, crystallographic methods principles and data', 2<sup>nd</sup> Edition, 532; 1952, New York, McGraw-Hill
133. J.Hirsch and K.Lucke: *Acta Metall.* 1988, **36**, 2883
134. R.H.Goodenow, *Trans ASM.* **56**, 804 (1966)
135. P.A.Beck, P.R.Sperry and H.Hu. *J. Appl. Phys.* **21**, 420 (1950)
136. S.Kohara, M.N.Parthasarathi and P.A.Beck. *Trans. AIME*, **212**, 875 (1958)
137. M.N.Parthasarathi and P.A.Beck. *Trans. AIME*, **221**, 831 (1961)
138. S.Kohara, M.N.Parthasarathi and P.A.Beck, *J. Appl. Phys.* **29**, 1125 (1958)
139. C.D.Graham Jr and R.W.Cahn. *Trans. AIME J. Metals.* 517 (1956)
140. A.P.Sutton and R.W.Balluffi. *Acta metall.*, **35**, No.9., 2177 (1987)
141. E.Lindh, B.Hutchinson and P.Bate. *Mater. Sci and Forum*, **154-162**, 997 (1994)
142. N.P.Goss. *Trans. ASM.* **23**, 511 (1934)
143. Y.Inokuti, and C.Maeda. *Trans. Iron Steel Inst. Jpn.*, **24**, 657(1984)
144. M.Matsuo. *ISIJ International.* **29**, 809 (1989)
145. R.Shimizu, and J.Harase. *Acta Metall.* **37**, 1241 (1989)
146. N.C.Pease, D.W. Jones, M.H.L.Wise, and W.B.Hutchison, *Met. Sci.*, **15**, 203 (1985)
147. A. Bottcher, T. Gerber and K. Lucke. *Materials Science and Technology.* **8**, No.1, 16 (1992)
148. D.Wolf, *Phil. Mag.* **B59**, 667 (1989)
149. J. Haraze, R. Shimizu, K. Kuroki, T. Nakayama, T. Wada and T. Watanabe, *Proc. 4th Japan Inst Metals Symp. on Grain Boundary Structure and Related Phenomena, Supplement to Trans. Japan Inst. Metals*, **27**, 563 (1986)

150. Harase, J. and Shimizu, R. (1988). *Trans. Iron Steel Inst. Jpn*, **29**, 388
151. Y. Hayakawa, J.A.Szpunar, G.Palumbo and P.Lin, *Journal of Magnetism and Magnetic Materials*, **160**,143 (1996)
152. Y. Hayakawa and J.A. Szpunar, *Acta mater.*, **45**, No.3, 1285 (1997)
153. Y. Hayakawa and J.A. Szpunar, *Acta mater.*, **45**, No.11, 4713 (1997)
154. Y. Hayakawa and J.A. Szpunar. Texture of Materials- ICOTOM-11, *Proceedings of the Eleventh International Conference on Textures of Materials*, Xi'an, China, International Academic Publishers. **1**. 435 (1996)
155. Y. Hayakawa. M. Muraki and J.A. Szpunar, *Acta Mater.*, **46**. 1063 (1998)
156. D.B. Titorov, *Fiz. metal. metalloved.*, **35**, No. 6, 1299 (1973)
157. D.B. Titorov, *The physics of Metals and Metallography*, **77**, No.1, 73 (1994)
158. T. Watanabe. *Mat. Sci. Forum.* **94**, 209 (1992)
159. B. Ralph. K.B. Shim. Z. Huda. J. Forley and M. Edirisinghe. *Mat.Sci.Forum.* **94-96**. 129 (1992)
160. S.E. Babcock and R.W. Balluffi. *Acta metall.*, **37**, 2367 (1989)
161. W. Hahn and H. Gleiter. *Acta metall.*, **29**, 601(1980)
162. H. Grimmer. *Acta cryst.*, **A30**, 685 (1974)
163. V.YA. Gol'dshteyn. O.P.Bobkova and S.G.Nitskaya. *Phys. Met. Metall.* **54**. No.3. 85 (1982)
164. N.L.Peterson. *Int Metals Rev.*, **28**. No.2. 65 (1983)
165. V.T.Borisov. V.M.Golikov. and G.V.Scherbedinskiy, *Phys. Met. Metall.* **17**, 80 (1964)
166. J. Pelleg. *Phil Mag* **14**. 595 (1966)
167. T. Gladman. *Proc Roy Soc Lond* **A294**. 298 (1966)
168. T. Gladman. *Scripta Metall. Mater.* **27**. 1569 (1992)
169. I.Ohnuma. H. Ohtani. K.Ishida and T.Nishizawa, *Mater. Sci. Forum*, **204**, pt 1, 313 (1996)

170. A.D.Rollett, D.J.Srolovitz, R.D.Doherty, M.P.Anderson and G.S.Grest, *Simulation and theory of Evolving Microstructure*, Ed. M.P.Anderson and A.D.Rollett, The Min. Met. & Mat. Soc. 103 (1990)
171. P.R.Rios, *Acta metall. mater.*, **40**, No.4, 649 (1992)
172. R.Brandt, G.Abbuzzese and K.Lücke, *Mater. Sci. Forum*, **204-206**, *Grain Growth in Polycrystalline Materials II*, Part I. Ed. H.Yoshinaga, T.Watanabe, N.Takahashi, 295 (1996)
173. I.M.Lifshitz and V.V.Slezhov, *Z.eksper.teor.Fiz*, **35**, 479 (1958)
174. C.Wagner. *Z.Electrochem.* **65**, 581 (1961)
175. M.V.Speight. *Acta metall.* **16**, 133 (1968)
176. H.O.Kirchner. *Met. Trans.* **2**, 1971 (1971)
177. R.D.Vengrenovitch. *Acta metall.* **30**, 1079 (1982)
178. J. J. Hoyt. *Acta metall. mater.* **39**, No. 9, 2091 (1991)
179. W.M.Swift. *Met. Trans.* **4**, 153 (1973)
180. W.M.Swift. *Met. Trans.* **4**, 842 (1973)
181. P.Hellmana and M.Hillert. *Scand. J. Metall*, **4**, 211 (1964)
182. N.Rajmohan. J.A.Szpunar and Y.Hayakawa. *Acta Metall.* **47**, No.10, 2999 (1999)
183. N.Rajmohan. J.A.Szpunar and Y.Hayakawa. *Mat. Sci. & Eng.* **A259**, 8 (1998)
184. T.R.Haasz. K.T.Aust. G.Palumbo. A.M.El-Sherik and U.Erb. *Script. Metall. Mater.* **32**, No.3, pp 423-426 (1995)
185. X.Zhu. R.Birringier. U.Herr and H.Gleiter. *Phys. Rev.* **B35**, 9085 (1987)
186. H.Gleiter. *Prog. Mater.Sci.* **33**, 223 (1989)
187. R.Birringier. *Mater. Sci. Eng.* **A117**, pp 33-43 (1989)
188. R.Z.Valiev. A.V.Korznikov and R.R.Mulyukov, *Mater. Sci. Eng.* **A168**, pp 141-148 (1993)

189. W.Wunderlich, Y.Ishida and R.Maurer, *Scripta Metall. Mater.*, **24**, pp 403-408. (1990)
190. V.Y.Gertsman, R.Birringer, R.Z.Valiev and H.Gleiter, *Scripta Metall. Mater.* **30**, 229 (1994)
191. C.A.Melendres, A.Narayanasamy, V.A.Moroni and R.W.Siegel, *J. Mater. Res.* **4**, 1246 (1989)
192. J.A.Eastman, M.R.Fitzsimmons and L.J.Thompson, *Phil. Mag.* **B66**, 667 (1992)
193. G.J.Thomas, R.W.Siegel and J.A.Eastman, *Scripta metall.*, **24**, 201 (1990)
194. R.W.Siegel, in *Metal Interfaces: Atomic level structure and properties*, edited by D.Wolf and S.Yip, Chapman and Hall, London, pp 431-460 (1992)
195. S.R.Phillpot and D.Wolf, *Scripta metall. Mater.*, **33**, No.8, pp 1245-1251 (1995)
196. P.Keblinski, S.R.Phillpot, D.Wolf and H.Gleiter, *Acta Mater.*, **45**, No.3, pp 987-998 (1997)
197. V.Y.Gertsman, Y.P.Lin, A.P.Zhilyaev and J.A.Szpunar, *Acta Mater.* (submitted)
198. C.Cheung, F.Djuanda, U.Erb and G.Palumbo, *NanoStructured Mater.*, **5**, No.5, pp 513-523 (1995)
199. A.Cziraki, I.Geroes, E.Toth-Kadar and I.Bakonyi, *NanoStructured Mater.*, **6**, pp 547-550 (1995)
200. R.Z.Valiev, V Y Gertsman, and O.A.Kaibyshev, *Scripta metall. Mater.*, **17**, 852 (1983)
201. R.Z.Valiev, V Y Gertsman, and O.A.Kaibyshev, *Scripta metall. Mater.*, **18**, 639 (1984)
202. D.Wolf, *Acta Metall.* **37**, No.7, 1983 (1989)
203. D.Wolf, *Acta Metall.*, **37**, No 10, 2823 (1989)
204. D.Wolf, *Acta Metall Mater.* **38**, No.5, 781 (1990)
205. C.Kittel, *Introduction to solid state physics*, 6<sup>th</sup> edition, John Wiley & Sons Inc., New York, 61 (1986)
206. N.Rajmohan, J A Szpunar and Y.Hayakawa, *Textures and microstructures*, **32**, 153 (1998)

207. M.Hillert, *Acta Metall.*, **13**. 227 (1965)